Topological matter explored with quantum gases

Jean Dalibard
Collège de France, chair *Atoms and Radiation*

Lecture series 2018

Translated from French by Raphaël Saint-Jalm

Contents

Introduction

This year's lecture series is an introduction to the study of topological phases of matter. This research field is developing fast, and its pioneers, David J. Thouless, F. Duncan M. Haldane, and J. Michael Kosterlitz, have been awarded the 2016 physics Nobel prize. Kosterlitz and Thouless have contributed to the emergence of the notion of *topological phase transitions*. We have studied it in details in last year's lecture and we will not discuss it further here. The contribution of Haldane and Thouless consisted in showing that some states of matter could be classified according to a different order than the usual geometrical order. It is the general subject of this set of lectures.

The geometrical order refers to simple properties related to spatial symmetries, such as rotation invariance or point reflection. The topological order, more subtle to point out, sets an equivalence between different types of forms – for the physicist, different phases of matter – which are *a priori* not similar. Two objects are said to be topologically equivalent if one can be turned into the other by a continuous transformation, without having to cross any singularity. A sphere, an orange, and a bowl thus belong to the topological class of *non-pierced objects*, whereas a torus, a doughnut, and a cup of coffee belong to the topological class of *singly-pierced objects* (figure 1). A celebrated example of the presence of a topological order in physics is the quantization of the Hall resistivity in the framework of the quantum Hall effect, as represented on figure 2.

Very often, the topological nature of a phase stays hidden if one only looks at the bulk of the material, and it reveals itself only when two non-equivalent phases of this material are placed side by side. Singularities then appear at the interface between these two phases, which are called *edge states*. They play an important role both at a fundamental level and for applications, in particular in photonics, as we will see in several examples

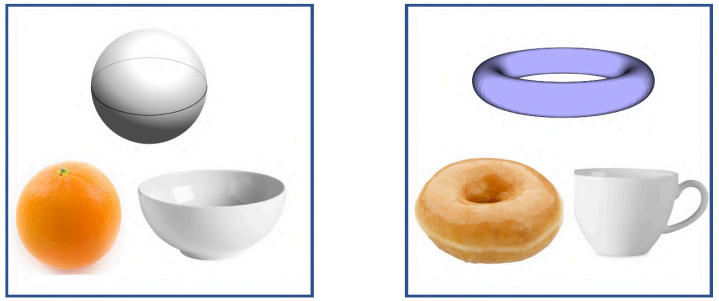

Figure 1. *A topological classification obtained by counting the numbers of handles of an object. This classification is robust, since an object stays in the same class when it is slightly distorted, and it does not depend on potential spatial geometrical symmetries of the object.*

in the following.

The emergence of topology in physics is relatively new. In his famous popularization book *The Great Physicists, from Galileo to Einstein* published in 1961, George Gamow cited topology as the only branch of mathematics (along with number theory) that had no application in physics[1]. The

[1]Gamow wrote: "When Einstein wanted to interpret gravity as the curvature of four-dimensional, space-time continuum, he found waiting for him Riemann's theory of curved multidimensional space. When Heisenberg looked for some unusual kind of mathematics to describe the motion of electrons inside of an atom, non-commutative algebra was ready for him. Only the number theory and topology (analysis situs) still remain purely mathematical disciplines without any application to physics. Could it be that they will be called to help in our further understanding of the riddles of nature?" However, one should moderate Gamow's remark by remembering that at the end of the XIXth century, physicists like Thomson or Maxwell looked at the topology of knots and links as possible models of atomic

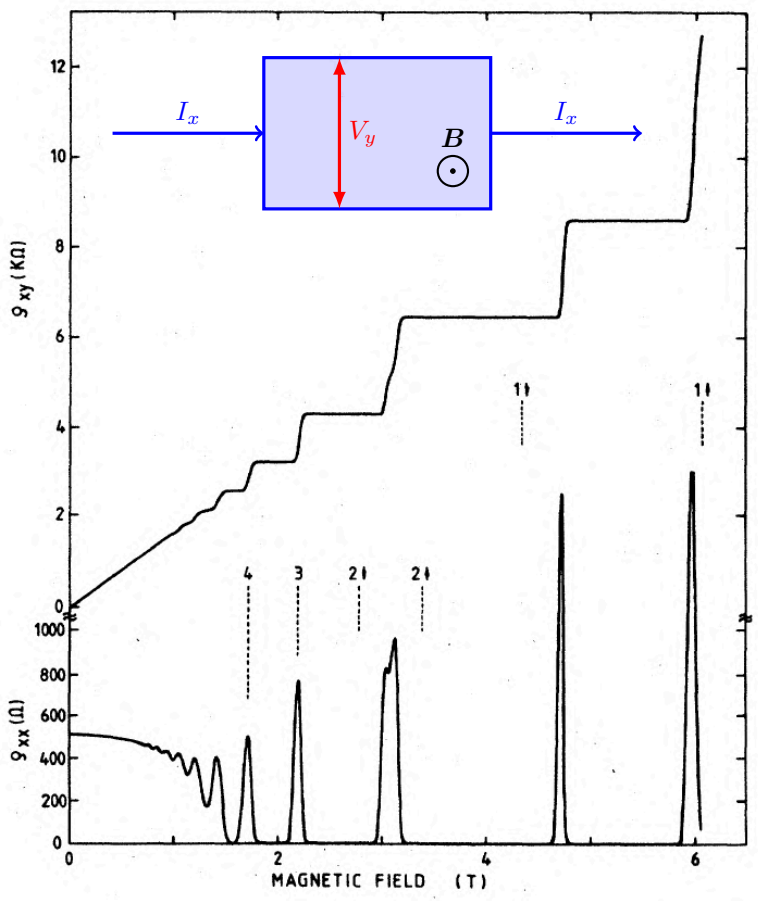

Figure 2. *An example of the manifestation of a topological order in a 2D electron gas in the presence of a large magnetic field: during a quantum Hall effect experiment, the measured Hall resistivity ρ_{xy} presents quantized plateaus as the magnetic field is varied; in this measurement a current I_x runs in a rectangular sample of size $L_x \times L_y$ and the voltage V_y across the sample is measured. This quantization is robust: it survives in the presence of a (moderate) disorder within the sample. Figure extracted from Von Klitzing (1986).*

situation changed completely at the turn of the 80's, in particular with the pioneering works of Thouless, Kohmoto, et al. (1982) and Haldane (1983). The notions of topology initially introduced in the context of the quantum Hall effect and of magnetic chains have been developed to give rise to the concepts of topological insulators and topological superconductors (Hasan & Kane 2010; Qi & Zhang 2011; Bernevig & Hughes 2013).They now nourish many domains of physics; the reader can find several examples in the *Commentary/Focus* that the journal *Nature Physics* has published in July 2016, with the contributions of Asorey (2016), Beenakker & Kouwenhoven (2016), Huber (2016), and Lu, Joannopoulos, et al. (2016) and Goldman, Budich, et al. (2016).

An essential feature of the classification according to topology is the notion of robustness. A topological class – in mathematics or in physics – is in general characterized by an integer number. A typical example is a belt that can be twisted before fastening the two ends: a belt is normally used without any twist, but one can twist it N times before closing it. Once the belt is attached, it is not possible to untwist it with smooth distortions. The number of twists N is therefore robust. This robustness is particularly important in physics. It indicates that a topological phase of matter displays certain properties that will not change if one adds (in a reasonable amount) disorder or impurities. This is what allows the quantum Hall effect to be used as a metrological standard. In the following, we will also see how this robustness is harnessed to realize "topological lasers", whose properties are almost insensitive to their environment (St-Jean, Goblot, et al. 2017; Bandres, Wittek, et al. 2018).

As written above, the topic of topological phases of matter has become extremely vast and it is impossible to cover it exhaustively[2]. Here we will limit our scope to atomic and photonic systems. We will focus in particular on spatially periodic setups; the atoms will thus evolve in an optical lattice formed by stationary light-waves, and the photons will propagate in periodical arrays of wave guides. The concepts of topology can also be applied to non-periodic systems, such as quasi-crystals (see for example Kraus & Zilberberg (2016) and Dareau, Levy, et al. (2017)), but their mathematical

structure. I thank Benoît Douçot for an interesting discussion on this subject.

[2] In 2017, 3115 articles have been uploaded on the database arXiv-physics which contained the words *topology* or *topological* in their title or their abstract. Some examples are shown on figure 3.

Figure 3. *Three recent (2017 and 2018) journal covers about topology.*

description is much more involved. Another limitation concerns the dimension of space: in order to simplify the discussion, we will consider 1D or 2D systems, even though the concepts of topology can be extended to three or more dimensions (for example, see Zhang & Hu (2001)). We should also mention that most of the situations that we will consider involve systems of particles without interactions, for which the topological properties are most simply evidenced.

Even with all these limitations, the subjects that we wish to cover remain plentiful and we will not be able to cite all the theoretical developments nor all the experiments that have been performed in the last years in photonics and atomic systems. Readers wishing to have a more complete bibliography can refer to two recent review articles, Ozawa, Price, et al. (2018) and Cooper, Dalibard, et al. (2018).

The outline of the lecture is the following:

- The first chapter will be dedicated to the presentation of the basic notions that will be used throughout the next chapters: on the one hand the notion of *geometrical phase* (Berry 1984) and on the other hand the notion of energy bands for a particle evolving in a spatially periodic potential.
- In the second chapter we study a simple 1D model, initially proposed by Su, Schrieffer, et al. (1979): the SSH model. With this study we will emphasize the role of the edge states and we will say a few words about topological superconductors with the Majorana modes of the 1D model proposed by Kitaev (2001).
- The third chapter will also focus on 1D problems (in particular the model of Rice & Mele (1982)), but now with an explicit time dependence, which will naturally bring us to 2D problems. In particular we will detail the notion of topological pumps (Thouless 1983).
- In chapter 4 we will start discussing 2D problems by first considering the graphene-like hexagonal lattice. Following arguments initially developed for the Hall effect (Thouless, Kohmoto, et al. 1982), we will determine which conditions on the *Berry curvature* provide a 2D energy band with a topologically non-trivial character, and we will detail how this Berry curvature can be experimentally measured.
- Chapter 5 deals with the model proposed by Haldane (1988) to generate topological 2D bands. We will see how this idea can be implemented with atomic and photonic systems. We will describe in details the bulk-edge correspondence and we will explain how the edge channels can be observed in these systems.
- The last chapter will be dedicated to the realization of setups close to the "traditional" quantum Hall effect with atoms or photons, with a uniform synthetic magnetic field applied to a sample. We will explain how the integer number characterizing a topological phase (the Chern number) can be measured and we will conclude with some research perspectives in this direction.

I am extremely grateful to Raphael Saint-Jalm for undertaking the difficult task of translating these notes from French to English.

Chapter I

From the Berry phase to the topology of an energy band

In this chapter, we establish the important notions that will be used throughout this lecture series. The first notion is the *geometrical phase*, also called *Berry phase*, which indicates how a physical system evolves when its control parameters are slowly varied. This notion is important in particular when these parameters go back to their initial value at the end of the evolution. We will use this notion in the context of quantum physics, but it is also relevant in classical physics, and Foucault's pendulum is one of its striking illustrations.

We will often work with two-level systems, which are systems for which the Hilbert space has dimension 2. We will therefore briefly recall some important features of the physics describing a spin 1/2, in particular the representation of the state of such a spin or pseudo-spin on the *Bloch sphere*.

As announced in the overall introduction, this set of lectures is centered on the emerging topological properties of particles moving in a spatially periodic potential: $V(x) = V(x + a)$ for a 1D problem. We will summarize the specific properties of these periodic systems, in particular Bloch's theorem and the notion of energy bands. Finally, we will present a first example of a topological system, the SSH model, named after those who proposed it, Su, Schrieffer, and Heeger.

1 The geometrical phase in quantum physics

Throughout this year's lectures, the notion of geometrical phase, also called *Berry phase*, will be used intensively. This notion, introduced[1] by Michael Berry in 1984, pertains to the adiabatic evolution of a quantum system. This system is initialized at $t = 0$ in a given eigenstate of a Hamiltonian that depends on a control parameter denoted by $\boldsymbol{\lambda}$, which can be a scalar or a vector with several real components $\boldsymbol{\lambda} = (\lambda_1, \lambda_2, \ldots)$. The Hamiltonian will thus be referred to as $\hat{H}_{\boldsymbol{\lambda}}$. We consider the case where the parameter $\boldsymbol{\lambda}$ varies in time [$\boldsymbol{\lambda} = \boldsymbol{\lambda}(t)$], but this variation is assumed to be arbitrarily slow. Moreover, we are interested in the case where $\boldsymbol{\lambda}$ describes a loop in the parameter space during the time interval T:

$$\boldsymbol{\lambda}(T) = \boldsymbol{\lambda}(0). \tag{1}$$

If the quantum state that is being followed always stays non-degenerate between 0 and T, the adiabatic theorem states that the final state of the system is the same as the initial state *up to a phase*:

$$|\psi(T)\rangle = \mathrm{e}^{\mathrm{i}\Phi} |\psi(0)\rangle. \tag{2}$$

The phase factor Φ is the sum of two terms:

- The first one corresponds to the *dynamical phase*, which is the integral over time of the energy $E(t)$ (up to a factor $1/\hbar$).

[1] Also note the pioneering works of Pancharatnam (1956) in optics, and of Mead & Truhlar (1979) in molecular physics.

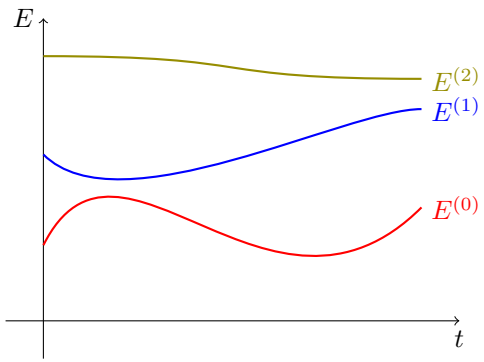

Figure 1. *Evolution in time of the eigenenergies of a quantum system driven by an external parameter* $\boldsymbol{\lambda}$*. We assume that the levels considered here are non-degenerate at all times* t*.*

- The second one is the *geometrical phase*, which depends only on the loop described by the parameter $\boldsymbol{\lambda}(t)$.

The goal of this first section is to introduce the formalism that is needed to determine this phase, which will come back under several forms in the following chapters.

1-1 The adiabatic approximation at zeroth order

Let us start with a Hamiltonian $\hat{H}_{\boldsymbol{\lambda}}$ for which a basis of eigenstates $\{|\psi_{\boldsymbol{\lambda}}^{(n)}\rangle\}$ is known for every value of $\boldsymbol{\lambda}$ (figure 1):

$$\hat{H}_{\boldsymbol{\lambda}}\,|\psi_{\boldsymbol{\lambda}}^{(n)}\rangle = E_{\boldsymbol{\lambda}}^{(n)}\;|\psi_{\boldsymbol{\lambda}}^{(n)}\rangle. \tag{3}$$

We suppose the system to be initialized at $t = 0$ in a given eigenstate, for example the ground state for the value of $\boldsymbol{\lambda}$ at that time:

$$|\psi(0)\rangle = |\psi_{\boldsymbol{\lambda}(0)}^{(0)}\rangle. \tag{4}$$

We also suppose that the ground state remains non-degenerate for all values of $\boldsymbol{\lambda}(t)$ explored between 0 and T.

If the parameter $\boldsymbol{\lambda}$ stays constant over time, the state of the system at time t is simply given by the free evolution obtained by solving the Schrödinger equation:

$$|\psi(t)\rangle = \mathrm{e}^{\mathrm{i}\Phi_{\mathrm{dyn}}}|\psi_{\boldsymbol{\lambda}(0)}^{(0)}\rangle \qquad \text{with} \quad \Phi_{\mathrm{dyn}} = -E_{\boldsymbol{\lambda}(0)}^{(0)}t/\hbar. \tag{5}$$

This state is always the same as the initial state, up to the *dynamical phase* Φ_{dyn}. This "non-evolution" of the system when it has been initialized in an eigenstate of the Hamiltonian explains why these states are often called *stationary states*.

We now consider that the parameter $\boldsymbol{\lambda}$ varies in time arbitrarily slowly (a quantitative criterion is given later). The adiabatic theorem asserts that a good approximation of the system's state at time t is

$$|\psi(t)\rangle \approx \mathrm{e}^{\mathrm{i}\Phi(t)}|\psi_{\boldsymbol{\lambda}(t)}^{(0)}\rangle. \tag{6}$$

In other terms, the system (roughly) stays in the ground state of the Hamiltonian, even if this ground state has changed between time 0 and time t since the two bases $\{|\psi_{\boldsymbol{\lambda}(0)}^{(n)}\rangle\}$ and $\{|\psi_{\boldsymbol{\lambda}(t)}^{(n)}\rangle\}$ do not coincide.

The demonstration of this theorem has been given in the lecture of 2013-2014 (chapter 3), and we will only recall here its main ingredients. Let us start by writing the state $|\psi(t)\rangle$ of the system in the "instantaneous basis" $\{|\psi_{\boldsymbol{\lambda}(t)}^{(n)}\rangle\}$:

$$|\psi(t)\rangle = \sum_n c^{(n)}(t)\;|\psi_{\boldsymbol{\lambda}(t)}^{(n)}\rangle \tag{7}$$

and let us insert this expression in the Schrödinger equation

$$\mathrm{i}\hbar\frac{\mathrm{d}|\psi(t)\rangle}{\mathrm{d}t} = \hat{H}_{\boldsymbol{\lambda}(t)}\;|\psi(t)\rangle. \tag{8}$$

By projecting this equation on the states $|\psi_{\boldsymbol{\lambda}(t)}^{(n)}\rangle$, one can find the set of first-order differential equations verified by the coefficients $c_n(t)$:

$$\mathrm{i}\hbar\;\dot{c}^{(n)} = E_{\boldsymbol{\lambda}}^{(n)}\;c^{(n)} \;-\; \hbar\sum_{\ell}\alpha_{\boldsymbol{\lambda}}^{(n,\ell)}\;c^{(\ell)}. \tag{9}$$

In this set of equations notably appears the time derivative of the vectors of the basis, through the coefficients

$$\alpha_{\boldsymbol{\lambda}}^{(n,\ell)} = \mathrm{i}\langle\psi_{\boldsymbol{\lambda}}^{(n)}|\left(\frac{\mathrm{d}}{\mathrm{d}t}|\psi_{\boldsymbol{\lambda}}^{(\ell)}\rangle\right), \tag{10}$$

a quantity that we will denote by

$$\alpha_{\boldsymbol{\lambda}}^{(n,\ell)} = \mathrm{i}\langle\psi_{\boldsymbol{\lambda}}^{(n)}|\partial_t\psi_{\boldsymbol{\lambda}}^{(\ell)}\rangle. \tag{11}$$

This notation is useful because of its compactness, but it presents an ambiguity: the states $|\psi_{\boldsymbol{\lambda}}^{(\ell)}\rangle$ do not explicitly depend on time, they only vary in time because they explicitly depend on the parameter $\boldsymbol{\lambda}$ that itself depends on time. The above notation should thus be understood as

$$\langle\psi_{\boldsymbol{\lambda}}^{(n)}|\partial_t\psi_{\boldsymbol{\lambda}}^{(\ell)}\rangle \equiv \dot{\boldsymbol{\lambda}}\cdot\langle\psi_{\boldsymbol{\lambda}}^{(n)}|\boldsymbol{\nabla}\psi_{\boldsymbol{\lambda}}^{(\ell)}\rangle, \tag{12}$$

where we have introduced the notation

$$|\boldsymbol{\nabla}\psi_{\boldsymbol{\lambda}}^{(\ell)}\rangle \equiv \left(\frac{\partial}{\partial\lambda_1}|\psi_{\boldsymbol{\lambda}}^{(\ell)}\rangle,\ \frac{\partial}{\partial\lambda_2}|\psi_{\boldsymbol{\lambda}}^{(\ell)}\rangle,\dots\right). \tag{13}$$

In a way, these coefficients $\alpha_{\boldsymbol{\lambda}}^{(n,\ell)}$ represent the "angular velocity" of the eigenstates in the Hilbert space as the parameter $\boldsymbol{\lambda}$ varies in time.

The adiabatic approximation consists in solving perturbatively this set of equations with the infinitesimal parameter

$$\epsilon \equiv \frac{|\alpha_{\boldsymbol{\lambda}}^{(n,\ell)}|_{\max}}{|\omega_{\boldsymbol{\lambda}}^{(n,\ell)}|_{\min}} \qquad \text{with} \quad \hbar\omega_{\boldsymbol{\lambda}}^{(n,\ell)} = E_{\boldsymbol{\lambda}}^{(n)} - E_{\boldsymbol{\lambda}}^{(\ell)}. \tag{14}$$

The "angular velocity" of the occupied state –here $\ell = 0$– has to remain small compared to all the Bohr frequencies involving this state (Messiah 1961). When the condition $\epsilon \ll 1$ is met at all time, the above set of differential equations boils down to:

$$\mathrm{i}\hbar\,\dot{c}^{(0)}(t) \approx \left[E_{\boldsymbol{\lambda}(t)}^{(0)} - \mathrm{i}\hbar\,\dot{\boldsymbol{\lambda}}\cdot\langle\psi_{\boldsymbol{\lambda}}^{(0)}|\boldsymbol{\nabla}\psi_{\boldsymbol{\lambda}}^{(0)}\rangle\right] c^{(0)}(t) \tag{15}$$

$$c^{(n)}(t) \approx 0 \qquad \text{if } n \neq 0. \tag{16}$$

Remark that the term within the square bracket $[\dots]$ on the right-hand side of (15) is always real. The eigenstate $|\psi_{\boldsymbol{\lambda}}^{(0)}\rangle$ indeed is always of norm 1, such that

$$0 = \frac{\mathrm{d}}{\mathrm{d}t}\langle\psi_{\boldsymbol{\lambda}}^{(0)}|\psi_{\boldsymbol{\lambda}}^{(0)}\rangle = \dot{\boldsymbol{\lambda}}\cdot\left(\langle\boldsymbol{\nabla}\psi_{\boldsymbol{\lambda}}^{(0)}|\psi_{\boldsymbol{\lambda}}^{(0)}\rangle + \langle\psi_{\boldsymbol{\lambda}}^{(0)}|\boldsymbol{\nabla}\psi_{\boldsymbol{\lambda}}^{(0)}\rangle\right) \tag{17}$$

and the quantity $\langle\psi_{\boldsymbol{\lambda}}^{(0)}|\boldsymbol{\nabla}\psi_{\boldsymbol{\lambda}}^{(0)}\rangle$ is an imaginary number. This implies that the solution of equation (15) is a function $c^{(0)}(t)$ with modulus 1. The state $|\psi(t)\rangle$ thus stays normalized, and the first-order solution corresponds to the expression given in (6).

1-2 The Berry connection and the geometrical phase

We focus on the evolution of the complex coefficient $c^{(0)}$, whose expression is given in (15). Since the modulus of this coefficient is always equal to 1, we are only left with the determination of its phase. In order to use compact expressions, let us introduce for each eigenstate of $\hat{H}_{\boldsymbol{\lambda}}$ the Berry curvature (Berry 1984; Berry 1989)

$$\boldsymbol{\mathcal{A}}_{\boldsymbol{\lambda}}^{(n)} = \mathrm{i}\ \langle\psi_{\boldsymbol{\lambda}}^{(n)}|\boldsymbol{\nabla}\psi_{\boldsymbol{\lambda}}^{(n)}\rangle. \tag{18}$$

It is a real-valued vector with as many components as the dimension of the space associated with $\boldsymbol{\lambda}$. In practice, this space will have here dimension 1, 2, or 3.

The equation of motion for $c^{(0)}$ can then be written as

$$\dot{c}^{(0)}(t) = \mathrm{i}\left[-E_{\boldsymbol{\lambda}}^{(0)}/\hbar\ +\ \dot{\boldsymbol{\lambda}}\cdot\boldsymbol{\mathcal{A}}_{\boldsymbol{\lambda}}^{(0)}\right] c^{(0)}(t) \tag{19}$$

with

$$\dot{\boldsymbol{\lambda}}\cdot\boldsymbol{\mathcal{A}}_{\boldsymbol{\lambda}}^{(0)} = \mathrm{i}\langle\psi_{\boldsymbol{\lambda}}^{(0)}|\partial_t\psi_{\boldsymbol{\lambda}}^{(0)}\rangle. \tag{20}$$

It can be integrated as

$$c^{(0)}(t) = \mathrm{e}^{\mathrm{i}\Phi_{\mathrm{dyn}}}\ \mathrm{e}^{\mathrm{i}\Phi_{\mathrm{geom}}}\ c^{(0)}(0). \tag{21}$$

The *dynamical phase* comes from the contribution of the energy $E_{\boldsymbol{\lambda}}^{(0)}$ to (19):

$$\Phi_{\mathrm{dyn}} = -\frac{1}{\hbar}\int_0^t E_{\boldsymbol{\lambda}(t')}^{(0)}\ \mathrm{d}t', \tag{22}$$

and it generalizes the result found in (5) in the case where the energy $E_{\boldsymbol{\lambda}}^{(0)}$ depends on time via the parameter $\boldsymbol{\lambda}$. The second contribution, called the *geometrical phase*, reads:

$$\Phi_{\mathrm{geom}} = \mathrm{i}\int_0^t \langle\psi_{\boldsymbol{\lambda}}^{(0)}|\partial_t\psi_{\boldsymbol{\lambda}}^{(0)}\rangle\ \mathrm{d}t = \int_0^t \dot{\boldsymbol{\lambda}}\cdot\boldsymbol{\mathcal{A}}_{\boldsymbol{\lambda}}^{(0)}\ \mathrm{d}t, \tag{23}$$

or:

$$\Phi_{\mathrm{geom}} = \int_{\boldsymbol{\lambda}(0)}^{\boldsymbol{\lambda}(t)} \boldsymbol{\mathcal{A}}_{\boldsymbol{\lambda}}^{(0)}\cdot\mathrm{d}\boldsymbol{\lambda}. \tag{24}$$

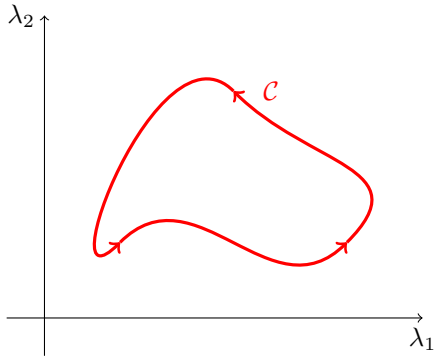

Figure 2. *A closed loop $\mathcal{C}$ for the parameter $\boldsymbol{\lambda}$, which we suppose here to evolve in a 2D space.*

From this last form, one can see that it only depends on the path that the parameter $\boldsymbol{\lambda}$ takes to go from $\boldsymbol{\lambda}(0)$ to $\boldsymbol{\lambda}(t)$, and it does not involve the time it took along this path. As Berry nicely put it, the dynamical phase answers the question "How long did your journey take?" whereas the geometrical phase answers the complementary question "Where did you go?"

1-3 A closed loop and the Berry curvature

In this lecture, we will often consider situations where the path $\mathcal{C}$ followed by the parameter $\boldsymbol{\lambda}(t)$ forms a closed loop (figure 2). We then have $\boldsymbol{\lambda}(t_f) = \boldsymbol{\lambda}(t_i)$, where t_i and t_f are respectively the initial and the final times (above we have chosen $t_i = 0$). The geometrical phase is then expressed as a line integral along a closed curve in the space of $\boldsymbol{\lambda}$:

$$\Phi_{\text{geom}} = \oint_{\mathcal{C}} \boldsymbol{\mathcal{A}}_{\boldsymbol{\lambda}}^{(0)} \cdot \mathrm{d}\boldsymbol{\lambda}. \tag{25}$$

This type of integrals of a vector field along a closed curve can often be calculated thanks to Stokes' theorem by replacing the line integral by an integral over a surface Σ bounded by the initial closed curve. In two or three dimensions, one can introduce for this purpose the *Berry curvature*:

$$\boldsymbol{\Omega}_{\boldsymbol{\lambda}}^{(n)} = \boldsymbol{\nabla} \times \boldsymbol{\mathcal{A}}_{\boldsymbol{\lambda}}^{(n)} \tag{26}$$

where the curl is taken (similarly to the previous gradients) with respect to the variable $\boldsymbol{\lambda} = (\lambda_1, \lambda_2, \lambda_3)$. By using (18), we can rewrite this definition as

$$\boldsymbol{\Omega}_{\boldsymbol{\lambda}}^{(n)} = \mathrm{i}\, \langle \boldsymbol{\nabla} \psi_{\boldsymbol{\lambda}}^{(n)} | \times | \boldsymbol{\nabla} \psi_{\boldsymbol{\lambda}}^{(n)} \rangle. \tag{27}$$

If $\boldsymbol{\mathcal{A}}_{\boldsymbol{\lambda}}^{(0)}$ has no singularity, we then have

$$\Phi_{\text{geom}} = \iint_{\Sigma} \boldsymbol{n} \cdot \boldsymbol{\Omega}_{\boldsymbol{\lambda}}^{(n)}\, \mathrm{d}\lambda \tag{28}$$

where $\boldsymbol{n}$ designates the normal vector to the oriented surface.

The role of the dimension of space. Starting from equations (25-28), it seems that a space of dimension at least 2 is required to obtain a non-zero geometrical phase along a closed loop. Intuitively, to perform a closed loop in a one-dimensional space, one has to move in one direction and to go back, and the two contributions balance each other out in (25). This reasoning is however too simplistic to be generally valid: the study of one-dimensional periodic potentials will provide us with a counter-example; in that case, the parameter $\boldsymbol{\lambda}$ is the Bloch momentum q and its space has a circular structure. It is then possible to perform a closed loop in parameter space without having to retrace one's steps.

Analogy with the Aharonov-Bohm effect. When a particle of charge q_e describes a closed trajectory $\mathcal{C}$ in real space in the presence of a magnetic field $\boldsymbol{B}(\boldsymbol{r})$ associated with the vector potential $\boldsymbol{A}(\boldsymbol{r})$, its wave function acquires a geometrical phase that can be measured by interferometric means. This phase is given by the expression (see Aharonov & Bohm (1959), Ehrenberg & Siday (1949) and the lecture of 2013-2014):

$$\Phi_{\text{AB}} = \frac{q_e}{\hbar} \oint_{\mathcal{C}} \boldsymbol{A}(\boldsymbol{r}) \cdot \mathrm{d}\boldsymbol{r} = \frac{q_e}{\hbar} \iint_{\Sigma} \boldsymbol{n} \cdot \boldsymbol{B}(\boldsymbol{r})\, \mathrm{d}^2 r \tag{29}$$

There is a clear analogy between the previous results and those of orbital magnetism. We will come back to this analogy in a following chapter.

Gauge transform. It is interesting to see how the Berry connection and the Berry curvature are modified when the definition of the eigenstates $|\psi_{\boldsymbol{\lambda}}^{(n)}\rangle$ are changed by multiplying them by a phase factor $\chi^{(n)}$ that depends on $\boldsymbol{\lambda}$:

$$|\psi_{\boldsymbol{\lambda}}^{(n)}\rangle \longrightarrow |\tilde{\psi}_{\boldsymbol{\lambda}}^{(n)}\rangle = \mathrm{e}^{\mathrm{i}\chi_{\boldsymbol{\lambda}}^{(n)}}\,|\psi_{\boldsymbol{\lambda}}^{(n)}\rangle. \tag{30}$$

Suppose for now that the function $\chi^{(n)}$ is regular in every point $\boldsymbol{\lambda}$. The Berry connection is modified in the following way:

$$\boldsymbol{\mathcal{A}}_{\boldsymbol{\lambda}}^{(n)} \longrightarrow \tilde{\boldsymbol{\mathcal{A}}}_{\boldsymbol{\lambda}}^{(n)} = \boldsymbol{\mathcal{A}}_{\boldsymbol{\lambda}}^{(n)} - \boldsymbol{\nabla}\chi_{\boldsymbol{\lambda}}^{(n)} \tag{31}$$

whereas the Berry curvature is unchanged, as shown by taking the curl of the previous expression:

$$\boldsymbol{\Omega}_{\boldsymbol{\lambda}}^{(n)} \longrightarrow \tilde{\boldsymbol{\Omega}}_{\boldsymbol{\lambda}}^{(n)} = \boldsymbol{\Omega}_{\boldsymbol{\lambda}}^{(n)}. \tag{32}$$

The Berry curvature is thus invariant in a gauge transformation (30), and so is the geometrical phase accumulated along a closed loop, since it is the integral of $\boldsymbol{\Omega}_{\boldsymbol{\lambda}}$ over the surface Σ bounded by this loop [eq. (28)].

It can also happen that the function $\chi^{(n)}$ is regular along the path $\mathcal{C}$, but not on the entire surface Σ. One can no longer use the equation (28) because the Berry connection $\boldsymbol{\mathcal{A}}_{\boldsymbol{\lambda}}$ can also be singular on some points of Σ. However, the result (25) stays valid and one can deduce from it:

$$\tilde{\Phi}_{\mathrm{geom}} = \oint_{\mathcal{C}} \tilde{\boldsymbol{\mathcal{A}}}_{\boldsymbol{\lambda}}^{(0)} \cdot \mathrm{d}\boldsymbol{\lambda} = \Phi_{\mathrm{geom}} - \oint_{\mathcal{C}} \boldsymbol{\nabla}\chi_{\boldsymbol{\lambda}}^{(n)} \cdot \mathrm{d}\boldsymbol{\lambda}. \tag{33}$$

Since the function $\mathrm{e}^{\mathrm{i}\chi_{\boldsymbol{\lambda}}^{(n)}}$ has to be single-valued so that the new gauge is well-defined, one has:

$$\oint_{\mathcal{C}} \boldsymbol{\nabla}\chi_{\boldsymbol{\lambda}}^{(n)} \cdot \mathrm{d}\boldsymbol{\lambda} = \chi^{(n)}\Big|_{\mathrm{end}} - \chi^{(n)}\Big|_{\mathrm{start}} = 0 \quad \text{modulo } 2\pi, \tag{34}$$

where "start" and "end" refer to the same parameter $\boldsymbol{\lambda}$ of the loop. The following relationship can then be derived for the geometrical phase in a gauge transformation that is *not singular on the closed loop* $\mathcal{C}$:

$$\mathrm{e}^{\mathrm{i}\tilde{\Phi}_{\mathrm{geom}}} = \mathrm{e}^{\mathrm{i}\Phi_{\mathrm{geom}}}. \tag{35}$$

1-4 The next order in the adiabatic approximation

In the following, we will regularly require the next order of the above perturbative development. More precisely, it is often useful to know the linear response of the system, which corresponds to the amplitude of the coefficients $c^{(n)}(t)$ of the initially non-populated states expressed at order 1 of the perturbation $\dot{\boldsymbol{\lambda}}$.

The approximate evolution equation of a $c^{(n)}$ coefficient with $n \neq 0$ is:

$$\mathrm{i}\hbar\,\dot{c}^{(n)}(t) \approx E_{\boldsymbol{\lambda}}^{(n)}\,c^{(n)}(t) \;-\; \mathrm{i}\hbar\,\dot{\boldsymbol{\lambda}}\cdot\langle\psi_{\boldsymbol{\lambda}}^{(n)}|\boldsymbol{\nabla}\psi_{\boldsymbol{\lambda}}^{(0)}\rangle\,c^{(0)}(t). \tag{36}$$

The solution to this differential equation depends *a priori* on the full "history"of the parameter $\boldsymbol{\lambda}$ and not only on its value at time t. However, the theory of linear response assumes in general, at least implicitly, that the system is coupled to a bath, which implies the existence of a dissipation process. We can take this dissipation process into account by phenomenologically adding a (weak) damping term in the evolution equation of $c^{(n)}(t)$:

$$\mathrm{i}\hbar\,\dot{c}^{(n)}(t) \approx (E_{\boldsymbol{\lambda}}^{(n)} - \mathrm{i}\hbar\gamma^{(n)})\,c^{(n)}(t) \;-\; \mathrm{i}\hbar\,\dot{\boldsymbol{\lambda}}\cdot\langle\psi_{\boldsymbol{\lambda}}^{(n)}|\boldsymbol{\nabla}\psi_{\boldsymbol{\lambda}}^{(0)}\rangle\,c^{(0)}(t). \tag{37}$$

In order to simplify the calculations, we consider the case where $E^{(n)}$ and $\gamma^{(n)}$ do not vary over time. This first-order differential equation with a source term integrates in

$$\begin{aligned} c^{(n)}(t) &= c^{(n)}(0)\,\mathrm{e}^{-\mathrm{i}(E^{(n)}-\mathrm{i}\hbar\gamma^{(n)})t/\hbar} \\ &- \int_0^t \mathrm{e}^{-\mathrm{i}(E^{(n)}-\mathrm{i}\hbar\gamma^{(n)})(t-t')/\hbar}\,\left\{\dot{\boldsymbol{\lambda}}\cdot\langle\psi_{\boldsymbol{\lambda}}^{(n)}|\boldsymbol{\nabla}\psi_{\boldsymbol{\lambda}}^{(0)}\rangle\,c^{(0)}(t')\right\}\,\mathrm{d}t'. \end{aligned} \tag{38}$$

Suppose that the damping described by $\gamma^{(n)}$ verifies at the same time the two following conditions:

- This parameter is small compared to all the Bohr frequencies $(E^{(n)} - E^{(0)})/\hbar$ so that it only barely modifies the "free" dynamics.
- On the contrary, it is large enough so that the memory timescale $1/\gamma^{(n)}$ is small compared to the characteristic time on which $\boldsymbol{\lambda}$ varies.

Under these conditions, one can approximate $c^{(0)}(t')$ in the curly brackets of the integral (38) by

$$c^{(0)}(t') \approx c^{(0)}(t)\ \mathrm{e}^{\mathrm{i}E^{(0)}(t-t')/\hbar} \tag{39}$$

and one can replace the other terms of these brackets, that are in principle evaluated at time t', by their value at time t. Suppose furthermore that the time t is larger than $1/\gamma^{(n)}$; the remaining integral is easily obtained, and gives:

$$\int_0^t \mathrm{e}^{-\mathrm{i}(E^{(n)}-E^{(0)}-\mathrm{i}\hbar\gamma^{(n)})(t-t')/\hbar}\,\mathrm{d}t' \approx \frac{-\mathrm{i}\hbar}{E^{(n)}-E^{(0)}} \tag{40}$$

which in turns gives, at order 1 in $\dot{\boldsymbol{\lambda}}$:

$$c^{(n)}(t) \approx \mathrm{i}\hbar\ \dot{\boldsymbol{\lambda}} \cdot \frac{\langle \psi_{\boldsymbol{\lambda}}^{(n)} | \boldsymbol{\nabla} \psi_{\boldsymbol{\lambda}}^{(0)} \rangle}{E_{\boldsymbol{\lambda}}^{(n)} - E_{\boldsymbol{\lambda}}^{(0)}}. \tag{41}$$

This expression describes the *linear response* of the system to the time variation of the parameter $\boldsymbol{\lambda}$. The phenomenological damping term $-\gamma^{(n)}$, which was assumed to be small compared to all the Bohr frequencies $\omega^{(n,0)}$, but sufficiently large to "erase" the memory of the values of $\boldsymbol{\lambda}(t')$ that are notably different from $\boldsymbol{\lambda}(t)$, does not appear in the result, at least at this order of the development.

2 The example of a spin $1/2$

In this lecture, we will often resort to the simplest model of a quantum system, the two-level system, which can be considered as a (pseudo-)spin $1/2$. We summarize in this part some of the important properties that will be used later and that are linked to the geometrical phase and its representation on the *Bloch sphere*.

2-1 The Hamiltonian of a two-level system

Let us consider a two-level system such as a spin $1/2$, and denote as $|+\rangle$ and $|-\rangle$ the two basis states. These states are by definition the eigenstates of the projection of the spin along a quantization axis, for example $\hat{S}_z$.

The most general Hamiltonian for such a system can be written as

$$\hat{H} = E_0\ \hat{1}\ -\ \boldsymbol{h} \cdot \hat{\boldsymbol{\sigma}}, \tag{42}$$

where E_0, h_x, h_y, h_z are real numbers with the dimension of an energy, and where $\hat{\sigma}_i$, $i = x, y, z$ are the three Pauli matrices:

$$\hat{\sigma}_x = \begin{pmatrix} 0 & 1 \\ 1 & 0 \end{pmatrix}, \quad \hat{\sigma}_y = \begin{pmatrix} 0 & -\mathrm{i} \\ \mathrm{i} & 0 \end{pmatrix}, \quad \hat{\sigma}_z = \begin{pmatrix} 1 & 0 \\ 0 & -1 \end{pmatrix}. \tag{43}$$

The term $E_0\hat{1}$ affects the two states $|\pm\rangle$ in the same way and corresponds only to the definition of the origin of energies. The term $-\ \boldsymbol{h} \cdot \hat{\boldsymbol{\sigma}}$ can represent a magnetic interaction in the case where the spin $1/2$ is associated to a magnetic moment $\hat{\boldsymbol{\mu}}$:

$$\hat{\boldsymbol{\mu}} = \mu\, \hat{\boldsymbol{\sigma}}, \tag{44}$$

Indeed, if this magnetic moment is immersed in an external magnetic field $\boldsymbol{B}$, the Hamiltonian can be written as

$$\hat{H} = -\boldsymbol{B} \cdot \hat{\boldsymbol{\mu}} = -\boldsymbol{h} \cdot \hat{\boldsymbol{\sigma}} \qquad \text{with} \quad \boldsymbol{h} = \mu \boldsymbol{B}. \tag{45}$$

2-2 The Bloch sphere

It is often useful to parametrize the vector $\boldsymbol{h}$ in the Hamiltonian (42) by its modulus $|\boldsymbol{h}|$ and its spherical angles (θ, ϕ):

$$\boldsymbol{h} = |\boldsymbol{h}|\ \boldsymbol{n} \qquad \text{with} \quad \boldsymbol{n} = \begin{pmatrix} \cos\phi \sin\theta \\ \sin\phi \sin\theta \\ \cos\theta \end{pmatrix},\ 0 \le \phi < 2\pi,\ 0 \le \theta \le \pi. \tag{46}$$

With this parametrization, the Hamiltonian reads:

$$\hat{H} = E_0\ \hat{1}\ -\ |\boldsymbol{h}|\ \begin{pmatrix} \cos\theta & \mathrm{e}^{-\mathrm{i}\phi}\sin\theta \\ \mathrm{e}^{\mathrm{i}\phi}\sin\theta & -\cos\theta \end{pmatrix}. \tag{47}$$

The eigenenergies depend only on E_0 and on the modulus of $\boldsymbol{h}$:

$$E^{(\pm)} = E_0 \pm |\boldsymbol{h}| \tag{48}$$

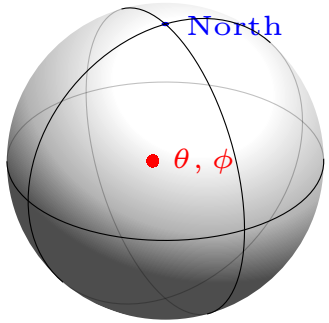

Figure 3. *The Bloch sphere. On this unit sphere, a point is localized by its spherical angles (θ, ϕ). Each point of the surface can be associated to one and only one state of the spin $1/2$, and this state is the eigenstate of the Hamiltonian (47) with the lowest energy $E^{(-)} = E_0 - |\boldsymbol{h}|$.*

whereas the eigenstates depend only on the orientation of $\boldsymbol{h}$:

$$|\psi^{(-)}\rangle = \begin{pmatrix} \cos(\theta/2) \\ \mathrm{e}^{\mathrm{i}\phi}\sin(\theta/2) \end{pmatrix} \qquad |\psi^{(+)}\rangle = \begin{pmatrix} \sin(\theta/2) \\ -\mathrm{e}^{\mathrm{i}\phi}\cos(\theta/2) \end{pmatrix}. \tag{49}$$

We will often have to choose one of these eigenstates, for example $|\psi^{(-)}\rangle$, and represent it geometrically. Since this state only depends on the angles θ and ϕ whose domains are given in (46), one can biunivocally associate to it a point on a unit sphere. In this context, this sphere is called the *Bloch sphere* (figure 3). The coordinates of this point are the ones of the unitary vector $\boldsymbol{n}$ introduced in (46).

The representation on the Bloch sphere is biunivocal: every point on the sphere corresponds to a single vector $\boldsymbol{n}$, and therefore to a single eigenstate $|\psi^{(-)}\rangle$ of the general Hamiltonian of a spin $1/2$. Moreover, a point of the sphere can almost always be associated to a unique pair (θ, ϕ). The only exceptions are the north pole and the south pole of the sphere, which respectively correspond to $\theta = 0$ and $\theta = \pi$, and for which the angle ϕ can have any value.

2-3 Berry curvature and geometrical phase (spin 1/2)

The notion of adiabatic process for a (pseudo-)spin $1/2$ described by the Hamiltonian $-\boldsymbol{h}\cdot\hat{\boldsymbol{\sigma}}$ directly applies by considering that the vector $\boldsymbol{h}$ plays the role of the external parameter:

$$\boldsymbol{\lambda} \equiv \boldsymbol{h}. \tag{50}$$

In this case, a simple but relatively long calculation gives (Berry 1984)

$$\boldsymbol{\Omega}^{(\pm)} = \pm\frac{\boldsymbol{h}}{2\,|\boldsymbol{h}|^3}. \tag{51}$$

This formula directly provides the geometrical phase that a spin acquires when $\boldsymbol{h}$ moves slowly along the closed path[2]

$$\mathcal{C}: \qquad \boldsymbol{h}(0) \to \boldsymbol{h}(t) \to \boldsymbol{h}(T) = \boldsymbol{h}(0), \tag{52}$$

The obtained result is:

$$\Phi^{(\pm)}_{\text{geom.}}(\mathcal{C}) = \iint_{\mathcal{S}} \boldsymbol{\Omega}^{(\pm)}\cdot \mathrm{d}^2\boldsymbol{S} = \pm\frac{1}{2}\iint_{\mathcal{S}} \frac{\boldsymbol{h}}{|\boldsymbol{h}|^3}\cdot \mathrm{d}^2\boldsymbol{S}, \tag{53}$$

where the surface $\mathcal{S}$ is bounded by the closed loop $\mathcal{C}$. One can also write this expression using the unit vector $\boldsymbol{n} = \boldsymbol{h}/|\boldsymbol{h}|$ on the Bloch sphere:

$$\Phi^{(\pm)}_{\text{geom.}}(\mathcal{C}) = \pm\frac{1}{2}\iint_{\mathcal{S}} \boldsymbol{n}\cdot \mathrm{d}^2\boldsymbol{s} \tag{54}$$

where $\mathrm{d}^2\boldsymbol{s} = \mathrm{d}^2\boldsymbol{S}/|\boldsymbol{h}|^2$ represents the oriented surface element on the unit sphere. One then gets

$$\Phi^{(\pm)}_{\text{geom.}}(\mathcal{C}) = \pm\frac{\alpha}{2} \tag{55}$$

where α is the solid angle defined by the unit vector $\boldsymbol{n}$ from the center of the unit sphere (figure 4).

More generally, if $\boldsymbol{\lambda}$ is a parametrization of the vector $\boldsymbol{h}$, and in particular of its spherical angles (θ, ϕ), one gets from the expression of the eigenvectors (49) :

$$\boldsymbol{\mathcal{A}}^{(\pm)} = -\frac{1}{2}(1 \pm \cos\theta)\,\boldsymbol{\nabla}_{\boldsymbol{\lambda}}(\phi), \qquad \boldsymbol{\Omega}^{(\pm)} = \pm\frac{1}{2}\boldsymbol{\nabla}_{\boldsymbol{\lambda}}(\phi)\times\boldsymbol{\nabla}_{\boldsymbol{\lambda}}(\cos\theta). \tag{56}$$

[2] Let us remind the hypothesis required to use the adiabatic theorem: the energy levels of $\hat{H}$ should be non-degenerate, which in this case means that the path does not cross the point of zero field $\boldsymbol{h} = 0$.

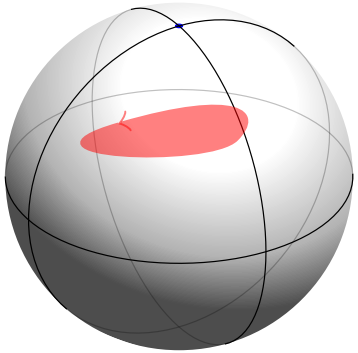

Figure 4. *The solid angle α defined by the unit vector $\boldsymbol{n} = \boldsymbol{h}/|\boldsymbol{h}|$ when the parameter $\boldsymbol{\lambda}$ describes the closed loop $\mathcal{C}$. The geometrical phase for a spin $1/2$ is equal to $\alpha/2$.*

Note that the result (51) can be recovered from these general expressions by using the fact that, for $\boldsymbol{\lambda} = \boldsymbol{h}$, one gets:

$$\boldsymbol{\nabla}_{\boldsymbol{h}}(\cos\theta) = \frac{1}{|\boldsymbol{h}|^3}\begin{pmatrix} -h_x h_z \\ -h_y h_z \\ h_x^2 + h_y^2 \end{pmatrix}, \qquad \boldsymbol{\nabla}_{\boldsymbol{h}}(\phi) = \frac{1}{|\boldsymbol{h}_\perp|^2}\begin{pmatrix} -h_y \\ h_x \\ 0 \end{pmatrix}, \tag{57}$$

with $|\boldsymbol{h}_\perp|^2 = h_x^2 + h_y^2$.

3 Periodic potentials in quantum physics

We now move to the second main ingredient of this lecture: the motion of particles in a spatially periodic potential. We will briefly recall Bloch's theorem and how the notion of energy bands emerges. We will work in a one-dimensional space to keep the notations simple, but the whole formalism can be easily generalized to higher dimensions.

3-1 Bloch's theorem

Let us consider the motion of a particle of mass m in a 1D space with a potential $V(x)$. This motion is described by the Hamiltonian

$$\hat{H} = \frac{\hat{p}^2}{2m} + V(\hat{x}) \tag{58}$$

where $\hat{p}$ is the momentum operator of the particle, which acts on a wave function $\psi(x,t)$ in the following way:

$$\hat{p}\,\psi(x,t) = -\mathrm{i}\hbar\frac{\partial\psi}{\partial x} \quad \text{also written} \quad -\mathrm{i}\hbar\,\partial_x\psi. \tag{59}$$

In this lecture the potentials $V(x)$ of interest are the ones which are spatially periodic, with a period noted a (figure 5):

$$V(x+a) = V(x). \tag{60}$$

This hypothesis simplifies a lot the task of searching for the eigenfunctions of the Hamiltonian, which are the states with a well-defined energy. The translation invariance of $\hat{H}$ can be mathematically written as

$$[\hat{H}, \hat{\mathcal{T}}_a] = 0 \tag{61}$$

where $\hat{\mathcal{T}}_a$ is the operator for the translation of a:

$$\hat{\mathcal{T}}_a\,\psi(x) = \psi(x-a). \tag{62}$$

One can then find a basis of eigenfunctions which are common to $\hat{H}$ and $\hat{\mathcal{T}}_a$, or more precisely find the eigenstates of $\hat{H}$ within the eigenspaces of $\hat{\mathcal{T}}_a$ (Ashcroft & Mermin 1976).

These eigenspaces are easy to determine. Since the operator $\hat{\mathcal{T}}_a$ is unitary ($\hat{\mathcal{T}}_a^{-1} = \hat{\mathcal{T}}_a^\dagger = \hat{\mathcal{T}}_{-a}$), its eigenvalues[3] are the complex numbers of modulus 1, that are conventionally written as $\mathrm{e}^{\mathrm{i}qa}$. The quantity q, with the dimension of a wave number, is called a *Bloch (quasi-)momentum*. We will precise its domain of definition in the next paragraph, but for now q can

[3] We restrict ourselves to the eigenfunctions which do not diverge exponentially fast in $\pm\infty$.

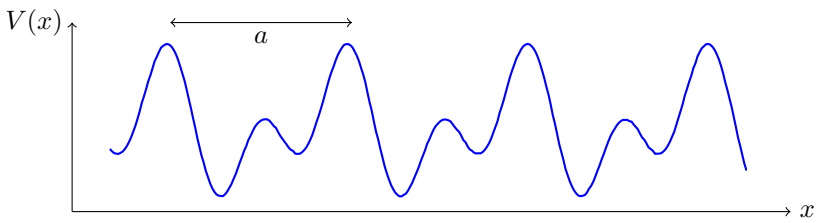

Figure 5. *A 1D periodic potential of period a.*

be any real number between $-\infty$ and $+\infty$. An eigenfunction of $\hat{\mathcal{T}}_a$ then verifies, by definition:

$$\hat{\mathcal{T}}_a\,\psi_q(x) = \mathrm{e}^{\mathrm{i}qa}\,\psi_q(x) \tag{63}$$

which, combined with (62), implies that $\psi_q(x)$ can be written under the form

$$\psi_q(x) = \mathrm{e}^{\mathrm{i}qx}\,u_q(x) \qquad \text{with} \quad u_q \text{ periodic}: \quad u_q(x+a) = u_q(x). \tag{64}$$

This is the form, called the *Bloch form*, under which we will search for the eigenstates of a space-periodic Hamiltonian. The physical meaning of this form is clear: the Bloch functions are the product of a plane wave $\mathrm{e}^{\mathrm{i}qx}$ (which would be the eigenstate of a free particle) and a periodic function $u_q(x)$ which has the same periodicity as the potential $V(x)$.

3-2 The Hamiltonian $\hat{H}_q$

We consider a common eigenstate of the Hamiltonian $\hat{H}$ and of the translation operator $\hat{\mathcal{T}}_a$. This eigenstate can be written with the Bloch form (64), and its energy is denoted by E_q. The eigenvalue equation for ψ_q can be written in terms of the periodic function $u_q(x)$:

$$\hat{H}\,\psi_q(x) = E_q\,\psi_q(x) \quad \Rightarrow \quad \hat{H}_q\,u_q(x) = E_q\,u_q(x) \tag{65}$$

where the operator $\hat{H}_q$ is defined by:

$$\hat{H}_q = \frac{(\hat{p}+\hbar q)^2}{2m} + V(x) = \frac{\hbar^2}{2m}\left(-\mathrm{i}\partial_x + q\right)^2 + V(x). \tag{66}$$

$\hat{H}_q$ is a hermitian operator, just as the initial Hamiltonian $\hat{H}$, and we will call it *Hamiltonian for the periodic part*, or *periodic Hamiltonian*.

We are now at an important point: the Hamiltonian $\hat{H}_q$ depends on a continuous parameter, the quasimomentum q. For each value of q, we expect to find a family of eigenstates and eigenenergies solution of equation (65) with the periodicity condition $u_q(x+a) = u_q(x)$:

$$\{u_q^{(n)}(x)\}, \quad \{E_q^{(n)}\}, \tag{67}$$

where the integer index n labels the states in ascending order of their energy:

$$E_q^{(0)} \leq E_q^{(1)} \leq E_q^{(2)} \leq \dots \tag{68}$$

By definition we have:

$$\hat{H}_q\,u_q^{(n)}(x) = E_q^{(n)}\,u_q^{(n)}(x) \tag{69}$$

and

$$\hat{H}\,\psi_q^{(n)}(x) = E_q^{(n)}\,\psi_q^{(n)}(x) \qquad \text{with} \quad \psi_q^{(n)}(x) = \mathrm{e}^{\mathrm{i}qx}\,u_q^{(n)}(x). \tag{70}$$

As q is a real parameter, one expects – unless there is a singularity – that the eigenstates $u_q^{(n)}(x)$ and the eigenenergies $E_q^{(n)}$ are continuous functions of q, and that these states can be followed adiabatically if the parameter q can be controlled and slowly varied. It is this continuous dependence of $\hat{H}_q$ with the parameter q that is at the heart of the topological properties that one can assign to the energy levels of a particle in a periodic potential.

3-3 The Brillouin zone

Until now, we have not said anything about the parameter q, except that it should be real so that the eigenvalue $\mathrm{e}^{\mathrm{i}qa}$ of the translation operator is a number of modulus 1. In fact, this expression of the eigenvalue directly shows that the two values of the quasimomentum

$$q_1 = q \quad \text{and} \quad q_2 = q + \frac{2\pi}{a} \tag{71}$$

correspond to the same value of $\mathrm{e}^{\mathrm{i}qa}$.

This identification is also valid for the wave functions associated with these two quasimomenta:

$$\psi_{q_1}(x) = \mathrm{e}^{\mathrm{i}q_1 x}\, u_{q_1}(x) \quad \text{and} \quad \psi_{q_2}(x) = \mathrm{e}^{\mathrm{i}q_2 x}\, u_{q_2}(x) \tag{72}$$

since ψ_{q_2} can be written as

$$\begin{aligned} \psi_{q_2}(x) &= \mathrm{e}^{\mathrm{i}q_1 x}\, \mathrm{e}^{\mathrm{i}2\pi x/a}\, u_{q_2}(x) \\ &= \mathrm{e}^{\mathrm{i}q_1 x}\, v(x) \qquad \text{with} \quad v(x) = \mathrm{e}^{\mathrm{i}2\pi x/a}\, u_{q_2}(x), \end{aligned} \tag{73}$$

where the function $v(x)$ is periodic of period a. The two eigenspaces in which we search for the eigenstates of $\hat{H}$ thus coincide if the two quasimomenta q_1 and q_2 differ by $2\pi/a$ (or by a multiple thereof).

As always in quantum physics, it is important to identify an eigenbasis of the Hamiltonian that is a set of orthogonal eigenvectors $\{|\psi_\alpha\rangle\}$ on which a physical state $|\psi\rangle$ of the system has a unique decomposition:

$$|\psi\rangle = \sum_\alpha c_\alpha |\psi_\alpha\rangle. \tag{74}$$

It is therefore essential not to select more than once the same vector in the set $\{|\psi_\alpha\rangle\}$. One then has to restrict the domain of q to an interval of length $2\pi/a$ by bounding it for example to

$$-\frac{\pi}{a} \;\leq\; q \;<\; +\frac{\pi}{a}. \tag{75}$$

This region in the q space is called the *(first) Brillouin zone*. Note that two functions ψ_{q_1} and ψ_{q_2} taken in this zone are always orthogonal since they are two eigenstates of the translation operator $\hat{\mathcal{T}}_a$ with different eigenvalues. The index α that appears in (74) then has to be understood as the pair formed by the quasimomentum q in the interval (75) and the index n that labels the eigenstates for a given q:

$$\alpha \equiv (q, n). \tag{76}$$

The geometrical structure of the Brillouin zone. Now that the value of the quasimomentum has been limited to the interval $[-\pi/a, \pi/a[$, one can wonder what relationship the two bounds of this interval have one with another. As stated above, a Bloch function $\psi_q(x)$ associated with the index q can also be seen as a Bloch function $\psi_{q+2\pi/a}$ associated with the index $q + 2\pi/a$. Suppose that the eigenstates $\psi_q^{(n)}(x)$ of the Hamiltonian $\hat{H}$ are non-degenerate for any value q (this is generally the case in one dimension). The two functions $\psi_{-\pi/a}^{(n)}(x)$ and $\psi_{\pi/a}^{(n)}(x)$ can then only differ by a phase factor

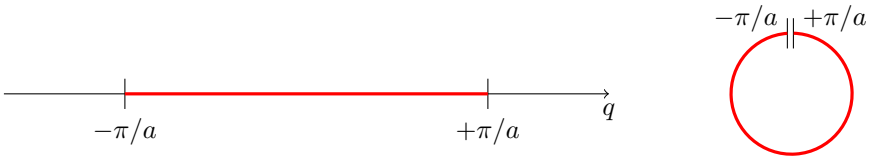

Figure 6. *Limitation of the quasimomentum to the first Brillouin zone, and representation of this Brillouin zone as a closed circle (or a torus in higher dimensions).*

$$\psi_{\pi/a}^{(n)}(x) = \mathrm{e}^{\mathrm{i}\alpha_n}\, \psi_{-\pi/a}^{(n)}(x). \tag{77}$$

and the eigenenergies are equal between the two bounds of the zone:

$$E_{\pi/a}^{(n)} = E_{-\pi/a}^{(n)}. \tag{78}$$

The task of searching for the eigenstates and eigenvalues of the Hamiltonian at one end of the Brillouin zone or the other is then exactly the same. This means that this zone should be thought of as a circle (or a torus in higher dimensions) rather than as a half-open line segment (figure 6).

Energy bands. When q varies in the interval $[-\pi/a, \pi/a]$, each energy $E_q^{(n)}$ describes a segment

$$E_{\min}^{(n)} \;\leq\; E_q^{(n)} \;\leq\; E_{\max}^{(n)}. \tag{79}$$

This segment represents the *n-th energy band*, whose width is

$$\Delta E^{(n)} = E_{\max}^{(n)} - E_{\min}^{(n)}. \tag{80}$$

An example is given in figure 7 for the sinusoidal potential $V(x) \propto \sin^2(\pi x/a)$. In one dimension, the energy bands that we will later consider are usually separated: the bottom of the band $n+1$ is higher than

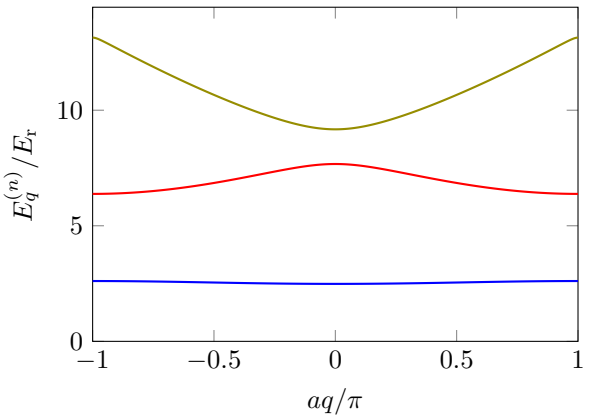

Figure 7. *The first three energy bands ($n = 0, 1, 2$) for the sinusoidal potential $V(x) = V_0 \sin^2(\pi x/a)$. They are represented here for $V_0 = 8E_r$, where E_r is the recoil energy defined by $E_r = \pi^2\hbar^2/(2ma^2)$.*

the top of the band n. This property is generally not true in two or three dimensions.

3-4 The Zak phase

We have seen in § 1 that the notion of geometrical phase appears for a closed loop in the space of parameters denoted by the general symbol $\boldsymbol{\lambda}$. As we have already mentioned, one could naively think that in one dimension, the closed paths consist in one or several segments that are followed in the forward direction and then in the backward direction; the notion of Berry phase would then be useless since the contributions of the back-and-forth displacements to the integral of the Berry connection on such a path cancel out.

There is however an exception to this result, which precisely relates to the case of the Brillouin zone of a periodic potential. This exception, expressed by Zak (1989), uses the circular structure of the Brillouin zone. If the parameter q follows the path

$$q_i \longrightarrow q_f = q_i + \frac{2\pi}{a}, \tag{81}$$

then the physical situations described by $\hat{H}_{q_i}$ and $\hat{H}_{q_f}$ are identical[4]. We then have a closed path, and in particular we have the same basis of eigenstates $\{|u_q^{(n)}\rangle\}$ (up to a phase) at the beginning and at the end of the path. Although the situation is one-dimensional, there is no reason why the geometrical phase acquired by a particle[5]

$$\Phi_{\text{geom}}^{(n)} = \mathrm{i}\int_{-\pi/a}^{+\pi/a} \langle u_q^{(n)}|\partial_q u_q^{(n)}\rangle \, \mathrm{d}q \tag{82}$$

should be null, since the parameter q has not moved in a back-and-forth motion.

One then understands that periodic potentials, even in one dimension, are well suited for the emergence of geometrical phases. In the following, we will go one step further and show that this phase can be *topological* if the physical situation displays some symmetries. More precisely, we will show that for the SSH model, this geometrical phase, called in this context the *Zak phase*, is quantized in multiples of π and that it is in general not modified by a small distortion of the lattice, provided that this distortion respects the symmetry.

4 The SSH (Su-Schrieffer-Heeger) model

We now address the simplest 1D model that presents this type of non-trivial topology (Su, Schrieffer, et al. 1979). It is a discrete model in which a particle can jump from one site to the two neighbouring sites, to the right or to the left. We will start with the case where all sites and all tunneling matrix elements are equivalent, for which no topology is present. Then, we will see that we only need to add a small modification to the initial hypotheses to have topological properties appearing.

[4] The two Hamiltonians $\hat{H}_{q_i}$ and $\hat{H}_{q_f}$ can be identical or different, according to the chosen parametrization of the unit cell.

[5] For a 1D problem, we replace the symbol of the gradient $\boldsymbol{\nabla}_{\boldsymbol{q}}$ by ∂_q.

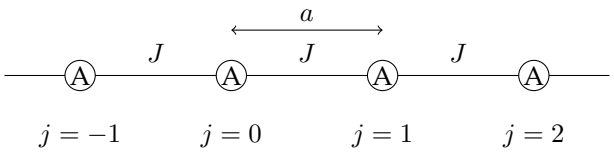

Figure 8. *The one-band tight-binding model, for which all the sites are equivalent and the tunneling amplitude from one site to a neighbouring site is always the same.*

We will not demonstrate how a discrete Hamiltonian can be obtained from the continuous Hamiltonian (58). It relies on the *tight-binding* approximation, which has been described in details in the lecture of 2012-2013. Here, we will only present the hypotheses of this approximation, which are very intuitive.

4-1 The one-band tight-binding model

Consider the infinite chain represented in figure 8, which is composed of identical sites separated by a distance a. We suppose that a particle sits on this lattice, and we denote by $|j\rangle$ the state that corresponds to the particle being localized on the j-th site ($j \in \mathbb{Z}$). All the sites have the same energy, which by convention we set at zero. The tunneling amplitude from one site to a neighbour is noted $-J$, where the coefficient J is chosen to be positive. The Hamiltonian thus reads:

$$\hat{H} = -J \sum_j |j+1\rangle\langle j| + \text{h.c.} \tag{83}$$

Bloch's theorem can be written in a very simple way in this case. There is (up to a multiplicative factor), only one periodic state on this lattice:

$$|u\rangle = \sum_j |j\rangle \tag{84}$$

and all the functions $|u_q\rangle$ are then equal. A Bloch state then has the form

$$|\psi_q\rangle = \sum_j \mathrm{e}^{\mathrm{i}jqa}\ |j\rangle. \tag{85}$$

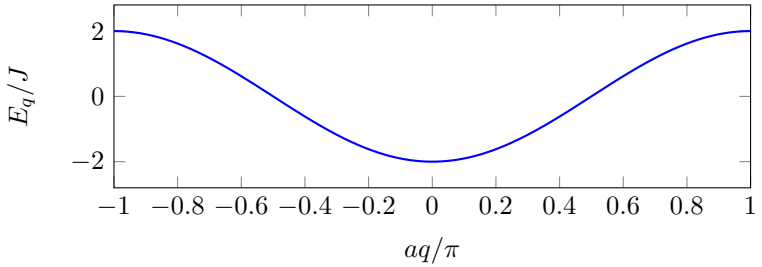

Figure 9. *The band of energy E_q for the Hubbard model.*

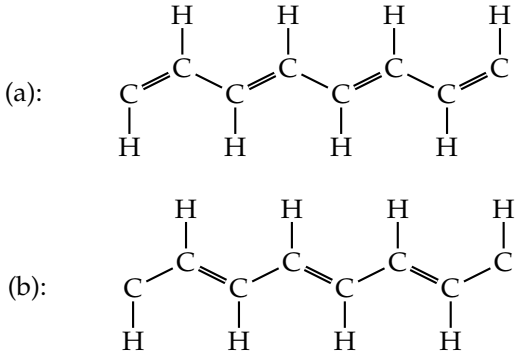

Figure 10. *The polyacetylene molecule, which can have the two dimerized forms (a) and (b).*

One can easily verify that this state is an eigenstate of the Hamiltonian (83) with the energy

$$E_q = -2J\ \cos(qa). \tag{86}$$

This model is therefore a one-band model (figure 9). Since $|u_q\rangle$ does not depend on q, the Berry curvature $\mathcal{A}_q = \mathrm{i}\ \langle u_q|\partial_q u_q\rangle$ associated to this band is null.

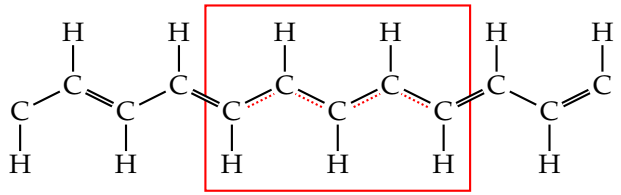

Figure 11. *A junction between the two phases (a) and (b) of figure 10.*

4-2 The SSH model and its Hamiltonian

The model introduced by Su, Schrieffer, et al. (1979) was designed to describe how solitonic waves could form on large polymer chains, such as polyacetylene, pictured in figure 10. This molecule displays alternatively a simple and double bond, and can exist under the two dimerized versions (a) and (b). The crucial point of the SSH article was the study of the junction between two molecules of different versions, as shown in figure 11, and the possibility to observe localized states (solitons or edge states) at this junction. We will see in the next chapter how this model can be implemented with atomic or photonic systems.

The simplest modelization of this chain relies on a tight-binding model directly inspired by the previous one (§4-1), the only modification being that the tunneling amplitude can have two values J and J' which correspond to the simple and double bonds. We thus consider the chain represented in figure 12, with two types of sites denoted as A and B. For this choice of dimerization, the A sites are linked to their left neighbour with the tunneling coefficient J and to their right neighbour with the coefficient J' and conversely for the B sites. The unit cell of this 1D lattice then comprises a pair of A and B sites, and the distance between two neighbouring cells is noted a, as previously.

The periodic functions on the lattice have, by definition, the same amplitude α (resp. β) on all sites A (resp. B) of the lattice, and they are written as

$$|u_q\rangle = \alpha_q \left(\sum_j |A_j\rangle \right) + \beta_q \left(\sum_j |B_j\rangle \right), \tag{87}$$

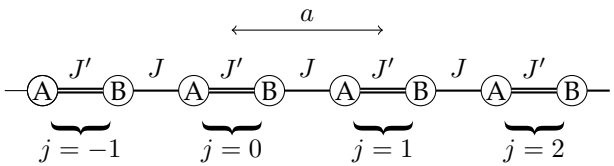

Figure 12. *A simplified representation of the SSH model.*

where we choose by convention

$$|\alpha_q|^2 + |\beta_q|^2 = 1. \tag{88}$$

In this model where a unit cell has two sites, a function $|u_q\rangle$ can then formally be seen as the state of a spin $1/2$:

$$|u_q\rangle \equiv \begin{pmatrix} \alpha_q \\ \beta_q \end{pmatrix}. \tag{89}$$

The associated Bloch functions are

$$|\psi_q\rangle = \sum_j \mathrm{e}^{\mathrm{i}\, jqa} \left(\alpha_q |A_j\rangle + \beta_q |B_j\rangle \right). \tag{90}$$

The Bloch function $|\psi_q\rangle$ is by definition an eigenstate with eigenenergy E_q of the Hamiltonian

$$\hat{H} = -J' \sum_j |B_j\rangle\langle A_j| - J \sum_j |B_{j-1}\rangle\langle A_j| \; + \; \text{h.c.} \tag{91}$$

This enables us to write the constraint on the coefficients α_q and β_q under a matrix form:

$$\hat{H}_q \begin{pmatrix} \alpha_q \\ \beta_q \end{pmatrix} = E_q \begin{pmatrix} \alpha_q \\ \beta_q \end{pmatrix} \tag{92}$$

where the periodic Hamiltonian $\hat{H}_q$ is the 2×2 matrix

$$\hat{H}_q = - \begin{pmatrix} 0 & J' + J\,\mathrm{e}^{-\mathrm{i}qa} \\ J' + J\,\mathrm{e}^{\mathrm{i}qa} & 0 \end{pmatrix}. \tag{93}$$

This Hamiltonian has the same form as the one of a spin $1/2$ with $E_0 = 0$ and

$$h(q) \equiv h_x(q) + \mathrm{i} h_y(q) = J' + J\,\mathrm{e}^{\mathrm{i}qa}. \tag{94}$$

The vector $\boldsymbol{h}$ is equal to

$$\boldsymbol{h}(q) = \begin{pmatrix} J' + J\cos(qa) \\ J\sin(qa) \\ 0 \end{pmatrix} \tag{95}$$

and always lies in the xy-plane. It can therefore be represented by the complex number $h(q)$. The eigenstates of the Hamiltonian $\hat{H}_q$ of the SSH model thus always lie on the equator of the Bloch sphere.

For each value of q we get two eigenenergies:

$$E_q^{(\pm)} = \pm|J' + J\,\mathrm{e}^{\mathrm{i}qa}| = \pm\left[J^2 + J'^2 + 2JJ'\cos(qa)\right]^{1/2}, \tag{96}$$

which give two energy bands when q varies in the Brillouin zone $[-\pi/a, +\pi/a[$:

$$\begin{aligned} \mathcal{B}^{(+)} \quad &: \quad |J - J'| \;\leq\; E \leq J + J' \\ \mathcal{B}^{(-)} \quad &: \quad -(J + J') \;\leq\; E \leq -|J + J'|. \end{aligned} \tag{97}$$

These energy bands, represented in figure 13, are separated except if $J = J'$, in which case we recover the model studied in the previous paragraph[6]. The energy levels for the two cases $J' > J$ and $J' < J$ have similar aspects, and there is for now no hint to assign a different topology for these two situations. But the physics is not all contained in the energy levels: the variation with q of the eigenstates contains another piece of information, which we now examine.

Remark: the structure of Bloch functions. In (90) we have chosen a form of the Bloch functions that ensures that the Hamiltonian $\hat{H}_q$ is periodic:

$$\hat{H}_q = \hat{H}_{q+2\pi/a}. \tag{98}$$

This choice simplifies the analysis, even if an arbitrary choice remains in the definition of the unit cell, that we will investigate in §4-4. We also could have encoded the relative position of a B site with respect to the A

[6]Note that the Brillouin zone is then twice as small since the period of the lattice has doubled.

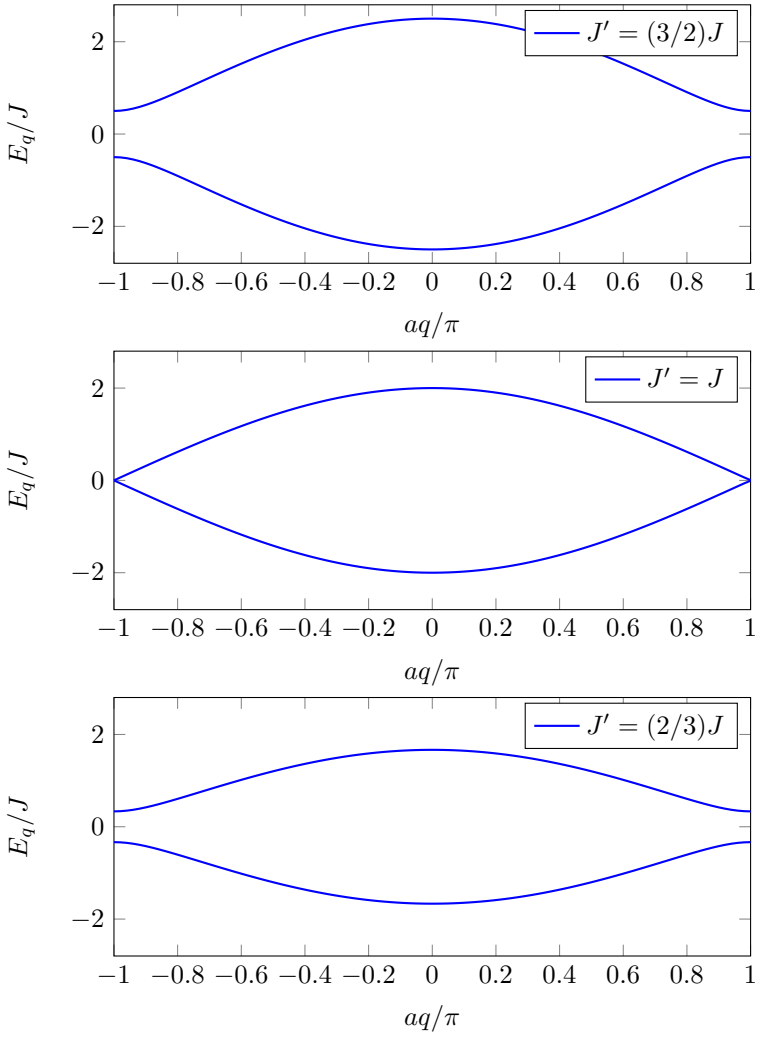

Figure 13. *The energy bands (96) of the SSH model for $J' = (3/2)\,J$ (top), $J' = J$ (middle) et $J' = (2/3)\,J$ (bottom).*

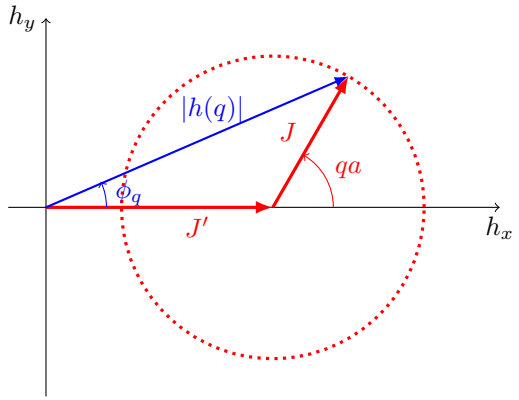

Figure 14. *Trace of $h(q) \equiv J' + Je^{iqa} = |h(q)|\, e^{i\phi_q}$ in the complex plane in the case where $J' > J$. The path followed by $h(q)$ does not wind around the origin and the phase ϕ_q starts and ends at $\phi_q = 0$ when q describes the Brillouin zone $[-\pi/a, \pi/a[$.*

site of the same cell. If b designates the distance AB, this choice leads us to choose Bloch functions under the form:

$$|\psi_q\rangle = \sum_j \left(e^{i\,jaq}\ \alpha'_q\ |A_j\rangle\ +\ e^{i\,(ja+b)q}\ \beta'_q\ |B_j\rangle \right). \tag{99}$$

and gives the Hamiltonian

$$\hat{H}'_q = -\begin{pmatrix} 0 & J'\,e^{iqb} + J\,e^{-iq(a-b)} \\ J'\,e^{-iqb} + J\,e^{iq(a-b)} & 0 \end{pmatrix} \tag{100}$$

which is in general not a periodic function of q. Its eigenenergies are of course not affected by this different definition of the Bloch states, but its eigenvectors are. In practice, this encoding leads to more complicated expressions to study the topology of the bands, and we will not use it. It can nevertheless be useful when a uniform force is applied on the particles on top of the periodic potential. This force indeed derives from the potential $-Fx$, and it is then useful to keep the exact position of each site $x = ja$ or $x = ja + b$ in the expression of the Bloch functions.

4-3 Eigenstates and topology

The eigenstates of the matrix $\hat{H}_q$ associated with the energies $E_q^{(\pm)}$ are

$$|u_q^{(\pm)}\rangle = \frac{1}{\sqrt{2}} \begin{pmatrix} 1 \\ \mp e^{i\phi_q} \end{pmatrix} \tag{101}$$

where we have introduced the argument ϕ_q of the non-diagonal complex coefficient of $\hat{H}_q$ (figure 14):

$$h(q) \equiv J' + J\,e^{iqa} = |h(q)|\,e^{i\phi_q}. \tag{102}$$

This argument is well-defined for all value of q provided that $|h(q)|$ does not become null in the Brillouin zone, that is provided that $J \neq J'$.

One can then easily calculate the Berry connection

$$\mathcal{A}_q^{(\pm)} = i\,\langle u_q^{(\pm)} | \partial_q u_q^{(\pm)} \rangle = -\frac{1}{2}\frac{d\phi_q}{dq} \tag{103}$$

and the Zak phase, obtained by integrating the Berry connection on the Brillouin zone:

$$\Phi_{\text{Zak}} = \int_{-\pi/a}^{+\pi/a} \mathcal{A}_q^{(\pm)}\, dq = -\frac{1}{2}\int_{-\pi/a}^{+\pi/a} \frac{d\phi_q}{dq}\, dq. \tag{104}$$

This result has a clear geometrical interpretation: the Zak phase, or more precisely the quantity

$$N \equiv -\frac{1}{\pi}\Phi_{\text{Zak}} = \frac{1}{2\pi}\int_{-\pi/a}^{+\pi/a} \frac{d\phi_q}{dq}\, dq = \frac{1}{2\pi}\left[\phi_{+\pi/a} - \phi_{-\pi/a}\right] \tag{105}$$

measures how many times the complex number $h(q)$ winds around 0 when q describes the Brillouin zone.

Figures 14 and 15 show possible trajectories of $h(q) = J' + Je^{iqa}$ in the complex plane when the quasimomentum q varies from $-\pi/a$ to π/a. This trajectory is a circle centered on $(J', 0)$ with a radius J. There are then two possible cases for ϕ_q when q describes the Brillouin zone:

- If $J' > J$ (figure 14), the circle is entirely in the region of the complex plane of positive real part. This circle does not surround the origin: $N = 0$ and $\Phi_{\text{Zak}} = 0$ for each of the two bands (figure 16). In this case we say that the bands are *topologically trivial*.

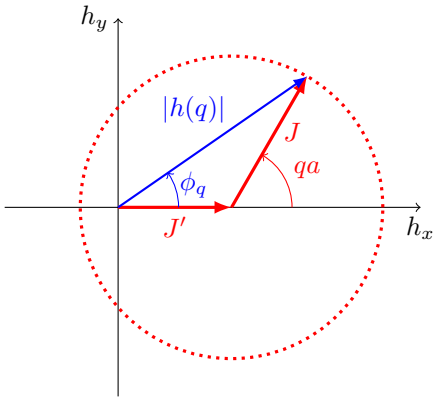

Figure 15. *Trace of $h(q) \equiv J' + Je^{iqa} = |h(q)|\, e^{i\phi_q}$ in the complex plane in the case where $J' < J$. The path followed by $h(q)$ winds around the origin and the phase ϕ_q varies continuously from $\phi_q = -\pi$ to $\phi_q = \pi$ when q describes the Brillouin zone $[-\pi/a, \pi/a[$.*

- If $J' < J$ (figure 15), the circle surrounds the origin and it is followed counterclockwise by $h(q)$. We then have $N = 1$ and $\Phi_{\text{Zak}} = -\pi$ for each of the two bands (figure 16). In this case we say that the two bands are *topologically non-trivial*.

The number N is a topological invariant, in the sense that is does not change when the parameter of the SSH model are slightly modified (the period a, the tunneling coefficients J and J'), provided that the frontier $J = J'$ is not crossed.

From the point of view of the pseudo-spin associated to $|u_q\rangle$, the Zak phase is linked to the solid angle described by this spin along the equator of the Bloch sphere when q goes through the Brillouin zone (figure 17). In the topologically trivial case, this pseudo-spin goes back and forth on the equator. In the other case it does a full turn on the Bloch sphere.

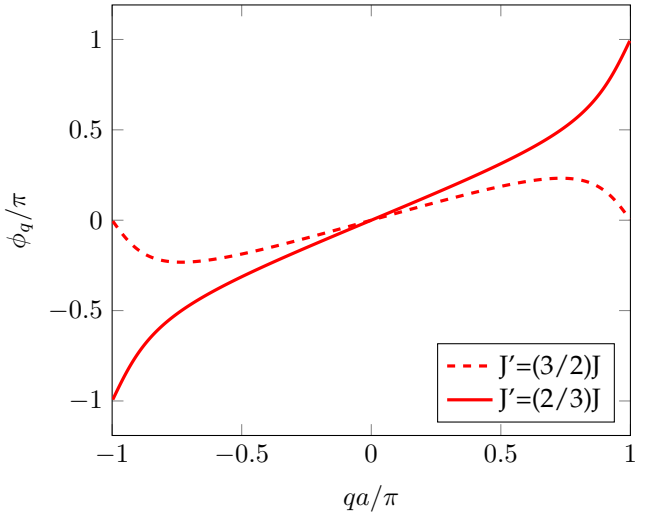

Figure 16. *Variation of the phase ϕ_q when q goes through the Brillouin zone $[-\pi/a, \pi/a[$, for the case $J' > J$ (no winding) and the case $J' < J$ (winding number $N = 1$).*

4-4 What is the physical reality of this topology?

The distinction we made between the two regimes $J' > J$ and $J' < J$ seems convincing, but it deserves a deeper analysis. The way the A_j and B_j sites have been assigned to a unit cell is arbitrary. Instead of the choice made in figure 12 and represented again in figure 18a, one could also choose the parametrization of figure 18b. With this parametrization, the j-th cell comprises the site A_j and the site B_{j-1}. The form of the Bloch functions with this new parametrization is

$$|\psi_q\rangle = \sum_j e^{ijqa} \left(\tilde{\alpha}_q |A_j\rangle + \tilde{\beta}_q |B_{j-1}\rangle \right) \tag{106}$$

with coefficients $(\tilde{\alpha}_q, \tilde{\beta}_q)$ which are linked to the previous coefficients (α_q, β_q) by

$$\tilde{\alpha}_q = \alpha_q, \qquad \tilde{\beta}_q = e^{-iqa}\, \beta_q. \tag{107}$$

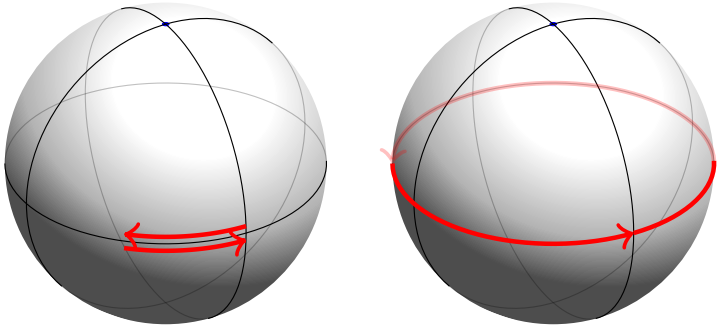

Figure 17. *The trajectories of the state $|u_q^{(-)}\rangle$ on the Bloch sphere when q describes the Brillouin zone. Left: the topologically trivial case, $N = 0$; Right: the topologically non-trivial case, $N = 1$.*

This transformation is not a gauge transformation of the type considered in (30) because it does not correspond to a global multiplication of the function $|u_q\rangle$ by a coefficient $\mathrm{e}^{\mathrm{i}\chi_q}$. One cannot straightforwardly predict its consequence on the Zak phase.

Let us follow again the procedure presented for the first parametrization. We write that ψ_q is an eigenstate of $\hat{H}$ (which is unchanged), and we find that the coefficients $(\tilde{\alpha}_q, \tilde{\beta}_q)$ verify:

$$\hat{\tilde{H}}_q \begin{pmatrix} \tilde{\alpha}_q \\ \tilde{\beta}_q \end{pmatrix} = E_q \begin{pmatrix} \tilde{\alpha}_q \\ \tilde{\beta}_q \end{pmatrix} \qquad \text{with} \quad \hat{\tilde{H}}_q = -\begin{pmatrix} 0 & J + J'\,\mathrm{e}^{\mathrm{i}qa} \\ J + J'\,\mathrm{e}^{-\mathrm{i}qa} & 0 \end{pmatrix}. \tag{108}$$

This new Hamiltonian is also periodic with q, but the roles of J and J' are interchanged (as one could have expected), and q is changed into $-q$.

Of course, this new parametrization does not change the shape of the energy bands. However, it affects the form of the eigenstates and the Zak phase. We now find that:

- For $J' < J$, $\tilde{\Phi}_{\mathrm{Zak}} = 0$, which means that there is no winding of the complex number $J + J'\,\mathrm{e}^{-\mathrm{i}qa}$ around the origin.
- For $J' > J$, $\tilde{\Phi}_{\mathrm{Zak}} = +\pi$, which means that there is a clockwise winding of the complex number $J + J'\,\mathrm{e}^{-\mathrm{i}qa}$ around the origin.

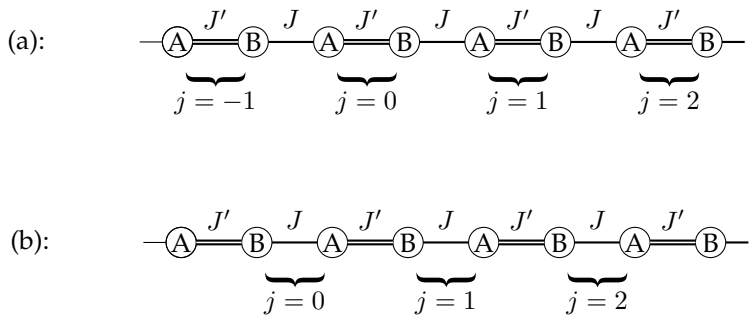

Figure 18. *Two possible parametrizations of the SSH model.*

The takeaway message is that the "absolute" notion of topologically trivial or topologically non-trivial phase has no meaning for this infinite 1D chain. The only physically relevant conclusion is that the two phases obtained when switching from the case $J' > J$ and the case $J' < J$ are different:

$$\Phi_{\mathrm{Zak}}^{[J'>J]} - \Phi_{\mathrm{Zak}}^{[J'<J]} = \pi. \tag{109}$$

In order to reveal this difference, we will see in the next chapter that one can physically exchange the values of J and J' within an experimental sequence, as it has been done by Atala, Aidelsburger, et al. (2013). One can also consider a finite chain with a given number of cells, for example three cells in figure 19. It is then not equivalent to have a large or a small tunneling matrix element at the ends of the chain. One can finally connect the two phases $[J' > J]$ and $[J' < J]$, as indicated in figure 11, and study the localized states that may appear near the junction. We will see in the next chapter how these edge states emerge for the SSH model in a finite or a semi-infinite chain, and their possible applications in photonics.

Remark : Back to the encoding of the position. In (100) we have given the expression of $\hat{H}'_q$ when the distance b between two A and B sites is encoded in the Bloch function. One can observe that this Hamiltonian $\hat{H}'_q$ continuously links $\hat{H}_q$ and $\hat{\tilde{H}}_q$ when b is varied from 0 to a. If we use again

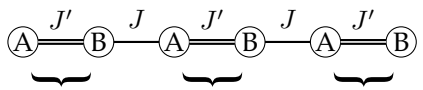

Figure 19. *A finite SSH chain, with three unit cells. The two configurations $J' > J$ and $J' < J$ have different fates regarding the existence of edge states.*

the previous formalism with this Hamiltonian, we find that the phase ϕ_q is replaced by $\phi_q - qb$, such that Φ_{Zak} becomes $\Phi_{\text{Zak}} + \pi b/a$. The Zak phase is then not a multiple of π anymore. Indeed, the Hamiltonian $\hat{H}'_q$ is not periodic in q, and the associated complex number $h'(q)$ does not follow a closed trajectory in the complex plane when q describes the Brillouin zone. However, the relationship (109) which gives a phase difference of π between the cases $J' < J$ and $J' > J$ stays valid.

Chapter II

Topology in one dimension: from the SSH model to Majorana modes

After the presentation in the first chapter of the formalism that one needs to study topological states of matter, we move on to search for practical manifestations of this topology. The main point of the discussion is the existence of robust edge states that appear at the interface of two phases with different topologies.

We will first focus on the SSH model introduced by Su, Schrieffer, et al. (1979) to describe the molecular chain of polyacetylene. We will further characterize the topology of a band that we already have sketched in chapter 1 in terms of winding around the Bloch sphere. We will demonstrate for this model that robust edge states can exist in a finite or in a semi-infinite chain.

We will then come to the description of a recent experiment performed with light where these topological properties are evidenced, and where the edge states are used to realize a *topological laser* (St-Jean, Goblot, et al. 2017).

In the last section, we will compare the SSH chain to another remarkable toy-model introduced by Kitaev (2001) to describe a 1D topological superconductor. We will see that the edge states have very particular properties, described by modes of quasi-particles for which the creation and annihilation operators coincide. These modes are called *Majorana modes*, in analogy to the formalism presented by Majorana (1937) to study the Dirac equation.

The investigation of these two models will lead us to underline the importance of symmetries for the stability of topological phases (see also appendix 2 of this chapter). These symmetries are the sublattice symmetry for the SSH model and the particle-hole symmetry for the Kitaev model. As long as the system has this symmetry, the topological phases that we describe are robust: they can transform into a normal phase only if a gap between two energy bands closes, which implies an important modification of the parameters of the Hamiltonian. On the other hand, as we will see in chapter 3, the topological robustness can disappear without closing a gap if this symmetry is lost.

1 The edge states of the SSH model

1-1 Going back to the SSH Hamiltonian

As we have seen in chapter 1, the SSH model aims at describing a long polymer chain, such as polyacetylene (figure 1a). It is a 1D chain that has two types of bonds, simple or double, between neighbouring carbon atoms. It is modeled by describing the movement of an electron on this chain in the tight-binding regime, with a line of alternating A and B sites.

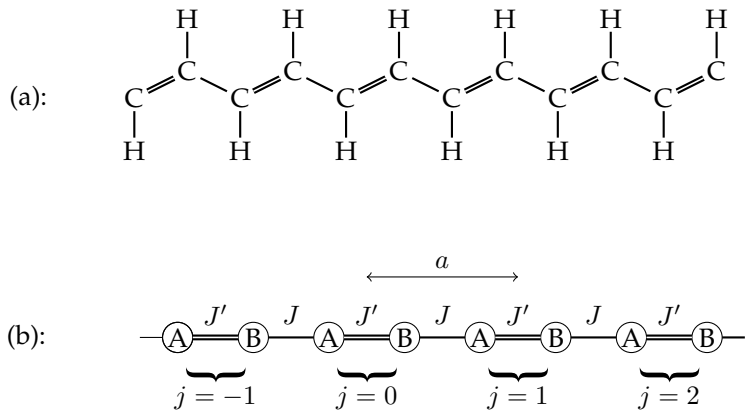

Figure 1. *(a) A molecule of polyacetylene. (b) Its modeling in a tight-binding approach.*

The electron can hop from one site to its two neighbours with tunneling coefficients J and J' (figure 1 b).

A crucial assumption of the SSH model is that the A and B sites have the same energy, conventionally set at $E = 0$. The Hamiltonian of an electron on the chain can then be written as

$$\hat{H} = -J' \sum_j |B_j\rangle\langle A_j| - J \sum_j |B_{j-1}\rangle\langle A_j| \; + \; \text{h.c.} \tag{1}$$

The infinite chain constitues a spatially periodic system that one can treat with the formalism of the Bloch waves. The eigenstates of the Hamiltonian are searched under the form

$$|\psi_q\rangle = \sum_j \mathrm{e}^{\mathrm{i}\, jqa} \left(\alpha_q |A_j\rangle + \beta_q |B_j\rangle\right), \tag{2}$$

where q is Bloch's quasimomentum, whose value is limited to the Brillouin zone $-\pi/a \leq q < \pi/a$ where the two endpoints $q = \pm\pi/a$ are identified one with the other. The coefficients α_q and β_q are determined by the equation that the state $|\psi_q\rangle$ verifies as an eigenstate of the Hamiltonian of the chain:

$$\hat{H}_q \begin{pmatrix} \alpha_q \\ \beta_q \end{pmatrix} = E_q \begin{pmatrix} \alpha_q \\ \beta_q \end{pmatrix} \tag{3}$$

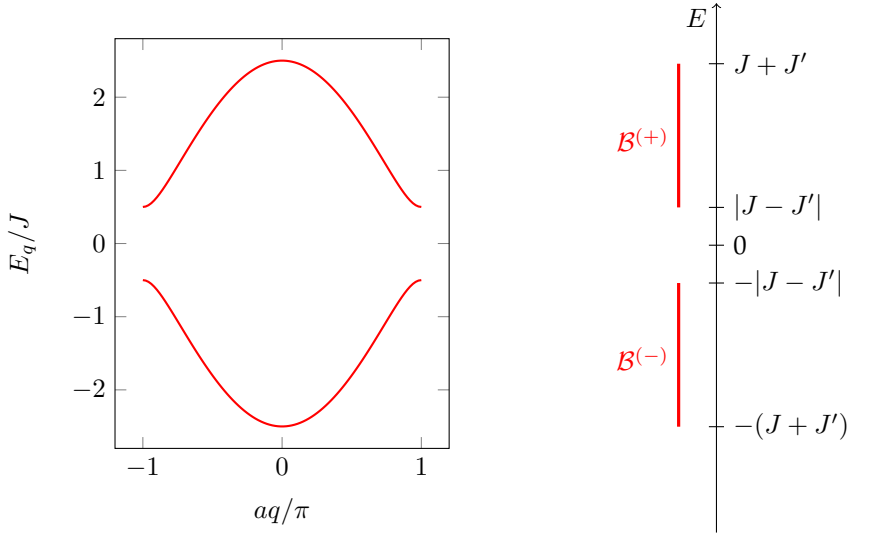

Figure 2. *The energy bands of the SSH model for an infinite chain, in the case where $J' = (3/2)\, J$.*

where the periodic Hamiltonian $\hat{H}_q$ is the 2×2 matrix:

$$\hat{H}_q = -\begin{pmatrix} 0 & J' + J\,\mathrm{e}^{-\mathrm{i}qa} \\ J' + J\,\mathrm{e}^{\mathrm{i}qa} & 0 \end{pmatrix}. \tag{4}$$

Its eigenvalues are

$$E_q^{(\pm)} = \pm \left[J^2 + J'^2 + 2JJ' \cos(qa)\right]^{1/2}, \tag{5}$$

which leads to the two energy bands:

$$\begin{aligned} \mathcal{B}^{(+)} \quad &: \qquad |J - J'| \;\leq\; E \leq J + J' \\ \mathcal{B}^{(-)} \quad &: \qquad -(J + J') \;\leq\; E \leq -|J - J'|. \end{aligned} \tag{6}$$

An example of the variation of $E_q^{(\pm)}$ with q is shown in figure 2 for $J' = (3/2)\, J$. These two bands are separated, except if $J = J'$ (see figure 3).

Let us recall the compact notation introduced in chapter 1 for a Hamiltonian represented by a 2×2 matrix. By using the three Pauli matrices

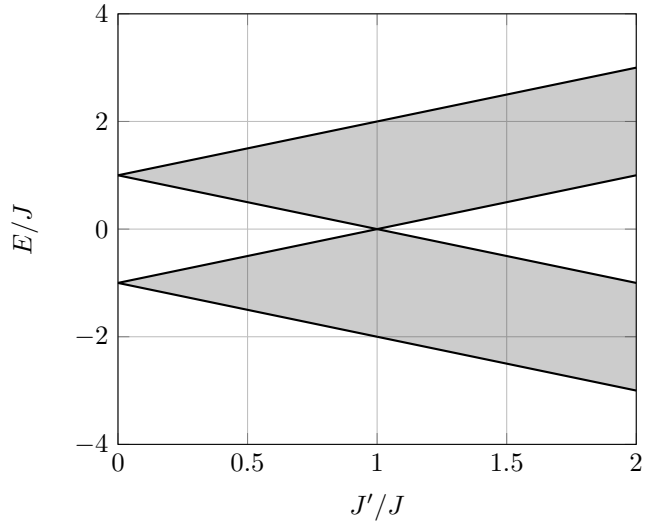

Figure 3. *The energy bands of the SSH model for an infinite chain as a function of the ratio J'/J. We obtain two separated bands, except for $J' = J$.*

$$\hat{\sigma}_x = \begin{pmatrix} 0 & 1 \\ 1 & 0 \end{pmatrix}, \qquad \hat{\sigma}_y = \begin{pmatrix} 0 & -\mathrm{i} \\ \mathrm{i} & 0 \end{pmatrix}, \qquad \hat{\sigma}_z = \begin{pmatrix} 1 & 0 \\ 0 & -1 \end{pmatrix}, \tag{7}$$

we can write any hermitian matrix under the form

$$\hat{H}_q = E_0(q)\ \hat{1}\ -\ \boldsymbol{h}(q) \cdot \hat{\boldsymbol{\sigma}}, \tag{8}$$

where the functions $h_\alpha(q)$, $\alpha = x, y, z$ are real. For the SSH model, we have chosen as origin of energies $E_0 = 0$ and

$$h_x(q) + \mathrm{i}h_y(q) = J' + J\mathrm{e}^{\mathrm{i}qa}, \qquad h_z = 0. \tag{9}$$

The form (8) obtained for $\hat{H}_q$ for each value of q can be seen as the Hamiltonian of a spin $1/2$ in the magnetic field $\boldsymbol{h}(q)$. The two eigenstates are

$$|u_q^{(-)}\rangle = \frac{1}{\sqrt{2}} \begin{pmatrix} 1 \\ \mathrm{e}^{\mathrm{i}\phi_q} \end{pmatrix}, \qquad |u_q^{(+)}\rangle = \frac{1}{\sqrt{2}} \begin{pmatrix} 1 \\ -\mathrm{e}^{\mathrm{i}\phi_q} \end{pmatrix} \tag{10}$$

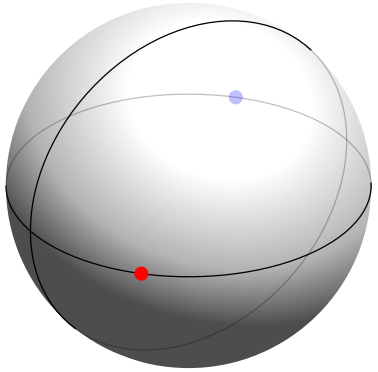

Figure 4. *The representation of the two eigenstates $|u_q^{(\pm)}\rangle$ on the Bloch sphere of radius 1. For the SSH model, these two eigenstates are always on the equator.*

where we have introduced the number of unit modulus

$$\mathrm{e}^{\mathrm{i}\phi_q} = \frac{J' + J\,\mathrm{e}^{\mathrm{i}qa}}{|J' + J\,\mathrm{e}^{\mathrm{i}qa}|}, \tag{11}$$

a definition that is valid as long as the denominator does not cancel out, that is as long as $J' \neq J$.

In the following, we will use the representation of the quantum state $|u\rangle$ of a two-level system on the Bloch sphere, also introduced in chapter 1. This representation uses the fact that such a state can be written in a unique way (up to a global phase) as:

$$|u\rangle = \begin{pmatrix} \cos(\theta/2) \\ \mathrm{e}^{\mathrm{i}\phi} \sin(\theta/2) \end{pmatrix} \tag{12}$$

where $\theta \in [0, \pi]$ and $\phi \in]-\pi, \pi]$. The representation on the Bloch sphere then consists in considering this state as the point with spherical angles θ and ϕ. In this representation, the two eigenstates $|u_q^{(\pm)}\rangle$ of the SSH model are located on the equator of the Bloch sphere, with the azimuthal angle ϕ_q for $|u_q^{(-)}\rangle$ and $\phi_q \pm \pi$ for $|u_q^{(+)}\rangle$.

Let us finally recall that the topology of the two energy bands of the SSH model is directly linked to the winding number of the phase ϕ_q of the

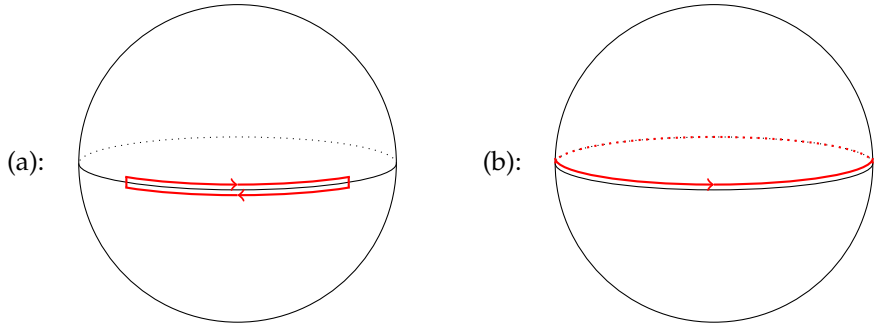

Figure 5. *The trajectory of the eigenstate $|u_q^{(-)}\rangle$ of the SSH model as the quasi-momentum q goes through the Brillouin zone $]-\pi/a, \pi/a]$. The cases (a) and (b) correspond respectively to $J' > J$ (non-topological) and $J' < J$ (topological).*

complex number $J' + Je^{iqa}$:

$$\mathcal{N} \equiv \frac{1}{2\pi} \int_{-\pi/a}^{+\pi/a} \frac{\mathrm{d}\phi_q}{\mathrm{d}q}\, \mathrm{d}q. \tag{13}$$

Since ϕ_q represents the azimuthal angle of $|u_q^{(-)}\rangle$, this winding number can be geometrically interpreted with the trajectory of this state (or of its partner $|u_q^{(+)}\rangle$) when q describes the Brillouin zone $[-\pi/a, \pi/a[$:

- If $\boldsymbol{h}$ goes back and forth along the equator, then $\phi_q = 0$ for $qa = \pm\pi$ and $\mathcal{N} = 0$. This corresponds to the case $J' > J$ (figure 5a). This configuration is called *normal* or *non-topological*.

- If $\boldsymbol{h}$ does a round trip along the equator, then $\phi_q = \pm\pi$ for $qa = \pm\pi$ and $\mathcal{N} = 1$. This corresponds to the case $J' < J$ (figure 5b). This configuration is called *topological*.

As the states $|u_q^{(\pm)}\rangle$ are bound to stay on the equator, one cannot continuously deform one type of trajectory into the other; it is at the origin of the topological protection of the winding number (and of the Zak phase $\Phi_{\text{Zak}}^{(-)} = -\pi\mathcal{N}$).

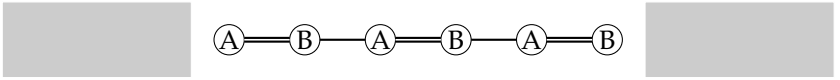

Figure 6. *A finite-size SSH chain (here with 6 sites, therefore with 3 AB pairs).*

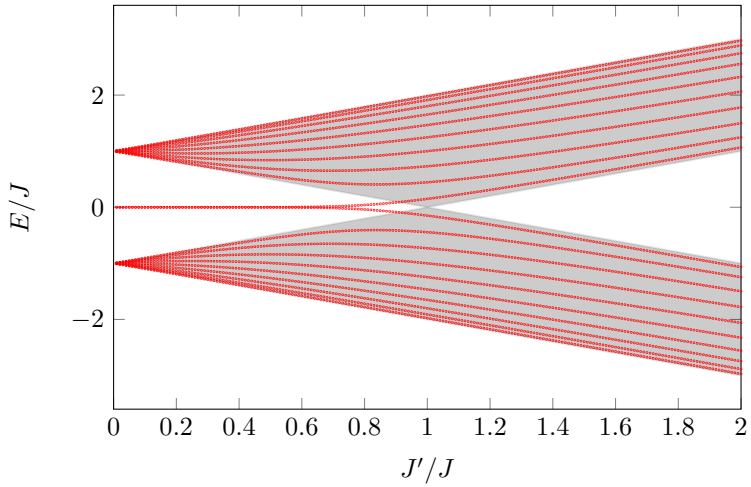

Figure 7. *The eigenstates of a SSH chain with 20 sites, therefore with 10 AB pairs. For $J' < J$, two edge states of quasi-null energy are present. These states gradually disappear when going to the region $J' > J$. The shaded area corresponds to the energy bands of the infinite chain, already shown in figure 3.*

1-2 The case of a finite chain

We start our study of the edge states by considering a finite chain that has a given number of AB pairs (figure 6). As the system is not translational invariant anymore, Bloch's theorem does not apply anymore, and it is not possible to have an analytical approach. We give in figure 7 the result of a numerical diagonalization of the Hamiltonian for a chain with 10 pairs.

Several remarkable features appear on this figure:

- Most of the energies found with the diagonalization are inside the bands found analytically for an infinite chain, and these energies fill

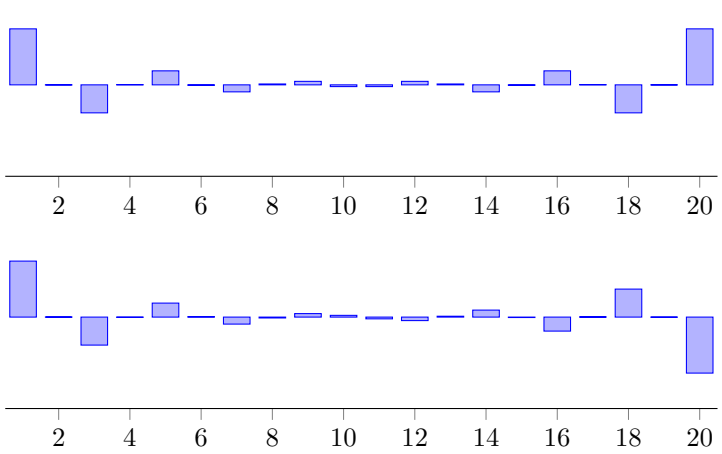

Figure 8. *The finite SSH chain with 20 sites, therefore with 10 unit cells, for $J' = J/2$. The probability amplitudes $a_1, b_1, a_2, b_2, \ldots$ of the two states lying in the gap are represented. The probability distributions of these two states are symmetric because of the symmetry of the chain.*

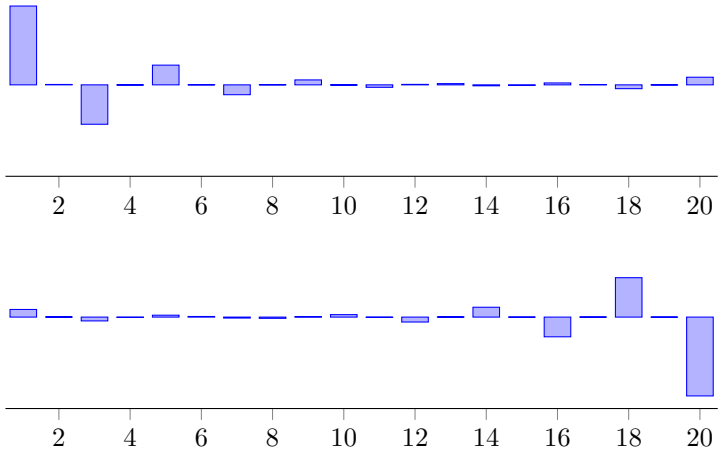

Figure 9. *The SSH chain with 20 sites, therefore with 10 unit cells, for $J' = J/2$, and with a slight offset of $-J/100$ of site A_1. The probability amplitudes $a_1, b_1, a_2, b_2, \ldots$ for the two states lying in the gap are represented. The energy offset of site A_1 leads to an almost complete localization of the edge states on one side or the other of the chain.*

the zone that these bands define: in the limit where the length of the chain becomes larger and larger, all the energies E_q will be recovered.

- The energy spectrum is symmetric with respect to the origin of energies.
- For $J' \lesssim J$, that is in the "topological" region, two states of quasi null energies are found, outside of the shaded area delimiting the allowed energy bands.

These states located inside the forbidden gap are the edge states that we want to study. We have represented in figure 8 the probability amplitudes (a_j, b_j) for these two states in the case $J' = J/2$. One finds that these two states are indeed localized at the end of the chain, with a probability higher than $3/4$ to find the particle on one of the extremities A_1 and B_{10}. Since the chain is symmetric, the probability distributions associated with these two states are also symmetric. However, this spatial symmetry is easily broken. One only needs to slightly modify the on-site energy of one these extremities (for example A_1) so that one of the edge states gets localized almost entirely on A_1 and the other one on B_{10}. To illustrate this statement, the result obtained when the energy of site A_1 has been changed from 0 to $-J/100$ is represented in figure 9. This sensitivity contrasts with the one of the Majorana modes that we will encounter later.

Delplace, Ullmo, et al. (2011) have proposed a simple and efficient method to quantitatively establish the *bulk–edge* correspondence for the SSH model, that is the direct link between the winding of the phase ϕ_q and the existence of states whose energy lies in the gap for a finite chain. The idea is to count the number of states that one can form with the Bloch functions of the bulk and see if they amount to $2N$, as expected from the dimension of the Hilbert space. If it is not the case, it means that additional states are necessary to get a basis: these are precisely the edge states that we have found numerically.

The states that one can form with the bulk states are standing waves,

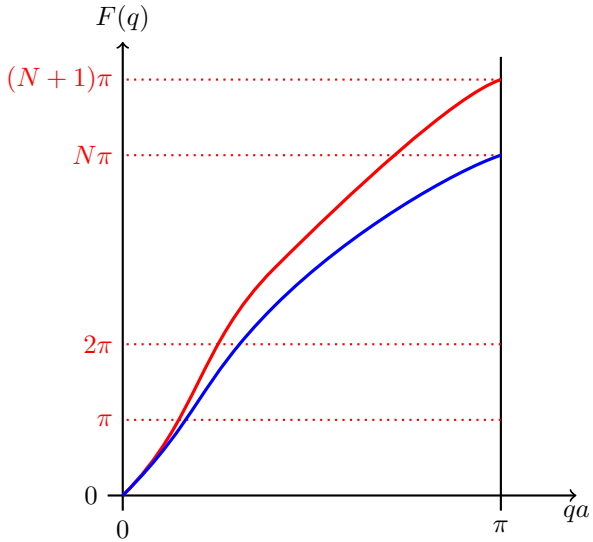

Figure 10. *Graphical solution of equation (16) that allows to determine the eigenstates of the open SSH chain constructed with bulk Bloch states. In the normal case, in red, one finds N solutions that are physically acceptable for each of the energy bands: this allows one to have a complete basis. In the topological case, in blue, one only finds $N-1$ states per band. The two missing states are the edge states, whose energy is located in the gap of the infinite chain.*

obtained by the superposition of two Bloch waves of momenta q and $-q$ with the same weight and a phase factor α which is undetermined for now:

$$\text{standing wave:} \qquad \mathrm{e}^{\mathrm{i}\alpha}|\psi_q^{(-)}\rangle + \mathrm{e}^{-\mathrm{i}\alpha}|\psi_{-q}^{(-)}\rangle. \tag{14}$$

We have chosen here $q \geq 0$ by convention and for now we have restrained to the lowest band. The finite character of the chain leads us to take into account "open" boundary conditions. If the chain is composed by sites $1, 2, \ldots, N$, we have to impose a null amplitude on the "fictitious" sites $|B_0\rangle$ and $|A_{N+1}\rangle$, which implies

$$\cos(\alpha + \phi_q) = 0, \qquad \cos[\alpha + (N+1)qa] = 0, \tag{15}$$

where we have used $\phi_{-q} = -\phi_q$. We eliminate α and obtain the condition on the momentum q:

$$F(q) \equiv (N+1)qa - \phi_q = 0 \ \text{ modulo } \pi \tag{16}$$

which can be solved graphically (figure 10).

For a sufficiently large amount N of sites, the function $F(q)$ is strictly increasing between $q = 0$ and $q = \pi/a$ [as a reminder, q is assumed to be positive to avoid counting twice the standing waves (14)]. It is always null at $q = 0$ and its value at $q = \pi/a$ depends on the topology of the band:

- In the normal case, $\phi_q = 0$ for $qa = \pi$ and $F(q)$ is equal to $(N+1)\pi$ there. Then, there are N physically acceptable solutions to equation (16), knowing that the points $q = 0$ and $qa = \pi$ both lead to a standing wave equal to zero everywhere.
- In the topological case, $\phi_q = \pi$ for $qa = \pi$ because of the winding around the Bloch sphere, and $F(q)$ is equal to $N\pi$ there. Then, there are only $N-1$ physically acceptable solutions to equation (16).

An identical reasoning can be made for the upper band states, and we thus obtain the number of bulk states that one can construct: $2N$ in the normal case, which provides us with a complete basis, and $2N-2$ in the topological case, which leads to the existence of two states outside of the bulk: these are the two edge states whose energy is close to zero, and which appear in figure 7.

1-3 The sublattice symmetry

We now explain the symmetry of the energy spectrum of the SSH chain, finite or infinite. An important feature of the Hamiltonian $\hat{H}_q = -\boldsymbol{h}(q) \cdot \hat{\boldsymbol{\sigma}}$ is that the unit vector $\boldsymbol{n}(q) = \boldsymbol{h}(q)/|\boldsymbol{h}(q)|$ always stays on the equator of the Bloch sphere, which allows us to sort the energy bands by the winding number around this sphere. The topological protection of the SSH model is thus ensured by the symmetry between the two sublattices A and B, which fixes $h_z = 0$.

This *sublattice symmetry*, which is also present in models much more advanced than the SSH model, is also called *chiral symmetry* for reasons that

have to do with field theory. Its mathematical translation is very simple in our case. Let us introduce the projectors $\hat{P}_A$ and $\hat{P}_B$ on each of the sublattices. The (unitary) operator

$$\hat{\mathcal{S}} \equiv \hat{P}_A - \hat{P}_B \tag{17}$$

anticommutes with the SSH Hamiltonian:

$$\hat{H}\hat{\mathcal{S}} = -\hat{\mathcal{S}}\hat{H}. \tag{18}$$

We emphasize the particular structure of how this symmetry manifests itself. For symmetries linked with a geometrical invariance (translational invariance, rotational invariance), we are used to having an operator $\hat{\mathcal{O}}$ that *commutes* with the Hamiltonian: this property allows one to search for a common basis of $\hat{H}$ and $\hat{\mathcal{O}}$ and thus find Bloch states in the case of translational invariance, or states whose energy and angular momentum are well-defined in the case of rotational invariance.

Let us explain the consequences of the anticommutation relationship (18). We multiply it to the left and to the right by $\hat{P}_A$, we use the fact that $\hat{P}_A$ and $\hat{P}_B$ are orthogonal projectors ($\hat{P}_A^2 = \hat{P}_A$, $\hat{P}_A\hat{P}_B = 0$), and we obtain

$$\hat{P}_A\hat{H}\hat{P}_A = 0, \tag{19}$$

and similarly for $\hat{P}_B$:

$$\hat{P}_B\hat{H}\hat{P}_B = 0. \tag{20}$$

This expression highlights the fact that the matrix $\hat{H}_q$ does not have diagonal coefficients ($\forall q$), which ensures that the vector $\boldsymbol{h}/|\boldsymbol{h}|$ stays on the equator of the unit sphere. One can also show that the converse is true: if $\hat{P}_A\hat{H}\hat{P}_A = 0$ and $\hat{P}_B\hat{H}\hat{P}_B = 0$, then one finds[1] the anticommutation relationship (18).

[1]The proof is easy when using $\hat{P}_A + \hat{P}_B = \hat{1}$:

$$\hat{H}\hat{\mathcal{S}} = \hat{H}\left(\hat{P}_A - \hat{P}_B\right) = \left(\hat{P}_A + \hat{P}_B\right)\hat{H}\left(\hat{P}_A - \hat{P}_B\right) = \hat{P}_B\hat{H}\hat{P}_A - \hat{P}_A\hat{H}\hat{P}_B \tag{21}$$

and

$$\hat{\mathcal{S}}\hat{H} = \left(\hat{P}_A - \hat{P}_B\right)\hat{H} = \left(\hat{P}_A - \hat{P}_B\right)\hat{H}\left(\hat{P}_A + \hat{P}_B\right) = \hat{P}_A\hat{H}\hat{P}_B - \hat{P}_B\hat{H}\hat{P}_A = -\hat{H}\hat{\mathcal{S}}. \tag{22}$$

A consequence of this relationship is that the energy spectrum is symmetric with respect to $E = 0$. Indeed, if $|\Psi\rangle$ is an eigenstate of $\hat{H}$ with eigenvalue E, then

$$\hat{H}\left(\hat{S}\,|\psi\rangle\right) \;=\; -\hat{S}\left(\hat{H}\,|\psi\rangle\right) \;=\; -E\,\left(\hat{S}\,|\psi\rangle\right) \tag{23}$$

which indicates that $\hat{\mathcal{S}}|\psi\rangle$ is also an eigenstate of $\hat{H}$ with eigenvalue $-E$.

This symmetry, when applied to the edge states, has important consequences:

- If this edge state is unique, such as the one appearing for a semi-infinite chain (*cf.* the exact diagonalization performed in § 1-4), then its energy is null.

- Still in the case of the uniqueness of the edge state $|\psi_0\rangle$, $\hat{\mathcal{S}}|\psi_0\rangle$ which is also an eigenstate of null energy has to be collinear with $|\psi_0\rangle$, which means that $|\psi_0\rangle$ is an eigenstate of $\hat{\mathcal{S}}$. Since we have

  $$\hat{\mathcal{S}}^2 = 1, \tag{24}$$

  the eigenvalues of $\hat{\mathcal{S}}$ are $+1$ and -1. If the state $|\psi_0\rangle$ is associated with the eigenstate $+1$, then we have

  $$\hat{\mathcal{S}}|\psi_0\rangle = |\psi_0\rangle \quad \Rightarrow \quad \hat{P}_B|\psi_0\rangle = 0 \tag{25}$$

  and $|\psi_0\rangle$ is localized only on A sites. If $|\psi_0\rangle$ is associated with the eigenvalue -1, then it is localized only on B sites. We will recover this result in the next paragraph when studying the case of the semi-infinite chain (§ 1-4).

1-4 The semi-infinite chain

To understand how the edge states appear in this 1D system, it is interesting to study the semi-infinite SSH chain, which is an exactly solvable model. Let us then consider the system represented in figure 11. As in the case of the finite chain, the system is not periodic and one cannot use

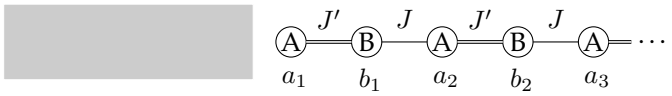

Figure 11. *A semi-infinite SSH chain.*

Bloch's theorem to find its eigenstates. However, it is relatively simple to find them directly. Let us write an eigenstate of energy E under the form

$$|\psi\rangle = \sum_{j=1}^{+\infty} (a_j\,|A_j\rangle \;+\; b_j\,|B_j\rangle)\,. \tag{26}$$

When inserting this form in the eigenvalue equation $\hat{H}|\psi\rangle = E|\psi\rangle$, one gets an infinite set of equations:

$$-J'b_1 \;=\; E\,a_1 \tag{27}$$
$$-J'a_1 - Ja_2 \;=\; E\,b_1 \tag{28}$$

and for $j \geq 2$:

$$-J'b_j - Jb_{j-1} \;=\; E\,a_j \tag{29}$$
$$-J'a_j - Ja_{j+1} \;=\; E\,b_j. \tag{30}$$

One can solve this system with standard methods of linear algebra (see the appendix) and there are one or two types of solutions, depending on the case (cf. figure 12):

- When the energy E is chosen in one of the two domains

$$[-(J+J'), -|J-J'|] \quad \text{or} \quad [|J-J'|, J+J'], \tag{31}$$

one always finds a solution with coefficients a_j and b_j with a modulus (approximately) constant when $j \to \infty$. This solution represents a wave coming from $+\infty$, propagating in the negative x direction, reflecting on site A_1 and going back to $+\infty$. This standing-wave-like solution exists if and only if the energy is chosen in the allowed bands that we have found above [cf. (6)], which is reassuring: it is a bulk solution whose existence is not affected by the cut in the chain at $j = 1$.

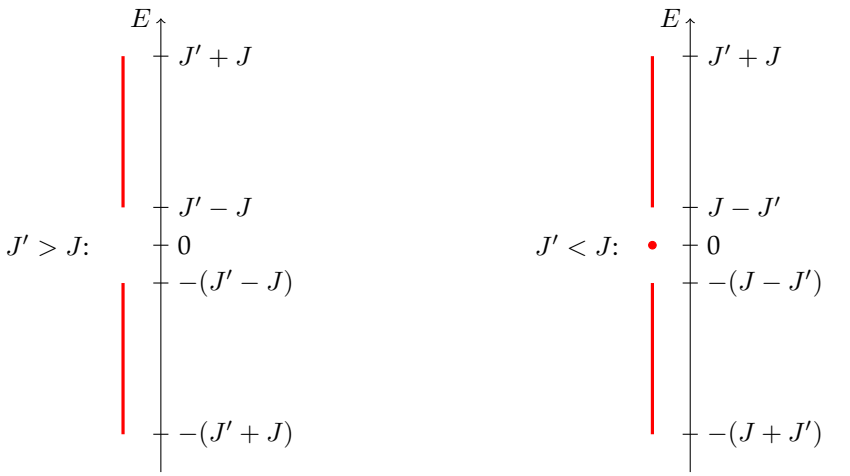

Figure 12. *The energy spectrum of a semi-infinite chain. Additionally to the two energy bands found for the infinite case, an edge state at zero energy appears in the "topological" case $J' < J$.*

- If $J' < J$, an additional solution appears at zero energy, corresponding to a discrete state. This state is given (up to a normalization factor) by:

$$a_j = (-J'/J)^j, \qquad b_j = 0. \tag{32}$$

This state is thus localized only on A sites, as it is expected from the sublattice symmetry (§1-3), its probability of being on the j-th site $P_j = |a_j|^2$ decreases exponentially with the distance from the end point A_1, and the characteristic length of this decrease is

$$\ell = \frac{a}{2\ln(J/J')}, \tag{33}$$

which is on the order of a, unless J and J' are very close. It is the edge state that we were looking for.

Note that the position in energy of this bound state is very different from what one is used to for potentials $V(x)$ that are localized in space. In that case, the energy spectrum is composed of discrete states for the low

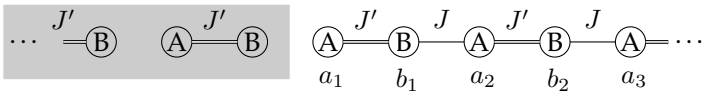

Figure 13. *The semi-infinite chain can be seen as an infinite chain with a space-dependent J coefficient. More precisely, the shaded area represents a chain with coefficient $J = 0$, that falls in the topological class $J' > J$, whereas the "real" chain can be in the class $J' > J$ or $J' < J$. In the latter case, an edge state appears, that is localized mostly on site A_1.*

energy part, and a continuum of energies above a given threshold. Here the discrete state has an intermediate energy and a continuum both above and below it.

Junctions between SSH chains. As we have already mentioned, the existence of edge states for the finite or semi-infinite chain in the case $J' < J$, and their non-existence for $J' > J$, is a very simple illustration of the *bulk–edge* correspondence. This correspondence indicates what happens at the interface between two zones with different or identical topologies. Our half-chain can be obtained by starting with an infinite chain and setting $J = 0$ in the left part ($j \leq 0$) of the chain. It is represented with the shaded area of figure 13. This gray zone is in the topological class $[J' > J]$. If we also choose for the real chain tunneling coefficients so that $J' > J$, the two parts of the chain we be in the same topological class, and there will be no edge states, that is no state localized at the border between the two zones. On the contrary, if we choose for the real chain $J' < J$, then the gray and non-gray zones will be in two different topological classes: an edge state will then appear at the interface between the two zones.

1-5 Edge state between two chains (continuous case)

The generality of the existence of an edge state between two regions with different topologies can be easily demonstrated for the SSH model. Let us consider a chain of $A - B$ sites along which the coefficients J and J' vary in the central region around site 0. We assume that far from this region, the ratio J'/J tends to a constant, but that this constant corresponds to different topologies on the right ($j \to +\infty$) and to the left ($j \to -\infty$). We take for example:

- $\lim_{j\to+\infty}(J'/J) = r_+ > 1$ to the right,
- $\lim_{j\to-\infty}(J'/J) = r_- < 1$ to the left.

It is then easy to show that there is always a bound state at energy $E = 0$ localized around the border region $j = 0$. We indeed write the expression of such a state as

$$|\psi\rangle = \sum_{j=-\infty}^{+\infty} (a_j\,|A_j\rangle \;+\; b_j\,|B_j\rangle) \tag{34}$$

with

$$\sum_j |a_j|^2 + |b_j|^2 = 1, \tag{35}$$

and we suppose that it is an eigenstate of the Hamiltonian with a null eigenvalue. We obtain the set of equations [cf (29-30)]:

$$-J'a_{j+1} - Ja_j = 0, \qquad -J'b_{j+1} - Jb_j = 0, \tag{36}$$

where the coefficients J and J' vary over space.

In the region $j \to +\infty$, one then finds that

$$\frac{|a_{j+1}|}{|a_j|} = \frac{1}{r_+} < 1, \qquad \frac{|b_{j+1}|}{|b_j|} = r_+ > 1. \tag{37}$$

The progressions a_j and b_j are thus geometric in this region. The common ratio of a_j is lower than 1, therefore this sequence decreases and can lead to a normalizable state in the sense of (35), at least in this region. On the contrary, the common ratio of b_j is higher than 1, and this sequence is increasing, which leads us to setting $b_j = 0$. Equation (36) then imposes that all the b_j coefficients are null.

In the region $j \to -\infty$, one finds

$$\frac{|a_{j-1}|}{|a_j|} = r_- < 1. \tag{38}$$

Thanks to the inversion $J' > J \longrightarrow J' < J$, we find again a decreasing geometrical progression for a_j when $j \to -\infty$. Starting for example with $a_0 = 1$, one can therefore construct all the numbers a_j for $j \to \pm\infty$ that will satisfy the recursion relation (36) and the obtained sequence can then be normalized. This eigenstate at zero energy is localized on the A_j sites and it is mostly concentrated around $j = 0$, since the probability density decreases exponentially fast (as $r_{\pm}^{\mp|j|}$) when $j \to \pm\infty$.

Following the above reasoning, it is clear that we would have found a state localized only on the B_j sites if we had initially set $r_+ < 1$ and $r_- > 1$. In addition, if two regions with the same topology are connected together, even with pairs of coefficients (J, J') very different, we would not have found this bound state at zero energy because the geometric progressions for a_j and b_j would both diverge on one side or the other, $j \to +\infty$ or $j \to -\infty$.

2 The SSH model in photonics

2-1 Topological effects in photonics

The idea of extending the concepts of topology from the quantum Hall effect to electromagnetic waves has been suggested by Haldane & Raghu (2008). Their proposal was based on the non-reciprocity property that can be observed for example in the Faraday effect due to the breaking of time-reversal symmetry by a magnetic field in an optical system. Since then, this idea has been implemented in a series of experiments, starting from the works of Wang, Chong, et al. (2009) with a photonic crystal in the microwave domain. To keep the discussion concise, we will not present all these experiments here and we will limit ourselves to the description of a few of them, either in 1D in this chapter, or in two dimensions in following chapters. The reader who wishes to have an exhaustive list of these works in photonics can refer to the review articles of Lu, Joannopoulos, et al. (2014), Lodahl, Mahmoodian, et al. (2017), Khanikaev & Shvets (2017), Ozawa, Price, et al. (2018).

In this section, we will only describe how the SSH model has been implemented with electromagnetic waves. This implementation has first been made in the microwave domain by Poli, Bellec, et al. (2015). More recently, it has been performed in the visible or near-infrared domain by Weimann, Kremer, et al. (2017) and St-Jean, Goblot, et al. (2017). We will focus on this last project.

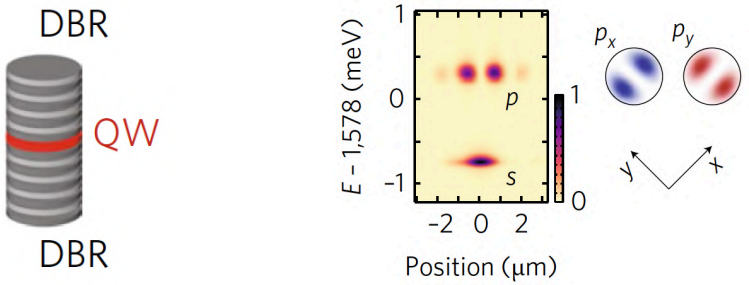

Figure 14. *The unit cell, composed of a GaAs quantum well lying between two Bragg mirrors made of several tens of layers of GaAlAs. Figure extracted from St-Jean, Goblot, et al. (2017).*

2-2 The unit cell and the SSH model

In the experiment of St-Jean, Goblot, et al. (2017), the unit cell is constituted by a GaAs quantum well placed between two mirrors (figure 14, left). The amplitude of the field in this cylinder-shaped resonant cavity represents the complex coefficients denoted by a_j and b_j in the above [*cf.* . eq. (26)]. This quantum well is illuminated with non-resonant light and the photoluminescence revealing the amplitude of the electromagnetic field in the cavity is observed. One can perform "real space" measurements by imaging the quantum well(s) on the camera, or "Fourier space" measurements to measure what is emitted in a given direction, irrespective of the exact position of the quantum well(s). All these experiments are performed in a cryogenic environment at 4 K.

The electromagnetic field in this cavity can occupy several transverse spatial modes. The mode with the lowest energy is a cylindrically symmetric mode, called the s-orbital. The next mode, which is the one used in this experiment, is doubly degenerate. A basis of this two-dimensional

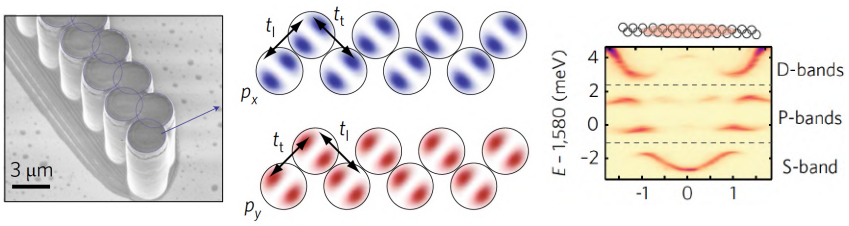

Figure 15. *Left: a zigzag chain of micropillars (distance between two pillars: 3.4 μm). Middle: The coupling between p_x (resp. p_y) orbitals happens with an alternation of J, J' (resp. J', J) that are here denoted as t_l and t_t. The ratio t_t/t_l is on the order of 0.15. Right: The measurement of the spectrum of the photoluminescence light as a function of the emission angle (that is the transverse momentum of the photons) reveals the structure of the band associated with the modes s, p, d. Here, the bulk of the chain has been excited, but not its end points. Figure extracted from St-Jean, Goblot, et al. (2017).*

subspace is composed of the p_x and p_y orbitals, which have two lobes of opposite sign and a symmetry axis along x or y (figure 14, on the right). The modes with higher energy (for example mode d) do not play any significant role here.

To construct a SSH chain, the pillars are placed regularly to form a zigzag line, represented in figure 15 (on the left). The role of the tunnel coupling between neighbouring sites is played by the evanescent wave that surrounds the micropillars. For the electromagnetic field in the s wave, all the coupling between neighbouring sites are identical and a single-band chain without any topological property is realized. One then retrieves the energy band corresponding to the well-known dispersion relation $-2J\cos(qa)$ (figure 15, on the right).

On the contrary, the coupling of the p modes allows the alternation of the couplings J, J'. Depending whether the two lobes of the p orbital of two neighbouring pillars are aligned in the same direction or face to face, the coupling efficiency is different (figure 15, in the middle). The experimentally measured ratio is $J'/J \approx 0.15$. Remarkably, the two orbitals p_x and p_y simultaneously realize the two possible configurations: if two pillars are coupled by the coefficient J for the p_x orbital, they are coupled by the coefficient J' for the p_y orbital, and conversely.

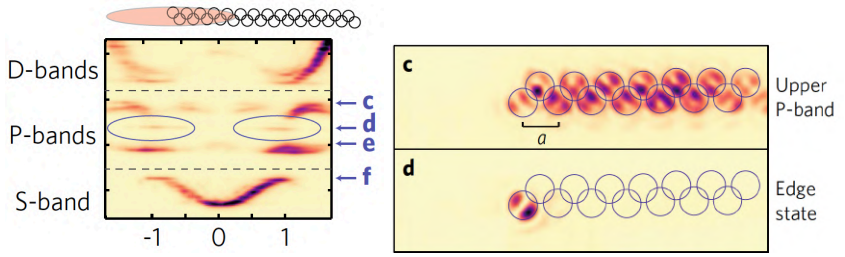

Figure 16. *The observation of edge states for the p_y wave, corresponding to topologically non-trivial band $J > J'$, that is $t_l > t_t$ with the notations of figure 15. Figure extracted from St-Jean, Goblot, et al. (2017).*

This alternation of the couplings leads to the separation of the energy band into two separated subbands that are effectively observed in a "Fourier space" measurement, as shown in figure 15, on the right. Note that for now, the illumination that gives rise to the photoluminescence only hits the bulk and no edge state is excited.

2-3 Observation of an edge state and topological laser

The left part of figure 16 shows the same photoluminescence measurement when the end point of the chain is illumnated. Additional states appear in the energy spectrum, in the spectral gap of the light emitted by p wave modes. It is a direct observation of the edge states found in figure 7. The real space imaging of the chain (figure 16, on the right) shows that these states correspond to the p_y polarization, for which the topologically non-trivial band $J > J'$ appears.

One of the practical interests of such an implementation of the concepts of topology in photonics is to create "robust" lasers which would not be sensitive to imperfections that may occur during their realization. This argument is illustrated in figure 17 that demonstrates the lasing effect that takes place when the power of the pumping light is increased. Above a given threshold, the power emitted in the edge mode surpasses by far the power emitted by all the bulk modes. The spectral width of the peak de-

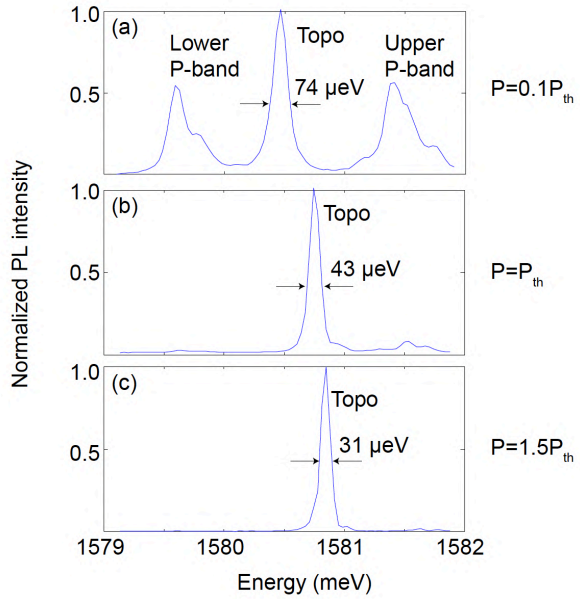

Figure 17. *The measurement of the emission spectrum as the power of the pumping light is increased above the lasing threshold of the topological mode. Figure extracted from St-Jean, Goblot, et al. (2017), supplementary information.*

creases, which indicates an increase in the temporal coherence of this laser. The enhancement of this edge mode compared to the bulk modes can be explained by the fact that the polaritons in the bulk modes have a large mobility and rapidly leave the pumping region.

3 The Kitaev model

The rest of the chapter is dedicated to a problem regarding interacting particles; we will consider the toy-model introduced by Kitaev (2001) to show how a non-trivial topology can appear in a 1D chain of fermions with interactions similar to the ones that lead to superconductivity.

In this section, we will first describe the model proposed by Kitaev, then we will briefly present the Bogoliubov–de Gennes method, with which one can in general address with this type of Hamiltonian. We will examine the case of an infinite chain, thus translational invariant, and we will show how this problem can be linked – as for the SSH chain – to a pseudo-spin $1/2$. We will thus be able to use the arguments made above about the winding of the eigenstates on the Bloch sphere, and they will give us a first indication of the topological nature of the phases that may appear. This point will then be further discussed in § 4.

3-1 The Kitaev Hamiltonian

The Hamiltonian that describes the model of Kitaev (2001) has three terms (figure 18):

- We consider particles that obey Fermi statistics, but without any spin degree of freedom. These particles evolve on a 1D chain that is treated in the framework of tight-binding, with J as the tunneling coefficient between neighbouring sites. The first term of the Hamiltonian describes the tunnel coupling between two sites, and in the second quantization formalism[2], it is written as

$$-J\sum_j |j+1\rangle\langle j| + \text{h.c.} \longrightarrow -J\sum_j \hat{a}^\dagger_{j+1}\hat{a}_j + \text{h.c.} \tag{39}$$

  where $\hat{a}_j$ (resp. $\hat{a}^\dagger_j$) annihilates (creates) a fermion on site j. These operators satisfy the standard anticommutation relations of fermions:

$$\hat{a}_i\hat{a}_j + \hat{a}_j\hat{a}_i = 0, \qquad \hat{a}^\dagger_i\hat{a}_j + \hat{a}_j\hat{a}^\dagger_i = \delta_{i,j}. \tag{40}$$

- We suppose that this chain is coherently coupled to a superfluid (or superconducting) bath that provides neighbouring sites with a pair of fermions. This coupling is characterized by the parameter Δ that

[2] Until here we have used the first quantization formalism which is well-suited when the total number of particles is conserved. We have to use the second quantization in this paragraph to describe superconductivity in the Bogoliubov – de Gennes formalism.

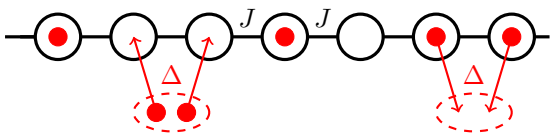

Figure 18. *The Kitaev chain, characterized by the tunneling coupling J and the superfluid gap Δ. A third parameter, the chemical potential μ, fixes the mean number of particles on the chain.*

represents the superconducting gap[3] imposed by the bath. It is written as

$$\sum_j \left(\Delta\ \hat{a}_{j+1}^\dagger \hat{a}_j^\dagger + \Delta^*\ \hat{a}_j \hat{a}_{j+1}\right) \tag{41}$$

The parameter Δ is *a priori* complex, but we can choose it real without any loss of generality by integrating its phase into the definition of the $\hat{a}_j$ coefficients.

- It is clear that the coupling (41) does not conserve the particle number; in order to impose a mean particle number on the chain, one has to introduce a third term $-\mu\hat{N}_\mathrm{p}$ that features the chemical potential μ of the bath, where $\hat{N}_\mathrm{p}$ is the *total particle number* operator:

$$\hat{N}_\mathrm{p} = \sum_j \hat{a}_j^\dagger \hat{a}_j \tag{42}$$

We then obtain the overall Hamiltonian:

$$\hat{H} = \sum_j \left\{-J\left(\hat{a}_j^\dagger \hat{a}_{j+1} + \hat{a}_{j+1}^\dagger \hat{a}_j\right) - \mu\, \hat{a}_j^\dagger \hat{a}_j + \ \Delta\left(\hat{a}_j \hat{a}_{j+1} + \hat{a}_{j+1}^\dagger \hat{a}_j^\dagger\right)\right\}, \tag{43}$$

and we will search for its eigenstates and eigenvalues.

[3]The existence of a superconducting gap supposes that the particles are interacting. In general, the interactions in a superconductor take place between fermions of opposite spin in the partial wave $\ell = 0$ (the s wave), which is favoured at low temperatures. Here, we have frozen the spin degree of freedom and the Pauli principle forbids these s wave interactions. The interactions thus have to occur in odd waves, for example in the p wave. This point will appear clearly when we will write the Hamiltonian in momentum space [eq. (60)]. We will indeed find an interaction term $\Delta\sin(qa)$, that is an odd function of q.

3-2 The Bogoliubov – de Gennes formalism

We suppose that the chain has N sites and boundary conditions that have to be specified, for example open or periodic. The Hilbert space has dimension 2^N, since each site can be either empty or occupied by a particle. This exponential growth of the dimension of space with the number of sites makes it very difficult to treat a generic many-body Hamiltonian. Fortunately, for a Hamiltonian quadratic in $\hat{a}_i, \hat{a}_i^\dagger$ such as the one in (43), one can use a method that uses a matrix with the much smaller size of $2N \times 2N$.

To construct this matrix, let us consider the row vector $\hat{A}^\dagger$ and the associated column vector $\hat{A}$ of size $2N$ (the Nambu spinors) defined by :

$$\hat{A}^\dagger = \begin{pmatrix} \hat{a}_1^\dagger & \dots & \hat{a}_N^\dagger & \hat{a}_1 & \dots & \hat{a}_N \end{pmatrix} \qquad \hat{A} = \begin{pmatrix} \hat{a}_1 \\ \vdots \\ \hat{a}_N \\ \hat{a}_1^\dagger \\ \vdots \\ \hat{a}_N^\dagger \end{pmatrix} \tag{44}$$

A Hamiltonian $\hat{H}$ quadratic with $\hat{a}_i, \hat{a}_i^\dagger$ can then be written (up to an additive constant) under the form

$$\hat{H} = \frac{1}{2}\hat{A}^\dagger \hat{H}_\mathrm{BdG} \hat{A} \tag{45}$$

where $\hat{H}_\mathrm{BdG}$ is a $2N \times 2N$ matrix that can be written with 4 blocks of size $N \times N$

$$\hat{H}_\mathrm{BdG} = \begin{pmatrix} \hat{M}_1 & \hat{M}_2 \\ -\hat{M}_2^* & -\hat{M}_1^* \end{pmatrix} \tag{46}$$

The (hermitian) matrices $\hat{M}_1, \hat{M}_1^*$ take into account the terms in $a_i^\dagger a_j$ that conserve the particle number, and the (antisymmetric) matrices $\hat{M}_2, \hat{M}_2^*$ take into account the terms in $a_i a_j$ and $\hat{a}_j^\dagger \hat{a}_i^\dagger$ that come from the superfluid gap. For the Hamiltonian (43), one finds that the matrices M_1 and M_2 are

the real band matrices

$$\hat{M}_1 = -\begin{pmatrix} \mu & J & 0 & 0 & \dots & 0 & 0 & 0 \\ J & \mu & J & 0 & \dots & 0 & 0 & 0 \\ \vdots & & & & & & & \vdots \\ 0 & 0 & 0 & 0 & \dots & J & \mu & J \\ 0 & 0 & 0 & 0 & \dots & 0 & J & \mu \end{pmatrix} \tag{47}$$

and

$$\hat{M}_2 = \Delta \begin{pmatrix} 0 & -1 & 0 & 0 & \dots & 0 & 0 & 0 \\ 1 & 0 & -1 & 0 & \dots & 0 & 0 & 0 \\ \vdots & & & & & & & \vdots \\ 0 & 0 & 0 & 0 & \dots & 1 & 0 & -1 \\ 0 & 0 & 0 & 0 & \dots & 0 & 1 & 0 \end{pmatrix} \tag{48}$$

Once the eigenenergies E_j of $\hat{H}_{\mathrm{BdG}}$ and their associated eigenstates are known, we can put the initial Hamiltonian $\hat{H}$ under the form of a sum of modes:

$$\hat{H} = \frac{1}{2} \sum_{j=1}^{2N} E_j \, \hat{b}_j^\dagger \hat{b}_j, \tag{49}$$

where the operators $\hat{b}_j^\dagger$ and $\hat{b}_j$ are linear combinations of the $\hat{a}_j^\dagger$ and the $\hat{a}_j$, with coefficients that depend on the eigenvectors of $\hat{H}_{\mathrm{BdG}}$. Each mode $(\hat{b}_j^\dagger, \hat{b}_j)$ corresponds to a Bogoliubov quasiparticle that follows the fermionic statistics. For example the groundstate of $\hat{H}$ is obtained by leaving the modes $(\hat{b}_j^\dagger, \hat{b}_j)$ of positive energy E_j empty and filling the ones of negative energy.

3-3 The particle–hole symmetry

The diagonal form of the Hamiltonian $\hat{H}$ seems paradoxical. We indeed started from a Hilbert state of dimension 2^N and we now arrive to $2N$ modes, each of which can be empty or full, which seems to correspond to a Hilbert space of dimension 2^{2N}. Where does this (huge) increase of the dimension of the space come from?

Its origins lie in the very structure of the Bogoliubov – de Gennes formalism, which leads to $2N$ non-independent modes which arise in pairs. In equation (45), the Hamiltonian $\hat{H}_{\mathrm{BdG}}$ acts on the vector $\hat{A}$ that is composed with annihilation operators for its first half and of creation operators for its second half. The same operators appear in opposite order in $\hat{A}^\dagger$, so that every term of the type $\hat{a}_i^\dagger \hat{a}_j$ appears twice in the development obtained with (45). On a mathematical point of view, one can translate this doubling of terms by a symmetry property of the Bogoliubov – de Gennes Hamiltonian:

$$\hat{\mathcal{C}} \, \hat{H}_{\mathrm{BdG}} \hat{\mathcal{C}}^\dagger = -\hat{H}_{\mathrm{BdG}}, \tag{50}$$

where we have introduced the anti-unitary operator for the *particle–hole symmetry*:

$$\hat{\mathcal{C}} = \hat{K}_0 \hat{\tau}_x \tag{51}$$

where $\hat{K}_0$ is the operator for the complex conjugation

$$\hat{K}_0 \psi(x) = \psi^*(x), \tag{52}$$

and where $\hat{\tau}_x$ exchanges the creation and annihilation operators of a given site:

$$\hat{\tau}_x = \begin{pmatrix} 0 & \hat{1} \\ \hat{1} & 0 \end{pmatrix} \tag{53}$$

where each submatrix has size $N \times N$.

The anticommutation relation (50) has two immediate consequences:

- As for the sublattice (chiral) symmetry, it leads to the symmetry of the energy spectrum of $\hat{H}_{\mathrm{BdG}}$ with respect to zero energy. If an energy $E \neq 0$ appears in the spectrum of $\hat{H}_{\mathrm{BdG}}$, then we know that the energy $-E$ also has to appear.

- It also leads to a simple relation between the two eigenmodes associated with an energy pair $(E, -E)$. If a given eigenmode $(\hat{b}_E, \hat{b}_E^\dagger)$ appears in the diagonalization of $\hat{H}_{\mathrm{BdG}}$ with energy E with

$$\hat{b}_E = \sum_{j=1}^{N} u_j \hat{a}_j + v_j \hat{a}_j^\dagger \tag{54}$$

then we know that the mode obtained by the action of $\hat{\mathcal{C}}$ on $(u_j, v_j)^{\mathrm{T}}$, that is

$$\sum_{j=1}^{N} v_j^* \hat{a}_j + u_j^* \hat{a}_j^\dagger \tag{55}$$

will be an eigenmode $(\hat{b}_{-E}, \hat{b}_{-E}^\dagger)$ with energy $-E$, which means that

$$\hat{b}_{-E} = \hat{b}_E^\dagger, \qquad \hat{b}_{-E}^\dagger = \hat{b}_E. \tag{56}$$

In other terms, annihilating a quasiparticle of energy $-E$ is equivalent to creating a particle of energy E. We can paraphrase Beenakker (2015), by saying that the particle–hole symmetry translates the ambiguity of the definition of a quasiparticle, which can be seen as a Cooper pair that lacks a particle, or a Cooper pair with one particle too many.

By using

$$(-E)\ \hat{b}_{-E}^\dagger \hat{b}_{-E} = (-E)\ \hat{b}_E \hat{b}_E^\dagger = E\left(\hat{b}_E^\dagger \hat{b}_E - 1\right), \tag{57}$$

we can then rewrite the Hamiltonian $\hat{H}$ given in (49) under the form

$$\hat{H} = \sum_{j=1}^{N} E_j\ \left(\hat{b}_j^\dagger \hat{b}_j - 1/2\right), \tag{58}$$

where the sum only involves the positive energy modes E_j. There are therefore N independent quasiparticle modes for this problem, where each mode can be occupied by 0 or 1 quasiparticle, which gives a Hilbert space of dimension 2^N, as expected.

Remark. The case of a mode with zero energy, therefore doubly degenerate, may need to be handled in a particular way. It is precisely the subject of the Kitaev model on which we will come back in section 4.

3-4 The infinite Kitaev chain

For an infinite chain, or for a chain with N sites and periodic boundary conditions, the translational invariance simplifies the problem (as for the SSH model). We introduce[4] the *creation operator of a particle with quasimomentum* q:

$$\hat{a}_q^\dagger = \frac{1}{\sqrt{N}} \sum_j \mathrm{e}^{\mathrm{i}qja}\ \hat{a}_j^\dagger \tag{59}$$

which allow us to write $\hat{H}$ as

$$\hat{H} = \sum_q \left\{ -\left[2J\cos(qa) + \mu\right]\ \hat{a}_q^\dagger \hat{a}_q + \mathrm{i}\Delta \sin(qa) \left(\hat{a}_{-q}\hat{a}_q - \hat{a}_q^\dagger \hat{a}_{-q}^\dagger\right)\right\}. \tag{60}$$

We thus obtain a Hamiltonian quadratic with $\hat{a}_q^\dagger$, $\hat{a}_q$ for which a momentum q is only coupled to the momentum $-q$.

The Bogoliubov – de Gennes method can again be used and it takes here a particularly simple form. Let us introduce the vectors with two components:

$$\hat{A}_q^\dagger = \begin{pmatrix} \hat{a}_q^\dagger & \hat{a}_{-q} \end{pmatrix} \qquad \hat{A}_q = \begin{pmatrix} \hat{a}_q \\ \hat{a}_{-q}^\dagger \end{pmatrix} \tag{61}$$

which gives

$$\hat{H} = \frac{1}{2} \sum_q\ \hat{A}_q^\dagger\ \hat{H}_q\ \hat{A}_q \tag{62}$$

where $\hat{H}_q$ is the 2×2 hermitian matrix:

$$\begin{aligned} \hat{H}_q &= \begin{pmatrix} -\left[2J\cos(qa) + \mu\right] & -2\mathrm{i}\Delta\ \sin(qa) \\ 2\mathrm{i}\Delta\ \sin(qa) & 2J\cos(qa) + \mu \end{pmatrix} \\ &= -\boldsymbol{h}(q) \cdot \hat{\boldsymbol{\sigma}} \quad \text{with} \begin{cases} h_x(q) = 0 \\ h_y(q) = -2\Delta\ \sin(qa) \\ h_z(q) = 2J\cos(qa) + \mu \end{cases} \end{aligned} \tag{63}$$

As explained in § 3-2, knowing the eigenstates of $\hat{H}_q$ and the associated energies $\pm E_q$, with

$$E_q = |\boldsymbol{h}(q)| = \left\{4\Delta^2 \sin^2(qa) + \left[2J\cos(qa) + \mu\right]^2\right\}^{1/2} \tag{64}$$

[4] In order not to have too many notations, we denote with the same symbol $\hat{a}_{j/q}^\dagger$ the creation operator on site j and the creation operator with momentum q; this should not create any confusion since the sites are always designated by the letters i or j, whereas the momenta are always designated by the letters q or q'.

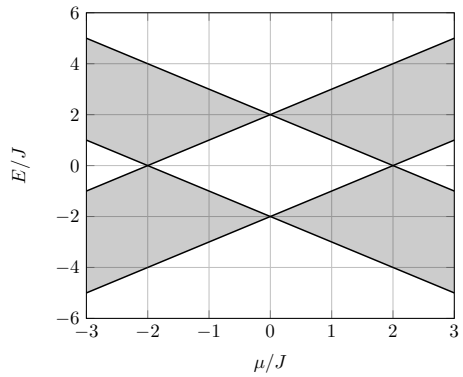

Figure 19. *The spectrum of quasiparticles for the infinite Kitaev chain in the particular case $\Delta = J$.*

allows us to write $\hat{H}$ in a diagonal form that represents an assembly of interactionless particles:

$$\hat{H} = \sum_q E_q \ \left(\hat{c}_q^\dagger c_q \ - \ 1/2\right) \tag{65}$$

where the sum involves all the q's, but only the positive energies[5] $+E_q$. The annihilation and creation operators $\hat{c}_q, \hat{c}_q^\dagger$ for the quasiparticles are linear combinations of the a_q et $a_q^\dagger$:

$$\hat{c}_q^\dagger = u_q \ \hat{a}_q^\dagger + v_q \ \hat{a}_{-q}, \tag{66}$$

where the coefficients (u_q, v_q) are directly linked to the eigenvectors of $\hat{H}_q$. We will not write them explicitly because they are not necessary for this discussion (see for example Alicea (2012)). The groundstate $|\psi_0\rangle$ is obtained by solving $\hat{c}_q|\psi_0\rangle = 0$ for all q, and its energy is

$$-\frac{1}{2}\sum_q E_q \tag{67}$$

[5]Note that in the momentum space, the particle-hole symmetry consists in assimilating the creation of a quasiparticle of energy $+E_q$ and momentum $+q$ with the annihilation of a quasiparticle of energy $-E_q$ and momentum $-q$.

This state is separated by the gap $\min_q(E_q)$ from the quasicontinuum (for $N \gg 1$) formed by the excited states of the system, and this gap cancels out for the two points $\mu = \pm 2J$. For the particular case where $\Delta = J$, this gap is equal to $||\mu| - 2J|$ (figure 19).

The topological structure of this model. We see that this physical problem, although different from the SSH model, gives a Hamiltonian $\hat{H}_q$ in momentum space that has a similar structure in $-\boldsymbol{h}(q) \cdot \hat{\sigma}$. In particular, searching for the topological phases can be done by analyzing the trajectory of the vector $\boldsymbol{h}(q)$ when q describes the Brillouin zone. More precisely, one can see in (63) that the vector $\boldsymbol{h}$ always lies in a plane (here yz), so that the discussion is exactly the same as the one of the SSH model. The excitation spectrum is given by E_q [eq. (64)], and it always displays a gap, except if $|\mu| = 2J$ (in that case, the excitation corresponding to $qa = 0$ or π has energy zero). One can thus expect to observe two phases with different topologies (figure 20):

- For $\mu > 2J$ (a chain with a high filling) or $\mu < -2J$ (low filling), the trajectory of vector $\boldsymbol{h}(q)$ does not circle around the origin. It is the *normal superconducting phase* for which no protected edge states are expected at the end of a finite chain.
- For $|\mu| < 2J$ (a chain with "intermediate" filling), the trajectory of vector $\boldsymbol{h}(q)$ circles around the origin with a 2π winding when q describes the Brillouin zone. This corresponds to the *topological superconducting phase*. We will see in the next paragraph that, for a finite chain, this phase leads to the appearance of modes localized at the two ends of the chain.

These two phases can be connected only by the singular point $|\mu| = 2J$ where the gap between the two energy bands closes.

4 The Majorana modes

The goal of this last part is twofold. On the one hand we want to demonstrate that the bulk-edge correspondence that we have found for the SSH

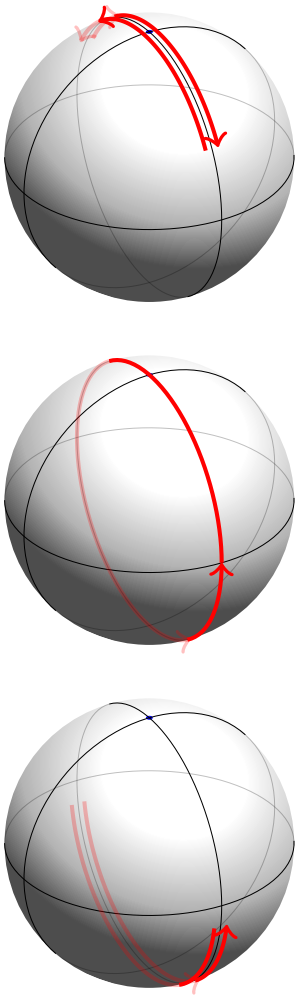

Figure 20. *The trajectory of vector $\boldsymbol{n}(q) = \boldsymbol{h}(q)/|\boldsymbol{h}(q)|$ on the unit sphere when q describes the Brillouin zone. When $\mu > 2J$ (on the top) or $\mu < -2J$ (on the bottom), the winding number is null and we expect a normal phase. On the contrary, for $|\mu| < 2J$ (in the middle), the vector $\boldsymbol{n}$ winds around the sphere and we expect a topological phase.*

model also exists for the Kitaev model; for that we will verify that the topological phase that we suspect for $|\mu| < 2J$ indeed leads to edge states that do not exist outside of this phase. On the other hand, we wish to examine the particular structure of these edge modes and show that they display, because of their collective nature, a spectacular robustness which make them serious candidates for quantum processing of information.

To simplify our analysis, we concentrate in this part on the particular case

$$\Delta = J, \tag{68}$$

that we have already considered in figure 19, and that will allow us to perform calculations analytically.

4-1 The open Kitaev chain

Let us consider a chain with N sites, and with boundary conditions that can be chosen open or periodic. For an open chain, we lose the periodicity property and we cannot search the eigenstates and their energies by using Bloch's theorem. We then have to go back to the Bogoliubov – de Gennes general method, and, for a chain with N sites, diagonalize numerically the $2N \times 2N$ matrix $\hat{\mathcal{H}}_{\mathrm{BdG}}$. In practice we will consider a chain with $N = 20$ sites, which is sufficient to point out the important features.

We first verify the consistency of our approach and take periodic boundary conditions for this chain (figure 21, on the top). For each value μ, we find $2N$ eigenvalues that perfectly fit in the energy bands that we found for the infinite chain (figure 19). In particular we recover the closing of the gap at $\mu = \pm 2J$.

Let us now switch to the case of an open chain. The variation with μ of the $2N$ eigenvalues is shown in figure 21, bottom. This spectrum looks similar to the one with periodic boundary conditions, with a (major!) difference however: in the zone $|\mu| < 2J$ that we presume to be topological, we see a pair $(E, -E)$ of eigenstates appearing with E close to zero, thus in the center of the gap of the infinite system. The study of the corresponding eigenvectors confirms that these modes are localized in the vicinity of the end points of the chain. We now look into more details at these edge states and focus on the particular value $\mu = 0$, at the center of the topological

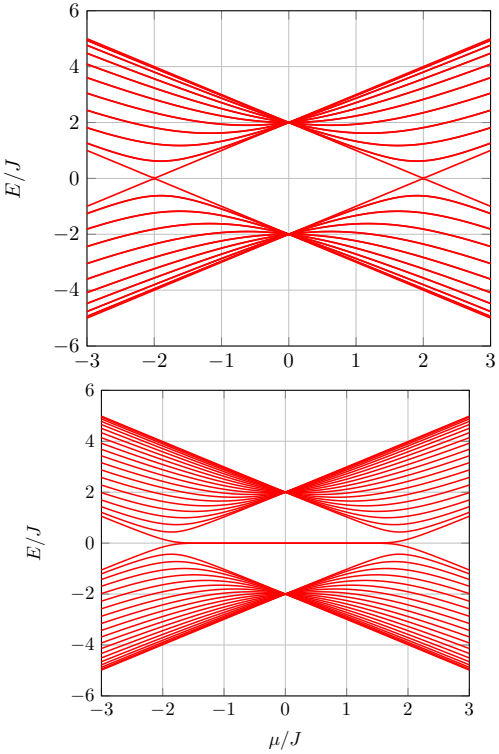

Figure 21. *The spectrum of the quasiparticles for a Kitaev chain with $\Delta = J$, $N = 20$ sites, and with periodic (top) and open (bottom) boundary conditions. In the latter case, a mode $(E, -E)$ with a quasi null energy (Majorana) appears between $\mu = -2J$ and $\mu = 2J$.*

region.

4-2 The groundstate for $\mu = 0$

This particular case, which is simple to handle, has been brought forward by Kitaev (2001) because it allows a fully analytic treatment of the problem. We first observe that this case leads to a flat energy spectrum for the infinite chain, since the vector $\boldsymbol{h}$ is equal to:

$$\boldsymbol{h}(q) = 2J\left(\sin(qa)\,\boldsymbol{u}_y + \cos(qa)\,\boldsymbol{u}_z\right) \quad \Rightarrow \quad E_q = |\boldsymbol{h}(q)| = 2J. \tag{69}$$

This statement can be directly verified in figure 19, since the two energy bands each consist in only one point when $\mu = 0$.

We now consider an open finite chain with N sites, for which the Hamiltonian reads

$$\begin{aligned}\hat{H} &= J\sum_{j=1}^{N-1}\left(-\hat{a}_j^\dagger\hat{a}_{j+1} - \hat{a}_{j+1}^\dagger\hat{a}_j + \hat{a}_j\hat{a}_{j+1} + \hat{a}_{j+1}^\dagger\hat{a}_j^\dagger\right)\\ &= J\sum_{j=1}^{N-1}\left(\hat{a}_j - \hat{a}_j^\dagger\right)\left(\hat{a}_{j+1} + \hat{a}_{j+1}^\dagger\right)\end{aligned} \tag{70}$$

Remarkably, it is possible to find analytically the eigenstates and energies of this Hamiltonian. We introduce N new operators:

$$\hat{b}_j = \frac{\mathrm{i}}{2}\left(\hat{a}_j^\dagger - \hat{a}_j + \hat{a}_{j+1}^\dagger + \hat{a}_{j+1}\right) \quad \text{for } j = 1, \ldots, N-1 \tag{71}$$

$$\hat{b}_N = \frac{\mathrm{i}}{2}\left(\hat{a}_N^\dagger - \hat{a}_N + \hat{a}_1^\dagger + \hat{a}_1\right). \tag{72}$$

This new set $\{\hat{b}_j\}$ of operators and their hermitian conjugates $\{\hat{b}_j^\dagger\}$ have the two following important properties:

- The N pairs $\{\hat{b}_j, \hat{b}_j^\dagger\}$ verify the canonical commutation relations of fermions:

$$\hat{b}_i\hat{b}_j = -\hat{b}_j\hat{b}_i \quad \text{if } i \neq j, \qquad \hat{b}_i\hat{b}_j^\dagger + \hat{b}_j^\dagger\hat{b}_i = \delta_{i,j}. \tag{73}$$

The map

$$\{\hat{a}_j, \hat{a}_j^\dagger\} \quad \longrightarrow \quad \{\hat{b}_j, \hat{b}_j^\dagger\} \tag{74}$$

is thus from a mathematical point of view a mere change of basis.

- The operators $\{\hat{b}_j, \hat{b}_j^\dagger\}$ " diagonalize " the Hamiltonian (43), since it can be written as

$$\hat{H} = \sum_{j=1}^{N} E_j \left(\hat{b}_j^\dagger \hat{b}_j - \frac{1}{2}\right) \tag{75}$$

with

$$E_j = 2J \quad \text{for } j = 1, \ldots, N-1 \tag{76}$$
$$E_N = 0. \tag{77}$$

For this particular case, we have analytically achieved the program, presented in its generality in § 3-2, of looking for the eigenmodes of the quadratic Hamiltonian.

Since all the energies E_j are positive or null, a groundstate $|\psi_0\rangle$ of $\hat{H}$ is obtained by leaving all the quasiparticle modes $(\hat{b}_j, \hat{b}_j^\dagger)$, empty, which amounts to solving

$$\hat{b}_j|\psi_0\rangle = 0, \qquad j = 1, \ldots, N. \tag{78}$$

This set of equations has a unique solution $|\psi_0\rangle$. For a chain with 4 sites, this solution can be written in the basis of the occupation numbers as

$$\begin{aligned}\sqrt{8}\,|\psi_0\rangle &= |1000\rangle + |0100\rangle + |0010\rangle + |0001\rangle \\ &+ |1110\rangle + |1101\rangle + |1011\rangle + |0111\rangle.\end{aligned} \tag{79}$$

It is a superposition with equal weights of the 2^{N-1} states with an odd occupation number. One can verify, after a quite tedious calculation, that this form can be generalized to a chain of arbitrary (and even) length N.

If all the energies E_j were strictly positive, this groundstate would be unique and the $2^N - 1$ excited states would be obtained by filling the quasiparticule modes, through the action of the operators $\hat{b}_j^\dagger$ on $|\psi_0\rangle$. But we have to take into account the fact that $E_N = 0$. The state obtained by the action of $\hat{b}_N^\dagger$ on $|\psi_0\rangle$

$$|\psi_1\rangle = \hat{b}_N^\dagger|\psi_0\rangle \tag{80}$$

thus has the same energy as $|\psi_0\rangle$, which means that the groundstate is doubly degenerate, a possible basis being $\{|\psi_0\rangle, |\psi_1\rangle\}$. Note that the states $|\psi_0\rangle$ and $|\psi_1\rangle$ correspond to different parities of the total number of fermions on the chain. For example, in the case of the chain with 4 sites that we considered above, we have:

$$\begin{aligned}\sqrt{8}\,|\psi_1\rangle &= |1100\rangle + |1010\rangle + |1001\rangle + |0110\rangle + |0101\rangle + |0011\rangle \\ &+ |0000\rangle + |1111\rangle\end{aligned} \tag{81}$$

which is the superposition with equal weights of all the states with an even number of particles. This form can also be generalized to a chain of any (even) length N.

The situation is thus very different from the one of a usual superconductor, for which the groundstate is non degenerate and represents a condensate of Cooper pairs, that is a superposition of states with an even number of fermions.

Let us recall that this degenerate groundstate is separated from the first excited states by the gap $2J$. These excited states are obtained by the action on one of the two groundstates $|\psi_{0,1}\rangle$ of the creation operator of a quasiparticle $\hat{b}_j^\dagger$ for one of the modes $j = 1, \ldots, N-1$. This gap corresponds to the result that we expect from the analysis in § 3 of the infinite chain.

4-3 The Majorana operators

In this last paragraph, we discuss the very peculiar nature of the groundstate $\{|\psi_0\rangle, |\psi_1\rangle\}$, that relies on its degeneracy and on the fact that the operator $\hat{b}_N$ that allows to pass from one to the other:

$$|\psi_1\rangle = \hat{b}_N^\dagger|\psi_0\rangle, \qquad |\psi_0\rangle = \hat{b}_N|\psi_1\rangle \tag{82}$$

is delocalized at the two ends of the chain:

$$\hat{b}_N = \frac{\mathrm{i}}{2}\left(\hat{a}_N^\dagger - \hat{a}_N + \hat{a}_1^\dagger + \hat{a}_1\right). \tag{83}$$

This delocalization, linked to the particle-hole symmetry, leads to a high robustness of the groundstate with respect to external perturbations, contrary to the low robustness that we found for the SSH chain. To lift the

degeneracy of this groundstate, one has indeed to transform the mode of null energy of $\hat{\mathcal{H}}_{\rm BdG}$ into a pair of modes $(E, -E)$ with $E > 0$. This can be done only by acting simultaneously and coherently at the two ends of the chain.

In order to better understand this crucial point, one can introduce, for each site j of the chain, the two operators

$$\hat{\gamma}_{j,+} = \hat{a}_j + \hat{a}_j^\dagger, \qquad \hat{\gamma}_{j,-} = \mathrm{i}\left(\hat{a}_j^\dagger - \hat{a}_j\right). \tag{84}$$

All these $2N$ operators are hermitian: $\gamma^\dagger = \gamma$. If we had bosonic particles, these operators would simply be (up to a factor $\sqrt{2}$) the position and momentum operators associated to the harmonic oscillator algebra $\{\hat{a}_j, \hat{a}_j^\dagger\}$. For fermions, the properites of these operators are quite different. First, they follow the canonical commutation relations ($\sigma = \pm$)

$$\hat{\gamma}_{j,\sigma}\hat{\gamma}_{j',\sigma'} = -\hat{\gamma}_{j',\sigma'}\hat{\gamma}_{i,\sigma} \qquad \text{if } (j,\sigma) \neq (j',\sigma'). \tag{85}$$

In addition, the square of these operators is

$$\hat{\gamma}^2 = \hat{\gamma}^\dagger\hat{\gamma} = \hat{1}. \tag{86}$$

If an operator $\hat{\gamma}_{j,\sigma}$ is interpreted as the creation operator of a quasiparticle, equation (86) indicates that this particle is its own antiparticle. We then have a description that is formally similar to the one introduced by Majorana (1937). Starting from the Dirac equation that describes a complex field in which particles and antiparticles have distinct roles, Majorana suggested to split this equation into two parts, each of which describes the evolution of a real field for which particles and antiparticles are the same. By analogy, the operators $\hat{\gamma}$ that we have introduced here are called *Majorana operators*. There is of course a major difference between the fundamental particles to which Majorana wanted to apply his theory (the neutrino is still a possible candidate) and the modes that appear here, which are emerging quasiparticles that are built with "usual" fermions, electrons in a condensed matter or neutral atoms in a quantum gas experiment.

Using the operators $\hat{\gamma}_{j,\pm}$ instead of the operators $\hat{a}_j^\dagger, \hat{a}_j$ is often nothing more than a different way of writing the same thing. For example, the operator which gives the energy $\pm\epsilon_j/2$ on site j depending on its occupancy

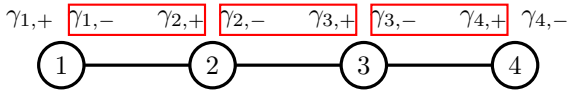

Figure 22. *The couplings between neighbouring Majorana modes that correspond to the Hamiltonian (88) for a chain with $N = 4$ sites. The two modes at the ends of the chain, $\hat{\gamma}_{1,+}$ and $\hat{\gamma}_{N,-}$ are not coupled.*

can be written with both points of view:

$$\epsilon_j\left(\hat{a}_j^\dagger\hat{a}_j - 1/2\right) = \frac{\mathrm{i}}{2}\,\epsilon_j\,\hat{\gamma}_{j,+}\,\hat{\gamma}_{j,-} \tag{87}$$

A local perturbation can thus be written as the product of neighbouring Majorana operators.

Let us now go back to the Kitaev chain. Its Hamiltonian (70) can be written with the Majorana operators:

$$\hat{H} = \mathrm{i}\,J\sum_{j=1}^{N}\hat{\gamma}_{j,-}\,\hat{\gamma}_{j+1,+} \tag{88}$$

which describes a coupling between the mode $\hat{\gamma}_-$ of each site j to the mode $\hat{\gamma}_+$ of site $j+1$ (figure 22). Note that the two modes $\hat{\gamma}_{1,+}$ and $\hat{\gamma}_{N,-}$ at the end of the chain do not appear in this expression.

Let us now focus on a perturbation to $\hat{H}$ and on the influence it has on the groundstate at first order of the perturbation theory. To lift the degeneracy of this level, the perturbation has to contain a term

$$\hat{V} = \epsilon\,\hat{b}_N^\dagger\,\hat{b}_N + \ldots \qquad \text{with} \quad \hat{b}_N = \frac{1}{2}\left(\hat{\gamma}_{N,-} + \mathrm{i}\gamma_{1,+}\right) \tag{89}$$

It is convenient to write these expressions in terms of Majorana operators, because this immediately reveals the non-local character that $\hat{V}$ must have:

$$\hat{V} = \frac{\mathrm{i}}{2}\epsilon\,\hat{\gamma}_{N,-}\hat{\gamma}_{1,+} + \ldots \tag{90}$$

One then has to act coherently at the two ends of the chain to lift the degeneracy between $|\psi_0\rangle$ and $|\psi_1\rangle$. A local perturbation has no influence on this groundstate, which explains its robustness.

We insist on the fact that these two Majorana modes, each localized at one end of the chain, describe a single fermionic excitation, with the mode $\hat{b}_N$ that can be either empty or occupied; one thus refer to these modes as fractional quasiparticles. This situation is very different from the one found for the SSH model, where we had a (bosonic or fermionic) mode localized on each end of the chain, both of which could be empty or occupied (therefore 4 possibilities for spinless fermions, all with an energy close to zero).

The fact that we have considered a spinless model is crucial to end up with this unique fermionic mode. If the initial fermions had a spin $1/2$, this would double the number of modes, and lead to two Majorana modes at each end of the chain. A spin-orbit coupling could then couple these two modes to create a "usual" fermionic excitation, and we would find a situation similar to the one of the SSH model.

The existence of a degenerate groundstate that is protected from the rest of the energy levels by a gap opens new opportunities in the framework of quantum processing of information. Consider an ensemble of n Kitaev chains, each of which have a doubly degenerate groundstate. The groundstate of the ensemble is 2^n times degenerate[6] and an adiabatic evolution within this level gives rise to a non-abelian statistics when the Majorana modes are mixed together (Alicea, Oreg, et al. 2011; Alicea 2012).

Searching for these Majorana modes in topological superconductors is currently at the center of an intense activity in condensed matter physics, with the first experimental indications described by Mourik, Zuo, et al. (2012) in a indium antimonide nanowire placed at the vicinity of a superconducting electrode and of a normal electrode, and by Nadj-Perge, Drozdov, et al. (2014) in a chain of iron atoms deposited at the surface of a superconductor. We will not describe them here and the reader can refer to one of the most recent articles on this topic, Zhang, Yaji, et al. (2018), and to the references therein.

In the field of atomic physics, no experimental realization has been published yet, but realistic propositions are being implemented in various laboratories (Zhang, Tewari, et al. 2008a; Nascimbene 2013; Yan, Wan, et al. 2015), including in a dissipative environment (Bardyn, Baranov, et al. 2012). We can also mention the important question of how the Kitaev model, where the number of particles is not conserved, can be transposed to an isolated system where the number of particles is fixed, which is closer to what can be realized in a cold atom experiment; in this optic, Iemini, Mazza, et al. (2015) have proposed such an exactly solvable model in which modes at null energy and similar to Majorana modes can emerge (also see Ruhman, Berg, et al. (2015)).

[6] or rather 2^{n-1} if one considers only operations that conserve the parity of the total number of fermions on the chains. We therefore need at least $n = 2$ chains to realize such operations.

Appendix 1: The semi-infinite SSH chain

The set of equations (29-30) can be written in a matrix form for $j \geq 1$:

$$\begin{pmatrix} a_{j+1} \\ b_{j+1} \end{pmatrix} = \hat{M} \begin{pmatrix} a_j \\ b_j \end{pmatrix}, \tag{91}$$

with

$$\hat{M} = \begin{pmatrix} -J'/J & -E/J \\ E/J & E^2/(JJ') - J/J' \end{pmatrix} \tag{92}$$

and the initial condition (up to a normalization factor):

$$\begin{pmatrix} a_1 \\ b_1 \end{pmatrix} = \begin{pmatrix} J' \\ -E \end{pmatrix}. \tag{93}$$

The real matrix $\hat{M}$ has determinant 1 and its trace is

$$T = \frac{E^2 - J^2 - J'^2}{JJ'}. \tag{94}$$

Two cases are possible for the eigenvalues $\lambda_\pm$ of this matrix. They are either:

- complex of modulus 1 if the discriminant of the characteristic polynomial $\lambda^2 - T\lambda + 1$ is negative or null, that is if $|T| \leq 2$. The energy thus has to lie in one of the two energy bands of the complete chain, eq. (6).
- real and verifying $|\lambda_-| < 1$, $|\lambda_+| > 1$ if the discriminant is strictly positive.

Once the eigenvalues $\lambda_\pm$ and the corresponding eigenvectors $\boldsymbol{V}_\pm$ are known, the solution of the system can be written as

$$\begin{pmatrix} a_j \\ b_j \end{pmatrix} = \lambda_-^j \boldsymbol{V}_- + \lambda_+^j \boldsymbol{V}_+. \tag{95}$$

In the first case, the eigenvalues are $\mathrm{e}^{\pm \mathrm{i}qa}$ and we recover the "standing wave" solution mentioned in the text, with coefficients a_j and b_j whose modulus stay bounded and of order 1 when $j \to \infty$.

In the second case, the contribution of the eigenvalue λ_+ has to be canceled in equation (95) so that the coefficients a_j and b_j do not diverge at infinity. This means that the vector (a_1, b_1) given in (93) is an eigenstate of $\hat{M}$ with eigenvalue λ_-. We then write that

$$\hat{M} \begin{pmatrix} a_1 \\ b_1 \end{pmatrix} \quad \text{and} \quad \begin{pmatrix} a_1 \\ b_1 \end{pmatrix} \quad \text{are collinear} \tag{96}$$

and we obtain the condition $EJ = 0$, hence $E = 0$.

Appendix 2 : Topology and symmetries

We have encountered in this lecture two symmetries that are relevant to study topological problems: the sublattice symmetry (also called chiral symmetry), and the particle-hole symmetry. We briefly explain in this appendix how this type of symmetries can lead to a systematic classification of topological phases of matter. We recall that the symmetries that we discuss here are not the usual geometrical symmetries that can for example be linked to the translational and rotational invariance. These geometrical symmetries are by definition not well-suited to describe topological invariants: an orange or a rugby ball are topologically equivalent to a sphere, but they are not rotationally invariant.

Mathematically, the geometrical symmetries are described by a unitary operator $\hat{U}$ that commutes with the Hamiltonian $\hat{H}$, which allows one to search for a common basis of eigenstates. The mathematical formulation is different for the topological classification, either because the involved operators are not unitary but anti-unitary, or because their link with the Hamiltonian is not a commutation relation, but an anticommutation relation.

At the heart of the classification of the topological insulators and superconductors lie two discrete symmetries (for a detailed description, see the very complete review article by Chiu, Teo, et al. (2016)):

- The time-reversal symmetry, described by an anti-unitary operator $\hat{\mathcal{T}}$. The operation of time reversal consists in keeping the position of the particles, and inverting the direction of their velocity, hence of their (orbital or spin) angular momentum. A Hamiltonian is invariant under time reversal if
$$\hat{H}\hat{\mathcal{T}} = \hat{\mathcal{T}}\hat{H}, \tag{97}$$
an operation that is thus translated by a "traditional" commutator with the Hamiltonian, but applied to an operator $\hat{\mathcal{T}}$ that is not unitary, as for the geometrical symmetries, but anti-unitary. For a spinless particle, the operator for time reversal is simply the complex conjugation $\hat{K}_0$:
$$\hat{K}_0 \, \psi(x) = \psi^*(x) \tag{98}$$
which has the particular effect of changing a plane wave $\mathrm{e}^{\mathrm{i}px/\hbar}$ (with momentum p) into the plane wave $\mathrm{e}^{-\mathrm{i}px/\hbar}$, (with momentum $-p$). In the spinless case, the action of $\hat{\mathcal{T}}^2$ is always $+\hat{1}$ for a time-reversal invariant system. When the spin of the particles is taken into account, one can show that the action of $\hat{\mathcal{T}}^2$ on an eigenstate of a Hamiltonian that verifies (97) can be $+\hat{1}$ or $-\hat{1}$ (Messiah 2003). For this operation, there are then three possibilities: the action of $\hat{\mathcal{T}}^2$ is $+1$ or -1, or there is no such symmetry.

- For ensembles of fermions, the "particle-hole" symmetry consists in exchanging the role of the operators for the *creation of a particle at position* $\boldsymbol{r}$ and of the operators for the *annihilation of a particle at position* $\boldsymbol{r}$. We have seen this symmetry appearing in the framework of the Bogoliubov – de Gennes method, where it can be described by the anti-unitary operator $\hat{\mathcal{C}}$ that anticommutes with the Hamiltonian $\hat{H}_{\mathrm{BdG}}$ (*cf.* § 3-3):
$$\hat{H}_{\mathrm{BdG}}\hat{\mathcal{C}} = -\hat{\mathcal{C}}\hat{H}_{\mathrm{BdG}}. \tag{99}$$
We also find here that the action of $\hat{\mathcal{C}}^2$ is $\pm\hat{1}$ when the symmetry is present.

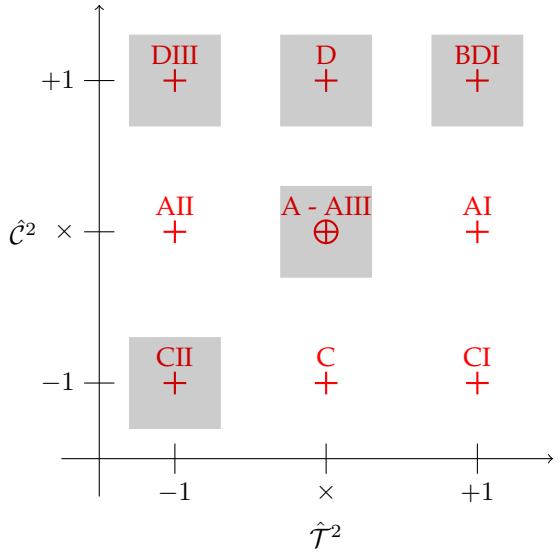

Table 1. *Ten-fold classification for Hamiltonians describing topological insulators and superconductors. The × symbol indicates the absence of the symmetry. This classification uses the naming system proposed by Elie Cartan in 1926 for the* symmetric spaces. *The highlighted boxes are those which are possible for one-dimensional systems, with the AIII class for the central box, that corresponds to the chiral symmetry.*

We therefore obtain $3 \times 3 = 9$ possibilities, according to the presence or not of these two symmetries, and the sign ± 1 that is associated to their square when they are present.

The chiral symmetry that we have found for the SSH model is more generaly associated to the product $\hat{\mathcal{S}} = \hat{\mathcal{T}} \cdot \hat{\mathcal{C}}$, which is a unitary operator (the product of two anti-unitary operators). It has a central role in one of the nine cases that we have mentioned, the one where both $\hat{\mathcal{C}}$ and $\hat{\mathcal{T}}$ are not relevant. Two situations can then occur, according to the presence or not of this last symmetry. We arrive at 10 possible situations, the famous *tenfold way* (table 1) (Chiu, Teo, et al. 2016).

For a given dimension of space, all these possibilities are not realized, but only five of them. For dimension 1, which we have considered up to now, these possibilities are highlighted in grey on table 1. The spinless SSH Hamiltonian that we have studied in § 1 is real, therefore time-reversal invariant $\mathcal{T}^2 = +1$. It also (trivially) respects the particle-hole symmetry since it does not contain any term linked to a superconductor gap ($\mathcal{C}^2 = +1$) and it falls in the BDI class. Note that it is always possible to redefine each lattice site A_j or B_j by multiplying its amplitude by $\mathrm{e}^{\mathrm{i}\alpha_j}$ or $\mathrm{e}^{\mathrm{i}\beta_j}$. Such a change of gauge immediately turns the tunneling coefficient into complex numbers (Velasco & Paredes 2017). The system then move to the AIII class, and keeps the chiral symmetry. The Kitaev model that we have investigated has spinless particles, and we have chosen a real gap Δ. It thus also verifies $\mathcal{C}^2 = +1$ and $\mathcal{T}^2 = +1$. If the gap is complex, the time-reversal symmetry is lost, but the particle-hole symmetry is conserved (D class).

Finally, we insist on the fact that these brief explanations, along with the examples of the spinless SSH and the Kitaev models, constitute only a very partial perspective on the classification of the topological insulators and superconductors. This classification is much more relevant when spin-orbit couplings are added, which enables one to generate richer (and more complex) classes of materials than the ones considered here.

Chapter III

Adiabatic pumps

The two first chapters have been mostly dedicated to the study of a particular 1D lattice which corresponds to the model introduced by Su, Schrieffer, et al. (1979). We have identified two distinct topological classes for this model, characterized by the value 0 or π of the Zak phase. We have emphasized that the difference between these two classes was underpinned by the *sublattice symmetry*, also refered to as *chiral symmetry*, which ensured the required topological protection.

In this chapter, we will try to go beyond the SSH model to investigate what happens when the sublattice symmetry is lost. There are of course many ways to do so. We will first add the minimal number of ingredients: we will stay in the tight-binding regime and we will also only consider cells with two sites A and B. We will however relax the constraint on the equivalence of the two sites, which will bring us to the model of Rice & Mele (1982). We will then describe how to implement this general class of 1D bipartite lattices with cold atoms trapped in optical standing waves, and we will present the principle of the Zak phase measurement performed by Atala, Aidelsburger, et al. (2013).

We will then come to the notion of *adiabatic pumps*, that emerges when the parameters of the lattice – that is the couplings between sites and the onsite energies – are allowed to be slowly varied in time. We will see that a periodic variation of these parameters and an adequate preparation of the particles lead to a displacement of the center of mass of these particles that is quantized in units of the spatial period of the lattice. We will describe the experiment of Nakajima, Tomita, et al. (2016) that has demonstrated this quantization in a cold atom experiment.

The adiabatic pump is in fact a two-dimensional problem, with one dimension of space and one dimension of time, for which we will show that the quantization can be expressed as the integral of a Berry curvature. This will be the first step in the topological problems of dimension larger than 1, and the results of this chapter will reappear in an almost unchanged form for the truly 2D problems that we will consider in the next chapters.

1 1D lattices beyond the SSH model

1-1 A Hamiltonian for two sites

Our starting point is the same as for the previous chapter. We consider a one dimensional periodic lattice in the tight-binding regime, with two sites A and B per unit cell. Bloch's theorem can be applied, and the dynamics of a particle is described by the Hamiltonian $\hat{H}_q$, which is represented by a 2×2 hermitian matrix. We have already mentioned the fact that this type of matrices can be written as a linear combination of the identity and of the three Pauli matrices

$$E_0(q)\ \hat{1}\ -\ \boldsymbol{h}(q) \cdot \hat{\boldsymbol{\sigma}}, \tag{1}$$

where the vector $\boldsymbol{h}_q$ is characterized by its modulus $|\boldsymbol{h}(q)|$ and its direction, which itself is parametrized by the two spherical angles θ_q, ϕ_q.

The term proportional to the identity, displaying the energy $E_0(q)$, has no influence on the topological properties of the energy bands: it does not intervene in the expression of the eigenstates, and thus does not contribute to the expression of the Berry–Zak phase. In the following, we will focus on the physics associated to the second part of (1)

$$\hat{H}_q = -\boldsymbol{h}(q)\cdot\hat{\boldsymbol{\sigma}} = -|\boldsymbol{h}(q)| \begin{pmatrix} \cos\theta_q & \mathrm{e}^{-\mathrm{i}\phi_q}\sin\theta_q \\ \mathrm{e}^{\mathrm{i}\phi_q}\sin\theta_q & -\cos\theta_q \end{pmatrix}, \tag{2}$$

whose eigenstates are, in the gauge of chapter 1:

$$|u_q^{(-)}\rangle = \begin{pmatrix} \cos(\theta_q/2) \\ \mathrm{e}^{\mathrm{i}\phi_q}\sin(\theta_q/2) \end{pmatrix} \qquad |u_q^{(+)}\rangle = \begin{pmatrix} \sin(\theta_q/2) \\ -\mathrm{e}^{\mathrm{i}\phi_q}\cos(\theta_q/2) \end{pmatrix}. \tag{3}$$

The Hamiltonian $\hat{H}_q$ is linked to the motion of a particle in a periodic potential with spatial period a. Here, this Hamiltonian is built to be periodic in q with period $2\pi/a$:

$$\hat{H}_{q+2\pi/a} = \hat{H}_q. \tag{4}$$

The study of the SSH model has shown that the emergence of distinct topological classes came from the sublattice symmetry, in other words from the fact that the diagonal elements of $\hat{H}_q$ are null ($\theta_q = \pi/2$). The state $|u_q^{(\pm)}\rangle$ then lies on the equator of the Bloch sphere, and from this we deduced that the state $|u_q^{(\pm)}\rangle$ describes an integer number of circles on the equator of the Bloch sphere when q spans the Brillouin zone of length $2\pi/a$. This integer constituted the topological invariant of the SSH model. We will now remove this constraint, and the first consequence will be that the state $|u_q^{(\pm)}\rangle$ will be able to sit at any point of the Bloch sphere.

The choice of gauge. In equation (3), we have fixed the phase of $|u_q^{(\pm)}\rangle$ by setting its first component as a real and positive value (or null since θ_q is in $[0,\pi]$). Unless we specify otherwise, we will choose this gauge in the following. This leads to the following expression for the Berry connection of the two bands:

$$\mathcal{A}^{(-)}(q) = \mathrm{i}\langle u_q^{(-)}|\partial_q u_q^{(-)}\rangle = -\frac{\mathrm{d}\phi_q}{\mathrm{d}q}\sin^2(\theta_q/2), \tag{5}$$

$$\mathcal{A}^{(+)}(q) = \mathrm{i}\langle u_q^{(+)}|\partial_q u_q^{(+)}\rangle = -\frac{\mathrm{d}\phi_q}{\mathrm{d}q}\cos^2(\theta_q/2), \tag{6}$$

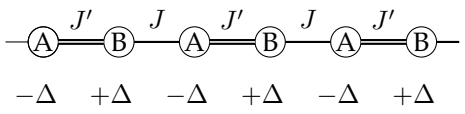

Figure 1. *The Rice–Mele model.*

which can be written in the compact form:

$$\mathcal{A}^{(\pm)}(q) = -\frac{1}{2}\frac{\mathrm{d}\phi_q}{\mathrm{d}q}\,(1\pm\cos\theta_q)\,. \tag{7}$$

1-2 The Rice-Mele model

The model introduced by Rice & Mele (1982) consists in broadening the SSH model by allowing the two sites A and B to have different energies E_A and E_B (figure 1). The Hamiltonian $\hat{H}_q$ then becomes

$$\begin{aligned} \hat{H}_q &= \begin{pmatrix} E_A & -(J'+J\,\mathrm{e}^{-\mathrm{i}qa}) \\ -(J'+J\,\mathrm{e}^{\mathrm{i}qa}) & E_B \end{pmatrix} \\ &= \frac{1}{2}(E_A+E_B)\,\hat{1} - \begin{pmatrix} \Delta & J'+J\,\mathrm{e}^{-\mathrm{i}qa} \\ J'+J\,\mathrm{e}^{\mathrm{i}qa} & -\Delta \end{pmatrix} \end{aligned} \tag{8}$$

where we have defined

$$2\Delta = E_B - E_A. \tag{9}$$

In the following we will choose the origin of energies so that $E_A + E_B = 0$, in order to cancel out the term proportional to the identity, which plays no role in the topology of the problem, as stated above.

The Hamiltonian $\hat{H}_q$ can be written under the canonical form $\hat{H}_q = -\boldsymbol{h}(q)\cdot\hat{\boldsymbol{\sigma}}$ with

$$\boldsymbol{h}(q) = \begin{pmatrix} J'+J\cos(qa) \\ J\sin(qa) \\ \Delta \end{pmatrix}. \tag{10}$$

The vector $\boldsymbol{h}(q)$ is characterized by its modulus

$$\begin{aligned} |\boldsymbol{h}(q)| &= \left[\Delta^2 + |J'+J\,\mathrm{e}^{\mathrm{i}qa}|^2\right]^{1/2} \\ &= \left[\Delta^2 + J^2 + J'^2 + 2JJ'\cos(qa)\right]^{1/2} \end{aligned} \tag{11}$$

and by the two angles $\theta_q \in [0,\pi]$ and $\phi_q \in]-\pi,+\pi]$:

$$\cos\theta_q = \frac{\Delta}{|\boldsymbol{h}_q|}, \qquad \mathrm{e}^{\mathrm{i}\phi_q}\,\sin\theta_q = \frac{J' + J\,\mathrm{e}^{\mathrm{i}qa}}{|\boldsymbol{h}_q|}. \tag{12}$$

This model has of course two energy bands

$$E_q^{(\pm)} = \pm|\boldsymbol{h}(q)| \tag{13}$$

and these two bands are separated by a gap that can close only if we have at the same time

$$\text{no gap if and only if} \qquad \Delta = 0 \quad \text{and} \quad J' = J. \tag{14}$$

1-3 The Zak phase of the Rice–Mele model

Starting from the expression of these states, one can determine the Berry-Zak geometrical phase of this model, that is the phase accumulated by a particle that describes the full Brillouin zone $[-\pi/a, \pi/a]$. For the lower band, we get:

$$\begin{aligned}\Phi_{\mathrm{Zak}}^{(-)} &= \mathrm{i}\int_{\mathrm{BZ}} \langle u_q^{(-)}|\partial_q u_q^{(-)}\rangle\,\mathrm{d}q = -\int_{\mathrm{BZ}} \frac{\partial\phi_q}{\partial q}\,\sin^2(\theta_q/2)\,\mathrm{d}q \\ &= -\frac{1}{2}\int_{\mathrm{BZ}} \frac{\partial\phi_q}{\partial q}\,\mathrm{d}q + \frac{1}{2}\int_{\mathrm{BZ}} \frac{\partial\phi_q}{\partial q}\,\cos\theta_q\,\mathrm{d}q.\end{aligned} \tag{15}$$

The first term was already present for the SSH model, and it is equal to 0 or π, depending on the case we are in, normal ($J' > J$) or topological ($J' < J$). The second term is specific to the Rice–Mele model, for which $\cos\theta_q$ is not equal to zero. The determination of this phase is rather long, but does not present any difficulty. The result has been drawn in figure 2. More precisely, since a phase is a quantity defined modulo 2π, we have represented this phase by a unit vector in the $[J'/J, \Delta]$ plane.

The particular case of the SSH model is represented on the horizontal axis $\Delta = 0$ of the graph, where the phase is equal to π or 0, depending if we are on the left or on the right of the point $J' = J$. We see that we can continuously connect the two sides of the axis if we consider a trajectory in

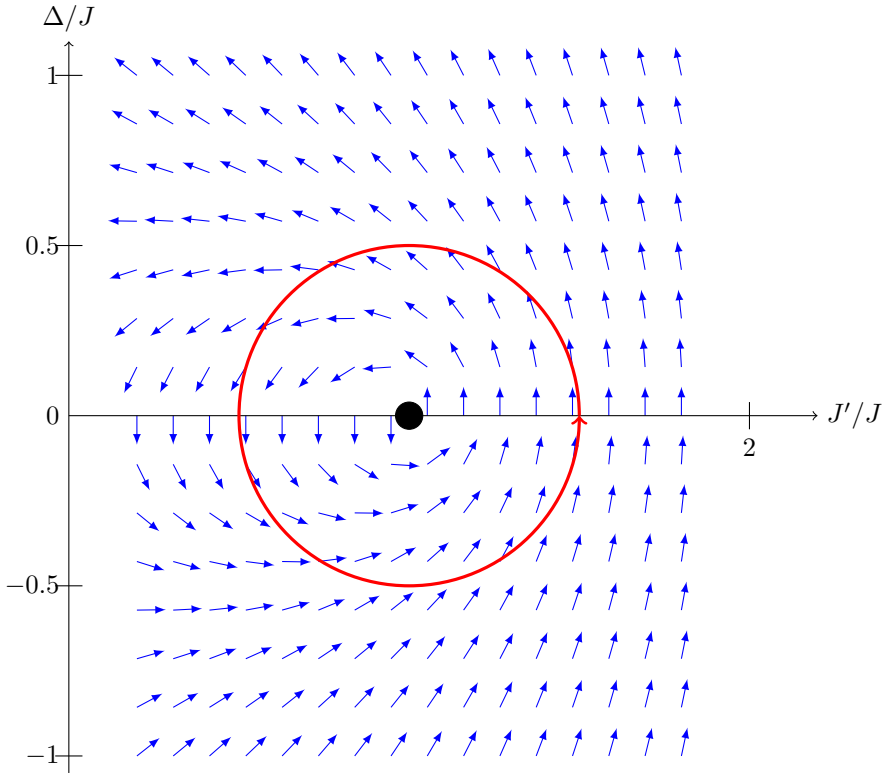

Figure 2. *Vector-field representation of the Zak phase $\Phi_{\mathrm{Zak}}^{(-)}$ of the lowest band of the Rice–Mele model. We have drawn in blue a unit vector of polar angle $\Phi_{\mathrm{Zak}}^{(-)} + \pi/2$, so that a zero Zak phase (modulo 2π) is represented by an arrow pointing upwards, and a Zak phase of $\pm\pi$ by an arrow pointing downwards. The vector field displays has a vortex structure around the singular point where the gap between the two bands closes: $\Delta = 0$, $J' = J$. The red circle represents a possible cycle for a geometrical pump (§ 3).*

the $[J'/J, \Delta]$ plane that departs from the x axis. In other words, the possibility of choosing $\Delta \neq 0$ blurs out the distinction between the topological character of the two phases of the SSH model, and we can go from one to the other without ever closing the gap between the two energy bands.

We also notice that the variation of the Zak phase around the singular point $\Delta = 0$, $J' = J$ has a vortex structure: this phase winds by $\pm 2\pi$ if the system follows a trajectory that circles around this singular point. This winding will play a crucial role in the *adiabatic pumps* that we will study in § 3.

2 Optical lattices and superlattices

We now come to the description of how the SSH and RM models can be implemented with cold atoms by placing them in an optical lattice. These lattices are formed by a standing light wave that creates for the atoms a potential proportional to the local intensity of the light field. The origin of this potential, called the *dipolar potential*, lies in the induction of an electrical dipole in the atom by the electric field of the laser, and in the interaction of this dipole with the electric field of the light. We will not discuss the detailed formalism that allows to quantitatively compute this potential, but the reader can refer to the lectures of 2012-2013 and 2014-2015, and to the references therein. In the following, we only need to know that a monochromatic laser of intensity $I(\boldsymbol{r})$ creates for an atom a potential $V(\boldsymbol{r}) = \alpha\, I(\boldsymbol{r})$, where the coefficient α depends on the wavelength of the light.

2-1 1D optical lattices

The most simple 1D optical lattice is created by a standing light wave, which gives rise to the potential

$$V(x) = V_0 \ \sin^2(kx). \tag{16}$$

The lattice introduces a length scale, the period $a = \pi/k = \lambda/2$, where $k = 2\pi/\lambda$ is the wave number of the light, and λ is its wavelength. It also

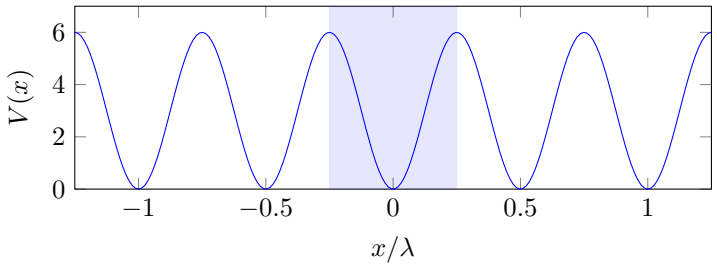

Figure 3. *The sinusoidal potential (16) of period $a = \lambda/2$ and its unit cell.*

introduces an energy scale, called the *recoil energy*:

$$E_{\mathrm{r}} = \frac{\hbar^2 k^2}{2m} \tag{17}$$

where m is the mass of an atom. The tight-binding regime, on which we have built our analysis, corresponds to the case where the height V_0 of the barrier between two neighbouring minima is large compared to the recoil energy:

$$\text{Tight-binding}: \quad E_{\mathrm{r}} \ll V_0. \tag{18}$$

In this regime, the tunneling rate J from one site to the next is small compared to V_0, and the lattice Hamiltonian is well approximated by the single-band model:

$$\hat{H} = -J \sum_j |j+1\rangle\langle j| + \text{h.c.}, \tag{19}$$

where all sites have the same energy. One can show that the asymptotic value of J in this limit is (cf. the 2012-2013 lecture series):

$$\frac{J}{E_{\mathrm{r}}} \approx \frac{4}{\sqrt{\pi}} \left(\frac{V_0}{E_{\mathrm{r}}}\right)^{3/4} \exp\left[-2\left(\frac{V_0}{E_{\mathrm{r}}}\right)^{1/2}\right]. \tag{20}$$

We have drawn in figure 4 the band spectrum obtained for $V_0 = 6\, E_{\mathrm{r}}$. Figure 5 zooms on the lowest band, and we check that the variation with q of $E_q^{(0)}$ is described (up to an additive constant) by the prediction of the single-band model

$$E_q = -2J\cos(qa) \tag{21}$$

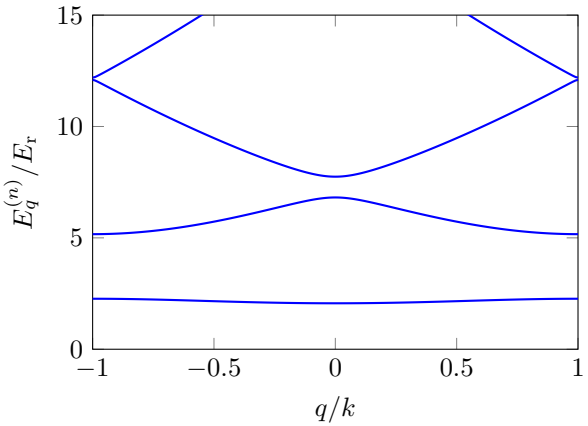

Figure 4. *Lowest energy bands of the sinusoidal lattice with $V_0 = 6\,E_r$.*

with the tunneling rate $J \approx 0.05\,E_r$. Note that equation (20) would give $J \approx 0.065\,E_r$ for $V_0 = 6\,E_r$, which indicates that the value $6\,E_r$ is not large enough to reach the asymptotic limit.

2-2 Optical superlattice

In order to have a richer potential and obtain a unit cell with two sites corresponding to the SSH and RM models, one has to engineer

- two types of hopping terms in the lattice with an alternation of the tunneling coefficients J and J';
- an alternation of the energies $E_A = -\Delta$ and $E_B = +\Delta$.

A configuration of lasers called a *superlattice* that allows to implement this model has been represented in figure 6, and it realizes the following potential of period λ:

$$V(x) = V_{\text{princ.}} \sin^2(kx) + V_{\text{sec.}} \sin^2[(kx+\phi)/2], \tag{22}$$

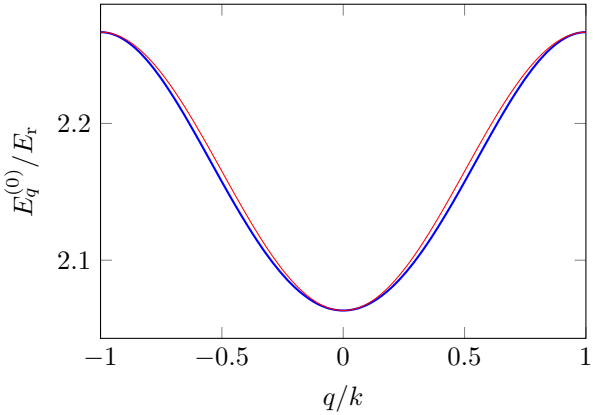

Figure 5. *Blue: the lowest band of the sinusoidal lattice with $V_0 = 6\,E_r$. Red: variation of E_q given by the single-band model (21) with $J = 0.05\,E_r$ (shifted in energy by $+2.16\,E_r$).*

Figure 6. *The principle of a superlattice: two standing light waves are superimposed, the first one with wavelength λ and the second one with wavelength 2λ.*

where we will suppose (without any loss of generality) that the origin of space and the origin of energy are such that $V_{\text{princ.}}$ et $V_{\text{sec.}}$ are both positive.

- A first optical lattice, called *principal lattice*, of wavelength λ, hence of period $a = \lambda/2$, creates the regular lattice mentioned above, which we assume to be described by the tight-binding model. The minima of this lattice are located at $kx = n\pi$, that is $x = n\lambda/2$, where n is a positive or negative integer.
- A *secondary* optical lattice with a lower intensity and a wavelength 2λ modulates the potential of the principal lattice with a spatial period $2a = \lambda$.

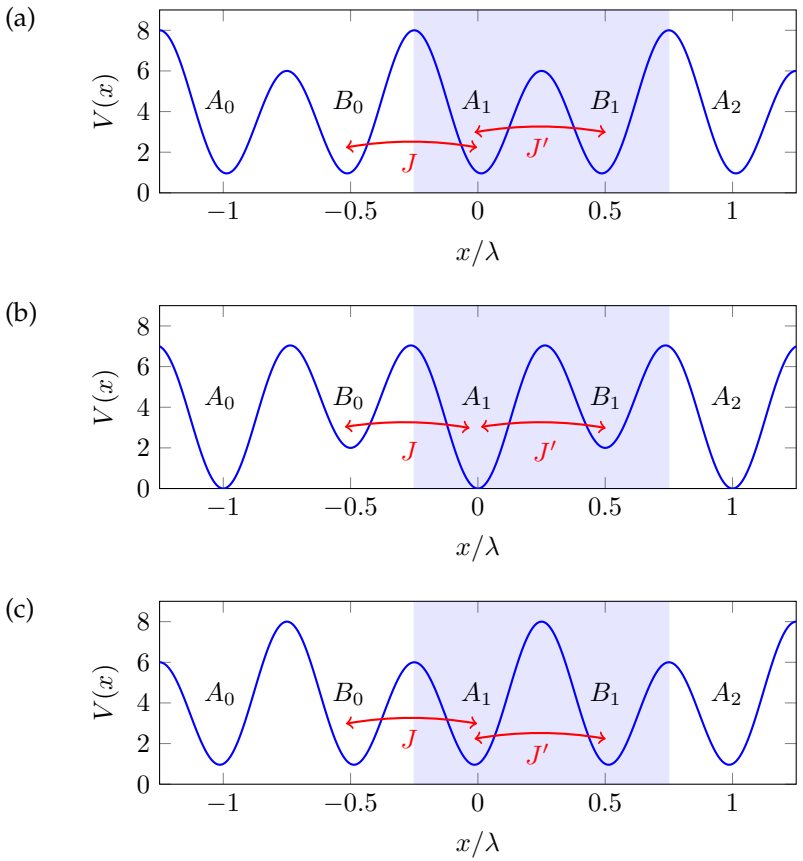

Figure 7. *The potential (22) of the superlattice with which one can realize the different phases of the Rice–Mele model. (a) and (c) correspond to the particular case of the SSH model, with $\Delta = 0$ and : $\phi = -\pi/2$, $J' > J$ for (a), $\phi = +\pi/2$, $J' < J$ for (c). Case (b) is obtained for $\phi = 0$ and corresponds to the Rice–Mele model with $\Delta > 0$, $J' = J$. The shaded area indicates the choice of the unit cell.*

The effect of the secondary lattice is described by two parameters: its modulation amplitude $V_{\text{sec.}}$ (which is supposed to be small compared to $V_{\text{princ.}}$) and its spatial phase shift ϕ with respect to the principal lattice. Controlling these two parameters allows one to implement the Rice–Mele model that also depends on two parameters.

We start by focusing on the case where $\phi = \pm\pi/2$. The secondary potential has the same value $V_{\text{sec.}}/2$ on all the minima $x = n\lambda/2$ of the principal lattice, but it modulates the height of the barrier between these minima. We obtain the potential represented in figures 7 (a) and (c), which implements the SSH model. We arbitrarily decide to label with letter A the minima located around $x = n\lambda$, and with letter B the minima around $x = (n + \frac{1}{2})\lambda$, which leads to:

- For $\phi = -\pi/2$, the barrier between A_1 and B_1 is lower than the barrier between B_0 and A_1, and we thus have $J' > J$ [figure 7 (a)];
- For $\phi = +\pi/2$, we have on the contrary $J' < J$ [figure 7 (c)].

By switching the phase ϕ between the two values $\pm\pi/2$, one can then realize (in the tight-binding approximation) the two cases of the SSH model with different topologies $J' < J$ and $J' > J$.

We now suppose that the relative phase between the two standing waves is $\phi = 0$; the corresponding potential is shown in figure 7 (b). The secondary lattice now has different values on the minima of the principal lattice. At $x = n\lambda$, this value is equal to zero, whereas it is equal to $V_{\text{sec.}}$ at $kx = (n + \frac{1}{2})\pi$. In a tight-binding model, two types of sites are generated, with $E_A \neq E_B$. On the other hand, the barrier between one minimum to the next minimum is identical on the right and on the left of each site. The RM model is then realized in the particular configuration $J' = J$, $\Delta > 0$. For all the intermediate values of the phase ϕ, one has at the same time $J \neq J'$ and $\Delta \neq 0$, which realizes the general case of the RM model.

The numerical computation of the band spectrum of this superlattice is straightforward. The unit cell has now size λ, and the Brillouin zone is $q \in [-k/2, k/2[$. This band spectrum is represented in figure 8 for $V_0 = 6\,E_{\text{r}}$, $V_1 = 2E_{\text{r}}$, with the phase $\phi = \pi/2$, which leads to a SSH-like situation[1].

[1]Its spectrum is reminiscent of the purely sinusoidal lattice if the latter is drawn in a

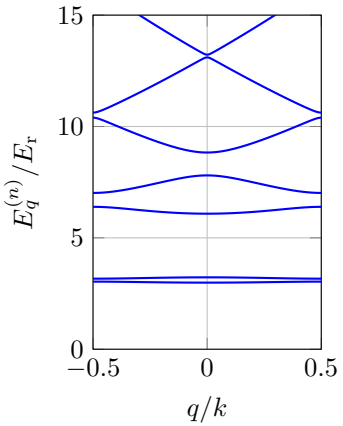

Figure 8. *The energy bands of the superlattice (22) for $V_{\mathrm{princ.}} = 6E_\mathrm{r}$, $V_{\mathrm{sec.}} = 2E_\mathrm{r}$, $\phi = \pm\pi/2$.*

In the following, we focus on the lower part of the spectrum of this superlattice, and we show in figure 9 the two lowest bands in the presence of the two lattices, for increasing values of $V_{\mathrm{sec.}}$. We take the value $V_{\mathrm{sec.}} = E_\mathrm{r}$ as an example in figure 10 to verify that the variations of these two energy bands are in good agreement with the prediction of the SSH model seen in chapter 1 (with an irrelevant energy shift):

$$E_q^{(\pm)} = \pm\left[J^2 + J'^2 + 2JJ'\cos(qa)\right]^{1/2}, \tag{23}$$

with in this case $J = 0.069\,E_\mathrm{r}$, $J' = 0.037\,E_\mathrm{r}$. These values are to be compared to the value $J = 0.051\,E_\mathrm{r}$ obtained in the previous paragraph for the same value $V_{\mathrm{princ.}} = 6E_\mathrm{r}$ and $V_{\mathrm{sec.}} = 0$: the secondary lattice, even if weak, is sufficient to change a lot the values of the two coefficients J and J'.

"folded" way, which is obtained with a unit cell of size λ, and therefore a Brillouin zone twice as small as the one of figure 4 (see appendix 1). Note however the gap opening at the edge of the bands for $q \approx \pm k/2$, gaps that are due to the secondary lattice and to the difference that appears between J and J'.

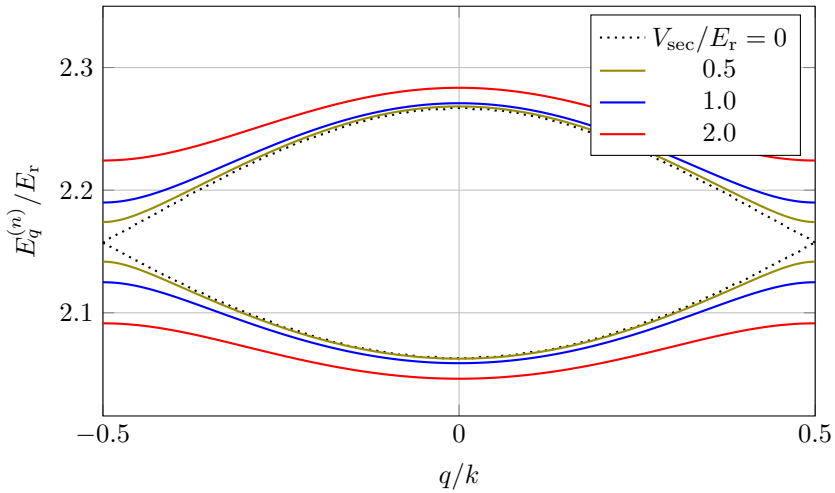

Figure 9. *The two lowest energy bands of the superlattice (22), for $V_{\mathrm{princ.}} = 6\,E_\mathrm{r}$ and different values of $V_{\mathrm{sec.}}$. We have chosen $\phi = \pm\pi/2$, corresponding to the realization of the SSH model. The energy of the pairs of bands for $V_{\mathrm{sec.}} \neq 0$ has been shifted so that they are centered at the same energy as the pair corresponding to $V_{\mathrm{sec.}} = 0$.*

2-3 Measuring the Zak phase

As already mentioned at the end of lecture 1 for the SSH model, the Zak phase is not in itself a topological invariant, because its value is modified when changing the parametrization of the unit cell of the lattice. Going from a unit cell composed by $\{A_j, B_j\}$ to another unit cell composed by $\{B_{j-1}, A_j\}$ amounts to adding $+\pi$ to the Zak phase. However, when the choice of a parametrization has been made, the difference between the two topologies $J' < J$ and $J' > J$ is fixed:

$$\mathrm{e}^{\mathrm{i}\Delta\Phi} = -1 \qquad \text{with} \quad \Delta\Phi \equiv \Phi_{\mathrm{Zak}}^{[J'>J]} - \Phi_{\mathrm{Zak}}^{[J'<J]}. \tag{24}$$

This difference is therefore the physically measurable quantity.

To access it, Atala, Aidelsburger, et al. (2013) have performed an experiment that can be schematically described as follows, for a given

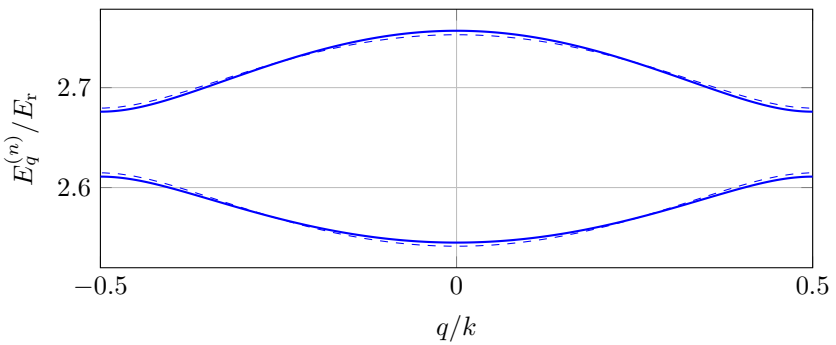

Figure 10. *Continuous line: lowest energy bands for $V_{\text{princ.}} = 6E_r$ and $V_{\text{sec.}} = E_r$. We have chosen $\phi = \pi/2$, corresponding to the implementation of the SSH model. Dashed line: prediction (23) for the SSH model with $J = 0.069\,E_r$, $J' = 0.037\,E_r$ (with a global energy shift).*

parametrization of the unit cell:

- We start with atoms localized around a given momentum q_i of the Brillouin zone, in the superlattice obtained with $\phi = -\pi/2$, that is the SSH model with $J' > J$ for the parametrization of figure 7.
- We apply a weak force F to the atoms, which drive them across the Brillouin zone in the lowest band; this is the Bloch oscillations phenomenon on which we will come back later in the lecture. At this point, we only need to know that the momentum of the atoms follows with a good degree of approximation a "law of motion" that gives a linear dependence with time:

$$\hbar\frac{\mathrm{d}q}{\mathrm{d}t} = F \quad \longrightarrow \quad q(t) = q_i + Ft/\hbar. \tag{25}$$

- At time $t_B = 2\pi\hbar/(F\lambda)$, the atoms have crossed the full Brillouin zone:

$$q(t_B) \equiv q_f = q_i + 2\pi/\lambda \tag{26}$$

  and they have accumulated (in addition to the dynamical phase) the geometrical phase $\Phi_{\text{Zak}}^{[J'>J]}$.
- At that time, the phase of the lattice is suddenly switched and goes from $\phi = -\pi/2$ to $\phi = +\pi/2$. We thus stay in the context of the SSH model, but now with $J' < J$ (*cf.* figure 7).
- At the same time, the direction of the force F is inverted so that the atoms cross the Brillouin zone in the other direction:

$$\hbar\frac{\mathrm{d}q}{\mathrm{d}t} = -F \quad \longrightarrow \quad q(t) = q_f - Ft/\hbar. \tag{27}$$

- At time $2t_B$, the atoms are back in q_i and they have accumulated the total geometrical phase $\Delta\Phi = \Phi_{\text{Zak}}^{[J'>J]} - \Phi_{\text{Zak}}^{[J'<J]}$.

An interferometric measurement of this phase is performed and the result is compared to the theoretical prediction (24): $\Delta\Phi = \pi$ modulo 2π.

In practice, the situation is a bit more involved. The atoms are prepared in a Zeeman sublevel that is sensitive to magnetic field and the force F is created by a magnetic field gradient. The atoms are initially prepared with momentum $q_i = 0$, and a microwave pulse is applied to create a coherent superposition of two spin states $|\uparrow\rangle$ and $|\downarrow\rangle$ that feel a force $\pm F$ in opposite directions. The wavepacket thus splits in two in momentum space. When each packet reaches the edge of the Brillouin zone, the phase is instantaneously shifted $\phi : -\pi/2 \to +\pi/2$ to go from $J' > J$ to $J' < J$. To reduce the noise due to the fluctuations of magnetic field, the two states $|\uparrow\rangle$ and $|\downarrow\rangle$ are inverted by a π pulse of microwaves, which corresponds to a *spin-echo* technique. The combination of these two actions changes the band that the atoms occupy. The two wavepackets then evolve back to momentum $q = 0$. There, a last $\pi/2$ pulse allows one to "read" the relative phase of the two packets. A detailed analysis shows that the dynamical phases accumulated on each of the trajectories – in particular the ones due to the Zeeman shifts – compensate and do not contribute to the signal.

The measurement by Atala, Aidelsburger, et al. (2013) has shown with a good precision that the measured relative phase is indeed equal to π (with a precision of 3%), in agreement with the topology expected for the SSH model (figure 12). Atala, Aidelsburger, et al. (2013) have then extended their procedure to the general case of a Rice–Mele lattice ($\Delta \neq 0$), which is obtained by taking $\phi \neq \pm\pi/2$. They have also obtained results in very good agreement with the prediction (15) plotted in figure 2.

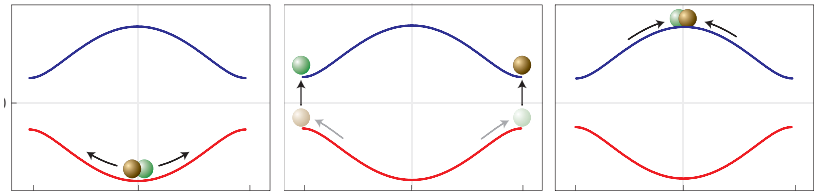

Figure 11. *The protocol followed by Atala, Aidelsburger, et al. (2013) to measure the Zak phase of the SSH model, featuring a superlattice and a $\pi/2$–π–$\pi/2$ sequence of microwave pulses.*

3 Adiabatic pump in the RM model

We now come to an important aspect of topological phases of matter: the realization of *adiabatic pumps*, also called *Thouless pumps*, after the initial proposal by Thouless (1983).

Very generally, an adiabatic pump can be defined as a process for which:

- The parameters that control a fluid, for example its Hamiltonian, are varied in a cyclic way.
- At the end of a cycle, the fluid has not come back to its initial position, but there has been a transport of matter by a quantity that does not depend on the duration of the cycle.

A celebrated example is Archimedes' screw, represented in figure 13, for which a fixed quantity of the fluid is transferred from the bottom to the top with each turn of the crank, no matter what the angular velocity of this crank is.

Here we will address the quantum version of this concept. In particular, we will see how the vortex structure of the Zak phase around the singular point $\Delta = 0$, $J' = J$ enables the realization of such a pump. Note that this notion first applies to fully filled energy bands, a situation that can easily be obtained with polarized fermions. To fill the lowest band, one can put one particle per unit cell of the lattice. This notion can also be generalized

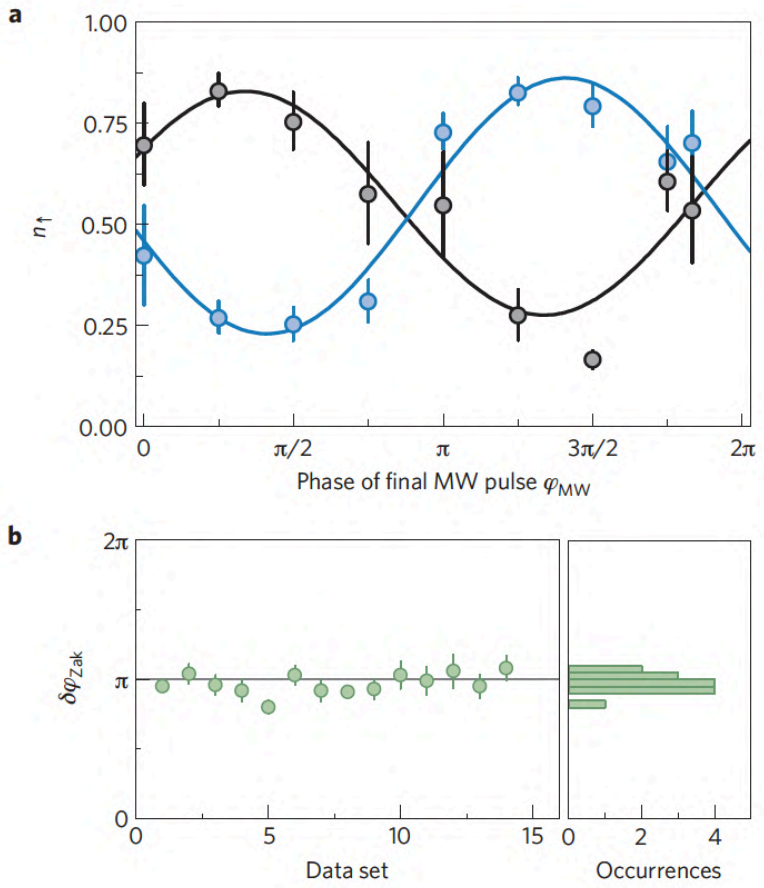

Figure 12. *Top: The result obtained by Atala, Aidelsburger, et al. (2013) for the occupancy of the state $|\uparrow\rangle$ after the sequence described in the main text. The blue points have been obtained by switching ϕ from $-\pi/2$ to $\pi/2$, and the black points correspond to the case where ϕ has not been changed. The difference of phase between the two curves gives $\Delta\Phi = \Phi_{\text{Zak}}^{[J'>J]} - \Phi_{\text{Zak}}^{[J'<J]}$. Bottom: the result obtained for $\Delta\Phi$. The average of 14 independent sequences gives $\Delta\Phi = 0.97\,(2)\,\pi$.*

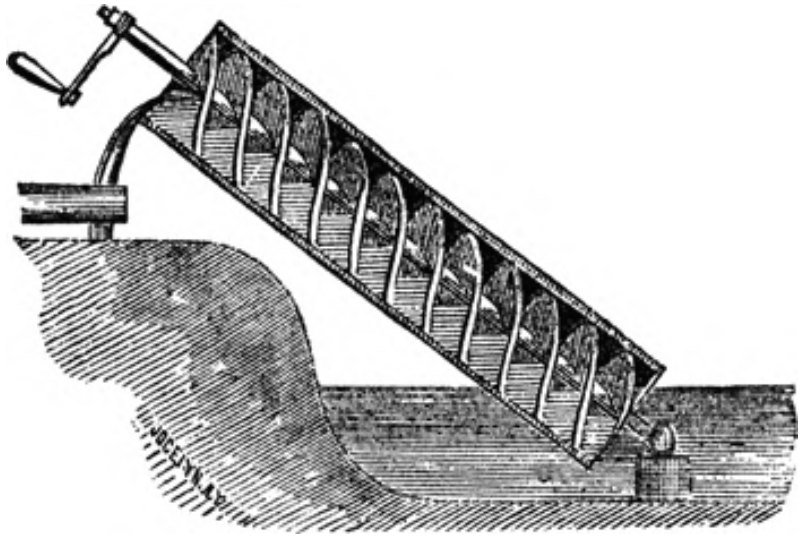

Figure 13. *An example of (classical) adiabatic pump: Archimedes' screw (figure : Wikipedia).*

to bosons, provided that each Bloch state $|\psi_q^{(n)}\rangle$ of the considered band, for example the lowest band $n = 0$, has the same mean population.

In order to see how the notion of adiabatic pump can arise, we will first consider two simple situations that resort to optical lattices and that both lead to a quantized displacement of a particle in the lattice.

3-1 Translating a lattice

The first (and almost too simple!) example features a simple sinusoidal lattice

$$V(x) = V_0 \sin^2(kx - \phi), \tag{28}$$

which is assumed to be very deep, so that the tunneling is blocked. A particle prepared in a potential well thus stays there indefinitely. If the value of ϕ is varied very slowly in time from 0 to π, all the minima are displaced by the period a of the lattice, and the particle has moved by a

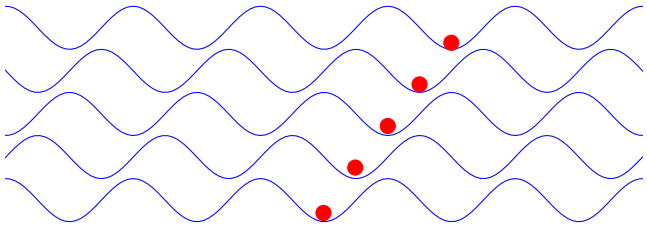

Figure 14. *The adiabatic transport performed by a simple translation of the lattice.*

(figure 14).

3-2 Distortion of a deep lattice

The second example is much more interesting. We continuously distort the potential of a superlattice of period $a = 2\pi/k$:

$$V(x) = V_{\text{princ.}} \sin^2(kx) + V_{\text{sec.}} \sin^2[(kx + \phi)/2] \tag{29}$$

by varying only the phase ϕ. The corresponding distortion is represented in figure 15. Let us consider a particle initially located in one of the wells, and suppose that the lattice is sufficiently deep so that the tunneling through the "high" barriers is negligible. The particle will then adiabatically go from one site to the other when these sites are separated by a low barrier and when they have the same energy. The problem is identical to the one of an initially asymmetric double well that momentarily becomes symmetric and shifts to the opposite asymmetry (figure 16).

The series of drawings in figure 15 shows that a particle initially located on site A_j moves by one unit a to the right and end up on site A_{j+1} when the phase ϕ increases by 2π. At the same time, a particle initially located on site B_j ends up on site B_{j-1} after the same increase of phase. According to the initial state of the particle, two opposite currents are generated for the same pumping cycle, which is much less intuitive than the previous example of the translated lattice.

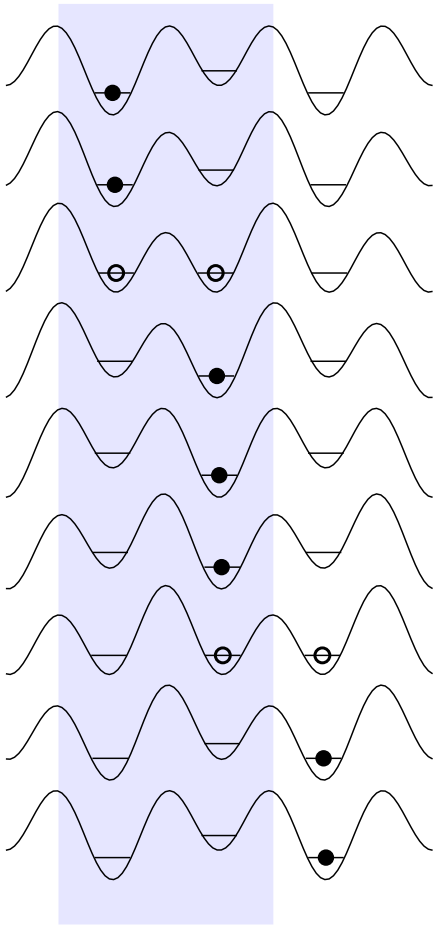

Figure 15. *The quantized displacement of a particle initially localized on an A site when the potential of the superlattice (29) is distorted by changing ϕ from 0 to 2π. A particle initially localized on a B site would be displaced in the opposite direction.*

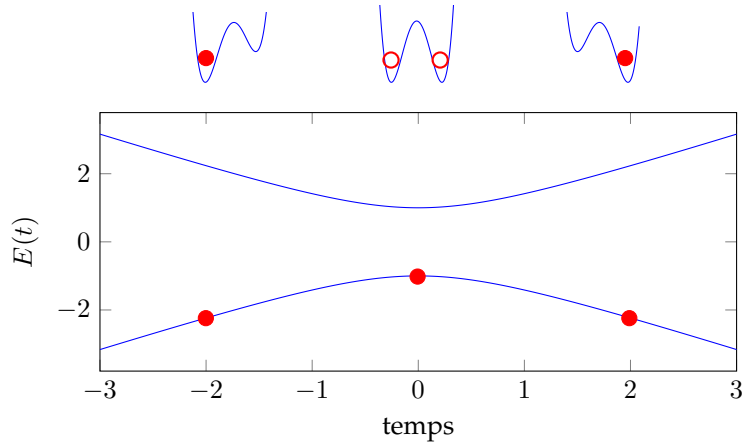

Figure 16. *The adiabatic passage from a site to the next in a double well, when the relative energy of the two minima is slowly changed.*

3-3 The experiment of Nakajima *et al.*

The idea of an adiabatic (or "topological") pump goes back to 1983 with the article of Thouless, but it is truly with the experiments with cold atoms in optical lattices that it has been put into practice (Hatsugai & Fukui 2016). It is indeed not possible to modulate in time the crystal structure for electrons, and the photonic version of the adiabatic pump is not easy to implement either [see however Wimmer, Price, et al. (2017) and Ozawa, Price, et al. (2018)].

For cold atoms, the periodic distortion of the confining potential can be done relatively easily by using an optical superlattice and by modulating in time the relative phase and the intensity of the two standing waves. We describe here an experiment performed in Kyoto with a gas of fermionic atoms (Nakajima, Tomita, et al. 2016). Note that two other experimental results with bosons have been almost simultaneously published, in Munich (Lohse, Schweizer, et al. 2016) and at JQI Maryland (Lu, Schemmer, et al. 2016).

The Kyoto experiment has been performed with $\sim 10^4$ Ytterbium atoms

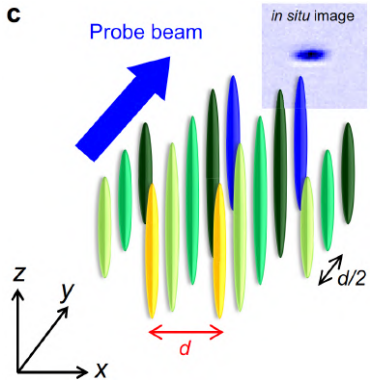

Figure 17. *A series of independent vertical tubes. The superlattice potential is applied along the z axis. Figure taken from Nakajima, Tomita, et al. (2016), sup.mat.*

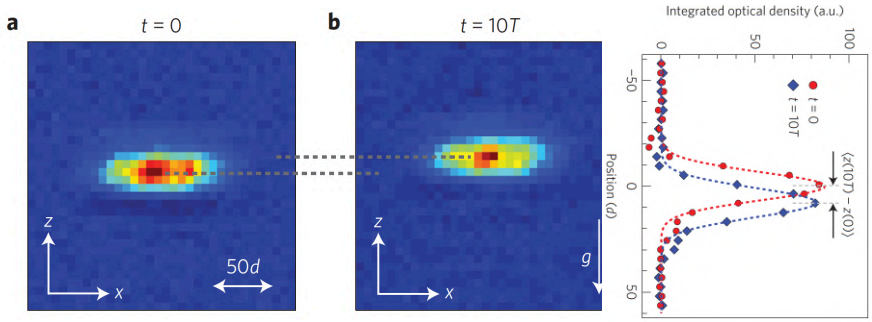

Figure 18. *An* in situ *image of the atomic cloud before and after 10 cycles of the adiabatic pump. The duration T of a cycle is 50 ms. The displacement of the center of mass along the z axis reveals the expected quantization. Figure taken from Nakajima, Tomita, et al. (2016).*

(isotope ^{171}Yb) trapped in a series of independent vertical tubes (figure 17). In each tube, the atoms are placed in a potential of spatial period 266 nm, on which a potential with twice this period, 532 nm, is superimposed. The relative phase between these two standing waves, denoted as ϕ in (22), is controlled by an ancillary interferometer. In this experiment, it can be varied continuously by $\sim 20\pi$, which corresponds to approximately ten pumping cycles.

The atoms are prepared in the lowest band of the lattice with a filling factor of ~ 0.7 per spin state at the center of the cloud. The starting point is therefore not exactly a band insulator (unit filling), but the band is filled uniformly. The temperature is indeed notably larger than the width of the band while staying notably smaller than the gap between the lowest band and the first excited band. This is sufficient to observe a quantization of the center-of-mass motion.

Once the pumping cycles have been performed, an *in situ* picture of the cloud is taken and compared to the reference image for which the cloud has not been displaced (figure 18); the distance between the centers of mass along the vertical direction z is thus measured.

The first experiment performed by Nakajima, Tomita, et al. (2016) consisted in measuring the displacement induced by a translated lattice. One simply needs to remove the intensity of the lattice with short period and to vary linearly in time the phase ϕ. The measured displacement is indicated with red dots in figure 19. It is indeed linear with the number of pumping cycles, with a coefficient compatible with the expected value of $a = 532$ nm after every duration T, that is every time ϕ gains 2π.

The second experiment consists in applying a time-periodic distortion of the Rice–Mele potential. This distortion is similar to the one shown in figure 15 and it is obtained by varying ϕ linearly for a constant value of the amplitude of the two lattices:

$$V_{\text{princ.}} = 30\, E_{\text{r}} \qquad V_{\text{sec.}} = 20\, E_{\text{r}} \tag{30}$$

where $E_{\text{r}} = \hbar^2 k^2/(2m)$ is the recoil energy for wavelength $\lambda = 2\pi/k = 532$ nm. For such large values of the lattice depth, the simplified mechanism presented in figure 15 describes well the principle of the adiabatic pump. The corresponding results are also shown in figure 19 (blue points). When the number of pumping cycles in not too large ($\lesssim 6$), we find a displacement in agreement with the expected quantization. For longer pumping durations, the displacement is smaller than expected. Nakajima, Tomita, et al. (2016) attribute this effect to the additional harmonic confinement along the z axis that creates an energy shift comparable with the width of the band when the center of mass has moved by more that $6\,a$.

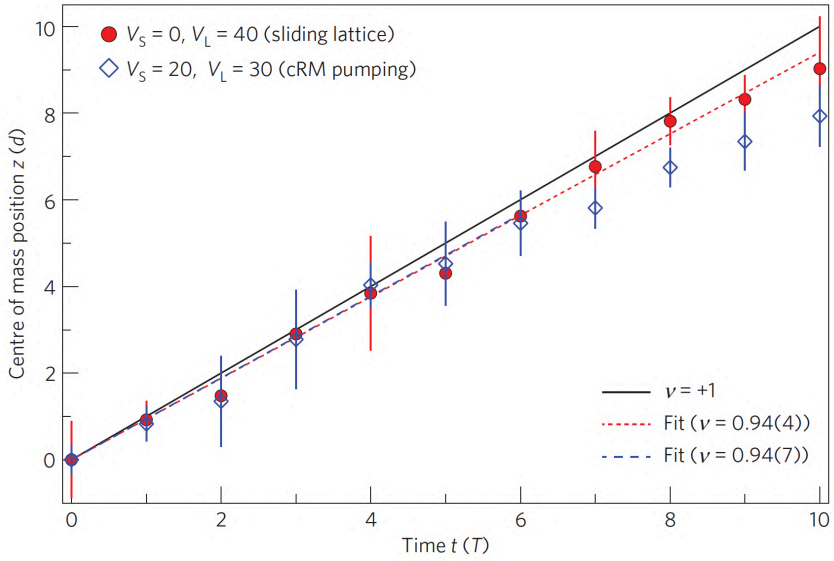

Figure 19. *Displacement of the center of mass of the atomic cloud as a function of the number of pumping cycles of the geometrical pump. The red dots correspond to a simple translated lattice, the blue points to a distortion similar to the one represented in figure 15. Figure taken from Nakajima, Tomita, et al. (2016).*

Nakajima, Tomita, et al. (2016) have also tested the robustness of this adiabatic pump by distorting the trajectory followed in the (J', Δ) plane. We recall that the pump is expected to work if and only if this trajectory circles around the critical point $J' = J, \Delta = 0$. In addition, the sign of the displacement reflects the direction in which the trajectory is followed. The experiment of Nakajima, Tomita, et al. (2016) has confirmed these predictions, as shown in figure 20.

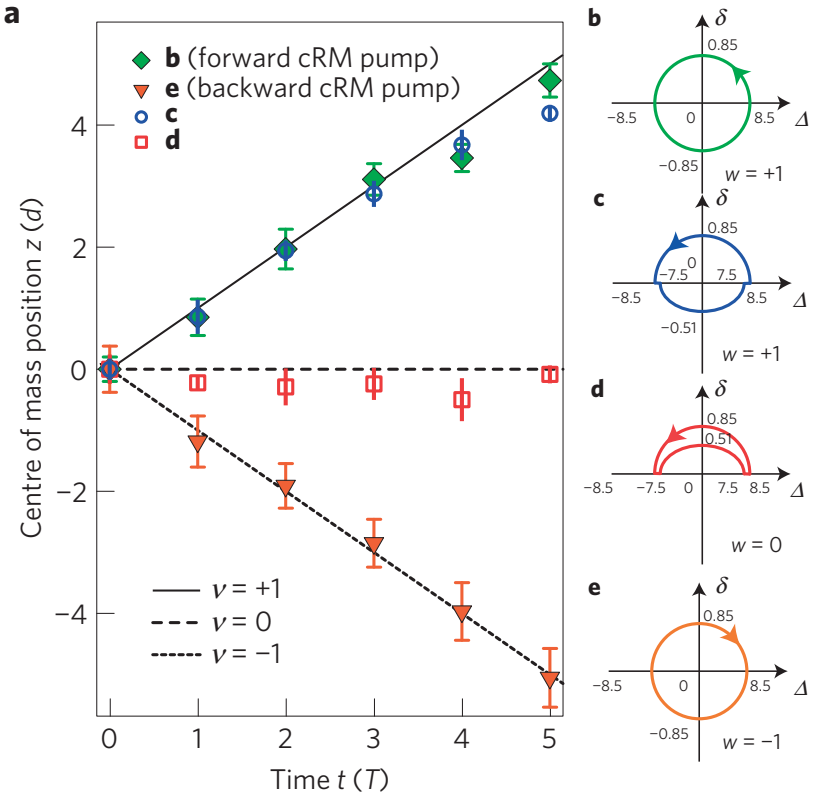

Figure 20. *Topological robustness of the adiabatic pump when the trajectory in the J', Δ is modified (with here $2\delta = J' - J$). Figure taken from Nakajima, Tomita, et al. (2016).*

4 Adiabatic pump and Berry phase

The examples reviewed in the previous paragraph were based on the negligible role of the tunneling, which simplified a lot the analysis. The result

of Thouless (1983) has a much broader scope, as we see now. In this section, we will mainly use a geometrical reasoning that is well-adapted to the RM model for which the states can be represented as a pseudo-spin 1/2. In section 5, we will use a more general approach, based on a linear response analysis.

4-1 Cycling Hamiltonian and geometrical phase

We study the evolution of the system during one pumping cycle by starting from a Bloch state $|\psi_q^{(-)}\rangle$ in the lowest band of the Rice–Mele model, with momentum q. We consider a slow variation of parameters J' and Δ that describes a closed loop during the cycling period T, as represented by a red circle in figure 2. There are two steps in the reasoning:

- Since the Hamiltonian $\hat{H}(t)$ is of period a for all time t between 0 and T, we can apply the time-dependent version of Bloch's theorem: the state of the system is at all time a Bloch wave, that is the product of the plane wave $\mathrm{e}^{\mathrm{i}qx}$ and a periodic function $u(x,t)$ (or $|u(t)\rangle$) with the same periodicity as the lattice.

- We now take into account the slow variation of parameters J' and Δ. The adiabatic theorem tells us that, in good approximation, the state of the system characterized by the periodic function $|u(t)\rangle$ stays in the lowest band, thus in state $|u_{q,t}^{(-)}\rangle$ given in (3). This state varies in time since it depends on the instantaneous values of J' and Δ via the angles θ_q and ϕ_q. We know that the adiabatic approximation is valid for a cycling time T sufficiently long, provided that the gap between the followed state and the other reachable states does not cancel out, in our case the state of same momentum q but in the other band $|u_{q,t}^{(+)}\rangle$.

For the previous reasoning to apply for all the momenta q of the Brillouin zone, the gap between the lowest band and the excited band must not close, therefore the closed loop must not pass through the central point of the vortex of figure 2, $J' = J, \Delta = 0$. Once this is established, we are sure that the state of the system at time T is identical to the initial state $|\psi_{q,t}^{(-)}\rangle$, up to a phase.

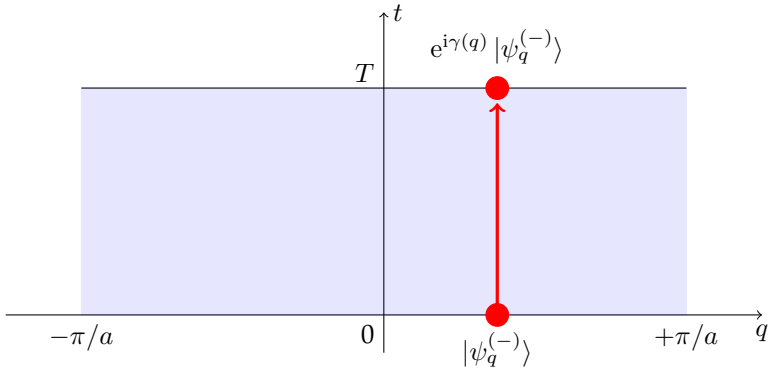

Figure 21. *Two-dimensional diagram with momenta on the horizontal axis and time on the vertical axis. The adiabatic motion corresponds to linear trajectories such as the red arrow, and the knowledge of the dynamics lies entirely in the phase $\gamma(q)$.*

We need to determine this phase factor, which comprises two terms, as previously:

$$\mathrm{e}^{\mathrm{i}\gamma(q)} = \mathrm{e}^{\mathrm{i}\Phi_{\mathrm{dyn}}(q)}\,\mathrm{e}^{\mathrm{i}\Phi_{\mathrm{geom}}(q)}. \tag{31}$$

The dynamical phase reads (*cf.* chapter 1)

$$\Phi_{\mathrm{dyn}}(q) = -\frac{1}{\hbar}\int_0^T E_{\boldsymbol{q}}^{(-)}(t)\,\mathrm{d}t, \tag{32}$$

where $E_{\boldsymbol{q}}^{(-)}(t)$ is the energy of the state $|\psi_q^{(-)}\rangle$ on the lowest band, with the values of parameters J, J' and Δ taken at time t. The geometrical phase is equal to

$$\Phi_{\mathrm{geom}}(q) = \int_0^T \mathcal{A}_2(q,t)\,\mathrm{d}t. \tag{33}$$

where we have introduced[2] the *temporal Berry connection*

$$\mathcal{A}_2(q,t) = \mathrm{i}\langle u_{q,t}|\partial_t u_{q,t}\rangle, \tag{34}$$

[2]We forget here the notation $^{(-)}$ referring to the band, since only the lowest band should be occupied.

where the index 2 reminds that there are here two variables, q and t, and that the derivative of ket $|u_{q,t}\rangle$ is taken with respect to the second one.

We thus have shown that the action of the single-particle evolution operator $\hat{U}(T)$ over one pumping cycle of duration T is diagonal in the Bloch states basis $|\psi_q^{(-)}\rangle$:

$$\hat{U}(T) = \exp[\mathrm{i}\gamma(\hat{q})] \tag{35}$$

where $\hat{q}$ is the *momentum operator* of the particle, whose eigenstates are the states $|\psi_q\rangle$, associated with the eigenvalue q.

4-2 The motion of the center of mass

The diagonal form of the evolution operator in the $|\psi_q\rangle$ basis leads to a simple derivation of the motion of the center of mass X of an ensemble of N non-interacting identical particles. We first note that the operator *position of the center of mass*

$$\hat{X} = \frac{1}{N}\sum_{n=1}^{N} \hat{x}_n \tag{36}$$

is a "single-particle" operator. Its mean value can thus be calculated from the one-body density operator $\hat{\rho}^{(1)}$, which is obtained by taking the trace of the density operator over $N-1$ particles:

$$\langle X(T)\rangle = \mathrm{Tr}\left(\hat{x}\ \hat{\rho}^{(1)}(T)\right). \tag{37}$$

Additionally, if the particles are independent, the evolution of the one-body density operator $\hat{\rho}^{(1)}$ is given by

$$\hat{\rho}^{(1)}(T) = \hat{U}(T)\ \hat{\rho}^{(1)}(0)\ \hat{U}^{\dagger}(T), \tag{38}$$

so that, after a circular permutation in the trace, we get:

$$\langle X(T)\rangle = \mathrm{Tr}\left(\hat{x}(T)\ \hat{\rho}^{(1)}(0)\right) \tag{39}$$

where we have defined:

$$\hat{x}(T) = \hat{U}^{\dagger}(T)\ \hat{x}\ \hat{U}(T) = \hat{x} - \partial_q\gamma(\hat{q}). \tag{40}$$

In the last equation, we have used the fact that the position operator of each particle is defined here as canonically associated to its momentum, that is $[\hat{x},\hat{q}] = \mathrm{i}$ and

$$\mathrm{e}^{-\mathrm{i}\gamma(\hat{q})}\ \hat{x}\ \mathrm{e}^{+\mathrm{i}\gamma(\hat{q})} = \hat{x} - \partial_q\gamma(\hat{q}). \tag{41}$$

We then find the displacement of the center of mass

$$\Delta x \equiv \langle X(T)\rangle - \langle X(0)\rangle\ =\ -\langle\partial_q\gamma(\hat{q})\rangle. \tag{42}$$

We now suppose that the lowest band is uniformly filled when the assembly of particles is in the state $|\Psi\rangle$, which means that the one-body density operator is proportional to the identity in the $|\psi_q^{(-)}\rangle$ basis. The average in equation (42) now becomes a simple integral over the Brillouin zone (of size $2\pi/a$):

$$\Delta x = -\frac{a}{2\pi}\int_{-\pi/a}^{+\pi/a} \partial_q\gamma(q)\ \mathrm{d}q. \tag{43}$$

In this integral, the contribution of the dynamical phase cancels out because of the periodicity of energy E_q with q, and we only need to evaluate

$$\Delta x = -\frac{a}{2\pi}\int_{-\pi/a}^{+\pi/a} \frac{\mathrm{d}\Phi_{\mathrm{geom}}}{\mathrm{d}q}\ \mathrm{d}q \qquad \text{with} \quad \Phi_{\mathrm{geom}}(q) = \int_0^T \mathcal{A}_2(q,t)\ \mathrm{d}t. \tag{44}$$

4-3 The trajectories on the Bloch sphere

When looking at equation (44), the first idea is simply to integrate the result, which gives:

$$\Delta x = -\frac{a}{2\pi}\left[\Phi_{\mathrm{geom}}(+\pi/a) - \Phi_{\mathrm{geom}}(-\pi/a)\right] \tag{45}$$

and to find then the value of this geometrical phase $\Phi_{\mathrm{geom}}(\pm\pi/a)$ for the two end points of the Brillouin zone.

This approach, which we develop right afterwards, has however a caveat. We are using here mathematical expressions which may be singular at some points (q,t). The parametrization (3) for the state $|u_{q,t}\rangle$ with

the spherical angles $\theta_{q,t}$ and $\phi_{q,t}$ can indeed lead to ill-defined mathematical expressions for the "temporal" Berry connection $\mathcal{A}_2 = \mathrm{i}\langle u_{q,t}|\partial_t u_{q,t}\rangle$ that is appearing in $\Phi_{\mathrm{geom}}(q)$ (see § 5). In order to perform the calculation without encountering any problem, the safest method is to express the motion of the center of mass in terms of the Berry *curvature*, a method that we will apply in the next paragraph (§ 4-4).

But right now, we want to give a meaning to (44-45) thanks to a geometrical reasoning. We know since the first chapter that, for a problem that can be mapped to a pseudo-spin $1/2$, the geometrical phase $\Phi_{\mathrm{geom}}(q)$ is, up to a factor $1/2$, equal to the solid angle that is described on the Bloch sphere by the trajectory of the state $|u_{q,t}\rangle$ when t varies from 0 to T. Let us investigate this trajectory for various values of q (figure 22) by using the expressions of $\theta_{q,t}$ and $\phi_{q,t}$

$$\cos\theta_q = \frac{\Delta}{|\boldsymbol{h}(q)|}, \qquad \mathrm{e}^{\mathrm{i}\phi_q}\ \sin\theta_q = \frac{J' + J\,\mathrm{e}^{\mathrm{i}qa}}{|\boldsymbol{h}(q)|}. \tag{46}$$

with $|\boldsymbol{h}(q)| = \left[\Delta^2 + J^2 + J'^2 + 2JJ'\cos(qa)\right]^{1/2}$ and the two angles $\theta_q \in [0,\pi]$ and $\phi_q \in]-\pi,+\pi]$.

- For $q = 0$, the quantity $\mathrm{e}^{\mathrm{i}\phi_q}\sin\theta_q = (J + J')/\epsilon_q$ is always a positive real number when J' and Δ vary and follow the circle of figure 2. We then have a simple back-and-forth motion on the Bloch sphere along the meridian of longitude 0, and the solid angle corresponding to this trajectory, represented in purple in figure 22 is equal to zero.
- The trajectories corresponding to the values $qa/\pi = \pm 1/4, 1/2, 3/4, 7/8$ are represented respectively in blue, green, yellow and orange, and they depart from the central meridian. They delineate larger and larger solid angles with opposite signs for $\pm q$, and they tend to a half space (solid angle of 2π) when q approaches $\pm\pi/a$.
- For $q = \pm\pi/a$, the two trajectories are identical: these are the large red circles that pass through the poles. The solid angle is therefore $\pm 2\pi$ and the associated geometrical phase is $\pm\pi$.

This geometrical analysis tells us two things. On the one hand, all the points of the Bloch sphere are reached at least once when q and t vary, re-

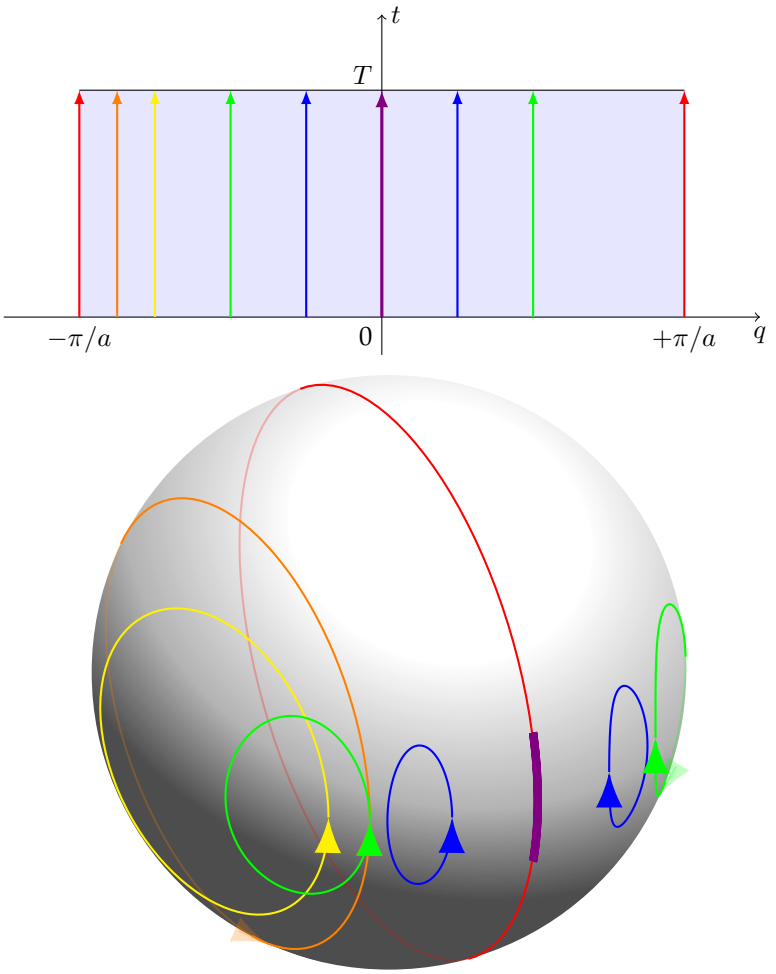

Figure 22. *The followed trajectories, for a q that is fixed during the pumping cycle. The geometrical phase $\Phi_{\mathrm{geom}}(t)$ is given, up to a factor $1/2$, by the solid angle that the corresponding trajectory describes. We have chosen a circular trajectory in the plane $(J'/J,\ \Delta)$, centered on (1,0) and with radius 0.5, followed with a uniform velocity.*

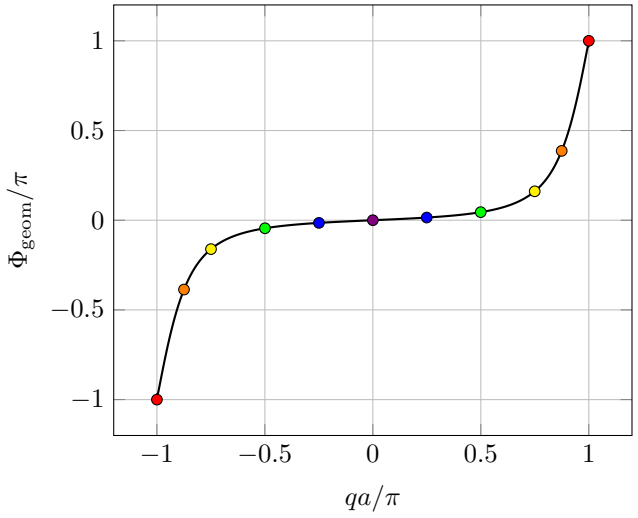

Figure 23. *The geometrical phase deduced from the solid angle delimited by the trajectory of the state $|u_{q,t}\rangle$ on the Bloch sphere during a pumping cycle. This geometrical phase varies continuously from $-\pi$ to $+\pi$ when q varies in the Brillouin zone, which leads to a quantization of the motion Δx given in (44). The color code of the points is the same as the one in figure 22.*

spectively in the segments $[-\pi/a, +\pi/a]$ and $[0, T]$: the Bloch sphere is fully covered by these trajectories. On the other hand, for the sake of continuity, one has to assign the value $\Phi_{\rm geom} = -\pi$ to the trajectory corresponding to $q = -\pi/a$, and the value $\Phi_{\rm geom} = +\pi$ to the one corresponding to $q = \pi/a$. The result (45) thus has to be understood as

$$\Delta x = -\frac{a}{2\pi}\left[\lim_{q\to+\pi/a}\Phi_{\rm geom}(q) - \lim_{q\to-\pi/a}\Phi_{\rm geom}(q)\right] \tag{47}$$

where the first limit is taken when $+\pi/a$ is approached from below, and the second when $-\pi/a$ is approached from above. This leads to:

$$\Delta x = -\frac{a}{2\pi}\left[(+\pi) - (-\pi)\right] = -a. \tag{48}$$

The displacement of the center of mass during a pumping cycle is then indeed quantized in units of the lattice period.

We observe that, for this two-dimensional problem (one dimension of time and one of space), the Bloch sphere is entirely wrapped by the states $|u_{q,t}\rangle$. This constitutes the topological invariant of the problem which cannot be modified by a "smooth" modification of the path followed in the (J', Δ) plane. This invariant is the equivalent for this 2D problem of the winding of a phase in a 1D problem.

4-4 Quantized displacement and Berry curvature

We still ignore the possibility of having singularities in the definition of the state $|u_{q,t}\rangle$ and we look for another expression of the displacement of the center of mass Δx. For this problem with one spatial and one temporal coordinate, we can define the two components of the Berry connection [$\mathcal{A}_2$ has already been introduced in (34)]:

$$\mathcal{A}_1(q,t) = \mathrm{i}\langle u_{q,t}|\partial_q u_{q,t}\rangle, \quad \mathcal{A}_2(q,t) = \mathrm{i}\langle u_{q,t}|\partial_t u_{q,t}\rangle, \tag{49}$$

which constitute a vector with two real components. We also define the Berry curvature:

$$\Omega(q,t) = \begin{pmatrix}\partial_q\\ \partial_t\end{pmatrix} \times \begin{pmatrix}\mathcal{A}_1\\ \mathcal{A}_2\end{pmatrix} = \mathrm{i}\left(\langle\partial_q u_{q,t}|\partial_t u_{q,t}\rangle - \langle\partial_t u_{q,t}|\partial_q u_{q,t}\rangle\right) \tag{50}$$

which is a scalar and real quantity.

The expression (44) for the displacement Δx contains the derivative with respect to q of the geometrical phase

$$\Phi_{\rm geom}(q) = \int_0^T \mathcal{A}_2(q,t)\,\mathrm{d}t. \tag{51}$$

An integration by parts gives

$$\begin{aligned}
\frac{\mathrm{d}\Phi_{\rm geom}}{\mathrm{d}q} &= \mathrm{i}\frac{\mathrm{d}}{\mathrm{d}q}\left[\int_0^T \langle u_{q,t}|\partial_t u_{q,t}\rangle\,\mathrm{d}t\right]\\
&= \mathrm{i}\int\langle\partial_q u_{q,t}|\partial_t u_{q,t}\rangle\,\mathrm{d}t + \mathrm{i}\int\langle u_{q,t}|\partial_q\partial_t u_{q,t}\rangle\,\mathrm{d}t\\
&= \mathrm{i}\int\langle\partial_q u_{q,t}|\partial_t u_{q,t}\rangle\,\mathrm{d}t + \mathrm{i}\left[\langle u_{q,t}|\partial_q u_{q,t}\rangle\right]_0^T - \mathrm{i}\int\langle\partial_t u_{q,t}|\partial_q u_{q,t}\rangle\,\mathrm{d}t\\
&= \int_0^T \Omega(q,t)\,\mathrm{d}t,
\end{aligned} \tag{52}$$

where the fully-integrated term equals zero due to the time periodicity.

When using this result in the motion of the center of mass, we get

$$\Delta x = -\frac{a}{2\pi}\int_{-\pi/a}^{+\pi/a}\int_0^T \Omega(q,t)\,\mathrm{d}q\,\mathrm{d}t. \tag{53}$$

This expression is "robust" in the sense that the Berry curvature is gauge invariant. It does not present any singularity, in contrast with the expressions that use the Berry connection. We will come back to this point in paragraph 5. In particular, we will see that, due to the periodicity in q and t, the integral

$$\frac{1}{2\pi}\int_{-\pi/a}^{+\pi/a}\int_0^T \Omega(q,t)\,\mathrm{d}q\,\mathrm{d}t \tag{54}$$

is necessarily an integer, the Chern number, which is here equal to 1.

5 Adiabatic pump and Chern number

In the last part of this chapter, we present a general analysis of adiabatic pumps. We start by specifying the nature of the already mentioned singularities that can occur when calculating the Berry connection. We then present the adiabatic pump in the case of an arbitrary 1D lattice, seen as a two-dimensional problem, one of space and one of time. The notations that we find here will thus come back in the next chapters when investigating problems with two dimensions of space. We demonstrate in particular that the quantization of the pump is nothing else but the consequence of the existence of a Chern number. Note that another approach of the adiabatic pump resorts to the Floquet formalism. The interested reader can refer to the review article of Cooper, Dalibard, et al. (2018) and to the references therein.

5-1 The singularities of the Berry connection

In these lectures, we have used many times the representation of a state $|u_{q,t}^{(-)}\rangle$ on the Bloch sphere. This biunivocal representation is extremely useful to follow simple geometrical reasonings in terms of trajectory winding on the sphere. However it presents an ambiguity at two particular points, the north and south poles of the Bloch sphere, that are respectively reached for the latitudes $\theta_q = 0$ and $\theta_q = \pi$. The azimuthal angle ϕ_q (the longitude) is indeed not determined at these points, which can lead to the singularities that we discuss in the following.

We have previously chosen to express the state $|u_{q,t}\rangle$ in the eigenbasis of the operator $\hat{\sigma}_z$ with a positive real amplitude for the component along the vector $|+\rangle_z$. This has lead us to write

$$|u_{q,t}\rangle = \begin{pmatrix} \cos(\theta/2) \\ \mathrm{e}^{\mathrm{i}\phi}\,\sin(\theta/2) \end{pmatrix} \tag{55}$$

where the angles $\theta \equiv \theta_{q,t}$ and $\phi \equiv \phi_{q,t}$ are defined as

$$\cos\theta = \frac{\Delta_t}{\epsilon_{q,t}}, \qquad \mathrm{e}^{\mathrm{i}\phi}\sin\theta = \frac{J_t' + J\,\mathrm{e}^{\mathrm{i}qa}}{\epsilon_{q,t}}, \tag{56}$$

with

$$\epsilon_{q,t} = \left[\Delta_t^2 + J^2 + {J_t'}^2 + 2JJ_t'\cos(qa)\right]^{1/2} \tag{57}$$

and $\theta \in [0,\pi]$, which means that $\sin\theta \geq 0$. As long as the trajectory followed by (J_t', Δ_t) does not go through the central point $(J, 0)$, the definition (56) bears no ambiguity, except for a particular point, the pair (J', Δ) for which the south pole $\theta = \pi$ is reached. At that point, the state $|u_{q,t}\rangle$ is indeed

$$|u_{q,t}\rangle = \begin{pmatrix} 0 \\ \mathrm{e}^{\mathrm{i}\phi} \end{pmatrix} \tag{58}$$

but the phase ϕ cannot be determined from (56), since $\sin\theta = 0$ there.

This ambiguity is directly transfered to the Berry connection that we have defined in (49) for our two-dimensional problem (one dimension of space q and one of time t)

$$\boldsymbol{\mathcal{A}}(q,t) = \mathrm{i}\langle u_{q,t}|\boldsymbol{\nabla} u_{q,t}\rangle, \qquad \boldsymbol{\nabla} = \begin{pmatrix}\partial_q \\ \partial_t\end{pmatrix}. \tag{59}$$

A direct calculation gives

$$\boldsymbol{\mathcal{A}}(q,t) = -\boldsymbol{\nabla}\phi\,\sin^2(\theta/2) \tag{60}$$

which is singular at the south pole, where $\theta = \pi$. Note that at the north pole, ϕ is also undetermined, but the fact that $\sin^2(\theta/2) = 0$ washes out the singularity for $\boldsymbol{\mathcal{A}}$. This difference between the north and the south pole comes from the fact that the component of $|u_{q,t}\rangle$ along the vector $|+\rangle_z$ has been chosen real and positive, whereas the component along $|-\rangle_z$ is complex.

Let us examine this singularity from a general point of view. We denote as (q_0, t_0) a point where the south pole of the Bloch sphere is reached. We parametrize the vicinity of this point by

$$q = q_0 + \delta q, \qquad t = t_0 + \delta t, \tag{61}$$

and we consider a first-order power expansion around this point:

$$\mathrm{e}^{\mathrm{i}\phi} \sin\theta \approx \alpha\, \delta q + \beta\, \delta t, \tag{62}$$

where α, β are complex numbers that depend on the considered situation. The constraint $\sin\theta \geq 0$ leads to:

$$\mathrm{e}^{\mathrm{i}\phi} \approx \frac{\alpha\, \delta q + \beta\, \delta t}{|\alpha\, \delta q + \beta\, \delta t|}, \qquad \sin\theta \approx |\alpha\, \delta q + \beta\, \delta t|, \tag{63}$$

and thus

$$\cos\theta \approx -1 + \frac{1}{2}|\alpha\, \delta q + \beta\, \delta t|^2. \tag{64}$$

We then deduce the variation of the Berry connection around the singular point:

$$\boldsymbol{\mathcal{A}} \approx -\boldsymbol{\nabla}\phi \approx \gamma\, \frac{1}{|\alpha\, \delta q + \beta\, \delta t|^2} \begin{pmatrix} -\delta t \\ \delta q \end{pmatrix} \tag{65}$$

where we have introduced the real number

$$\gamma = \frac{\mathrm{i}}{2}\left(\alpha^* \beta - \alpha \beta^*\right). \tag{66}$$

The vector $\boldsymbol{\mathcal{A}}$ has a vortex structure around the singular point (q_0, t_0): it has an orthoradial direction and its modulus diverges as the inverse distance to the origin.

This divergence indeed appears for the adiabatic pump in the Rice–Mele model, as it can be seen in figure 24. This figure is drawn considering that the circular trajectory in the (J', Δ) plane of figure 2 is followed at uniform velocity. The south pole of the Bloch sphere is then reached for:

$$\text{Singularity at the south pole for:} \quad qa = \pm\pi,\ t = 3T/4, \tag{67}$$

since at these points we have

$$J' = J,\ \Delta < 0 \quad \Rightarrow \quad \cos\theta_q = \frac{\Delta}{\epsilon_q} = -1, \qquad \mathrm{e}^{\mathrm{i}\phi_q}\ \sin\theta_q = \frac{J' + J\,\mathrm{e}^{\mathrm{i}qa}}{\epsilon_q} = 0. \tag{68}$$

The geometrical phase $\Phi_{\mathrm{geom}}(q)$ and the Zak phase $\Phi_{\mathrm{Zak}}(t)$ (appendix 2) are then well-defined as long as they are not computed at $q = \pm\pi/a$ and $t = 3T/4$ respectively.

The divergence of the Berry connection that we just found depends on the choice of the gauge. We could have chosen to impose a real and positive component along the vector $|-\rangle_z$ instead of $|+\rangle_z$ by parametrizing the state $|u_{q,t}\rangle$ by

$$|\tilde{u}_{q,t}\rangle = \begin{pmatrix} \mathrm{e}^{-\mathrm{i}\phi}\, \cos(\theta/2) \\ \sin(\theta/2) \end{pmatrix} \tag{69}$$

and the new Berry connection $\tilde{\boldsymbol{\mathcal{A}}}$ would have been singular at the north pole of the Bloch sphere, that is for another pair $(\tilde{q}_0, \tilde{t}_0)$.

We have already mentioned that, contrary to the Berry connection, the Berry curvature defined in (50)

$$\boldsymbol{\Omega} = \boldsymbol{\nabla} \times \boldsymbol{\mathcal{A}} \tag{70}$$

is gauge invariant. The singularity that we have found for $\boldsymbol{\mathcal{A}}$ thus should not occur for $\boldsymbol{\Omega}$. We can demonstrate this statement starting from the previous power expansion. We have established in chapter 1 the general expression of $\boldsymbol{\Omega}$

$$\boldsymbol{\Omega} = -\frac{1}{2}\boldsymbol{\nabla}\phi \times \boldsymbol{\nabla}(\cos\theta) \tag{71}$$

which, at point (q_0, t_0), translates into

$$\boldsymbol{\Omega} \approx -\frac{\gamma}{2}\, \boldsymbol{u}_z, \tag{72}$$

and this expression is indeed regular. The computation for the adiabatic pump of the Rice–Mele model confirms this regularity (figure 24, bottom).

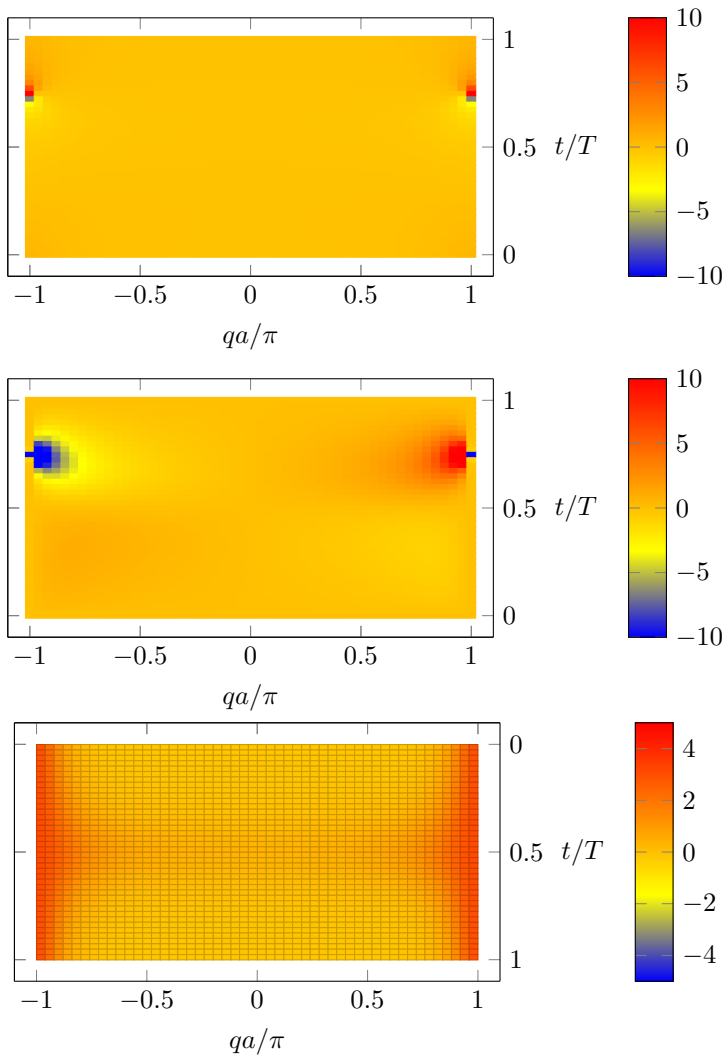

Figure 24. *Top and middle: the first and second components of the Berry connection $\boldsymbol{\mathcal{A}}(q,t)$ for the gauge chosen in the text. A singular point appears at time $t = 3T/4$ for $qa = \pm\pi$, because the state $|u_{q,t}\rangle$ reaches the south pole of the Bloch sphere. Bottom: the Berry curvature $\Omega(q,t)$ which is regular on the entire (q,t) plane. Its integral on the rectangle $[-\pi/a, \pi/a] \times [0,T]$ equals 2π, corresponding to a Chern number of 1.*

5-2 The current of an adiabatic pump

In the analysis presented in §3, we have used simple geometrical arguments obtained from the Rice–Mele Hamiltonian to determine the motion of the center of mass for a cloud of particles during one pumping cycle. We now establish a more general formalism that will allow us to emphasize the importance of the Berry curvature in these types of studies.

As previously, we start from an ensemble of non-interacting particles, and we suppose that the one-particle density operator is diagonal in the momentum basis. We can then calculate the flux of matter for a particle in a given Bloch state $|\psi_q\rangle$, and average the result over the momentum q.

We consider a particle prepared in the state of momentum q in the lowest band $n = 0$, and we look at one pumping cycle, during which some parameters that characterize the lattice (J' and Δ for the Rice–Mele model) vary slowly. The state of the particle at a given time can be written at first order of the adiabatic approximation (*cf.* chapter 1):

$$|\Psi(t)\rangle \approx |\psi^{(0)}\rangle + \mathrm{i}\hbar \sum_{n\neq 0} |\psi^{(n)}\rangle \, \frac{\langle\psi^{(n)}|\partial_t \psi^{(0)}\rangle}{E^{(n)} - E^{(0)}} + \dots . \tag{73}$$

In order to have simple notations, we have not explicitly indicated the dependence in q and t of the Bloch functions and of the energies:

$$|\psi^{(n)}\rangle \equiv |\psi^{(n)}_{q,t}\rangle, \qquad E^{(n)} \equiv E^{(n)}_{q,t}. \tag{74}$$

We want to calculate the average velocity in this state, at the lowest order. The velocity operator is

$$\hat{v} = \frac{\hat{p}}{m} \qquad \text{with} \quad \hat{p} = -\mathrm{i}\hbar \frac{\mathrm{d}}{\mathrm{d}x} \tag{75}$$

and we will thus need to determine matrix elements of type

$$\langle\psi^{(0)}| \, \hat{p} \, |\psi^{(n)}\rangle. \tag{76}$$

In general it is more convenient to work with the periodic functions $|u^{(n)}\rangle$ rather than with the Bloch functions $|\psi^{(n)}\rangle$ themselves. Going from one family of function to the other can be done by using

$$\hat{p}\left(\mathrm{e}^{\mathrm{i}qx} u^{(n)}_{q,t}(x)\right) = \mathrm{e}^{\mathrm{i}qx} \, (\hat{p} + \hbar q) \, u^{(n)}_{q,t}(x) \tag{77}$$

so that the matrix element (76) can be written as

$$\langle\psi^{(0)}|\,\hat{p}\,|\psi^{(n)}\rangle = \langle u^{(0)}|\,(\hat{p}+\hbar q)\,|u^{(n)}\rangle. \tag{78}$$

The average momentum in the state $|\Psi(t)\rangle$ is then, still at order 1 of the adiabatic approximation

$$\begin{aligned}\langle\Psi(t)|\,\hat{p}\,|\Psi(t)\rangle &= \langle u^{(0)}|\,(\hat{p}+\hbar q)\,|u^{(0)}\rangle \\ &+ \mathrm{i}\hbar\sum_{n\neq 0}\langle u^{(0)}|\,(\hat{p}+\hbar q)\,|u^{(n)}\rangle\,\frac{\langle u^{(n)}|\partial_t u^{(0)}\rangle}{E^{(n)}-E^{(0)}} + \text{c.c.}\end{aligned} \tag{79}$$

To move forward, we need the following lemmas, that are proven in appendix 3:

$$\langle u^{(0)}|(\hat{p}+\hbar q)|u^{(n)}\rangle = \frac{m}{\hbar}(E^{(0)}-E^{(n)})\,\langle\partial_q u^{(0)}|u^{(n)}\rangle. \tag{80}$$

and

$$\langle u^{(0)}|(\hat{p}+\hbar q)|u^{(0)}\rangle = \frac{m}{\hbar}\partial_q E^{(0)}. \tag{81}$$

By using a closure relation in the second line of (79), we obtain:

$$v_{q,t} \equiv \langle\Psi(t)|\,\frac{\hat{p}}{m}\,|\Psi(t)\rangle = \frac{1}{\hbar}\partial_q E^{(0)} - \left(\mathrm{i}\langle\partial_q u^{(0)}|\partial_t u^{(0)}\rangle + \text{c.c.}\right). \tag{82}$$

This mean velocity has two components:

- The first one, $\frac{1}{\hbar}\partial_q E^{(0)}$ is the group velocity. When taking its average over all q states and assuming that they are equally populated, we find a zero velocity due to the periodicity in q (at every time t) of the energy band $E^{(0)}_{q,t}$.
- The second contribution is (up to a minus sign) the Berry curvature that we introduced in (50):

$$\Omega_{q,t} = \mathrm{i}\left(\langle\partial_q u^{(0)}|\partial_t u^{(0)}\rangle - \langle\partial_t u^{(0)}|\partial_q u^{(0)}\rangle\right). \tag{83}$$

For a uniform population of the momenta q, the average velocity over all these momenta is thus at time t:

$$\bar{v}_t = -\frac{a}{2\pi}\int_{\mathrm{ZB}}\Omega_{q,t}\,\mathrm{d}q \tag{84}$$

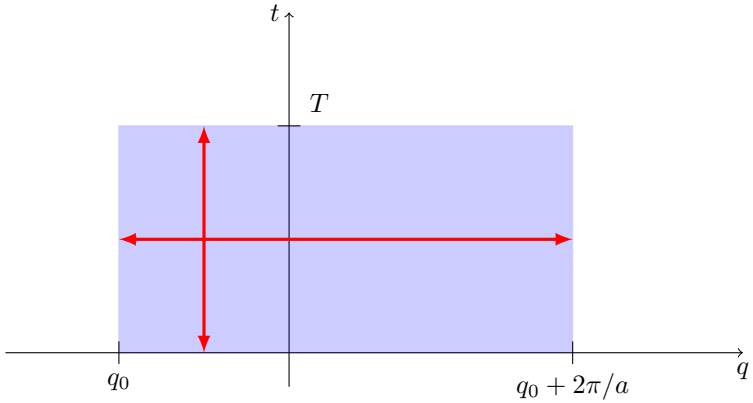

Figure 25. *Two-dimensional diagram of the (q,t) space: with the momentum on the horizontal axis and time on the vertical axis. The gray area represents the integration zone of (86), and the Berry curvature $\Omega_{q,t}$ is periodic in q with period $2\pi/a$ and periodic in t with period T.*

where a is the spatial period of the potential and $2\pi/a$ thus represents the size of the Brillouin zone.

The average displacement during a pumping cycle of duration T is obtained by integrating this velocity:

$$\Delta x = -\frac{a}{2\pi}\int_0^T\!\!\int_{\mathrm{ZB}}\Omega_{q,t}\,\mathrm{d}q\,\mathrm{d}t, \tag{85}$$

and we recover the result that we found for the Rice–Mele model with equation (53). The advantage of this derivation is that it does not need to resort to the Berry connection, which can be singular as we have seen, and relies entirely on the notion of Berry curvature, which is regular.

5-3 Chern number and quantization of the pumping

We now establish the quantization of the displacement Δx, which is only a particular case of the fact that

$$\mathcal{C} = \frac{1}{2\pi} \int_0^T \int_{q_0}^{q_0+2\pi/a} \Omega_{q,t} \, \mathrm{d}q \, \mathrm{d}t \tag{86}$$

is always an integer if Ω is a Berry curvature and if the integral is taken on a rectangular domain with periodic boundary conditions (figure 25):

- The periodicity of the Brillouin zone ensures that the Hamiltonian and its eigenstates are the same for momentum q_0 and momentum $q_0 + 2\pi/a$;
- The temporal periodicity of the pump ensures that the Hamiltonian and its eigenstates are the same at time $t = 0$ and at time $t = T$.

To prove that $\mathcal{C}$ is an integer, we recall that the Berry curvature $\Omega_{q,t}$ is defined from the Berry connection $\boldsymbol{\mathcal{A}}_{q,t}$ by

$$\boldsymbol{\nabla} \times \boldsymbol{\mathcal{A}}_{q,t} = \Omega \boldsymbol{u}_z. \tag{87}$$

One could consider applying Stokes' theorem, which links the surface integral of Ω and the integral of $\boldsymbol{\mathcal{A}}$ along the border of the rectangle of figure 26. However, some precautions have to be taken, again due to possible singularities of $\boldsymbol{\mathcal{A}}_{q,t}$ at one or several points q_j, t_j of the considered rectangle.

Let us suppose that there is only one such point, denoted as $S = (q_1, t_1)$ (one can easily generalize the result to several points). We consider the path that follows the border of the rectangle and dives inside this rectangle to avoid the singular point S (figure 26). The excluded region around S does not change the surface integral of Ω, since this function is regular. We then have

$$\iint \Omega_{q,t} \, \mathrm{d}q \, \mathrm{d}t = \left(\oint_{\text{rectangle}} + \oint_{\text{cercle}} \right) \boldsymbol{\mathcal{A}}_{q,t} \cdot \mathrm{d}\boldsymbol{l}, \tag{88}$$

where the excluded circle has an infinitesimal size.

Due to the periodicity in q and t of the problem, the contribution of the sides of the rectangle cancel out. We are left on the right-hand side with the

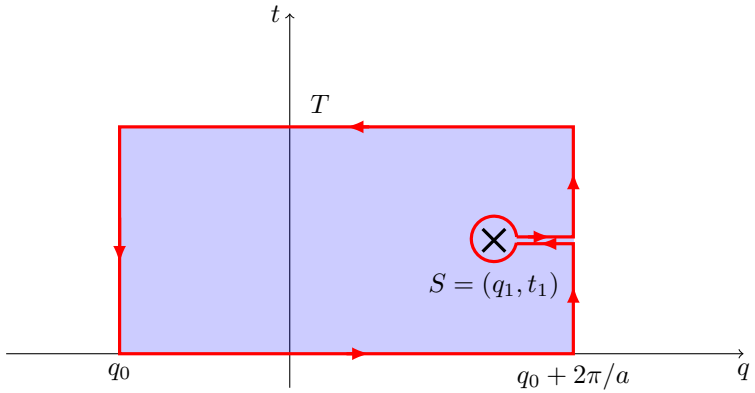

Figure 26. *The integration line used in (88) to avoid the singularity in $S = (q_1, t_1)$. The contribution of the straight parts cancel out because of the periodicity of $\mathcal{A}_{q,t}$. The contribution of the small circle is $\pm 2\pi$.*

contribution of the small circle, centered on the singular point S. We have seen that, around such a point, the Berry connection has a vortex structure, with

$$\boldsymbol{\mathcal{A}}_{q,t} \approx -\boldsymbol{\nabla}\phi \tag{89}$$

such that the line integral of $\boldsymbol{\mathcal{A}}$ along the small circle equals $\pm 2\pi$, with a sign that depends on the direction of the vortex (the sign of the coefficient γ introduced in (66)). In the case of a single singular point, we get

$$\iint \Omega_{q,t} \, \mathrm{d}q \, \mathrm{d}t = \pm 2\pi, \tag{90}$$

which is the expected result. In the case of multiple singular points, their contributions add up independently and algebraically, so that we obtain:

$$\iint \Omega_{q,t} \, \mathrm{d}q \, \mathrm{d}t \; = \; 2\pi(N_+ - N_-). \tag{91}$$

In any case, we find that $\mathcal{C}$ is an integer and the displacement during a pumping cycle is quantized in units of the spatial period a.

Appendix 1: Double cell and folded bands

It may happen that one needs to determine the bands of a periodic Hamiltonian with a non-optimal definition of the unit cell. For example, instead of seeing in figure 3 that the unit cell has a size $\lambda/2$, one could have chosen λ as the period of the potential (top of figure 27). While this statement is not wrong, it does not optimally use the functional form of the potential. With such a choice of the periodicity, the Brillouin zone is divided by two:

$$\begin{aligned} \text{Unit cell of period } \lambda/2 \quad &\rightarrow \quad \text{Brillouin zone: } q \in [-k, k[\\ \text{Unit cell of period } \lambda \quad &\rightarrow \quad \text{Brillouin zone: } q \in [-k/2, k/2[\end{aligned}$$

and one obtains the energy spectrum represented in figure 27, on the right. We can compare it to the left of the figure, where the spectrum already shown in figure 4 has been reproduced, and where the outer parts of the Brillouin zone have been shaded. We see that these parts are simply folded in the new Brillouin zone, and the overall spectrum is the same. However, for each value q of the new Brillouin zone, the number of eigenstates ψ_q has doubled since we now have the old states ψ_q and $\psi_{q\pm k}$.

Appendix 2. The adiabatic pump and the Zak phase

In section 3, we have drawn the link between the displacement Δx of the center of mass during a pumping cycle, the geometrical phase $\Phi_{\text{geom}}(q)$ and the Berry curvature $\Omega(q,t)$. It is also possible to link Δx to the Zak phase $\Phi_{\text{Zak}}(t)$ calculated for each time t of the pumping cycle:

$$\Phi_{\text{Zak}}(t) = \int_{-\pi/a}^{+\pi/a} \mathcal{A}_1(q,t)\, \mathrm{d}q. \tag{92}$$

The starting point is the relation:

$$\frac{\mathrm{d}\Phi_{\text{Zak}}}{\mathrm{d}t} = \mathrm{i}\frac{\mathrm{d}}{\mathrm{d}t}\left[\int_{-\pi/a}^{+\pi/a} \langle u_{q,t}|\partial_q u_{q,t}\rangle\, \mathrm{d}t\right] = -\int_{-\pi/a}^{+\pi/a} \Omega(q,t)\, \mathrm{d}q. \tag{93}$$

This expression is valid as long as the singularity at the south pole is avoided, thus for $t \neq 3T/4$.

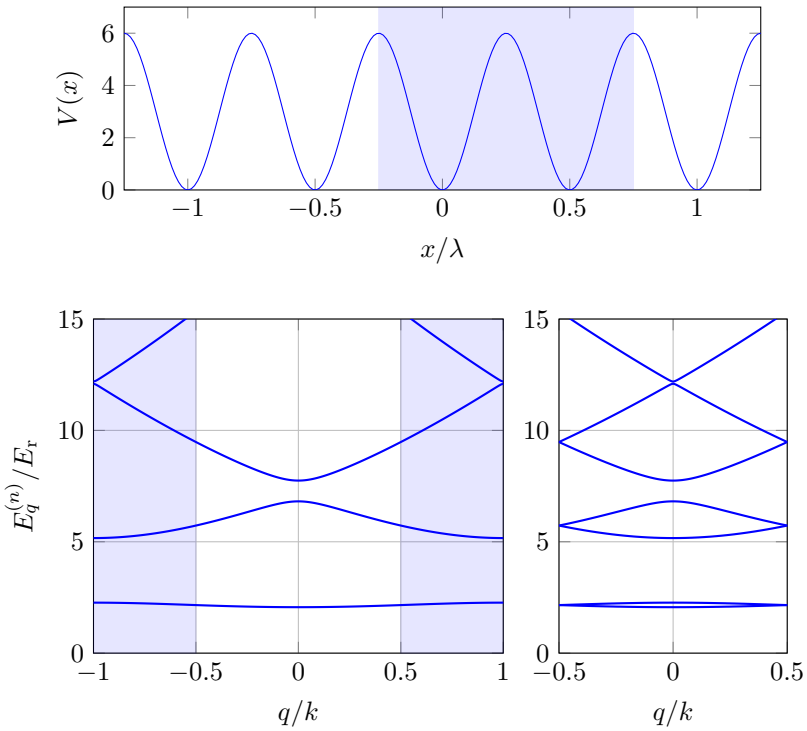

Figure 27. *Top: The "non-optimal" unit cell of size λ, for the sinusoidal potential of period $\lambda/2$. Bottom: the folding of the band spectrum when the size of the unit cell is chosen to be equal to λ (on the right) instead of $\lambda/2$ (on the left).*

With this expression, one can write the displacement Δx as:

$$\Delta x = \frac{a}{2\pi}\int_0^T \frac{\mathrm{d}\Phi_{\mathrm{Zak}}}{\mathrm{d}t}\,\mathrm{d}t = \frac{a}{2\pi}\left[\Phi_{\mathrm{Zak}}(T) - \Phi_{\mathrm{Zak}}(0)\right]. \tag{94}$$

To give a meaning to this expression, as for the geometrical phase, we need to follow continuously the evolution of the Zak phase when t goes from 0 to T. This can be done from the evolution of the corresponding paths on the Bloch sphere, as shown in figure 28, and we recover the previous result $\Delta x = -a$.

Appendix 3. Proof of the lemmas (80-81)

We prove here these lemmas in an arbitrary dimension, since they will also be useful for two-dimensional problems. We show that

$$\langle u^{(0)}|(\hat{\boldsymbol{p}} + \hbar\boldsymbol{q})|u^{(n)}\rangle = \frac{m}{\hbar}(E^{(0)} - E^{(n)})\,\langle \boldsymbol{\nabla}_{\boldsymbol{q}} u^{(0)}|u^{(n)}\rangle. \tag{95}$$

and

$$\langle u^{(0)}|(\hat{\boldsymbol{p}} + \hbar\boldsymbol{q})|u^{(0)}\rangle = \frac{m}{\hbar}\,\boldsymbol{\nabla}_{\boldsymbol{q}} E^{(0)}. \tag{96}$$

One can also refer to the very complete review article of Xiao, Chang, et al. (2010).

We recall that the periodic functions $u^{(n)}$ verify the eigenvalue equation (*cf.* chapter 1):

$$\hat{H}_{\boldsymbol{q}}|u_{\boldsymbol{q}}^{(n)}\rangle = E_{\boldsymbol{q}}^{(n)}\,|u_{\boldsymbol{q}}^{(n)}\rangle \qquad \text{with} \quad \hat{H}_{\boldsymbol{q}} = \frac{(\hat{\boldsymbol{p}} + \hbar\boldsymbol{q})^2}{2m} + V(\boldsymbol{r}). \tag{97}$$

By taking its scalar product with $\langle u_{\boldsymbol{q}}^{(0)}|$, we get:

$$\langle u_{\boldsymbol{q}}^{(0)}|\hat{H}_{\boldsymbol{q}}|u_{\boldsymbol{q}}^{(n)}\rangle = E_{\boldsymbol{q}}^{(n)}\,\delta_{n,0}. \tag{98}$$

This equation is verified for all $\boldsymbol{q}$. We can then take the gradient with respect to $\boldsymbol{q}$ of the two sides of the equality:

$$\langle \boldsymbol{\nabla}_{\boldsymbol{q}} u_{\boldsymbol{q}}^{(0)}|\hat{H}_{\boldsymbol{q}}|u_{\boldsymbol{q}}^{(n)}\rangle + \langle u_{\boldsymbol{q}}^{(0)}|\boldsymbol{\nabla}_{\boldsymbol{q}}\hat{H}_{\boldsymbol{q}}|u_{\boldsymbol{q}}^{(n)}\rangle + \langle u_{\boldsymbol{q}}^{(0)}|\hat{H}_{\boldsymbol{q}}|\boldsymbol{\nabla}_{\boldsymbol{q}} u_{\boldsymbol{q}}^{(n)}\rangle = \left(\boldsymbol{\nabla}_{\boldsymbol{q}} E_{\boldsymbol{q}}^{(n)}\right)\delta_{n,0}. \tag{99}$$

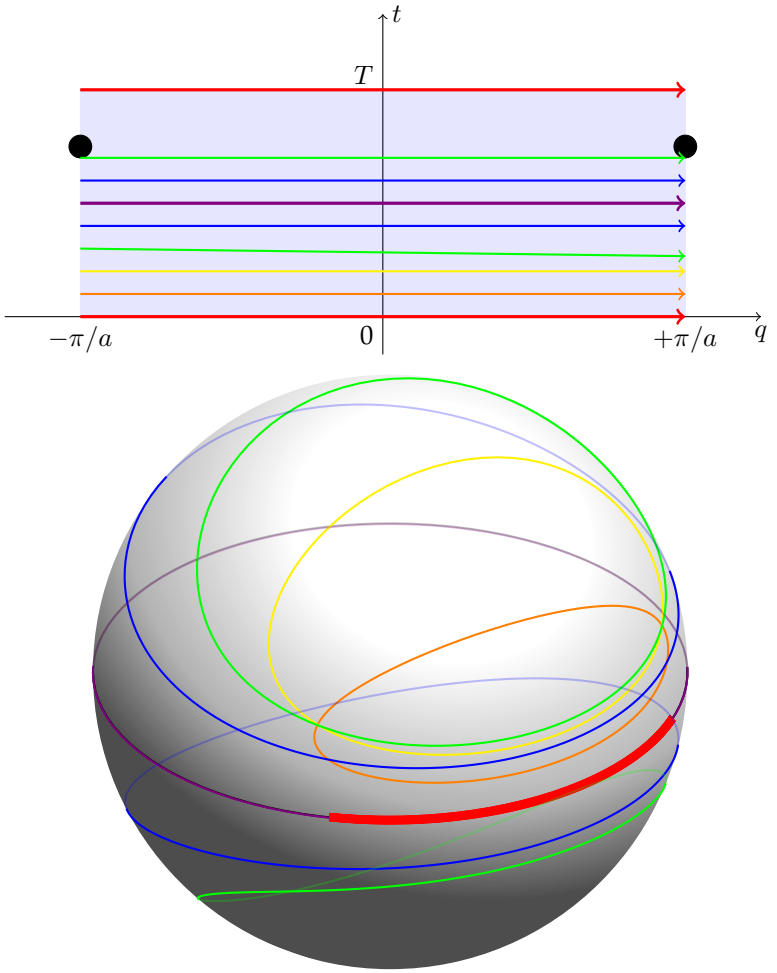

Figure 28. *The trajectories followed at a given time when q goes through the Brillouin zone. The Zak phase $\Phi_{\mathrm{Zak}}(t)$ is given, up to a factor 1/2, by the solid angle defined by the corresponding trajectory. We have chosen a circular path centered on (1,0) and with a radius 0.5 in the $(J'/J,\,\Delta)$ plane. The two small black disks indicate the point where the south pole is reached, which corresponds to a singularity in the definition of the azimuthal angle $\phi_{q,t}$ for the state $|u_{q,t}\rangle$.*

We have

$$\boldsymbol{\nabla}_{\boldsymbol{q}}\hat{H}_{\boldsymbol{q}} = \frac{\hbar}{m}(\hat{\boldsymbol{p}} + \hbar\boldsymbol{q}) \tag{100}$$

which is precisely the operator that appears in the matrix element (78).

For $n \neq 0$, we deduce from (99):

$$E^{(n)}_{\boldsymbol{q}}\,\langle \boldsymbol{\nabla}_{\boldsymbol{q}} u^{(0)}_{\boldsymbol{q}} | u^{(n)}_{\boldsymbol{q}}\rangle + \frac{\hbar}{m}\langle u^{(0)}_{\boldsymbol{q}} | (\hat{\boldsymbol{p}} + \hbar\boldsymbol{q}) | u^{(n)}_{\boldsymbol{q}}\rangle + E^{(0)}_{\boldsymbol{q}}\langle u^{(0)}_{\boldsymbol{q}} | \boldsymbol{\nabla}_{\boldsymbol{q}} u^{(n)}_{\boldsymbol{q}}\rangle = 0 \tag{101}$$

which we associate to

$$\langle u^{(0)}_{\boldsymbol{q}} | u^{(n)}_{\boldsymbol{q}}\rangle = \delta_{n,0} \quad \Rightarrow \quad \langle \boldsymbol{\nabla}_{\boldsymbol{q}} u^{(0)}_{\boldsymbol{q}} | u^{(n)}_{\boldsymbol{q}}\rangle + \langle u^{(0)}_{\boldsymbol{q}} | \boldsymbol{\nabla}_{\boldsymbol{q}} u^{(n)}_{\boldsymbol{q}}\rangle = 0 \tag{102}$$

to find the result (95)

$$\frac{\hbar}{m}\langle u^{(0)}_{\boldsymbol{q}} | (\hat{\boldsymbol{p}} + \hbar\boldsymbol{q}) | u^{(n)}_{\boldsymbol{q}}\rangle = (E^{(0)}_{\boldsymbol{q}} - E^{(n)}_{\boldsymbol{q}})\,\langle \boldsymbol{\nabla}_{\boldsymbol{q}} u^{(0)}_{\boldsymbol{q}} | u^{(n)}_{\boldsymbol{q}}\rangle. \tag{103}$$

For $n = 0$, we put together (99) and (102) to find

$$\frac{\hbar}{m}\langle u^{(0)}_{\boldsymbol{q}} | (\hat{\boldsymbol{p}} + \hbar\boldsymbol{q}) | u^{(0)}_{\boldsymbol{q}}\rangle = \boldsymbol{\nabla}_{\boldsymbol{q}} E^{(0)}_{\boldsymbol{q}}, \tag{104}$$

which is the result (96).

Chapter IV

Topology and Berry curvature in a 2D lattice

After having devoted the first part of this course to one-dimensional problems, we now turn to the study of topological systems in two dimensions. Let us recall that this two-dimensional geometry has played a major role in the emergence of topological concepts in physics, with the discovery of the quantum Hall effect in electron gases confined in quantum wells. It allows the characterization of topological phases by their transport properties, which was not directly possible in 1D. Moreover, it gives rise to topological numbers (Chern indices) that are more "robust" than the Zak phase which is dependent on the chosen parameterization for a given physical problem.

In this chapter, we will consider an isolated energy band and we will ask ourselves the question of the topology of this band. We will give two types of answers. The first one will be mathematical and directly inspired by what we have understood for the geometrical pumps concerning the coverage of the Bloch sphere. The second answer will be physical and will be about the transport properties that we can expect for these systems. Of course, both types of answers will lead to the same characterization. In Chapter 5, we will complete these two answers with a third one, dealing with the existence of edge channels.

To simplify our analysis, we will mainly study discrete systems with tunnel couplings only allowing hoppings between neighbouring sites. This will enable us to use the tight-binding approximation and to carry out almost all calculations analytically. As we have done in one dimension, we will also try to work with the simplest geometries that allow the appearance of a non-trivial topology. As in 1D, this leads to consider a lattice with two possible sites per unit cell. This type of lattice naturally leads to the emergence of Dirac points in a 2D geometry, and we will therefore start our study with this notion, before moving on to the characterization of the topology.

1 Bipartite lattices and Dirac points

In this first part, we will recall some important characteristics of regular two-dimensional lattices. We will start with a brief description of the triangular and square lattices in the tight-binding model. These two lattices have only one site per unit cell, thus only one energy band in the tight-binding approximation. Therefore, they cannot spontaneously lead to topological bands, except in the presence of an external gauge field, as we will see in Chapter 6.

We will then move on to the graphene-like hexagonal lattice; this lattice has two sites per unit cell, like the SSH and RM models we have studied in one dimension. We obtain *a priori* two energy bands in the tight-binding limit, which is favorable for the search of topological effects. We will discuss in particular the Dirac points of the standard graphene lattice, which will play a crucial role in the emergence of these topological properties. We will also give some illustrations of the realization of this lattice in photonics

and with cold atoms.

1-1 Triangular and square lattices

In two dimensions, the simplest regular lattices are triangular or square. In cold atom physics, the triangular lattice can be obtained by letting three identical coplanar light waves interfere with a 120 degrees angle between each other, and with their polarization perpendicular to the plane. The maxima[1] of intensity form a triangular lattice of points A_j, with a distance between nearest neighbours equal to $a = 2\lambda/3$. Atoms will get trapped if the light frequency is lower than the resonance frequency of the atoms. The square lattice can be generated by two orthogonal pairs of standing waves, with a distance $a = \lambda/2$ between two adjacent sites.

These two types are Bravais lattices, i.e. we can generate the whole lattice by translating a unit cell with only one site by

$$\boldsymbol{r_j} = j_1\boldsymbol{a}_1 + j_2\boldsymbol{a}_2, \quad j_1, j_2 \in \mathbb{Z} \tag{1}$$

where the vectors $\boldsymbol{a}_1$ and $\boldsymbol{a}_2$ are shown in figure 1.

Let us consider a Hamiltonian where only hoppings between nearest neighbours are allowed, with a tunnelling matrix element denoted $-J$ as in the previous chapters. Bloch's theorem indicates that we can search for Bloch states in the form

$$|\psi_{\boldsymbol{q}}\rangle = \sum_{\boldsymbol{j}} \mathrm{e}^{\mathrm{i}\boldsymbol{q}\cdot\boldsymbol{r}_j}|A_{\boldsymbol{j}}\rangle \tag{2}$$

with a single periodic function on the lattice

$$|u_{\boldsymbol{q}}\rangle = \sum_{\boldsymbol{j}} |A_{\boldsymbol{j}}\rangle. \tag{3}$$

and a single energy band[2] . The function $|u_{\boldsymbol{q}}\rangle$ is thus real and in fact independent of $\boldsymbol{q}$. Our experience from the previous chapters on the 1D case tells us that we cannot expect to observe any non-trivial topology in this one-band model.

[1] If one wishes to have trapping at the minima of intensity while keeping a triangular lattice, one must orient the polarizations in the plane of the beams.

[2] The energy associated with the $|\psi_{\boldsymbol{q}}\rangle$ state is $-2J\left[\cos(\boldsymbol{q}\cdot\boldsymbol{a}_1) + \cos(\boldsymbol{q}\cdot\boldsymbol{a}_2) + \cos(\boldsymbol{q}\cdot(\boldsymbol{a}_1 - \boldsymbol{a}_2)\right]$ for the triangular lattice and $-2J\left[\cos(\boldsymbol{q}\cdot\boldsymbol{a}_1) + \cos(\boldsymbol{q}\cdot\boldsymbol{a}_2)\right]$ for the square lattice.

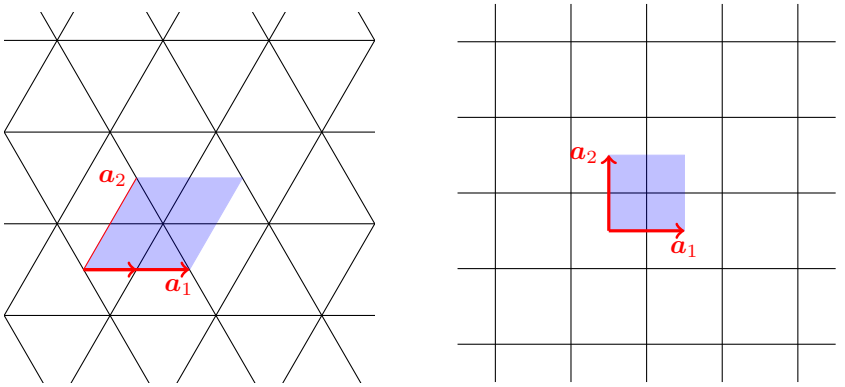

Figure 1. *Triangular lattice and square lattice. The shaded area indicates a possible unit cell.*

1-2 The hexagonal lattice "graphene"

To obtain a situation that generalizes the one studied in one dimension with the SSH model and the Rice–Mele model, we need to move to a lattice with (at least) two sites per unit cell. This naturally leads to a parameterization of the quasi-momentum eigenstates given by a pseudo-spin 1/2. The corresponding topology can then be understood by examining the position of this pseudo-spin on the Bloch sphere. The best known lattice of this type is the hexagonal lattice shown in figure 2.

The unit cell of this lattice has indeed two sites noted A and B, separated by the distance a and corresponding respectively to the bottom and the top of each vertical link. The tunnel coupling, limited to the nearest neighbours, can make a particle jump from a site A to three possible sites B, namely the one of the same cell and the two sites B from the cells shifted respectively by $-\boldsymbol{a}_1$ and $-\boldsymbol{a}_2$ with

$$\boldsymbol{a}_1 = \frac{\sqrt{3}}{2}a\begin{pmatrix}1\\ \sqrt{3}\end{pmatrix} \qquad \boldsymbol{a}_2 = \frac{\sqrt{3}}{2}a\begin{pmatrix}-1\\ \sqrt{3}\end{pmatrix}. \tag{4}$$

In momentum space $\boldsymbol{q}$, the Brillouin zone also has a hexagonal structure, and the reciprocal lattice is generated by the two vectors $\boldsymbol{b}_1$ and $\boldsymbol{b}_2$ defined

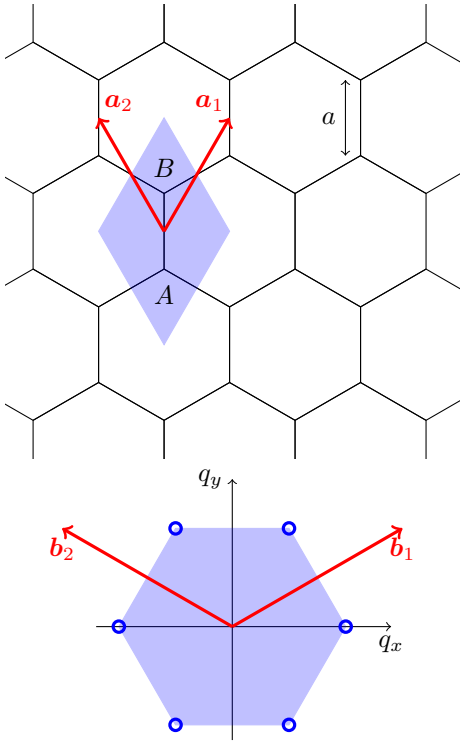

Figure 2. *Top: the hexagonal lattice and its unit cell of area $(3\sqrt{3}/2)a^2$. Bottom: the corresponding Brillouin zone of area $8\pi^2/(3\sqrt{3}a^2)$. The Dirac points are marked by blue circles.*

by [3] $\boldsymbol{a}_i \cdot \boldsymbol{b}_j = 2\pi\,\delta_{i,j}$:

$$\boldsymbol{b}_1 = \frac{2\pi}{3a}\begin{pmatrix}\sqrt{3}\\ 1\end{pmatrix} \qquad \boldsymbol{b}_2 = \frac{2\pi}{3a}\begin{pmatrix}-\sqrt{3}\\ 1\end{pmatrix}. \tag{6}$$

We can look for the eigenstates of this Hamiltonian in the Bloch form $\psi_{\boldsymbol{q}}(\boldsymbol{r}) = \mathrm{e}^{\mathrm{i}\boldsymbol{q}\cdot\boldsymbol{r}}\,u_{\boldsymbol{q}}(\boldsymbol{r})$ where $u_{\boldsymbol{q}}(\boldsymbol{r})$ is periodic on the lattice. This periodic function is written in the tight-binding limit considered here [*cf.* chapter 1]:

$$|u_{\boldsymbol{q}}\rangle = \alpha_{\boldsymbol{q}}\left(\sum_{\boldsymbol{j}}|A_{\boldsymbol{j}}\rangle\right) + \beta_{\boldsymbol{q}}\left(\sum_{\boldsymbol{j}}|B_{\boldsymbol{j}}\rangle\right), \quad |\alpha_{\boldsymbol{q}}|^2 + |\beta_{\boldsymbol{q}}|^2 = 1, \tag{7}$$

which amounts, as announced, to parametrize $|u_{\boldsymbol{q}}\rangle$ as a pseudo-spin 1/2:

$$|u_{\boldsymbol{q}}\rangle \equiv \begin{pmatrix}\alpha_{\boldsymbol{q}}\\ \beta_{\boldsymbol{q}}\end{pmatrix}. \tag{8}$$

With these notations, the Bloch state $|\psi_{\boldsymbol{q}}\rangle$ is given by

$$|\psi_{\boldsymbol{q}}\rangle = \sum_{\boldsymbol{j}}\mathrm{e}^{i\,\boldsymbol{q}\cdot\boldsymbol{r}_{\boldsymbol{j}}}\left(\alpha_{\boldsymbol{q}}|A_{\boldsymbol{j}}\rangle + \beta_{\boldsymbol{q}}|B_{\boldsymbol{j}}\rangle\right). \tag{9}$$

The Bloch state $|\psi_{\boldsymbol{q}}\rangle$ is the eigenstate of the Hamiltonian that describes a tunnel coupling with the eigenvalue $E_{\boldsymbol{q}}$, which is translated in terms of the pseudo-spin:

$$\hat{H}_{\boldsymbol{q}}\begin{pmatrix}\alpha_{\boldsymbol{q}}\\ \beta_{\boldsymbol{q}}\end{pmatrix} = E_{\boldsymbol{q}}\begin{pmatrix}\alpha_{\boldsymbol{q}}\\ \beta_{\boldsymbol{q}}\end{pmatrix} \tag{10}$$

where we have introduced the 2×2 matrix

$$\hat{H}_{\boldsymbol{q}} = \begin{pmatrix}E_A & -J\left(1+\mathrm{e}^{-\mathrm{i}\boldsymbol{q}\cdot\boldsymbol{a}_1}+\mathrm{e}^{-\mathrm{i}\boldsymbol{q}\cdot\boldsymbol{a}_2}\right)\\ -J\left(1+\mathrm{e}^{\mathrm{i}\boldsymbol{q}\cdot\boldsymbol{a}_1}+\mathrm{e}^{\mathrm{i}\boldsymbol{q}\cdot\boldsymbol{a}_2}\right) & E_B\end{pmatrix}. \tag{11}$$

For the moment, we assume that the two sites A and B are equivalent, and thus have the same energy. By convention we will set

$$E_A = E_B = 0 \tag{12}$$

so that $\hat{H}_{\boldsymbol{q}}$ can be written in terms of the Pauli matrices $\hat{\sigma}_i$, $i = x, y, z$:

$$\hat{H}_{\boldsymbol{q}} = -\boldsymbol{h}(\boldsymbol{q})\cdot\hat{\boldsymbol{\sigma}}, \qquad h_x(\boldsymbol{q}) + \mathrm{i}h_y(\boldsymbol{q}) = J\left(1+\mathrm{e}^{\mathrm{i}\boldsymbol{q}\cdot\boldsymbol{a}_1}+\mathrm{e}^{\mathrm{i}\boldsymbol{q}\cdot\boldsymbol{a}_2}\right), \tag{13}$$

or

$$\boldsymbol{h}(\boldsymbol{q}) = \begin{pmatrix}1+\cos(\boldsymbol{q}\cdot\boldsymbol{a}_1)+\cos(\boldsymbol{q}\cdot\boldsymbol{a}_2)\\ \sin(\boldsymbol{q}\cdot\boldsymbol{a}_1)+\sin(\boldsymbol{q}\cdot\boldsymbol{a}_2)\\ 0\end{pmatrix} \tag{14}$$

[3] We adopt here the general definition

$$\boldsymbol{b}_1 = 2\pi\frac{\mathcal{R}\boldsymbol{a}_2}{\boldsymbol{a}_1\cdot(\mathcal{R}\boldsymbol{a}_2)}, \qquad \boldsymbol{b}_2 = 2\pi\frac{\mathcal{R}\boldsymbol{a}_1}{\boldsymbol{a}_2\cdot(\mathcal{R}\boldsymbol{a}_1)} \tag{5}$$

where $\mathcal{R}$ denotes the rotation of $\pi/2$.

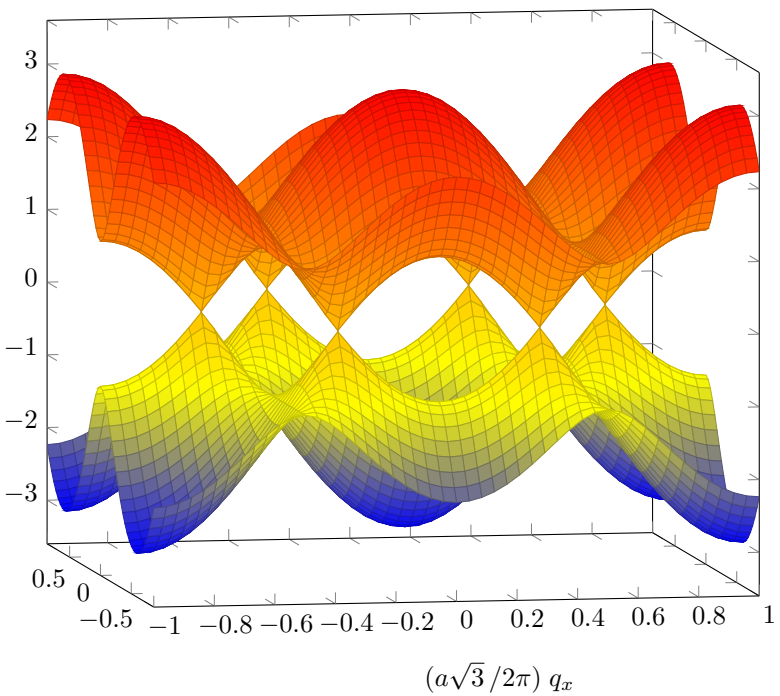

Figure 3. *Band structure of the hexagonal lattice.*

The eigenenergies of this Hamiltonian are

$$E_{\boldsymbol{q}}^{(\pm)} = \pm|\boldsymbol{h}(\boldsymbol{q})| = \pm J\,|1 + \mathrm{e}^{\mathrm{i}\boldsymbol{q}\cdot\boldsymbol{a}_1} + \mathrm{e}^{\mathrm{i}\boldsymbol{q}\cdot\boldsymbol{a}_2}| \tag{15}$$

which we will now discuss. The two corresponding eigenstates, $|u_{\boldsymbol{q}}^{(\pm)}\rangle$, are localized on the equator of the Bloch sphere since the vector $\boldsymbol{h}$ is itself localized in the xy plane.

1-3 The Dirac points

The band structure (15) is well known, in particular from studies on graphene (Castro Neto, Guinea, et al. 2009), and is shown in figure 3. The two energy bands $E_{\boldsymbol{q}}^{(\pm)}$ are not disjoint, but touch at particular $\boldsymbol{q}$ values, the Dirac points, which are the solutions of

$$1 + \mathrm{e}^{\mathrm{i}\boldsymbol{q}\cdot\boldsymbol{a}_1} + \mathrm{e}^{\mathrm{i}\boldsymbol{q}\cdot\boldsymbol{a}_2} = 0. \tag{16}$$

The first Brillouin zone has a hexagonal structure and a Dirac point sits at each of the six vertices of the hexagon (figure 2, bottom). Since each vertex is itself on the boundary of three hexagons, there are two Dirac points/Brillouin zone[4],

$$\boldsymbol{q} = \boldsymbol{Q}_\pm \qquad \text{with} \quad \boldsymbol{Q}_\pm = \pm\frac{4\pi}{3\sqrt{3}\,a}\begin{pmatrix}1\\0\end{pmatrix}. \tag{17}$$

The name "Dirac point" comes from the fact that the dispersion relation in the neighbourhood of $\boldsymbol{Q}_\pm$ is that of a relativistic quantum particle in dimension 2. By defining $\tilde{\boldsymbol{q}} = \boldsymbol{q} - \boldsymbol{Q}_\pm$, the Hamiltonian takes the Dirac form

$$\hat{H}_{\boldsymbol{q}}^{(\pm)} = \hbar v\,(\pm\tilde{q}_x\,\hat{\sigma}_x \;+\; \tilde{q}_y\,\hat{\sigma}_y) \tag{18}$$

for $\tilde{\boldsymbol{q}}$ small compared to the size of the Brillouin zone, and with the velocity $v = (3/2)Ja/\hbar$.

We are here in a marginal situation with respect to topological properties. We have seen for one-dimensional problems (and the same is true for two-dimensional problems) that the establishment of a contact between two energy bands is a singular point: this contact can disappear when one or more parameters of the problem are modified, and depending on this modification, the two resulting disjoint bands will have or not have topological properties. Our goal in the rest of this chapter and in the next one will be to understand which modifications to do in the Hamiltonian in order to switch to one side or the other[5].

Robustness of Dirac points. We have seen right above that the two energy bands touch at Dirac points. The existence of these points of contact

[4] see lecture of 2012-13, Chapter 6, for a detailed study

[5] Note that a particular topology for this marginal situation can be revealed from the study of edge states, as was studied theoretically by Delplace, Ullmo, et al. (2011), then experimentally by Milićević, Ozawa, et al. (2017).

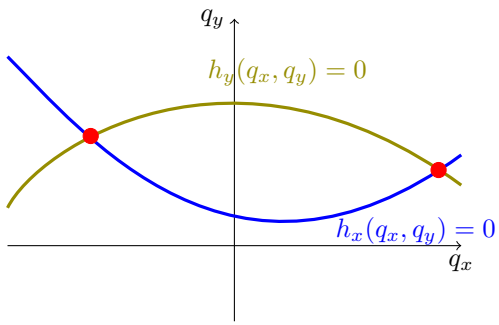

Figure 4. *Dirac points obtained at the intersection of the lines of the plane q_x, q_y along which $h_x(\boldsymbol{q})$ and $h_y(\boldsymbol{q})$ vanish. These points are robust in the sense that a small change in the Hamiltonian parameters slightly distorts these lines, but does not remove their intersection points which are only displaced.*

between the two bands is a direct consequence of the fact that the Hamiltonian of the lattices we have studied is written

$$\hat{H}_{\boldsymbol{q}} = -\left(h_x(\boldsymbol{q})\hat{\sigma}_x + h_y(\boldsymbol{q})\hat{\sigma}_y\right). \tag{19}$$

The energies of the two bands $\pm\left[h_x^2 + h_y^2\right]^{1/2}$ therefore coincide at the points where h_x and h_y cancel simultaneously. Now, when $\boldsymbol{q}$ varies in the plane (q_x, q_y), the existence of simultaneous zeros for h_x and h_y is "natural". The functions h_x and h_y can take positive and negative values, and each cancels on certain lines of the plane (figure 4). A Dirac point corresponds to the intersection of such lines, and the vector field $\boldsymbol{h} = (h_x, h_y)$ has a vortex structure around this point (figure 5).

This vortex structure ensures the robustness of the Dirac points as long as the Hamiltonian keeps the form (19). If we slightly change the value of some tunneling coefficients with respect to others, the Dirac points will shift, but will not disappear. For stronger deformations, two Dirac points of opposite winding can come into contact and annihilate (Montambaux, Piéchon, et al. 2009), in a manner formally similar to two vortices in a 2D superfluid in the description of the Kosterlitz–Thouless transition (see the lecture of years 2016-17).

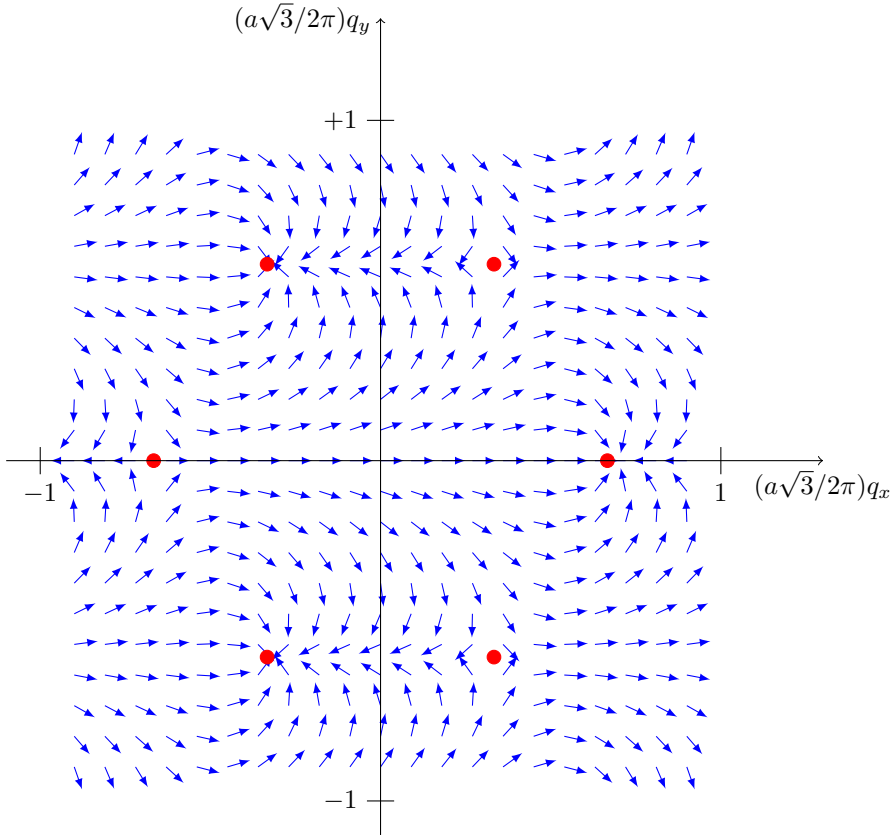

Figure 5. *Vector field $\boldsymbol{n}(\boldsymbol{q}) = \boldsymbol{h}(\boldsymbol{q})/|\boldsymbol{h}(\boldsymbol{q})|$ in the q_x, q_y plane for the hexagonal lattice. The Dirac points are indicated by the red circles and form themselves a hexagonal lattice in momentum space (*cf. *figure 2, bottom). In the vicinity of these points, the vector field $\boldsymbol{n}(\boldsymbol{q})$ has a vortex structure, with windings of opposite sign for two adjacent Dirac points.*

1-4 Hexagonal lattice for polaritons or atoms

In the last ten years, several platforms have been used to implement a hexagonal lattice in a wave system, and thus observe a dispersion relation with Dirac cones. Apart from electronic systems, let us quote without trying to be exhaustive acoustic waves (Torrent & Sánchez-Dehesa 2012), waveguide lattices (Rechtsman, Zeuner, et al. 2013b), or microwave resonators (Bellec, Kuhl, et al. 2013) (see figure 6).

The cavity polariton platform, which we have already described in Chapter 2 for the realization of an SSH chain, can also be used to realize such two-dimensional lattices (Jacqmin, Carusotto, et al. 2014). In figure 7 is shown an image of the microstructure in which holes have been dug in a triangular lattice, and where the active zone thus forms a hexagonal lattice. This active region is composed of a GaAlAs layer surrounded by two Bragg mirrors, creating a planar cavity with a quality factor of $Q \sim 7\ 10^4$. As described in chapter 2, the system is pumped with non-resonant light and the photoluminescence light is observed, either position-resolved (showing the active regions forming the hexagonal lattice) or momentum-resolved (showing the band structure with the characteristic Dirac cones).

With cold atoms, the first direct demonstration of Dirac points by Tarruell, Greif, et al. (2012) was described in the lecture of years 2012-13 and we will not come back to it. We will focus here on the more recent experiment by Duca, Li, et al. (2015) which demonstrated the phase winding around a Dirac point (figure 5).

Formally, the motion of a particle in momentum space in the presence of a Dirac point can be seen as analogous to the case of the motion of a particle of charge e in real space (i.e. of positions $\boldsymbol{r}$) in the presence of an infinitely narrow solenoid creating a finite magnetic flux (Mikitik & Sharlai 1999). This physical situation, represented on figure 8, leads to the Aharonov–Bohm effect (Aharonov & Bohm 1959). If we consider a trajectory along a $\mathcal{C}$ contour that surrounds the solenoid, the accumulated phase along the trajectory

$$\Phi_{\mathrm{AB}} = \frac{e}{2\pi\hbar} \oint_{\mathcal{C}} \boldsymbol{A}(\boldsymbol{r}) \cdot \mathrm{d}\boldsymbol{r}, \tag{20}$$

where $\boldsymbol{A}(\boldsymbol{r})$ is the vector potential describing the magnetic field of the solenoid, is proportional to the magnetic field flux in the solenoid. For a

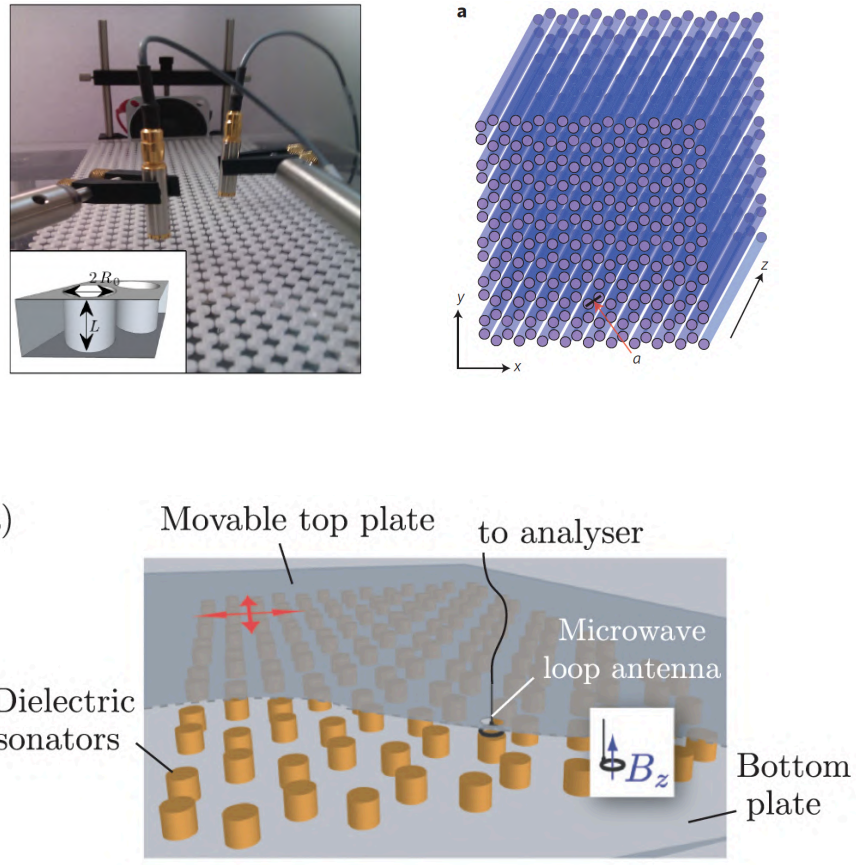

Figure 6. *Hexagonal lattice for acoustic waves (top, left), guided light waves (top, right) and electromagnetic waves in the $\sim 6\,$GHz range (bottom). Figures taken from Torrent & Sánchez-Dehesa (2012), Rechtsman, Zeuner, et al. (2013b) and Bellec, Kuhl, et al. (2013).*

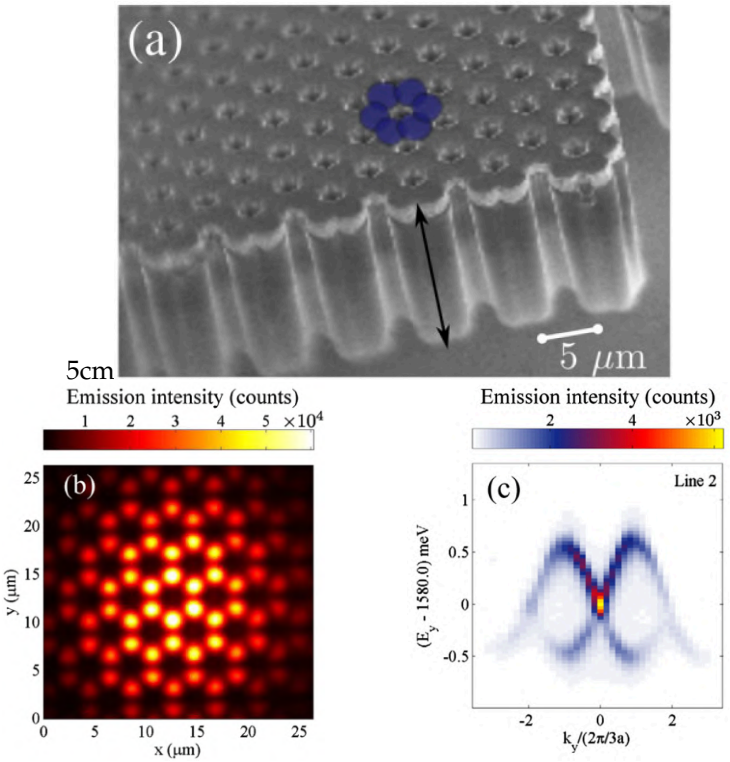

Figure 7. *Top: Microstructure of AlGaAs forming a hexagonal lattice. Bottom: photoluminescence spectrum in position space (left) and in momentum space (right). On the right figure, we plot $E(\boldsymbol{q})$ as a function of q_y, with a choice of q_x that allows to pass over a Dirac point. The figure on the left was obtained for a pump power sufficient to reach the polariton condensation regime. Figures extracted from Jacqmin, Carusotto, et al. (2014).*

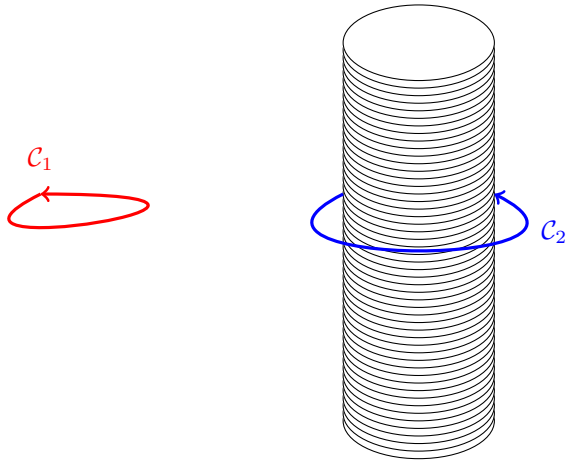

Figure 8. *The Aharonov–Bohm effect. An infinite solenoid generates a localized magnetic field inside the solenoid. We measure with an interferometric device the phase accumulated by the wave function of a charged particle following a closed contour. If the contour does not surround the solenoid (contour $\mathcal{C}_1$), the magnetic flux is undetectable. On the other hand, if the contour surrounds the solenoid (contour $\mathcal{C}_2$), the accumulated geometric phase is proportional to the flux (Eq. 20), although the classical trajectory of the particle never enters the non-zero magnetic field region.*

trajectory that does not surround the solenoid, this Aharonov–Bohm phase Φ_{AB} is zero.

Let us now consider a closed "trajectory" in $\boldsymbol{q}$ space which surrounds one of the Dirac points (figure 9). If the motion along this trajectory is slow enough, the particle initially prepared in a given state of the pseudo-spin, the ground state $|u_{\boldsymbol{q}}^{(-)}\rangle$ for example, will stay in this state and will accumulate a geometric phase. We know (see Chapter 1) that this geometrical phase is given by half of the solid angle subtended by the vector $\boldsymbol{h}(\boldsymbol{q})$ along this trajectory. As the vector $\boldsymbol{h}(\boldsymbol{q})$ describes in this case a whole turn on the equator of the Bloch sphere, the solid angle is $\pm 2\pi$ and the geometrical phase is $\pm\pi$ (contour $\mathcal{C}_1$ of figure 9). If, on the contrary, the trajectory does not surround a Dirac point or surrounds two points of opposite windings, the solid angle will be zero, as well as the corresponding geometrical phase

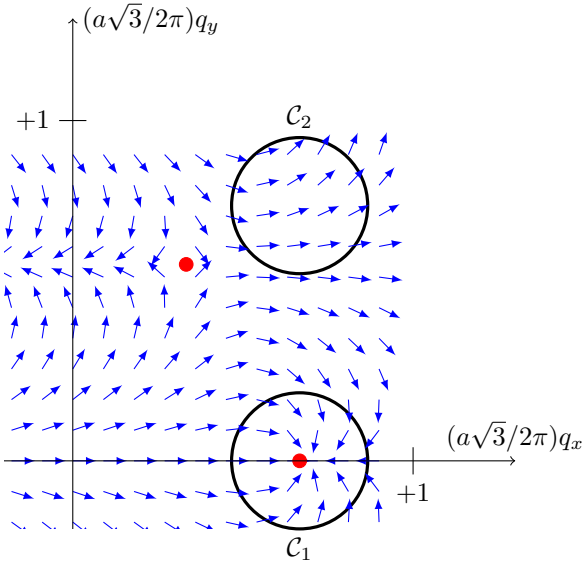

Figure 9. *Two possible "trajectories" in momentum space. The contour $\mathcal{C}_1$, which surrounds a Dirac point, corresponds to a geometrical phase $\pm\pi$. The contour $\mathcal{C}_2$ corresponds to a zero geometric phase.*

(contour $\mathcal{C}_2$ of figure 9).

To demonstrate this effect, a two-path interferometer was realized, and it was verified that the phase difference at the output of the interferometer is equal to π or 0 depending on whether the surface that the interferometer encloses includes a Dirac point or not. This experiment was performed with rubidium atoms prepared in an optical lattice formed by three light waves at 120 degrees from each other.

Initially the external state of the atoms is a wave packet localized at the center of the Brillouin zone ($\boldsymbol{q}_i = 0$) and their internal state is a given magnetic Zeeman sub-level[6] noted $|\uparrow\rangle$. One then realizes a $\frac{\pi}{2} - \pi - \frac{\pi}{2}$ interferometer with microwave pulses (figure 10):

[6]More precisely, the two relevant states are $|F = 2, m = 1\rangle$ and $|F = 1, m = 1\rangle$.

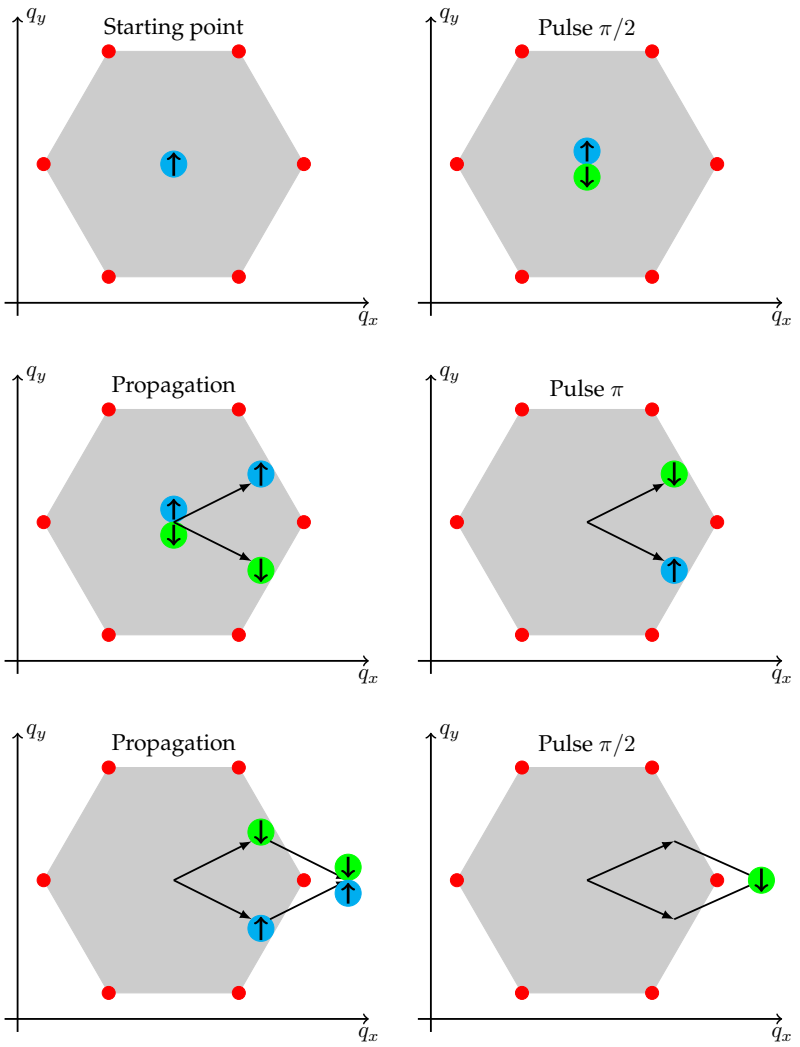

Figure 10. *The experimental sequence performed to realize a two-path interferometer in quasi-momentum space, allowing to reveal the phase winding of π around a Dirac point. Figure inspired by Duca, Li, et al. (2015).*

- A first $\pi/2$ microwave pulse prepares a coherent superposition of $|\uparrow\rangle$ and $|\downarrow\rangle$, the magnetic moment of $|\downarrow\rangle$ being opposite to the one of $|\uparrow\rangle$, and the global state can thus be written

$$|\boldsymbol{q}_i, \uparrow\rangle + |\boldsymbol{q}_i, \downarrow\rangle \tag{21}$$

- An acceleration of the lattice along the x axis, realized by shifting the frequency of one of the laser beams with respect to the two others, creates an inertial force F_x that is the same for the two spin states. This force will progressively shift the quasi-momentum $\boldsymbol{q}$ along the x axis. This is the Bloch oscillation phenomenon that we have already met and that we will develop a bit further.

- A magnetic field gradient creates an force along the y axis acting in opposite directions for each spin state, which separates the trajectories of $|\uparrow\rangle$ and $|\downarrow\rangle$. The quasi-momenta of the two spin states thus split on either side of $q_y = 0$, while keeping the same value of q_x.

- At time τ, a π pulse flips the spin state of the atoms, which allows to close the interferometer in momentum space.

- At time 2τ, the two wave packets have reached the same $\boldsymbol{q}_f$ and the global state of an atom is

$$|\boldsymbol{q}_f, \uparrow\rangle + \mathrm{e}^{\mathrm{i}\Phi}|\boldsymbol{q}_f, \downarrow\rangle, \tag{22}$$

  where Φ contains the desired phase information.

- To access this phase, one proceeds to a last $\pi/2$ microwave pulse with the phase Φ_{MW} and measures the population in both spin states

$$n_{\uparrow,\downarrow} \propto 1 \pm \cos(\Phi + \Phi_{\mathrm{MW}}). \tag{23}$$

As always, Φ contains both the geometric phase and the difference of the dynamical phases accumulated on each arm of the interferometer. In principle, the dynamical phases accumulated on each arm are identical by symmetry. In practice, Duca, Li, et al. (2015) have calibrated the residual dynamical phase thanks to the zero area interferometer obtained by reversing the acceleration of the lattice at the time of the π pulse.

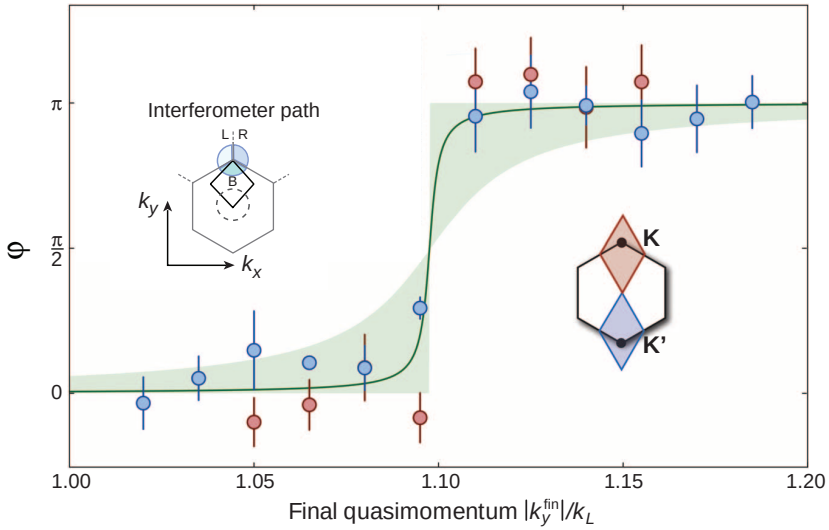

5cm

Figure 11. *Interferences in momentum space around a Dirac point. When one of the Dirac points K or K' is inside the interferometer, the measured value for Φ is in good agreement with the prediction $\Phi_{\mathrm{geom}} = \pi$. The slight shift of the tipping point (about 10 % in relative value) is explained by the finite extension of the wave packets in momentum space. Figure taken from Duca, Li, et al. (2015).*

The final result of this experiment, given in figure 11 shows that the phase between the two arms of the interferometer is $\Phi \sim \pi$ if the two paths pass on either side of a Dirac point, and $\Phi \sim 0$ otherwise. This is a direct confirmation of the phase winding around a Dirac point.

2 Geometrical characterization of topology

After having studied a concrete two-band model, corresponding to the hexagonal lattice of graphene, we now turn to the characterization of the possible topological nature of the bands that emerge in this type of model. In this paragraph we will focus on a geometrical characterization, which

will be based on the Bloch sphere. We will propose a criterion for having a topologically non-trivial band, which is the total covering of the sphere when $\boldsymbol{q}$ spans the Brillouin zone. In the next part (§3), we will make the link with a more physical criterion, based on the quantization of the Hall conductance.

2-1 The wrapping of the Bloch sphere

As in the previous section, we are interested here in a tight-binding model with two sites A and B per unit cell. Let us start by recalling the main ingredients:

- The Hamiltonian $\hat{H}_{\boldsymbol{q}}$ in this tight-binding model is written in a general way
$$\hat{H}_{\boldsymbol{q}} = E_0(\boldsymbol{q})\,\hat{1} - \boldsymbol{h}(\boldsymbol{q})\cdot\hat{\boldsymbol{\sigma}} \tag{24}$$
where E_0 and $\boldsymbol{h}$ are periodic functions of $\boldsymbol{q}$ on the Brillouin zone. We do not necessarily restrict ourselves to couplings between nearest neighbours, so the E_0 and $\boldsymbol{h}$ functions may differ from what we found for graphene.
- The eigenenergies are $E_0 \pm |\boldsymbol{h}|$.
- Apart from the Dirac points, for which the vector $\boldsymbol{h}(\boldsymbol{q})$ cancels, we can introduce the unit vector
$$\boldsymbol{n}(\boldsymbol{q}) = \frac{\boldsymbol{h}(\boldsymbol{q})}{|\boldsymbol{h}(\boldsymbol{q}|} \tag{25}$$
which we characterize by its polar and azimuthal angles $[\theta_{\boldsymbol{q}}, \phi_{\boldsymbol{q}}]$ in spherical coordinates. The Hamiltonian $\hat{H}_{\boldsymbol{q}}$ is thus written
$$\hat{H}_{\boldsymbol{q}} = E_0\hat{1} - |\boldsymbol{h}| \begin{pmatrix} \cos\theta & \mathrm{e}^{-\mathrm{i}\phi}\sin\theta \\ \mathrm{e}^{\mathrm{i}\phi}\sin\theta & -\cos\theta \end{pmatrix}. \tag{26}$$
- We are interested in the lowest energy band $E_0 - |\boldsymbol{h}|$, associated to the eigenvector
$$|u_{\boldsymbol{q}}^{(-)}\rangle = \begin{pmatrix} \cos(\theta/2) \\ \mathrm{e}^{\mathrm{i}\phi}\sin(\theta/2) \end{pmatrix}, \tag{27}$$
with the same choice of gauge as in the previous chapters, namely a first component that is real, positive or null.
- To any value of $\boldsymbol{q}$, we can therefore associate the point of the Bloch sphere with coordinates (θ, ϕ) (i.e. the vector $\boldsymbol{n}(\boldsymbol{q})$), which uniquely determines the eigenstate $|u_{\boldsymbol{q}}^{(-)}\rangle$.

In terms of topology, the characterization of a Hamiltonian $\hat{H}_{\boldsymbol{q}}$ is therefore given by the mapping:
$$\boldsymbol{q} = (q_x, q_y) \;\longrightarrow\; \boldsymbol{n}_{\boldsymbol{q}} = \begin{pmatrix} \cos\phi_q\ \sin\theta_q \\ \sin\phi_q\ \sin\theta_q \\ \cos\theta_q \end{pmatrix}, \tag{28}$$
which goes from the Brillouin zone to the Bloch sphere. Let us recall the periodicity of $\hat{H}_{\boldsymbol{q}}$ with respect to the quasi-momenta $\boldsymbol{q}$ when we add to them a vector of the reciprocal lattice, for example $\boldsymbol{b}_{1,2}$ for the graphene lattice (figure 2). The Brillouin zone thus has a torus structure and the area reached on the Bloch sphere when $\boldsymbol{q}$ explores the Brillouin zone is the same as when $\boldsymbol{q}$ explores the whole (q_x, q_y) plane.

To clarify the characterization of $\hat{H}_{\boldsymbol{q}}$, let us recall the two results we found in one dimension.

- For SSH Hamiltonians, where the 1D trajectory of $\boldsymbol{n}(q)$ is confined on the equator of the Bloch sphere, the classification is done according to the number of windings around the equator. This criterion allows to determine unambiguously the existence of possible edge states.
- For geometrical pumps, i.e. 1D systems evolving in time and thus effectively two-dimensional, we have classified these systems according to the wrapping of the Bloch sphere when the vector $\boldsymbol{n}(q,t)$ describes the rectangle $[-\pi/a, +\pi/a] \times [0, T]$. We called "topological" a system such that $\boldsymbol{n}(q,t)$ completely covers the Bloch sphere. This case corresponds to a non-zero displacement of matter and is quantized after a full pump cycle.

In both cases, we checked that this characterization of purely mathematical origin corresponded to clear physical properties.

We will adopt a similar definition here: we will characterize $\hat{H}_{\boldsymbol{q}}$ by the way $\boldsymbol{n}(\boldsymbol{q})$ covers the Bloch sphere when $\boldsymbol{q}$ describes the whole Brillouin zone. If $n(\boldsymbol{q})$ does not cover the whole sphere, we will say that we are in a *normal* or *topologically trivial* situation. If on the contrary $\boldsymbol{n}(\boldsymbol{q})$ covers the whole sphere, the situation will be qualified as *topological* or *topologically non-trivial*.

The precise mathematical definition of this covering is based on the wrapping number

$$\mathcal{C} = -\frac{1}{4\pi} \iint_{\mathrm{BZ}} \boldsymbol{n} \cdot \left[(\partial_{q_x} \boldsymbol{n}) \times (\partial_{q_y} \boldsymbol{n}) \right] \, \mathrm{d}q_x \, \mathrm{d}q_y. \tag{29}$$

An important property of differential geometry is that the quantity $\mathcal{C}$ defined in this way is always an integer and can therefore play the role of a topological invariant. In practice, we will essentially encounter situations for which $\mathcal{C} = 0$ (normal band, no wrapping) and $|\mathcal{C}| = 1$ (topological band, with wrapping). This definition can be seen as the generalization to 2D of the winding number that we had defined in 1D in the framework of the SSH model (Chapter 1):

$$\mathcal{N} = \frac{1}{2\pi} \int_{\mathrm{BZ}} \frac{\mathrm{d}\phi}{\mathrm{d}q} \, \mathrm{d}q, \tag{30}$$

where ϕ was the azimuthal angle defining the vector $\boldsymbol{n}$.

2-2 The case of graphene

In the case of graphene, we have seen that the Hamiltonian $\hat{H}_{\boldsymbol{q}}$ is written

$$\hat{H}_{\boldsymbol{q}} = -\boldsymbol{h}(\boldsymbol{q}) \cdot \hat{\boldsymbol{\sigma}} \qquad \text{with} \quad \boldsymbol{h} = J \begin{pmatrix} 1 + \cos(\boldsymbol{q} \cdot \boldsymbol{a}_1) + \cos(\boldsymbol{q} \cdot \boldsymbol{a}_2) \\ \sin(\boldsymbol{q} \cdot \boldsymbol{a}_1) + \sin(\boldsymbol{q} \cdot \boldsymbol{a}_2) \\ 0 \end{pmatrix}. \tag{31}$$

The vectors $\boldsymbol{h}$ and $\boldsymbol{n} = \boldsymbol{h}/|\boldsymbol{h}|$ are thus always in the equatorial plane. The mapping $\boldsymbol{q} \to \boldsymbol{n}(\boldsymbol{q})$ can therefore obviously not cover the whole Bloch sphere (figure 12).

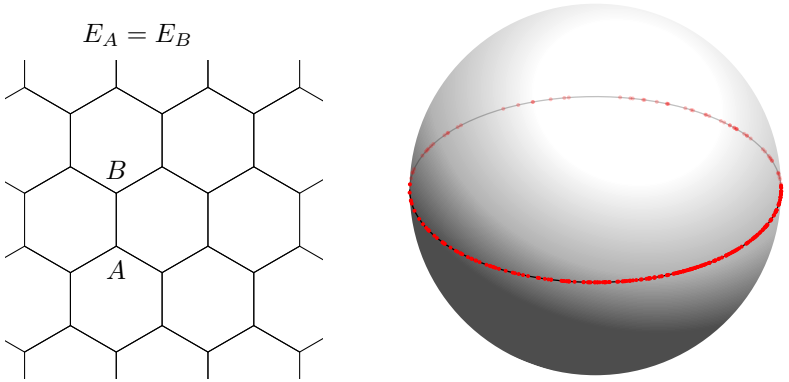

Figure 12. *Correspondence between the Brillouin zone of the hexagonal lattice and the Bloch sphere, with the same energy for sites A and B: only the equator of the Bloch sphere is reached. The red points have been obtained by a uniform draw of $\boldsymbol{q}$ in the Brillouin zone.*

2-3 Partial wrapping (trivial)

To obtain an covering of the Bloch sphere that goes beyond its equator, we need to add a $h_z(\boldsymbol{q})\,\hat{\sigma}_z$ component to the Hamiltonian. The simplest way to do this is to give an opposite energy $\mp\Delta$ to the two sites A and B, so that the Hamiltonian $\hat{H}_{\boldsymbol{q}}$ becomes

$$\hat{H}_{\boldsymbol{q}} = -\begin{pmatrix} \Delta & h_x(\boldsymbol{q}) - \mathrm{i}h_y(\boldsymbol{q}) \\ h_x(\boldsymbol{q}) + \mathrm{i}h_y(\boldsymbol{q}) & -\Delta \end{pmatrix}, \qquad i.e.\ h_z = \Delta \tag{32}$$

with the eigenenergies:

$$E^{\pm}_{\boldsymbol{q}} = \pm \left[h_x^2(\boldsymbol{q}) + h_y^2(\boldsymbol{q}) + \Delta^2 \right]^{1/2}. \tag{33}$$

The contact at the Dirac points disappears and we obtain two disjoint energy bands (figure 13). The gap at the location of the Dirac points is $2\,|\Delta|$.

Even if an extended surface of the Bloch sphere can now be covered when $\boldsymbol{q}$ describes the whole Brillouin zone, it is clear that the criterion of total coverage of the Bloch sphere that we introduced in the previous para-

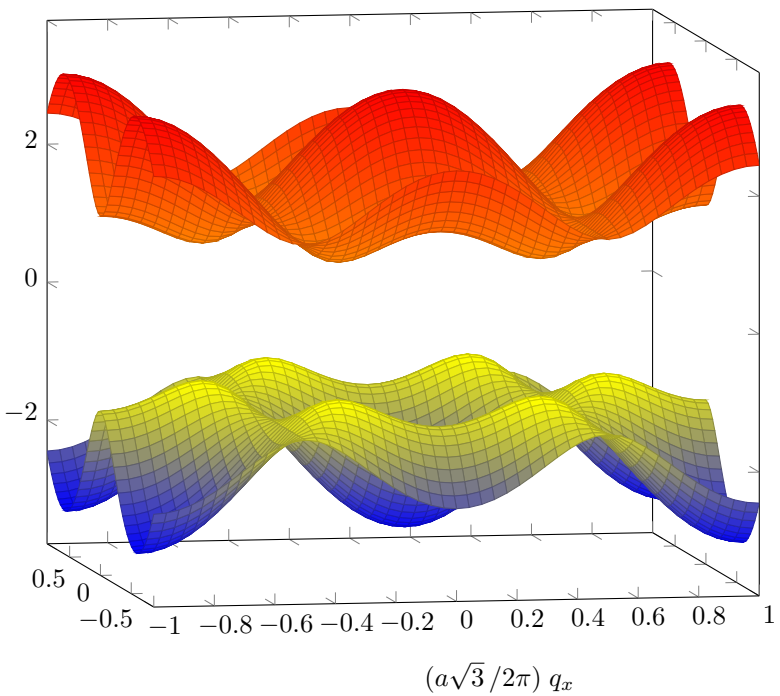

Figure 13. *Energy bands obtained for the hexagonal lattice with couplings between nearest neighbours and an energy on site $\pm\Delta$ with $\Delta = J$.*

graph cannot be realized. Indeed, the angle θ defined by

$$\cos(\theta) = \frac{\Delta}{\left[h_x^2 + h_y^2 + \Delta^2\right]^{1/2}} \tag{34}$$

is always less than $\pi/2$ if Δ is positive. All the states of the lower band $|u_{\boldsymbol{q}}^{(-)}\rangle$ thus have an image in the northern hemisphere of the Bloch sphere (figure 14); this lower band cannot be called topological according to the criterion we have set since not all the points of the sphere are reached. The same is true for the upper band: all its states $|u_{\boldsymbol{q}}^{(+)}\rangle$ have an image in the southern hemisphere of the Bloch sphere.

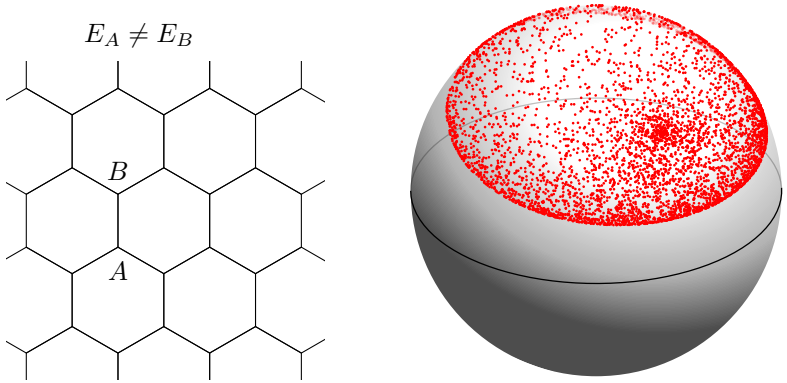

Figure 14. *Correspondence between the Brillouin zone of the hexagonal lattice (with $\Delta = J$) and the (partial) coverage of the Bloch sphere by the $|u_{\boldsymbol{q}}^{(-)}\rangle$ state of the fundamental band. The red points have been obtained by a uniform draw of $\boldsymbol{q}$ in the Brillouin zone.*

2-4 Total wrapping (non-trivial)

To finish this part devoted to the geometrical argument based on the Bloch sphere covering, let us give an example of a Hamiltonian $\hat{H}_{\boldsymbol{q}}$ which fulfills this purpose. Consider a "slight" modification of (32) where the quantity h_z itself depends on $\boldsymbol{q}$:

$$\hat{H}_{\boldsymbol{q}} = -\begin{pmatrix} h_z(\boldsymbol{q}) & h_x(\boldsymbol{q}) - \mathrm{i}h_y(\boldsymbol{q}) \\ h_x(\boldsymbol{q}) + \mathrm{i}h_y(\boldsymbol{q}) & -h_z(\boldsymbol{q}) \end{pmatrix} \tag{35}$$

with

$$h_z(\boldsymbol{q}) = \Delta_0 \left\{ -\sin(\boldsymbol{q}\cdot\boldsymbol{a}_1) + \sin(\boldsymbol{q}\cdot\boldsymbol{a}_2) + \sin\left[\boldsymbol{q}\cdot(\boldsymbol{a}_1 - \boldsymbol{a}_2)\right] \right\} \tag{36}$$

We will not try to justify this form here, which will naturally appear in the next chapter when we study the model developed by Haldane (1988), and where we will add couplings between second neighbours. The important point for us at this stage is that the whole Bloch sphere is non-trivially covered by the $|u_{\boldsymbol{q}}^{(-)}\rangle$ state when $\boldsymbol{q}$ explores the whole Brillouin zone (figure 15). More quantitatively, the calculation of the wrapping number from (29) gives $|\mathcal{C}| = 1$, confirming the topologically non-trivial nature of the band thus obtained.

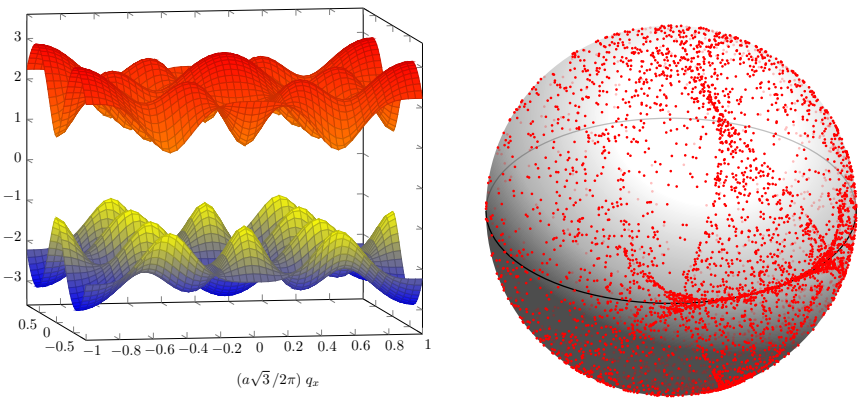

Figure 15. *Energy bands (left) and total coverage of the Bloch sphere by the $|u_{\boldsymbol{q}}^{(-)}\rangle$ state (right), obtained by placing the $\pm h_z(\boldsymbol{q})$ terms given in (36) on the diagonal of $\hat{H}_{\boldsymbol{q}}$ (with $\Delta_0 = J$). We will see in the next chapter that these terms appear in the Haldane model, taking into account complex couplings between second neighbours. The red points have been obtained by a uniform draw of $\boldsymbol{q}$ in the Brillouin zone.*

Link with the adiabatic pump in the Rice–Mele model. Another example of non-trivial coverage of the Bloch sphere is provided by our study of the adiabatic pump from the previous chapter. In that study we found a full coverage of the Bloch sphere by sending a state with pseudo-momentum q at time t onto the Bloch sphere:

$$(q,t) \;\to\; \boldsymbol{n}, \tag{37}$$

when q described the interval $[-\pi/a, \pi/a]$ and t the interval $[0,T]$ with periodic boundary conditions. If we formally replace q by q_x and t by q_y in this problem, we get the desired coverage. Thus the circular trajectory in the plane (J', Δ) centered at $(J, 0)$ and of radius J considered in the previous course is transcribed for the variables (q_x, q_y):

$$\hat{H}_q = -J \begin{pmatrix} \sin(q_y a) & 1+\cos(q_y a) + \mathrm{e}^{-\mathrm{i}q_x a} \\ 1+\cos(q_y a) + \mathrm{e}^{+\mathrm{i}q_x a} & -\sin(q_y a) \end{pmatrix}. \tag{38}$$

3 "Physical" characterization of the topology

After this "argument from authority" qualifying as topological a band with a wrapping number $\mathcal{C}$ different from 0, we will now move on to a more physical characterization of the possible topology of an energy band, based on the notion of *quantized transport*.

For this purpose, we will draw on the concepts developed for the study of the quantum Hall effect. We will detail them for the general modelling of a periodic system, thus momentarily leaving the two-band model. We will of course find this two-band model at the end of our reasoning and we will check that our physical criterion based on a quantized transport coincides with the geometrical criterion described in the previous paragraph.

3-1 The quantum Hall effect

The discovery of the quantum Hall effect and the theoretical work that followed have allowed to establish a correspondence between the topological nature of an energy band and the conductivity of this band. More precisely, a quantum Hall effect experiment consists very schematically in (*cf.* figure 16):

- taking a two-dimensional rectangular sample $[0, L_x] \times [0, L_y]$ containing a "gas of electrons" (quantum well) which is placed in a magnetic field oriented along z;
- applying a DC voltage V_x between the two opposite sides $x = 0$ and $x = L_x$, corresponding to an electric field $\mathcal{E}$ parallel to the x axis with $\mathcal{E}_x = V_x/L_x$. In experiments with neutral atoms, this voltage is replaced by a uniform force $\boldsymbol{F}$ parallel to the x axis;
- measuring the intensity I_y (or the current density $J_y = I_y/L_x$) propagating in the y direction.

The intensity I_y, when not zero, is proportional to the voltage V_x. The Hall conductivity tensor $\sigma_{xy} = -\sigma_{yx}$ is defined by

$$I_y = \sigma_{yx}\, V_x \quad \Leftrightarrow \quad J_y = \sigma_{yx}\, \mathcal{E}_x \tag{39}$$

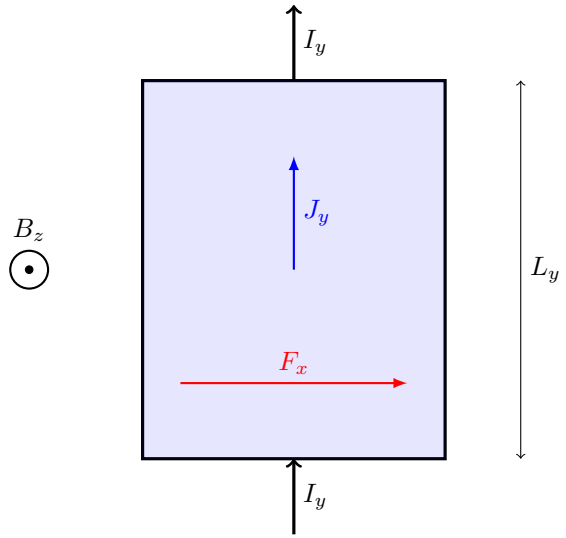

Figure 16. *Schematic representation of a Hall effect experiment. Applying a force F_x in the x direction induces a current density J_y in the y direction. The applied magnetic field is perpendicular to the plane.*

and the spectacular result of the (integer) quantum Hall effect is the quantization of this conductivity:

$$\sigma_{yx} = \frac{e^2}{h}\, n \tag{40}$$

where n is a positive, negative or zero integer, e the charge of the conducting particles and h the Planck constant. This quantization with a given integer n remains valid on a plateau of magnetic field, before switching to the integer $n+1$ when the magnetic field is decreased.

The integer n has a topological origin; more precisely, it reveals the topology of the populated energy bands for a given magnetic field. The standard treatment of the quantum Hall effect is to use linear response theory to calculate σ_{yx} for the occupied energy bands (Thouless, Kohmoto, et al. 1982). The result involves a (topological) Chern number related to the Berry curvature of these bands.

In what follows, we will take a slightly different approach from this traditional treatment. We will make a local analysis of the dynamics of a wave packet in the Brillouin zone. For a full band, we will of course find the known results, but this treatment will be better adapted to recent experiments with atoms or photons. These experiments allow one to work with bands which are only partially filled and they give access to richer information than the conductivity σ_{yx}.

3-2 Evolution of the quasi-momentum

To carry out our local analysis, we will consider a particle placed in the periodic potential $V(\boldsymbol{r})$ in two dimensions ($\boldsymbol{r} = (x, y)$). To be more specific, we will suppose the particle prepared at time $t = 0$ in the Bloch state $\boldsymbol{q}_0$ of the fundamental band $n = 0$:

$$\Psi_{t=0}(\boldsymbol{r}) \equiv \psi^{(0)}_{\boldsymbol{q}_0}(\boldsymbol{r}) = \mathrm{e}^{\mathrm{i}\boldsymbol{q}_0\cdot\boldsymbol{r}}\, u^{(0)}_{\boldsymbol{q}_0}(\boldsymbol{r}), \tag{41}$$

or in a wave packet centered on this quasi-momentum $\boldsymbol{q}_0$ and of small width compared to the size of the Brillouin zone. To simulate a quantum Hall effect experiment, we assume that a uniform (and possibly time dependent) force $\boldsymbol{F}_t$ parallel to the x axis is applied to the particle in addition to the potential $V(\boldsymbol{r})$. The Hamiltonian describing the motion of the particle is thus

$$\hat{H}_t = \frac{\hat{\boldsymbol{p}}^2}{2m} + V(\hat{\boldsymbol{r}}) - \boldsymbol{F}_t \cdot \hat{\boldsymbol{r}}. \tag{42}$$

We will proceed in two steps, looking separately at the evolution $\frac{\mathrm{d}\boldsymbol{q}}{\mathrm{d}t}$ of the quasi-momentum $\boldsymbol{q}$ of the particle and the evolution $\frac{\mathrm{d}\langle\boldsymbol{r}\rangle}{\mathrm{d}t}$ of its mean position, that is to say its velocity.

The first part of our reasoning will consist in recovering the Bloch oscillation phenomenon, that is to say the very simple evolution equation for the momentum $\boldsymbol{q}$:

$$\hbar\,\frac{\mathrm{d}\boldsymbol{q}}{\mathrm{d}t} = \boldsymbol{F}. \tag{43}$$

This phenomenon has already been discussed in the lecture of years 2012-13 and we recall here the steps that allowed us to establish this result.

Because of the presence of the force $\boldsymbol{F}$, the problem is no longer space periodic, and it seems that Bloch's theorem can no longer be invoked.

However it is easy to recover a periodic problem by using the unitary transformation generated by the operator

$$\hat{U}_t = \exp\left[-\mathrm{i}\,\hat{\boldsymbol{r}}\cdot\boldsymbol{A}_t\right] \qquad \text{with} \quad \boldsymbol{A}_t = \frac{1}{\hbar}\int_0^t \boldsymbol{F}_{t'}\,\mathrm{d}t' \tag{44}$$

to obtain the transformed Hamitonian

$$\begin{aligned}\hat{\tilde{H}}_t &= \hat{U}_t\hat{H}_t\hat{U}_t^\dagger + \mathrm{i}\hbar\frac{\mathrm{d}\hat{U}_t}{\mathrm{d}t}\hat{U}_t^\dagger \\ &= \frac{(\hat{\boldsymbol{p}}+\hbar\boldsymbol{A}_t)^2}{2m} + V(\hat{\boldsymbol{r}})\end{aligned} \tag{45}$$

which is indeed spatially periodic. We are thus interested in the evolution of the state of the particle after this unitary transformation

$$\tilde{\Psi}_t(\boldsymbol{r}) = \hat{U}_t\,\Psi_t(\boldsymbol{r}), \tag{46}$$

noticing that the two states Ψ and $\tilde{\Psi}$ coincide in $t=0$.

We can then reason in the following way for this transformed Hamiltonian:

- At the initial time we start from a Bloch state of quasi-momentum $\boldsymbol{q}_0$. As the Hamiltonian $\hat{\tilde{H}}_t$ is space-periodic, the particle stays at each time in a Bloch state
$$\tilde{\Psi}_t(\boldsymbol{r}) = \mathrm{e}^{\mathrm{i}\boldsymbol{q}_0\cdot\boldsymbol{r}}\,u_t(\boldsymbol{r}) \tag{47}$$
where $u_t(\boldsymbol{r})$ is a periodic function on the lattice.

- By inserting this expression for $\tilde{\Psi}_t$ into the Schrödinger equation, we find that the periodic function $u_t(\boldsymbol{r})$ must be solution of
$$\mathrm{i}\hbar\frac{\partial u_t}{\partial t} = \left\{\frac{\left[\hat{\boldsymbol{p}}+\hbar(\boldsymbol{q}_0+\boldsymbol{A}_t)\right]^2}{2m} + V(\boldsymbol{r})\right\}u_t(\boldsymbol{r}). \tag{48}$$
It is thus an evolution under the effect of the Hamiltonian $\hat{H}_{\boldsymbol{q}_0+\boldsymbol{A}_t}$ where
$$\hat{H}_{\boldsymbol{q}} = \frac{(\hat{\boldsymbol{p}}+\hbar\boldsymbol{q})^2}{2m} + V(\boldsymbol{r}) \tag{49}$$
is the usual Hamiltonian that one can use to determine the periodic part of Bloch functions. We are thus facing a problem with a Hamiltonian depending on an external parameter, in this case $\boldsymbol{A}_t$, for which the eigenfunctions are known at each time (the $u_{\boldsymbol{q}}^{(n)}$'s).

- If the fundamental band is separated from the upper bands at each instant (no Dirac point!) and if the force F evolves slowly in time, the particle will remain at each instant in the fundamental band and follow quasi-adiabatically the eigenstate $u^{(0)}_{\boldsymbol{q}_0+\boldsymbol{A}_t}$. If we go back to the state of the particle before the unitary transformation
$$\Psi_t(\boldsymbol{r}) = \hat{U}_t^\dagger\tilde{\Psi}_t(\boldsymbol{r}) = \mathrm{e}^{\mathrm{i}(\boldsymbol{q}_0+\boldsymbol{A}_t)\cdot\boldsymbol{r}}\,u^{(0)}_{\boldsymbol{q}_0+\boldsymbol{A}_t}(\boldsymbol{r}) \tag{50}$$
we find that this state coincides (up to a phase) with the Bloch state of the fundamental band with quasi-momentum
$$\boldsymbol{q}_t = \boldsymbol{q}_0 + \boldsymbol{A}_t \tag{51}$$
hence the evolution equation given in (43).

The quasi-momentum $\boldsymbol{q}$ thus travels through the Brillouin zone in a uniform way as time passes. Because of the periodic structure of this zone, we obtain a periodic motion, the Bloch oscillation, along the axis defined by the force $\boldsymbol{F}$.

This ends the first part of our analysis, which gives us the evolution of the quasi-momentum. We are now interested in the evolution of the position of the particle.

3-3 The anomalous velocity

To determine the evolution of the average velocity of the particle, we will follow a reasoning very similar to the one we used for the analysis of the geometrical pump in § 5 of Chapter 3.

Let us start from the expression of the state of the particle given by the two first orders of the adiabatic approximation for the Hamiltonian $\hat{H}_{\boldsymbol{q}+\boldsymbol{A}_t}$:

$$|u_t\rangle = |u^{(0)}_{\boldsymbol{q}_t}\rangle + \mathrm{i}\hbar\sum_{n\neq 0}|u^{(n)}_{\boldsymbol{q}_t}\rangle\,\frac{\langle u^{(n)}_{\boldsymbol{q}_t}|\partial_t u^{(0)}_{\boldsymbol{q}_t}\rangle}{E^{(n)}_{\boldsymbol{q}} - E^{(0)}_{\boldsymbol{q}}} + \dots \tag{52}$$

In this equation, the time dependence of the state $u^{(0)}_{\boldsymbol{q}_t}$ comes from the variation of $\boldsymbol{A} = \int^t \boldsymbol{F}_{t'}\ \mathrm{d}t'$. For a force $\boldsymbol{F} = F_x \boldsymbol{u}_x$ along the x axis, we have

$$\hbar\, |\partial_t u^{(0)}_{\boldsymbol{q}_t}\rangle = F_x\, |\partial_{q_x} u^{(0)}_{\boldsymbol{q}_t}\rangle \tag{53}$$

where we have used the equation of motion of $\boldsymbol{q}$ found above [*cf.* (43)]. The small parameter of the expansion (52) is thus

$$\frac{F_x a}{\Delta E} \ll 1 \tag{54}$$

where we have posed that the quasi-momentum scale on which $|u^{(0)}_{\boldsymbol{q}}\rangle$ varies is of the order of the size $1/a$ of the Brillouin zone, and where ΔE represents a typical gap between two energy bands.

We now evaluate the average of the velocity operator

$$\hat{\boldsymbol{v}} = \frac{\hat{\boldsymbol{p}}}{m} = -\mathrm{i}\frac{\hbar}{m}\boldsymbol{\nabla}_{\boldsymbol{r}} \tag{55}$$

at order 1 in this small parameter, for the Bloch state $\mathrm{e}^{\mathrm{i}\boldsymbol{q}_t\cdot\boldsymbol{r}}\, u_t(\boldsymbol{r})$. The dominant term comes from the contribution of $|u^{(0)}_{\boldsymbol{q}_t}\rangle$:

$$\begin{aligned}
\boldsymbol{v}_0 &= \left(\langle u^{(0)}_{\boldsymbol{q}_t}|\mathrm{e}^{-\mathrm{i}\boldsymbol{q}_t\cdot\boldsymbol{r}}\right)\frac{\hat{\boldsymbol{p}}}{m}\left(\mathrm{e}^{\mathrm{i}\boldsymbol{q}_t\cdot\boldsymbol{r}}|u^{(0)}_{\boldsymbol{q}_t}\rangle\right)\\
&= \frac{1}{m}\langle u^{(0)}_{\boldsymbol{q}_t}|\,(\hat{\boldsymbol{p}}+\hbar\boldsymbol{q}_t)\,|u^{(0)}_{\boldsymbol{q}_t}\rangle\\
&= \frac{1}{\hbar}\boldsymbol{\nabla}_{\boldsymbol{q}} E^{(0)}_{\boldsymbol{q}_t},
\end{aligned} \tag{56}$$

where we have used the result of one of the two lemmas established in the previous chapter. This first contribution is the well-known expression for the group velocity.

The next term in the expansion comes from the cross contribution of the first and second order terms:

$$\boldsymbol{v}_1 = \mathrm{i}\,\frac{F_x}{m}\sum_{n\neq 0}\langle u^{(0)}_{\boldsymbol{q}_t}|\,(\hat{\boldsymbol{p}}+\hbar\boldsymbol{q}_t)\,|u^{(n)}_{\boldsymbol{q}_t}\rangle\,\frac{\langle u^{(n)}_{\boldsymbol{q}_t}|\partial_{q_x}u^{(0)}_{\boldsymbol{q}_t}\rangle}{E^{(n)}_{\boldsymbol{q}_t}-E^{(0)}_{\boldsymbol{q}_t}} + \text{c.c.} \tag{57}$$

Using the second lemma seen in the previous chapter, this expression simplifies to

$$\boldsymbol{v}_1 = -\mathrm{i}\,\frac{F_x}{\hbar}\langle\boldsymbol{\nabla}_{\boldsymbol{q}}u^{(0)}_{\boldsymbol{q}_t}|\partial_{q_x}u^{(0)}_{\boldsymbol{q}_t}\rangle + \text{c.c.} \tag{58}$$

The component along x of $\boldsymbol{v}_1$ cancels when the contribution of the complex conjugate is added and we find for the component along y

$$v_{1,y} = \frac{F_x\,\Omega_{\boldsymbol{q}_t}}{\hbar} \tag{59}$$

where we have introduced the *Berry curvature* at point $\boldsymbol{q}$ of the Brillouin zone

$$\begin{aligned}
\Omega_{\boldsymbol{q}} &= \mathrm{i}\left(\langle\partial_{q_x}u^{(0)}_{\boldsymbol{q}}|\partial_{q_y}u^{(0)}_{\boldsymbol{q}}\rangle - \langle\partial_{q_y}u^{(0)}_{\boldsymbol{q}}|\partial_{q_x}u^{(0)}_{\boldsymbol{q}}\rangle\right) &(60)\\
&= \mathrm{i}\left(\langle\boldsymbol{\nabla}_{\boldsymbol{q}}u^{(0)}_{\boldsymbol{q}}|\times|\boldsymbol{\nabla}_{\boldsymbol{q}}u^{(0)}_{\boldsymbol{q}}\rangle\right)\cdot\boldsymbol{u}_z. &(61)
\end{aligned}$$

By introducing the vector notation $\boldsymbol{\Omega}_{\boldsymbol{q}} = \Omega_{\boldsymbol{q}}\boldsymbol{u}_z$, this contribution to the velocity is written as

$$\boldsymbol{v}_{1,t} = \frac{1}{\hbar}\boldsymbol{\Omega}_{\boldsymbol{q}_t}\times\boldsymbol{F}_t. \tag{62}$$

This velocity was introduced by Karplus & Luttinger (1954) and Adams & Blount (1959), the latter being at the origin of the denomination *anomalous velocity*. A "modern" presentation of the formalism leading to the above expression can be found in Chang & Niu (1995).

At this order of calculation, we obtain the second equation of motion giving the velocity for the quasi-momentum $\boldsymbol{q}$:

$$\hbar\boldsymbol{v}_{\boldsymbol{q}} = \boldsymbol{\nabla}_{\boldsymbol{q}}E^{(0)}_{\boldsymbol{q}} + \boldsymbol{\Omega}_{\boldsymbol{q}}\times\boldsymbol{F} \tag{63}$$

which completes the one written in (43) for the evolution of the quasi-momentum $\boldsymbol{q}$.

Orders of magnitudes. Using the idea that the energy $E^{(0)}_{\boldsymbol{q}}$ and the Bloch state $|u^{(0)}_{\boldsymbol{q}}\rangle$ vary appreciably on a scale q of the order of the size $1/a$ of the Brillouin zone, we find

$$v_0 \sim \frac{a\,\Delta E}{\hbar}, \quad v_1 \sim \frac{a^2 F}{\hbar}, \tag{64}$$

so that $v_1 \ll v_0$ if the validity condition (54) is verified[7]. However we will see in a moment that for a full band, the contribution of $\boldsymbol{v}_0$ vanishes and the

[7] We assume that the band gap ΔE which intervenes in (54) is comparable to the width of the band 0.

conduction is then entirely determined by $\boldsymbol{v}_1$. It was therefore necessary to push our calculation up to and including the first order.

3-4 Conductance of a uniformly filled strip

To find the quantized conductance of the Hall effect, let us give a two-dimensional sample with a unit cell of area A_{cell}, the corresponding Brillouin zone having an area in momentum space

$$A_{\text{BZ}} = \frac{(2\pi)^2}{A_{\text{cell}}}. \tag{65}$$

We consider the situation where the filling of the sample is one particle per unit cell, i.e. a surface density

$$\rho^{(2D)} = \frac{1}{A_{\text{cell}}}. \tag{66}$$

Thus, in the framework of the tight-binding model we developed for graphene, there are $\gamma = 2$ sites per unit cell, so a filling rate of $1/\gamma = 1/2$ particles per site. Since the existence of γ sites per unit cell leads to γ energy bands, our assumption on the filling of the sample amounts to say that the fundamental $n = 0$ band is full and the $\gamma - 1$ upper bands are empty.

We assume that the particles are fermions without interaction, so that the density operator of a particle is simply equal to the identity in the $|\psi_{\boldsymbol{q}}^{(0)}\rangle$ basis. The average particle flux

$$\boldsymbol{J} = \rho^{(2D)} \, \langle \boldsymbol{v} \rangle \tag{67}$$

is thus obtained by averaging the velocity $\boldsymbol{v}_{\boldsymbol{q}}$ given in (63) over all quasi-momenta $\boldsymbol{q}$ of the Brillouin zone:

$$\langle \boldsymbol{v} \rangle = \frac{1}{A_{\text{BZ}}} \iint_{\text{BZ}} \boldsymbol{v}_{\boldsymbol{q}} \, \mathrm{d}^2 q. \tag{68}$$

We immediately see that the contribution of $\boldsymbol{v}_0 = \frac{1}{\hbar} \boldsymbol{\nabla}_{\boldsymbol{q}} E_{\boldsymbol{q}}^{(0)}$ cancels out because the function $E_{\boldsymbol{q}}^{(0)}$ is regular and periodic on the Brillouin zone. This leaves only the contribution of $\boldsymbol{v}_1 = \frac{1}{\hbar} \boldsymbol{\Omega}_{\boldsymbol{q}} \times \boldsymbol{F}$, i.e. taking the force $\boldsymbol{F}$ along the x axis and using (65):

$$J_y = \sigma_{yx} F_x \tag{69}$$

with

$$\sigma_{yx} = \frac{1}{h} \mathcal{C} \tag{70}$$

where we introduced the *Chern number*

$$\mathcal{C} = \frac{1}{2\pi} \iint_{\text{BZ}} \Omega_{\boldsymbol{q}} \, \mathrm{d}^2 q. \tag{71}$$

The Hall conductance will be quantified in the way[8] announced in (40) provided that the Chern number $\mathcal{C}$ is an integer. Let us now prove this important result.

3-5 The Chern number is an integer

This point has in fact already been proved in Chapter 3 during our study of the geometric pump. The demonstration to be done here is in every respect similar. Let us introduce the Berry connection

$$\boldsymbol{\mathcal{A}}_{\boldsymbol{q}} = \mathrm{i} \, \langle u_{\boldsymbol{q}}^{(0)} | \boldsymbol{\nabla}_{\boldsymbol{q}} u_{\boldsymbol{q}}^{(0)} \rangle \tag{72}$$

so that

$$\boldsymbol{\Omega}_{\boldsymbol{q}} = \boldsymbol{\nabla}_{\boldsymbol{q}} \times \boldsymbol{\mathcal{A}}_{\boldsymbol{q}}. \tag{73}$$

The Stokes formula applied "naively" gives then for the Chern number

$$\frac{1}{2\pi} \iint_{\text{BZ}} \Omega_{\boldsymbol{q}} \, \mathrm{d}^2 q \overset{?}{=} \frac{1}{2\pi} \oint_{\text{BZ}} \boldsymbol{\mathcal{A}}_{\boldsymbol{q}} \cdot \mathrm{d}\boldsymbol{q} \tag{74}$$

where the contour corresponds to the perimeter of the Brillouin zone. When the states $|u_{\boldsymbol{q}}\rangle$ are defined periodically on this zone, this contour integral cancels. One could deduce that the Chern number is always zero. But this conclusion would be incorrect, because the definition of the Berry connection may have one or more singularities in the Brillouin zone (Kohmoto 1985).

There are two ways to get around this difficulty.

[8] Note that there is a factor e^2 of difference between the two expressions, e being the charge of the electron. Indeed, the usual conductance of the Hall effect characterizes the response of the electric current to an electric field $\boldsymbol{\mathcal{E}}$, while we are looking here at the response of the particle current to a force $\boldsymbol{F}$.

- The first one, already described in course 3, consists in choosing a gauge, then using a contour which avoids these singularities (figure 26 of chapter 3). Each singularity contributes then by a factor $\pm 2\pi$ to the curvilinear integral. The Chern number corresponds to the algebraic sum of these singularities: it can be non zero, but it will always be an integer.

- The other possibility consists in using in momentum space two choices of gauge (I) and (II) connected by the transformation

$$|u_{\boldsymbol{q}}^{(II)}\rangle = \mathrm{e}^{-\mathrm{i}\chi_{\boldsymbol{q}}}\ |u_{\boldsymbol{q}}^{(I)}\rangle \tag{75}$$

which leads for the Berry connections

$$\boldsymbol{\mathcal{A}}_{\boldsymbol{q}}^{(II)} = \boldsymbol{\mathcal{A}}_{\boldsymbol{q}}^{(I)} + \boldsymbol{\nabla}_{\boldsymbol{q}}\chi_{\boldsymbol{q}}. \tag{76}$$

For a two-site unit cell, the gauge choice (I) can correspond for example to the one made so far, with a first component of $|u\rangle$ real and positive, and the gauge choice (II) to a second component of $|u\rangle$ real and positive, i.e. for the lower band:

$$(I) : |u_{\boldsymbol{q}}^{(I)}\rangle = \begin{pmatrix} \cos(\theta/2) \\ \mathrm{e}^{\mathrm{i}\phi}\sin(\theta/2) \end{pmatrix}, \qquad (II) : |u_{\boldsymbol{q}}^{(II)}\rangle = \begin{pmatrix} \mathrm{e}^{-\mathrm{i}\phi}\cos(\theta/2) \\ \sin(\theta/2) \end{pmatrix} \tag{77}$$

with simply $\chi_{\boldsymbol{q}} = \phi_{\boldsymbol{q}}$. We have seen in chapter 3 that the (I) gauge leads to a singularity in $\boldsymbol{q}$ when the south pole is reached, while the (II) gauge leads to a singularity in $\boldsymbol{q}$ for the north pole. One can then separate the Brillouin zone into two complementary parts: part A does not contain any singularity for the (I) gauge choice and part B does not contain any singularity for (II) (figure 17)

Let us similarly split the surface integral of the Berry curvature into two parts, each of which can be computed by Stokes' formula for the nonsingular gauge. Denoting $\mathcal{C}$ the contour forming the boundary between the areas A and B, we have:

$$\begin{aligned} \iint_{\mathrm{BZ}} \Omega_{\boldsymbol{q}}\ \mathrm{d}^2q &= \iint_A \Omega_{\boldsymbol{q}}\ \mathrm{d}^2q + \iint_B \Omega_{\boldsymbol{q}}\ \mathrm{d}^2q \\ &= \left(\oint_{\mathrm{BZ}} - \oint_{\mathcal{C}}\right) \boldsymbol{\mathcal{A}}_{\boldsymbol{q}}^{(I)} \cdot \mathrm{d}\boldsymbol{q} + \oint_{\mathcal{C}} \boldsymbol{\mathcal{A}}_{\boldsymbol{q}}^{(II)} \cdot \mathrm{d}\boldsymbol{q}. \end{aligned} \tag{78}$$

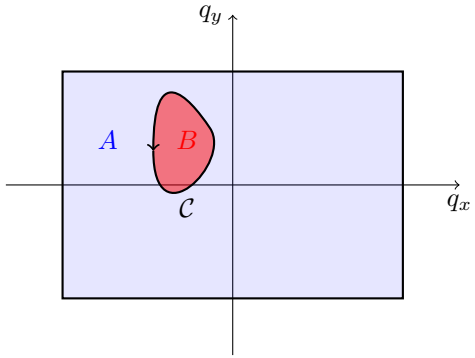

Figure 17. *A Brillouin zone (assumed here to be rectangular) is separated into two complementary regions A and B, associated to two different gauge choices (I) and (II). These regions are chosen such that there is no singularity for the gauge (I) in the region A, and the same for the gauge (II) in the region B. We note $\mathcal{C}$ the closed contour delimiting the border between these two regions.*

As mentioned above, the curvilinear integral of $\boldsymbol{\mathcal{A}}_{\boldsymbol{q}}^{(I)}$ on the edge of the Brillouin zone gives a null result, given the periodicity in $\boldsymbol{q}$. This leaves:

$$\iint_{\mathrm{BZ}} \Omega_{\boldsymbol{q}}\ \mathrm{d}^2q = \oint_{\mathcal{C}} \left(\boldsymbol{\mathcal{A}}_{\boldsymbol{q}}^{(II)} - \boldsymbol{\mathcal{A}}_{\boldsymbol{q}}^{(I)}\right) \cdot \mathrm{d}\boldsymbol{q} = \oint_{\mathcal{C}} \boldsymbol{\nabla}_{\boldsymbol{q}}\chi_{\boldsymbol{q}} \cdot \mathrm{d}\boldsymbol{q}. \tag{79}$$

Now for the gauge change (75) to be monovalent, this last integral must be a multiple of 2π, hence the result.

The conclusion of this approach based on the study of transport leads us to the following definition: an energy band will be qualified as topological if and only if its Chern number

$$\mathcal{C} = \frac{1}{2\pi} \iint_{\mathrm{BZ}} \Omega_{\boldsymbol{q}}\ \mathrm{d}^2q \tag{80}$$

is a non-zero integer. Otherwise when $\mathcal{C} = 0$, the band is topologically trivial. Let us recall that the Berry curvature $\Omega_{\boldsymbol{q}}$ of the considered band is well defined if this band is isolated from its neighbours by a gap. Our criterion therefore excludes band structures with Dirac points.

4 The Berry curvature in a 2D lattice

4-1 Comparison between the two approaches

We have given in the preceding sections two possible characterizations of the topology associated with a band. The first one was explicitly restricted to the case of tight-binding and two-site cells. By writing the Hamiltonian as a combination of Pauli matrices,

$$\hat{H}_{\boldsymbol{q}} = h_0(\boldsymbol{q})\hat{1} - \boldsymbol{h}(\boldsymbol{q}) \cdot \hat{\boldsymbol{\sigma}} \tag{81}$$

and by introducing the unit vector

$$\boldsymbol{n}(\boldsymbol{q}) = \frac{\boldsymbol{h}(\boldsymbol{q})}{|\boldsymbol{h}(\boldsymbol{q}|} \tag{82}$$

we have introduced the topological invariant

$$\mathcal{C} = -\frac{1}{4\pi} \iint_{\mathrm{BZ}} \boldsymbol{n} \cdot \left[(\partial_{q_x} \boldsymbol{n}) \times (\partial_{q_y} \boldsymbol{n}) \right] \, \mathrm{d}q_x \, \mathrm{d}q_y, \tag{83}$$

which indicates how the vector $\boldsymbol{n}_{\boldsymbol{q}}$ covers the Bloch sphere.

The second method, which we have developed for a general periodic Hamiltonian by analyzing the Hall conductivity, led us to the invariant

$$\begin{aligned} \mathcal{C} &= \frac{1}{2\pi} \iint_{\mathrm{BZ}} \Omega_{\boldsymbol{q}} \, \mathrm{d}^2 q \\ &= \frac{1}{2\pi} \iint_{\mathrm{BZ}} \mathrm{i} \left(\langle \partial_{q_x} u^{(0)}_{\boldsymbol{q}} | \partial_{q_y} u^{(0)}_{\boldsymbol{q}} \rangle - \langle \partial_{q_y} u^{(0)}_{\boldsymbol{q}} | \partial_{q_x} u^{(0)}_{\boldsymbol{q}} \rangle \right) \, \mathrm{d}^2 q. \end{aligned} \tag{84}$$

How do these two definitions compare?

It is in fact quite simple to show that they coincide for a two-site tight-binding model. We know that for this two-band model, the $|u^{(-)}_{\boldsymbol{q}}\rangle$ states of the fundamental band and the $\boldsymbol{n}$ vector are each expressed in terms of the θ and ϕ angles:

$$|u^{(-)}_{\boldsymbol{q}}\rangle = \begin{pmatrix} \cos(\theta/2) \\ \mathrm{e}^{\mathrm{i}\phi} \sin(\theta/2) \end{pmatrix}, \qquad \boldsymbol{n} = \begin{pmatrix} \sin\theta \, \cos\phi \\ \sin\theta \, \sin\phi \\ \cos\theta \end{pmatrix} \tag{85}$$

and the arguments of the two integrals can be evaluated in terms of $\boldsymbol{\nabla}_{\boldsymbol{q}}\theta$ and $\boldsymbol{\nabla}_{\boldsymbol{q}}\phi$. A slightly long calculation, but without difficulty, gives for these two terms[9]:

$$\begin{aligned} \boldsymbol{n} \cdot \left[(\partial_{q_x} \boldsymbol{n}) \times (\partial_{q_y} \boldsymbol{n}) \right] &= \sin\theta \, \left(\partial_{q_x}\theta \, \partial_{q_y}\phi \, - \, \partial_{q_y}\theta \, \partial_{q_x}\phi \right) \\ &= -2\mathrm{i} \left(\langle \partial_{q_x} u^{(-)}_{\boldsymbol{q}} | \partial_{q_y} u^{(-)}_{\boldsymbol{q}} \rangle - \langle \partial_{q_y} u^{(-)}_{\boldsymbol{q}} | \partial_{q_x} u^{(-)}_{\boldsymbol{q}} \rangle \right) \\ &= -2\Omega_{\boldsymbol{q}}. \end{aligned} \tag{87}$$

In summary, measuring the Berry curvature in a two-band model is equivalent to measuring the unit vector $\boldsymbol{n}_{\boldsymbol{q}}$. This is precisely what has been done in the recent Hamburg experiment (Fläschner, Rem, et al. 2016), which we will describe in § 4-3. Before doing so, we will take advantage of this established link between topology and Berry curvature to derive the necessary conditions for the observation of topologically nontrivial bands.

4-2 Chern number and space-time symmetries

Berry curvature and spatial inversion symmetry. A Hamiltonian exhibits reflection symmetry if for an appropriate choice of the origin of coordinates, it satisfies

$$[\hat{S}_0, \hat{H}] = 0 \tag{88}$$

where $\hat{S}_0$ is the linear unitary *reflection* operator (or *parity inversion*) defined by its action on a wave function $\psi(\boldsymbol{r})$:

$$\hat{S}_0 \, \psi(\boldsymbol{r}) = \psi(-\boldsymbol{r}) \qquad i.e., \quad \hat{S}_0 \, |\boldsymbol{r}\rangle = |-\boldsymbol{r}\rangle. \tag{89}$$

Let us consider a Hamiltonian $\hat{H}$ describing the motion of a particle in a periodic and reflection invariant potential. We deduce a simple relation between its eigenstates, the Bloch functions $\psi^{(n)}_{\boldsymbol{q}}(\boldsymbol{r}) = \mathrm{e}^{\mathrm{i}\boldsymbol{q}\cdot\boldsymbol{r}} u^{(n)}_{\boldsymbol{q}}(\boldsymbol{r})$. Indeed, the transformation via $\hat{S}_0$ of an eigenstate must still be an eigenstate, which leads to the fact that $u^{(n)}_{\boldsymbol{q}}(-\boldsymbol{r}) = u^{(n)}_{-\boldsymbol{q}}(\boldsymbol{r})$, up to a phase. We then deduce the invariance of the Berry curvature

$$\text{Reflection invariance:} \quad \Omega_{\boldsymbol{q}} = \Omega_{-\boldsymbol{q}}. \tag{90}$$

[9] This expression can also be written in terms of the vector $\boldsymbol{h}$ rather than $\boldsymbol{n}$:

$$\Omega_{\boldsymbol{q}} = -\frac{1}{2|\boldsymbol{h}|^3} \boldsymbol{h} \cdot \left[(\partial_{q_x} \boldsymbol{h}) \times (\partial_{q_y} \boldsymbol{h}) \right] \tag{86}$$

Berry curvature and time reversal symmetry. For the type of problems considered here, in which the spin does not intervene, the time reversal operation consists in keeping the position unchanged and reversing the direction of the velocity. Mathematically, the time reversal operation is obtained by applying the antilinear and unitary operator $\hat{K}_0$ defined by its action[10] on a wave function $\psi(\boldsymbol{r})$:

$$\hat{K}_0\,\psi(\boldsymbol{r}) = \psi^*(\boldsymbol{r}). \tag{91}$$

This transformation does not change the probability density in position $|\psi(\boldsymbol{r})|^2$. For the momentum, the initial probability amplitude associated to $\psi(\boldsymbol{r})$ is of course the Fourier transform $\phi(\boldsymbol{p})$ of $\psi(\boldsymbol{r})$. The new probability amplitude in momentum, which is the Fourier transform of the transformed wave function $\hat{K}_0\psi$, is therefore $\phi^*(-\boldsymbol{p})$, which leads to the announced inversion of the velocity distribution. For a periodic Hamiltonian invariant by time reversal, a reasoning similar to the previous one leads to $\left(u^{(n)}_{\boldsymbol{q}}(\boldsymbol{r})\right)^* = u^{(n)}_{-\boldsymbol{q}}(\boldsymbol{r})$, from which we deduce

$$\text{Time reversal invariance:}\quad \Omega_{-\boldsymbol{q}} = -\Omega_{\boldsymbol{q}}. \tag{92}$$

Consequences. In the framework of a tight-binding model like the ones we are mainly interested in this lecture, a Hamiltonian is time-reversal invariant if there exists a basis choice of sites $A_{\boldsymbol{j}}, B_{\boldsymbol{j}}, \ldots$ for which all tunnel matrix elements are real. When this is the case, the relation (92) entails that the Chern number of each band is zero, since the surface elements around $\boldsymbol{q}$ and $-\boldsymbol{q}$ have opposite contributions to the Berry curvature integral:

$$\text{Time reversal invariance:}\quad \mathcal{C} = \frac{1}{2\pi}\int \Omega_{\boldsymbol{q}}\ \mathrm{d}^2q = 0. \tag{93}$$

For the spinless problems we have considered here, one can only have a topologically non-trivial band by breaking the time reversal invariance.

If the considered Hamiltonian has in addition the property of being symmetric with respect to the origin, then the combination of (90) and (92) leads to the fact that the Berry curvature cancels out at any point of the Brillouin zone, the anomalous velocity being therefore also uniformly zero:

$$\text{Reflection + time reversal invariance:}\qquad \Omega_{\boldsymbol{q}} = 0. \tag{94}$$

This double spatial and temporal symmetry appears both for the hexagonal and for the brick wall lattices, provided that the energies of the sites A and B are equal (we can take the origin in the middle of a segment AB).

[10] The time reversal operation assumes that a phase choice has been made for the basis vectors; in this case, the kets $|\boldsymbol{r}\rangle$ are assumed here to be "real", i.e. $\hat{K}_0|\boldsymbol{r}\rangle = |\boldsymbol{r}\rangle$. The antilinearity of $\hat{K}_0$ then leads to $\hat{K}_0\left(\int \psi(\boldsymbol{r})|\boldsymbol{r}\rangle\right) = \int \psi^*(\boldsymbol{r})|\boldsymbol{r}\rangle$.

4-3 Local measurement of Berry curvature

A possible procedure for determining $\theta_{\boldsymbol{q}}$ and $\phi_{\boldsymbol{q}}$ at any point of the Brillouin zone in a two-band situation was proposed by Hauke, Lewenstein, et al. (2014), and then implemented by Fläschner, Rem, et al. (2016). The starting point is the momentum distribution associated with the $|u^{(-)}_{\boldsymbol{q}}\rangle$ state, which can be measured in ballistic expansion resulting from the sudden extinction of the optical lattice:

$$\begin{aligned}\mathcal{N}(\boldsymbol{q}) &= f(\boldsymbol{q})\ \left|\cos(\theta_{\boldsymbol{q}}/2) + \mathrm{e}^{\mathrm{i}\phi_{\boldsymbol{q}}}\sin(\theta_{\boldsymbol{q}}/2)\right|^2 \\ &= f(\boldsymbol{q})\left[1 - \sin\theta_{\boldsymbol{q}}\cos\phi_{\boldsymbol{q}}\right].\end{aligned} \tag{95}$$

The quantity $f(\boldsymbol{q})$ corresponds to the momentum distribution of the Wannier function associated with each site A or B, which is assumed to be much larger than the relevant structures related to the variation in $\boldsymbol{q}$ of the angles $\theta_{\boldsymbol{q}}$ and $\phi_{\boldsymbol{q}}$. The central point of (95) is that $\mathcal{N}(\boldsymbol{q})$ depends on the relative phase of the contributions of the two sites A and B in the expression of the Bloch state $|u^{(-)}_{\boldsymbol{q}}\rangle$. More precisely, although this measurement is not sufficient to completely determine the angles $\theta_{\boldsymbol{q}}$ and $\phi_{\boldsymbol{q}}$, it provides the value of the product $\sin\theta_{\boldsymbol{q}}\cos\phi_{\boldsymbol{q}}$.

To take it one step further, Hauke, Lewenstein, et al. (2014) suggested to apply a sudden quench to the lattice parameters so that the Hamiltonian becomes

$$\hat{H}'_{\boldsymbol{q}} = (\hbar\omega_0/2)\ \hat{\sigma}_z. \tag{96}$$

The gas then evolves in the lattice for an adjustable time interval t before the momentum distribution is measured. Since the evolution during this time t simply consists in adding the phase $\pm\omega_0 t/2$ to the amplitudes of

sites A and B, the momentum distribution at time t is now:

$$\mathcal{N}(\boldsymbol{q},t) = f(\boldsymbol{q})\left[1 - \sin\theta_{\boldsymbol{q}}\cos(\phi_{\boldsymbol{q}} + \omega_0 t)\right]. \tag{97}$$

By repeating this procedure for different durations t and by measuring the amplitude and the phase of the corresponding signal, one has access to both $\phi_{\boldsymbol{q}}$ and $\theta_{\boldsymbol{q}}$ at any point $\boldsymbol{q}$ of the Brillouin zone.

This procedure was implemented by Fläschner, Rem, et al. (2016) using a hexagonal lattice of tubes filled with ^{40}K fermionic atoms. The initial parameters are chosen so that there is initially a large energy shift $\hbar\omega_{AB}$ between the A and B sites. One then finds two flat bands in the tight-binding model, with no tunneling between sites, and the atoms are prepared in the lowest energy band. To establish dynamics in this lattice, Fläschner, Rem, et al. (2016) applied a resonant modulation at frequency $\Omega \approx \omega_{AB}$. This modulation is obtained by shaking the lattice in a circular way, thanks to a phase modulation of the three light waves forming the lattice. We will come back to the quantitative description of this mechanism in detail in the next lectures, the only important point for us at this stage is that we can thus obtain a Berry curvature which can take values significantly different from zero. The quench required for the procedure of Hauke, Lewenstein, et al. (2014) is then obtained by simply turning off the resonant modulation.

The amplitudes and phases of the time oscillation of $\mathcal{N}(\boldsymbol{q},t)$ measured by Fläschner, Rem, et al. (2016) are shown in figure 18, with the Berry curvature reconstructed from

$$\begin{aligned}\Omega_{\boldsymbol{q}} &= \mathrm{i}\left(\langle\partial_{q_x}u^{(-)}_{\boldsymbol{q}}|\partial_{q_y}u^{(-)}_{\boldsymbol{q}}\rangle - \langle\partial_{q_y}u^{(-)}_{\boldsymbol{q}}|\partial_{q_x}u^{(-)}_{\boldsymbol{q}}\rangle\right)\\ &= \frac{1}{2}\sin\theta_{\boldsymbol{q}}\ (\boldsymbol{\nabla}_{\boldsymbol{q}}\phi_{\boldsymbol{q}}\times\boldsymbol{\nabla}_{\boldsymbol{q}}\theta_{\boldsymbol{q}})\cdot\boldsymbol{u}_z.\end{aligned} \tag{98}$$

The "pixelization" of the Brillouin zone for this reconstruction is very precise, with more than 2800 points of measurement. In this figure, we distinguish very clearly areas of positive Berry curvature and areas of negative Berry curvature. We have seen that the integral of $\Omega_{\boldsymbol{q}}$ on the whole Brillouin zone is written $\mathcal{C}\times 2\pi$, where $\mathcal{C}$ is the Chern number of the band. For the Hamburg experiment, the reconstructed Berry curvature leads to a value of $\mathcal{C}$ compatible with 0, as expected for this type of modulated lattice. More precisely, Fläschner, Rem, et al. (2016) obtained the result $\mathcal{C} = 0.005(6)$.

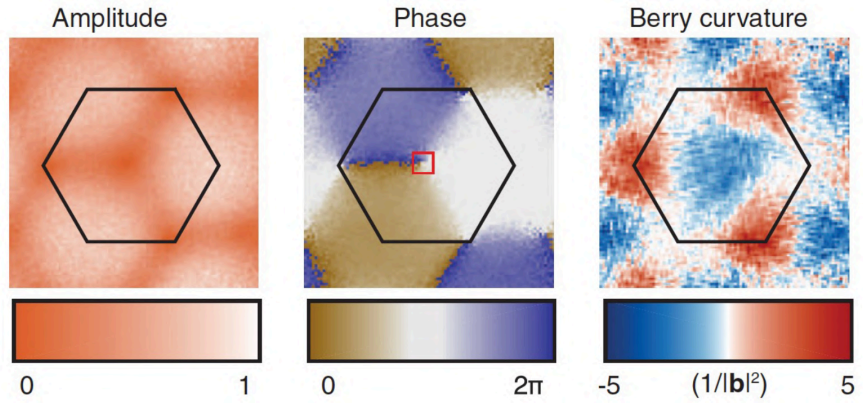

Figure 18. *Amplitude $\propto \sin\theta_{\boldsymbol{q}}$ (left) and phase $\phi_{\boldsymbol{q}}$ (middle) obtained from the measurement of the momentum distribution. Right: reconstructed Berry curvature. Figure taken from Fläschner, Rem, et al. (2016).*

The method proposed by Hauke, Lewenstein, et al. (2014) is inspired by an earlier proposal by Alba, Fernandez-Gonzalvo, et al. (2011) (see also Goldman, Anisimovas, et al. (2013)). In this proposal, sites A and B were assumed to be occupied by different internal states $|a\rangle$ and $|b\rangle$. The measurement of the momentum distribution can then be done independently for each internal state, which gives access to the local polarization for the lower band:

$$n_z(\boldsymbol{q}) \equiv \frac{h_z(\boldsymbol{q})}{|\boldsymbol{h}(\boldsymbol{q})|} = \cos\theta_{\boldsymbol{q}} = \frac{\mathcal{N}_b(\boldsymbol{q}) - \mathcal{N}_a(\boldsymbol{q})}{\mathcal{N}_a(\boldsymbol{q}) + \mathcal{N}_b(\boldsymbol{q})}. \tag{99}$$

The two other components of $\boldsymbol{n}$ can also be measured by applying a coherent coupling between $|a\rangle$ and $|b\rangle$ with an adjustable phase and duration, in order to rotate the pseudo-spin during the ballistic expansion. Once the direction of $\boldsymbol{n}(\boldsymbol{q})$ is known at any point in the Brillouin zone, the value of the Berry curvature can be determined as in the Hamburg experiment.

Appendix 1: coupling between nearest neighbours

The purpose of this appendix is to justify the expression of the Hamiltonian $\hat{H}_{\boldsymbol{q}}$ written in (11). The site A of the cell located in $\boldsymbol{r}_j$, which we note $|A, \boldsymbol{r}_j\rangle$, is coupled to 3 sites B: the one of the cell $\boldsymbol{r}_j$ and the ones of the cells located in $\boldsymbol{r}_j - \boldsymbol{a}_1$ and $\boldsymbol{r}_j - \boldsymbol{a}_2$ (*cf.* figure 2). The part of the Hamiltonian for this site is therefore:

$$-J\left(|A,\boldsymbol{r}_j\rangle\langle B,\boldsymbol{r}_j| \;+\; |A,\boldsymbol{r}_j\rangle\langle B,\boldsymbol{r}_j-\boldsymbol{a}_1| \;+\; |A,\boldsymbol{r}_j\rangle\langle B,\boldsymbol{r}_j-\boldsymbol{a}_2|\right) + \text{H.c.} \tag{100}$$

Starting from the Bloch function given in (9) and rewritten here more explicitly:

$$|\psi_{\boldsymbol{q}}\rangle = \sum_j \mathrm{e}^{\mathrm{i}\,\boldsymbol{q}\cdot\boldsymbol{r}_j}\left(\alpha_{\boldsymbol{q}}|A,\boldsymbol{r}_j\rangle + \beta_{\boldsymbol{q}}|B,\boldsymbol{r}_j\rangle\right), \tag{101}$$

the eigenvalue equation for the energy $\hat{H}|\psi_{\boldsymbol{q}}\rangle = E_{\boldsymbol{q}}|\psi_{\boldsymbol{q}}\rangle$ when projected on $\langle A,\boldsymbol{r}_j|$ reads:

$$-J'\beta_{\boldsymbol{q}}\left(\mathrm{e}^{\mathrm{i}\,\boldsymbol{q}\cdot\boldsymbol{r}_j} + \mathrm{e}^{\mathrm{i}\,\boldsymbol{q}\cdot(\boldsymbol{r}_j-\boldsymbol{a}_1)} + \mathrm{e}^{\mathrm{i}\,\boldsymbol{q}\cdot(\boldsymbol{r}_j-\boldsymbol{a}_2)}\right) = E_{\boldsymbol{q}}\;\mathrm{e}^{i\,\boldsymbol{q}\cdot\boldsymbol{r}_j}\;\alpha_{\boldsymbol{q}}, \tag{102}$$

or

$$H_{\boldsymbol{q},AB} = -J'\left(1 \;+\; \mathrm{e}^{-\mathrm{i}\,\boldsymbol{q}\cdot\boldsymbol{a}_1} \;+\; \mathrm{e}^{-\mathrm{i}\,\boldsymbol{q}\cdot\boldsymbol{a}_2}\right). \tag{103}$$

Similarly, $H_{\boldsymbol{q},BA} = H^*_{\boldsymbol{q},AB}$ and the 2×2 matrix of $\hat{H}_{\boldsymbol{q}}$ for the coupling between nearest neighbours can be written as:

$$\hat{H}_{\boldsymbol{q}} = \begin{pmatrix} 0 & H_{\boldsymbol{q},AB} \\ H_{\boldsymbol{q},BA} & 0 \end{pmatrix} \tag{104}$$

as indicated in (11) for $E_A = E_B = 0$.

Appendix 2: Momentum distribution

Consider a particle prepared in a state of the fundamental band of a lattice with two sites per unit cell:

$$|\psi\rangle = \int_{\mathrm{BZ}} c_{\boldsymbol{q}}\,|\psi^{(-)}_{\boldsymbol{q}}\rangle\;\mathrm{d}^2q \tag{105}$$

and let us look for its momentum distribution $\boldsymbol{p} = \hbar\boldsymbol{k}$:

$$\mathcal{N}(\boldsymbol{k}) = |\langle\boldsymbol{k}|\psi\rangle|^2. \tag{106}$$

Each Bloch state $|\psi^{(-)}_{\boldsymbol{q}}\rangle$ is written

$$|\psi^{(-)}_{\boldsymbol{q}}\rangle = \sum_{\boldsymbol{j}} \mathrm{e}^{\mathrm{i}\boldsymbol{q}\cdot\boldsymbol{r}_j}\;\left(\alpha_{\boldsymbol{q}}|A_{\boldsymbol{j}}\rangle + \beta_{\boldsymbol{q}}|B_{\boldsymbol{j}}\rangle\right). \tag{107}$$

Its scalar product with the plane wave $|\boldsymbol{k}\rangle$ of momentum $\hbar\boldsymbol{k}$ involves the two scalar products $\langle\boldsymbol{k}|A_{\boldsymbol{j}}\rangle$ and $\langle\boldsymbol{k}|B_{\boldsymbol{j}}\rangle$. Let us introduce the Wannier functions $w_{A/B}(\boldsymbol{r})$:

$$w_A(\boldsymbol{r}) = \langle\boldsymbol{r}|A_0\rangle, \qquad w_B(\boldsymbol{r}) = \langle\boldsymbol{r}|B_0\rangle \tag{108}$$

and let us assume for simplicity that these two functions are identical, up to the translation $\boldsymbol{a} \equiv a\boldsymbol{u}_y$:

$$w_B(\boldsymbol{r}) = w_A(\boldsymbol{r}-\boldsymbol{a}). \tag{109}$$

The Wannier functions of any site $\boldsymbol{j}$ then verify

$$\langle\boldsymbol{r}|A_{\boldsymbol{j}}\rangle = w_A(\boldsymbol{r}-\boldsymbol{r}_{\boldsymbol{j}}) \qquad \langle\boldsymbol{r}|B_{\boldsymbol{j}}\rangle = w_A(\boldsymbol{r}-\boldsymbol{r}_{\boldsymbol{j}}-\boldsymbol{a}) \tag{110}$$

and we find in momentum space

$$\langle\boldsymbol{k}|A_{\boldsymbol{j}}\rangle = \mathrm{e}^{-\mathrm{i}\boldsymbol{k}\cdot\boldsymbol{r}_j}\,\hat{w}_A(\boldsymbol{k}), \qquad \langle\boldsymbol{k}|B_{\boldsymbol{j}}\rangle = \mathrm{e}^{-\mathrm{i}\boldsymbol{k}\cdot(\boldsymbol{r}_j+\boldsymbol{a})}\hat{w}_A(\boldsymbol{k}), \tag{111}$$

where $\hat{w}_A(\boldsymbol{k})$ denotes the Fourier transform of $w_A(\boldsymbol{r})$.

The amplitude of the plane wave $\boldsymbol{k}$ in the expansion of the $|\psi\rangle$ state is thus

$$\langle\boldsymbol{k}|\psi\rangle = \hat{w}_A(\boldsymbol{k})\int_{\mathrm{BZ}}\mathrm{d}^2q\;c_{\boldsymbol{q}}\left\{\sum_{\boldsymbol{j}}\mathrm{e}^{\mathrm{i}\boldsymbol{q}\cdot\boldsymbol{r}_j}\;\left(\alpha_{\boldsymbol{q}}\mathrm{e}^{-\mathrm{i}\boldsymbol{k}\cdot\boldsymbol{r}_j} + \beta_{\boldsymbol{q}}\mathrm{e}^{-\mathrm{i}\boldsymbol{k}\cdot(\boldsymbol{r}_j+\boldsymbol{a})}\right)\right\} \tag{112}$$

The sum on the $\boldsymbol{j}$ sites of the lattice has a non-zero contribution only if $\boldsymbol{q} = \boldsymbol{k}$, which finally gives

$$\langle\boldsymbol{k}|\psi\rangle = \hat{w}_A(\boldsymbol{k})\;c_{\boldsymbol{k}}\;\left(\alpha_{\boldsymbol{k}} + \beta_{\boldsymbol{k}}\mathrm{e}^{-\mathrm{i}\boldsymbol{k}\cdot\boldsymbol{a}}\right) \tag{113}$$

provided that $\boldsymbol{k}$ is in the Brillouin zone. The situation considered in the Hamburg experiment corresponds to a uniform filling of the band ($|c_{\boldsymbol{k}}|$ independent of $\boldsymbol{k}$). Moreover, the term $\mathrm{e}^{-\mathrm{i}\boldsymbol{k}\cdot\boldsymbol{a}}$ corresponding to the shift of the B cell with respect to the a cell can be reincorporated in the $\phi_{\boldsymbol{k}}$ phase, hence the result (95).

Chapter V

Topological bands and edge states

The previous chapter was devoted to the establishment of a criterion for an energy band of a 2D periodic lattice to be considered as topological. This criterion was based on transport and directly inspired by the Hall effect: if this band is full, a force applied along x must create a quantized current in the orthogonal direction y. The quantization of this current involves the Chern number $\mathcal{C}$ of the considered band, which is computed from its Berry curvature Ω_q:

$$\mathcal{C} = \frac{1}{2\pi} \iint_{\mathrm{BZ}} \Omega_{\boldsymbol{q}} \, \mathrm{d}^2 q. \tag{1}$$

Designing and realizing lattices for which $\mathcal{C} \neq 0$ is not obvious. First of all, we have seen that for lattices invariant by time reversal and by reflection, the Berry curvature $\Omega_{\boldsymbol{q}}$ is zero at any point of the Brillouin zone. We must therefore break at least one of these two symmetries. We have also seen that if we keep the invariance by time reversal, then $\Omega_{\boldsymbol{q}} = -\Omega_{-\boldsymbol{q}}$: the integral of the Berry curvature on the Brillouin zone remains zero ; we can have locally (in momentum space) a non-trivial topology if $\Omega_{\boldsymbol{q}} \neq 0$, but we do not obtain a non-zero quantized conductance for a full band.

Starting from a simple 2D lattice of period a described in the tight-binding limit with hoppings between nearest neighbors, one must therefore break its invariance by time reversal; for a spinless problem, this imposes the realization of non-real tunnel coefficients. Two ways can be considered for this:

- One way is to transpose the geometry of the Hall effect to the lattice, i.e. to apply a uniform magnetic field on the lattice. This field breaks the translation invariance of period a and can give rise to a very rich energy spectrum, with a large number of energy sub-bands.
- The other way, proposed by Haldane, consists in keeping the same unit cell as the initial lattice, i.e. a two band model, while increasing (slightly) the number of tunnel couplings. This is what we explore in this chapter.

Once the principles of the Haldane model are established, we will see how it has been practically implemented with cold atoms in an experiment conducted by Jotzu, Messer, et al. (2014). We will then use this model to explain the *bulk-edge correspondence*, i.e., the inevitable emergence of edge channels at the interface between two areas of different topology. We will end with the experimental demonstration of these edge channels on photonic systems and we will say a few words about the spin Hall effect. This effect can be seen as a generalization of these topological concepts to time-reversal invariant problems, but for which two spin (or pseudo-spin) states undergo opposite dynamics.

1 The Haldane Model

The model proposed by Haldane (1988) is an extension of the hexagonal lattice encountered in the previous chapter in which an additional coupling

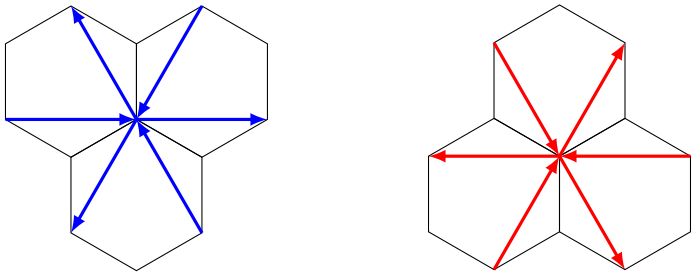

Figure 1. *The tunnel couplings between second neighbors in the Haldane model. Left, couplings to the six second neighbors for an A site, right for a B site. The direction of each arrow indicates the sign of the phase transferred during a tunnelling jump, according to the convention of figure 2. The phase winding inside a hexagon is the same for sites A and B (figure 3).*

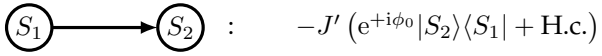

Figure 2. *Sign convention for the accumulated phase during a tunnelling jump of amplitude J' between sites S_1 and S_2.*

between second neighbors (*next-to-nearest neighbors – NNN*) is added. The unit cell does not change: it still contains two sites, which we will note A and B as before. With this model, Haldane showed that a topological band, characterized by a non-zero Chern number, can emerge in the absence of a uniform (or spatially averaged) magnetic field. This is thus a fundamentally different problem from the one of Landau levels and their discretized version, i.e. the Harper–Hoftstadter model, which we will encounter in the next chapter.

1-1 New couplings, new topology

We saw in chapter 4 that the necessary condition to obtain a topological band, with a non-zero Chern number, was to break the time reversal invariance. In the tight-binding model we will use here, this means that some tunneling matrix elements must be non-real and that their complex phase cannot be removed by a gauge transform.

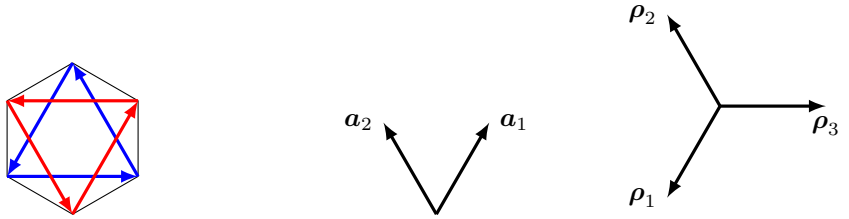

Figure 3. *Left: links between second neighbors within a given hexagon in the Haldane model. Right: the vectors used to parameterize the sites and links of the lattice.*

The Haldane model consists in keeping a real matrix element J to describe the transitions $A \leftrightarrow B$ between nearest neighbors, and taking a complex matrix element $J'\ \mathrm{e}^{\pm\mathrm{i}\phi_0}$ to describe the transitions between second neighbors $A \leftrightarrow A$ and $B \leftrightarrow B$ (figures 1 and 2). The choice of the sign of the phase $\pm\phi_0$ is such that on a cycle within a hexagon followed in the positive direction, we accumulate the phase $+3\phi_0$ for $A \to A \to A$ and $B \to B \to B$ (figure 3). We also keep the possibility to dissymmetrize the sites A and B by giving them a different energy $\pm\Delta$.

Compared to the graphene-type Hamiltonian that leads to a band spectrum with Dirac points, we therefore introduce two elements that can open a gap at these points: (i) the on-site energy $\pm\Delta$ already encountered previously and (ii) the couplings $A \leftrightarrow A$ and $B \leftrightarrow B$ proportional to $J'\mathrm{e}^{\pm\mathrm{i}\phi_0}$. We will now see that these two elements play antagonistic roles with respect to the emergence of a topologically non-trivial band.

1-2 Phase diagram

Since the periodicity of the problem is not modified by the introduction of the new couplings in J', the unit cell still has two sites and the periodic Hamiltonian $\hat{H}_{\boldsymbol{q}}$ remains a 2×2 matrix that can be decomposed into three parts:

- The on-site energy $\pm\Delta$:

$$\hat{H}_{0,\boldsymbol{q}} = \begin{pmatrix} -\Delta & 0 \\ 0 & \Delta \end{pmatrix} = -\Delta\,\hat{\sigma}_z. \tag{2}$$

- The tunnel coupling between nearest neighbors of the hexagonal lattice

$$\hat{H}_{1,\boldsymbol{q}} = -J \begin{pmatrix} 0 & 1+\mathrm{e}^{-\mathrm{i}\boldsymbol{q}\cdot\boldsymbol{a}_1}+\mathrm{e}^{-\mathrm{i}\boldsymbol{q}\cdot\boldsymbol{a}_2} \\ 1+\mathrm{e}^{\mathrm{i}\boldsymbol{q}\cdot\boldsymbol{a}_1}+\mathrm{e}^{\mathrm{i}\boldsymbol{q}\cdot\boldsymbol{a}_2} & 0 \end{pmatrix}, \tag{3}$$

where the vectors $\boldsymbol{a}_1$ and $\boldsymbol{a}_2$ are defined as in the previous chapter by (*cf.* figure 3)

$$\boldsymbol{a}_1 = \frac{\sqrt{3}\,a}{2}\begin{pmatrix} 1 \\ \sqrt{3} \end{pmatrix}, \qquad \boldsymbol{a}_2 = \frac{\sqrt{3}\,a}{2}\begin{pmatrix} -1 \\ \sqrt{3} \end{pmatrix}. \tag{4}$$

This coupling leads to Dirac points $\boldsymbol{Q}_\pm$ corresponding to the cancellation of the function $1+\mathrm{e}^{\mathrm{i}\boldsymbol{q}\cdot\boldsymbol{a}_1}+\mathrm{e}^{\mathrm{i}\boldsymbol{q}\cdot\boldsymbol{a}_2}$. We have for $j=1,2$:

$$\cos\left(\boldsymbol{Q}_\pm\cdot\boldsymbol{a}_j\right) = -\frac{1}{2}, \qquad \sin\left(\boldsymbol{Q}_\pm\cdot\boldsymbol{a}_1\right) = -\sin\left(\boldsymbol{Q}_\pm\cdot\boldsymbol{a}_2\right) = \pm\frac{\sqrt{3}}{2}. \tag{5}$$

- Couplings between second neighbors; each site A is coupled to the 6 other sites A that surround it and that form a regular hexagon, and the same thing occurs for the sites B. Let us introduce the three vectors $\boldsymbol{\rho}_\alpha$ with $\alpha=1,2,3$

$$\boldsymbol{\rho}_1 = -\boldsymbol{a}_1, \qquad \boldsymbol{\rho}_2 = \boldsymbol{a}_2, \qquad \boldsymbol{\rho}_3 = -(\boldsymbol{\rho}_1+\boldsymbol{\rho}_2), \tag{6}$$

represented in figure 3. With the convention adopted in figure 1, the wave function is multiplied by $\mathrm{e}^{+\mathrm{i}\phi_0}$ in a transition $|A,\boldsymbol{r}\rangle \to |A,\boldsymbol{r}+\boldsymbol{\rho}_\alpha\rangle$ and by $\mathrm{e}^{-\mathrm{i}\phi_0}$ in a transition $|A,\boldsymbol{r}\rangle \to |A,\boldsymbol{r}-\boldsymbol{\rho}_\alpha\rangle$ (and conversely for B).

Summing these six contributions, we arrive at (*cf.* appendix):

$$\begin{aligned} \hat{H}_{2,\boldsymbol{q}} &= -2J' \begin{pmatrix} \sum_{\alpha=1}^3 \cos(\boldsymbol{q}\cdot\boldsymbol{\rho}_\alpha-\phi_0) & 0 \\ 0 & \sum_{\alpha=1}^3 \cos(\boldsymbol{q}\cdot\boldsymbol{\rho}_\alpha+\phi_0) \end{pmatrix} \\ &= -2J'\cos\phi_0\;\mathcal{C}_{\boldsymbol{q}}\;\hat{1} \;-\; 2J'\sin\phi_0\;\mathcal{S}_{\boldsymbol{q}}\;\hat{\sigma}_z \end{aligned} \tag{7}$$

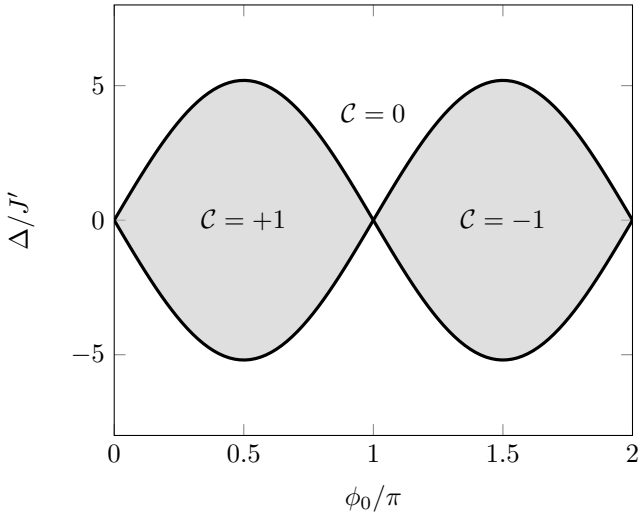

Figure 4. *Phase diagram for the Haldane model. Both bands are topological when the wrapping number $\mathcal{C}$ is nonzero.*

where we have defined

$$\mathcal{C}_{\boldsymbol{q}} = \sum_{\alpha=1}^3 \cos(\boldsymbol{q}\cdot\boldsymbol{\rho}_\alpha), \qquad \mathcal{S}_{\boldsymbol{q}} = \sum_{\alpha=1}^3 \sin(\boldsymbol{q}\cdot\boldsymbol{\rho}_\alpha). \tag{8}$$

The total Hamiltonian $\hat{H}_{\boldsymbol{q}}$, sum of the three Hamiltonians $\hat{H}_{0,1,2}$, can as before be written in the form

$$\hat{H}_{\boldsymbol{q}} = E_0(\boldsymbol{q})\,\hat{1} - \boldsymbol{h}(\boldsymbol{q})\cdot\hat{\boldsymbol{\sigma}} \tag{9}$$

with

$$h_x(\boldsymbol{q}) = J\left[1+\cos(\boldsymbol{q}\cdot\boldsymbol{a}_1)+\cos(\boldsymbol{q}\cdot\boldsymbol{a}_2)\right] \tag{10}$$

$$h_y(\boldsymbol{q}) = J\left[\sin(\boldsymbol{q}\cdot\boldsymbol{a}_1)+\sin(\boldsymbol{q}\cdot\boldsymbol{a}_2)\right] \tag{11}$$

$$h_z(\boldsymbol{q}) = \Delta + 2J'\sin\phi_0\;\mathcal{S}_{\boldsymbol{q}} \tag{12}$$

This Hamiltonian gives rise to the two energy bands

$$E_{\boldsymbol{q}}^{(\pm)} = E_0(\boldsymbol{q}) \pm |\boldsymbol{h}(\boldsymbol{q})|. \tag{13}$$

We have seen in the previous chapter that these two bands have a non-trivial topology, characterized by a non-zero Chern number, if and only if the vector $\boldsymbol{n} \equiv \boldsymbol{h}/|\boldsymbol{h}|$ completely covers the Bloch sphere when $\boldsymbol{q}$ varies in the whole Brillouin zone. When this is the case, the wrapping number

$$\mathcal{C} = -\frac{1}{4\pi} \iint_{\mathrm{BZ}} \boldsymbol{n} \cdot \left[(\partial_{q_x} \boldsymbol{n}) \times (\partial_{q_y} \boldsymbol{n}) \right] \, \mathrm{d}q_x \, \mathrm{d}q_y. \tag{14}$$

is non-zero.

Determining the set of points reached by $\boldsymbol{n}(\boldsymbol{q})$ on this sphere is feasible, but somewhat tedious, and we will focus here on the following necessary condition: the two poles (north and south) must certainly be reached for the sphere to be covered. Now the poles are reached when the projection of $\boldsymbol{h}$ in the xy plane cancels, that is to say at the two Dirac points $\boldsymbol{Q}_\pm$. For each Dirac point to correspond to a different pole, $h_z(Q_+)$ and $h_z(Q_-)$ must be of opposite signs. Using the fact that at the Dirac points, the three quantities $\sin(\boldsymbol{Q} \cdot \boldsymbol{\rho}_j)$ are equal to each other and have the value $\pm\sqrt{3}/2$, the condition for the two poles to be reached is written using (12):

$$\left(\Delta + 3\sqrt{3}J' \sin\phi_0\right)\left(\Delta - 3\sqrt{3}J' \sin\phi_0\right) < 0 \tag{15}$$

that is to say

$$\frac{|\Delta|}{J'} < 3\sqrt{3}\,|\sin\phi_0|. \tag{16}$$

A more detailed study of the problem shows that this necessary condition is in fact sufficient: when the two poles are reached, the vector $\boldsymbol{n}$ wraps around the Bloch sphere when $\boldsymbol{q}$ sweeps the Brillouin zone and the wrapping number is $\mathcal{C} = \pm 1$.

We thus obtain the phase diagram of figure 4, with two lobes leading to a non-trivial topology, surrounded by an infinite domain corresponding to $\mathcal{C} = 0$. The Chern numbers $\mathcal{C}^{(\pm)}$ of the two bands are opposite and $\mathcal{C} = \mathcal{C}^{(-)} = -\mathcal{C}^{(+)}$.

1-3 The brick wall version

The brick wall lattice, shown in figure 5, is obtained from a square lattice of period a by removing every second vertical link, while keeping all horizontal links. It was initially proposed as a convenient alternative to the hexagonal lattice that simplifies calculations. The basis vectors of the brick wall lattice in real space

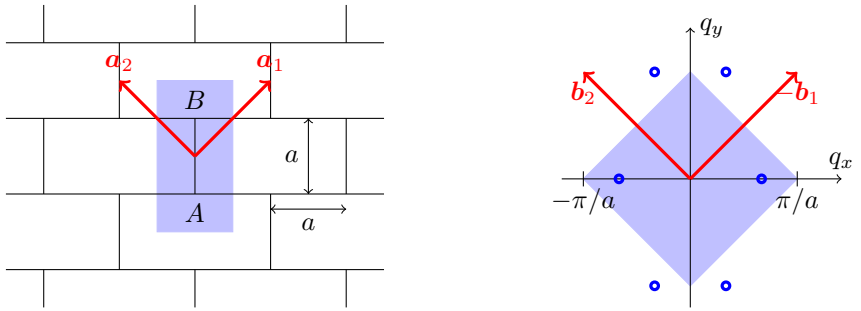

Figure 5. *The brick wall lattice (left) and its Brillouin zone (right); Dirac points are indicated by blue circles. The unit cell has area $2a^2$ and the Brillouin zone has area $2\pi^2/a^2$.*

$$\boldsymbol{a}_1 = a\begin{pmatrix}1\\1\end{pmatrix}, \qquad \boldsymbol{a}_2 = a\begin{pmatrix}-1\\1\end{pmatrix}, \tag{17}$$

are indeed orthogonal, as are the vectors generating the reciprocal space[1] :

$$\boldsymbol{b}_1 = \frac{\pi}{a}\begin{pmatrix}1\\1\end{pmatrix}, \qquad \boldsymbol{b}_2 = \frac{\pi}{a}\begin{pmatrix}-1\\1\end{pmatrix}. \tag{19}$$

Just as for the hexagonal lattice, the unit cell has two sites noted A and B on figure 5 which may have different energies $\pm\Delta$:

$$\hat{H}_{0,\boldsymbol{q}} = \begin{pmatrix}-\Delta & 0\\ 0 & \Delta\end{pmatrix}. \tag{20}$$

If we restrict the tunneling effect to hoppings between nearest neighbors, the Hamiltonian is written in the same way as in (3):

$$\hat{H}_{1,\boldsymbol{q}} = -J\begin{pmatrix}0 & 1+\mathrm{e}^{-\mathrm{i}\boldsymbol{q}\cdot\boldsymbol{a}_1}+\mathrm{e}^{-\mathrm{i}\boldsymbol{q}\cdot\boldsymbol{a}_2}\\ 1+\mathrm{e}^{\mathrm{i}\boldsymbol{q}\cdot\boldsymbol{a}_1}+\mathrm{e}^{\mathrm{i}\boldsymbol{q}\cdot\boldsymbol{a}_2} & 0\end{pmatrix}, \tag{21}$$

[1] As in the previous chapter, we adopt the definition

$$\boldsymbol{b}_1 = 2\pi\frac{\mathcal{R}\boldsymbol{a}_2}{\boldsymbol{a}_1\cdot(\mathcal{R}\boldsymbol{a}_2)}, \qquad \boldsymbol{b}_2 = 2\pi\frac{\mathcal{R}\boldsymbol{a}_1}{\boldsymbol{a}_2\cdot(\mathcal{R}\boldsymbol{a}_1)} \tag{18}$$

where $\mathcal{R}$ denotes the $\pi/2$ rotation.

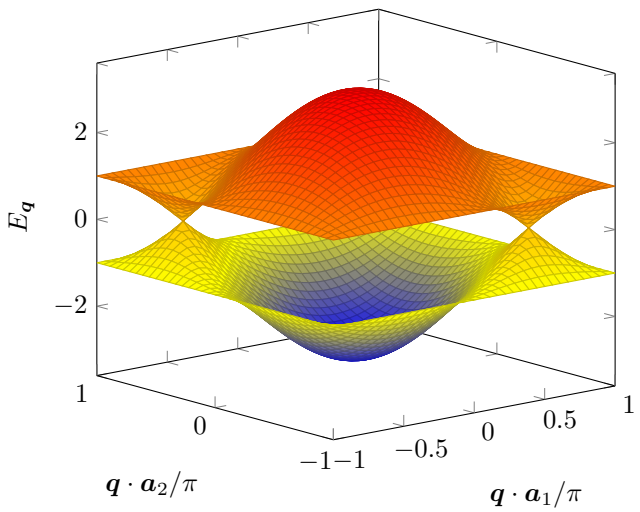

Figure 6. *Band structure of the brick wall lattice.*

and we obtain for $\Delta = 0$ two Dirac points at the cancellation points of $1 + e^{i\boldsymbol{q}\cdot\boldsymbol{a}_1} + e^{i\boldsymbol{q}\cdot\boldsymbol{a}_2}$. These points are located in

$$q_x = 0, \quad q_y = \pm\frac{2\pi}{3a}. \tag{22}$$

This lattice has acquired its experimental "credentials" with the Zurich experiment of Tarruell, Greif, et al. (2012), which showed how to realize it in practice by a superposition of standing light waves arranged along orthogonal axes. These experiments were described and analyzed in the lecture of years 2012-13 and we will not revisit them here.

As for the hexagonal lattice, we can open a gap at the Dirac points and obtain topologically non-trivial bands by adding a coupling between second neighbors as shown in figure 7. Each A or B site has four second neighbors, instead of six for the hexagonal lattice. With the phases shown in figure 7 and the convention specified in figure 2, the Hamiltonian de-

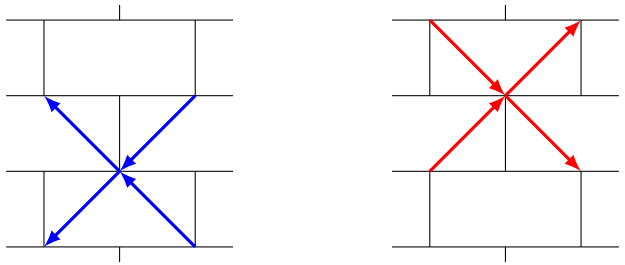

Figure 7. *Coupling between second neighbors in the brick wall lattice for a given A site (left) and for a given B site (right)*

.

scribing the coupling to the second neighbors is written (*cf.* appendix):

$$\begin{aligned}\hat{H}_{2,\boldsymbol{q}} &= -2J'\begin{pmatrix}\sum_{\alpha=1}^{2}\cos(\boldsymbol{q}\cdot\boldsymbol{\rho}_\alpha-\phi_0) & 0\\ 0 & \sum_{\alpha=1}^{2}\cos(\boldsymbol{q}\cdot\boldsymbol{\rho}_\alpha+\phi_0)\end{pmatrix}\\ &= -2J'\cos\phi_0\,\mathcal{C}_{\boldsymbol{q}}\,\hat{1} \;-\; 2J'\sin\phi_0\,\mathcal{S}_{\boldsymbol{q}}\,\hat{\sigma}_z\end{aligned} \tag{23}$$

where we have introduced the vectors

$$\boldsymbol{\rho}_1 = -\boldsymbol{a}_1, \qquad \boldsymbol{\rho}_2 = -\boldsymbol{a}_2, \tag{24}$$

and where we have defined

$$\mathcal{C}_{\boldsymbol{q}} = \sum_{\alpha=1}^{2}\cos(\boldsymbol{q}\cdot\boldsymbol{\rho}_\alpha), \qquad \mathcal{S}_{\boldsymbol{q}} = \sum_{\alpha=1}^{2}\sin(\boldsymbol{q}\cdot\boldsymbol{\rho}_\alpha). \tag{25}$$

The only difference from the original Haldane model is that the sum over the index α in (23-25) is now only over $\alpha = 1, 2$. Apart from this point, the analysis of the band topology of this lattice is in all respects similar to what we have seen above and we obtain a phase diagram similar to that in figure 4, with a topological region defined by:

$$\frac{|\Delta|}{J'} < 2\sqrt{3}\,|\sin\phi_0|. \tag{26}$$

1-4 Tight-binding limit and Berry curvature

In the previous chapter, we have shown why the Berry curvature $\Omega_{\boldsymbol{q}}$ appears to be a natural tool to characterize the transport induced by a force $\boldsymbol{F}$ in a topologically non-trivial band. We have treated the position of the particles as a continuous variable $\boldsymbol{r}$, with the Bloch functions

$$\psi_{\boldsymbol{q}}^{(j)}(\boldsymbol{r}) = \mathrm{e}^{\mathrm{i}\boldsymbol{q}\cdot\boldsymbol{r}} u_{\boldsymbol{q}}^{(j)}(\boldsymbol{r}), \tag{27}$$

and an infinite number of energy bands, marked by the index $j = 0, 1, 2, \ldots$. The action of the force $\boldsymbol{F}$ was described by the potential

$$\hat{V} = -\boldsymbol{F}\cdot\hat{\boldsymbol{r}}. \tag{28}$$

The tight-binding approximation we use here brings two modifications to this approach, the first one of practical order, and the other more conceptual. The practical modification comes from the fact that the number of bands is finite, which provides a simple relation between the Berry curvatures of the different bands. The conceptual modification comes from the fact that we discretize the position of the particles, which can lead to some ambiguity when writing the potentials as in (28).

Let us start by recalling a simple expression for the Berry curvature, whose detailed proof was given in the lecture of years 2013-14 (chapter 3). Starting from a unit cell with n sites (with $n = 2$ for the Haldane model), the periodic Hamiltonian $\hat{H}_{\boldsymbol{q}}$ is a $n \times n$ matrix and we find n energy bands $E_{\boldsymbol{q}}^{(j)}$, $j = 1, \ldots, n$, with eigenstates $|u_{\boldsymbol{q}}^{(j)}\rangle$. We can then show that

$$\boldsymbol{\Omega}_{\boldsymbol{q}}^{(j)} = \mathrm{i}\sum_{j'\neq j} \frac{\langle u_{\boldsymbol{q}}^{(j)}|\ \boldsymbol{\nabla}_{\boldsymbol{q}}\hat{H}_{\boldsymbol{q}}\ |u_{\boldsymbol{q}}^{(j')}\rangle\ \times\ \langle u_{\boldsymbol{q}}^{(j')}|\ \boldsymbol{\nabla}_{\boldsymbol{q}}\hat{H}_{\boldsymbol{q}}\ |u_{\boldsymbol{q}}^{(j)}\rangle}{\left(E_{\boldsymbol{q}}^{(j)} - E_{\boldsymbol{q}}^{(j')}\right)^2}. \tag{29}$$

The interest of this result is that it involves the gradient with respect to $\boldsymbol{q}$ of the Hamiltonian $\hat{H}_{\boldsymbol{q}}$, which is a regular function, rather than the gradient of the eigenvectors $|u_{\boldsymbol{q}}^{(j)}\rangle$, which can present singularities, as we have seen.

Once this result is acquired, it is simple to show that the sum of n Berry curvatures

$$\sum_{j=1}^{n} \boldsymbol{\Omega}_{\boldsymbol{q}}^{(j)} \tag{30}$$

is zero at any momentum $\boldsymbol{q}$ of the Brillouin zone, because each pair (j, j') contributes twice to the sum, and these two contributions are equal in absolute value and of opposite signs. We deduce that the sum of the Chern numbers of the n energy bands is also zero:

$$\sum_{j=1}^{n} \mathcal{C}^{(j)} = 0 \tag{31}$$

This result does not generalize to the infinite case: for example, for a free particle immersed in a magnetic field, the energy bands are the Landau levels which all have the same Chern number $|\mathcal{C}| = 1$.

Let us now turn to the second point, which deals with the ambiguity resulting from our discretization of the position. We will reason on a unit cell with two sites, but the generalization to n sites is immediate. We have chosen so far to parameterize our Bloch states in the form

$$|\psi_{\boldsymbol{q}}\rangle = \sum_{\boldsymbol{j}} \mathrm{e}^{i\,\boldsymbol{q}\cdot\boldsymbol{r}_{\boldsymbol{j}}}\ (\alpha_{\boldsymbol{q}}|A_{\boldsymbol{j}}\rangle + \beta_{\boldsymbol{q}}|B_{\boldsymbol{j}}\rangle) \tag{32}$$

which amounts to assigning the same position $\boldsymbol{r}_{\boldsymbol{j}}$ to both sites A and B of the cell $\boldsymbol{j}$. This can cause a problem when we have to take into account the presence of an external force; indeed, the potential $\hat{V}$ from which this force derives – which is the discretized version of (28) – should not in principle take the same value on the sites A and B of the same cell. The remedy is, at first sight, simple: it is enough to "encode" the position of each site A or B in a given cell by writing the Bloch functions in the form:

$$|\psi_{\boldsymbol{q}}\rangle = \sum_{\boldsymbol{j}} \left(\mathrm{e}^{i\,\boldsymbol{q}\cdot(\boldsymbol{r}_{\boldsymbol{j}}+\boldsymbol{R}_A)}\ \tilde{\alpha}_{\boldsymbol{q}}|A_{\boldsymbol{j}}\rangle\ +\ \mathrm{e}^{i\,\boldsymbol{q}\cdot(\boldsymbol{r}_{\boldsymbol{j}}+\boldsymbol{R}_B)}\ \tilde{\beta}_{\boldsymbol{q}}|B_{\boldsymbol{j}}\rangle\right) \tag{33}$$

and to use the same encoding in the expression of $\hat{V}$. In (33), the vectors $\boldsymbol{R}_{A,B}$ represent the offsets of sites A and B from the center $\boldsymbol{r}_j$ of their cell. The coefficients $\tilde{\alpha}_{\boldsymbol{q}}$ and $\tilde{\beta}_{\boldsymbol{q}}$ are deduced from $\alpha_{\boldsymbol{q}}$ and $\beta_{\boldsymbol{q}}$ by the simple unitary transformation

$$\begin{pmatrix}\tilde{\alpha}_{\boldsymbol{q}}\\ \tilde{\beta}_{\boldsymbol{q}}\end{pmatrix} = \hat{U}_{\boldsymbol{q}}\begin{pmatrix}\alpha_{\boldsymbol{q}}\\ \beta_{\boldsymbol{q}}\end{pmatrix} \qquad \text{with} \quad \hat{U}_{\boldsymbol{q}} = \begin{pmatrix}\mathrm{e}^{-\mathrm{i}\boldsymbol{q}\cdot\boldsymbol{R}_A} & 0\\ 0 & \mathrm{e}^{-\mathrm{i}\boldsymbol{q}\cdot\boldsymbol{R}_B}\end{pmatrix} \tag{34}$$

and the Hamiltonian allowing to determine them is

$$\hat{\tilde{H}}_{\boldsymbol{q}} = \hat{U}_{\boldsymbol{q}}\ \hat{H}_{\boldsymbol{q}}\ \hat{U}_{\boldsymbol{q}}^{\dagger}. \tag{35}$$

The disadvantage of this new Hamiltonian $\hat{\tilde{H}}_{\boldsymbol{q}}$ is that it is no longer periodic on the reciprocal lattice, contrary to the initial Hamiltonian $\hat{H}_{\boldsymbol{q}}$, because the operator $\hat{U}_{\boldsymbol{q}}$ is not:

$$\hat{H}_{\boldsymbol{q}+\boldsymbol{Q}} = \hat{H}_{\boldsymbol{q}} \qquad \text{but} \qquad \hat{\tilde{H}}_{\boldsymbol{q}+\boldsymbol{Q}} \neq \hat{\tilde{H}}_{\boldsymbol{q}}. \tag{36}$$

It is thus more delicate to use the results of the adiabatic theorem when one carries out a $\boldsymbol{q} \to \boldsymbol{q} + \boldsymbol{Q}$ path in the Brillouin zone. This is why we have preferred to use so far the Hamiltonian $\hat{H}_{\boldsymbol{q}}$ "without the encoding of the position".

On the other hand, for problems related to transport, in particular to local measurements in momentum space, it is preferable to use the expression (33) of the Bloch states and thus $\hat{\tilde{H}}$ because the effect of a force is easier to take into account. It is important to note that the Berry curvature is not invariant in the change

$$\hat{H}_{\boldsymbol{q}} \quad \longrightarrow \quad \hat{\tilde{H}}_{\boldsymbol{q}}. \tag{37}$$

This is not a simple change of gauge, but a more general unitary transformation[2]. An "experimental measurement of the Berry curvature" as we describe in this lecture supposes in fact an experimental protocol which includes a precise choice of the writing of the Bloch states (32) or (33), which must be specified in order to give an unambiguous meaning to the results. Switching from one convention to the other is of course possible, and the Appendix D of Cooper, Dalibard, et al. (2018) can be consulted for more details.

Finally, let us note that the topological characterization in terms of Chern number is fortunately not modified by the passage from (32) to (33); the Berry curvatures $\Omega_{\boldsymbol{q}}$ and $\tilde{\Omega}_{\boldsymbol{q}}$ may differ, but they have the same integral over the Brillouin zone.

1-5 Examples for the brick wall lattice

As an example, we have plotted in figures 8 and 9 (on the top) the Berry curvature $\Omega_{\boldsymbol{q}}$ of the lowest band computed for the brick wall lattice for

[2] A change of gauge is the same as multiplying the coefficients α, β by the same quantity $e^{i\chi_{\boldsymbol{q}}}$, which is not the case with the transformation (34).

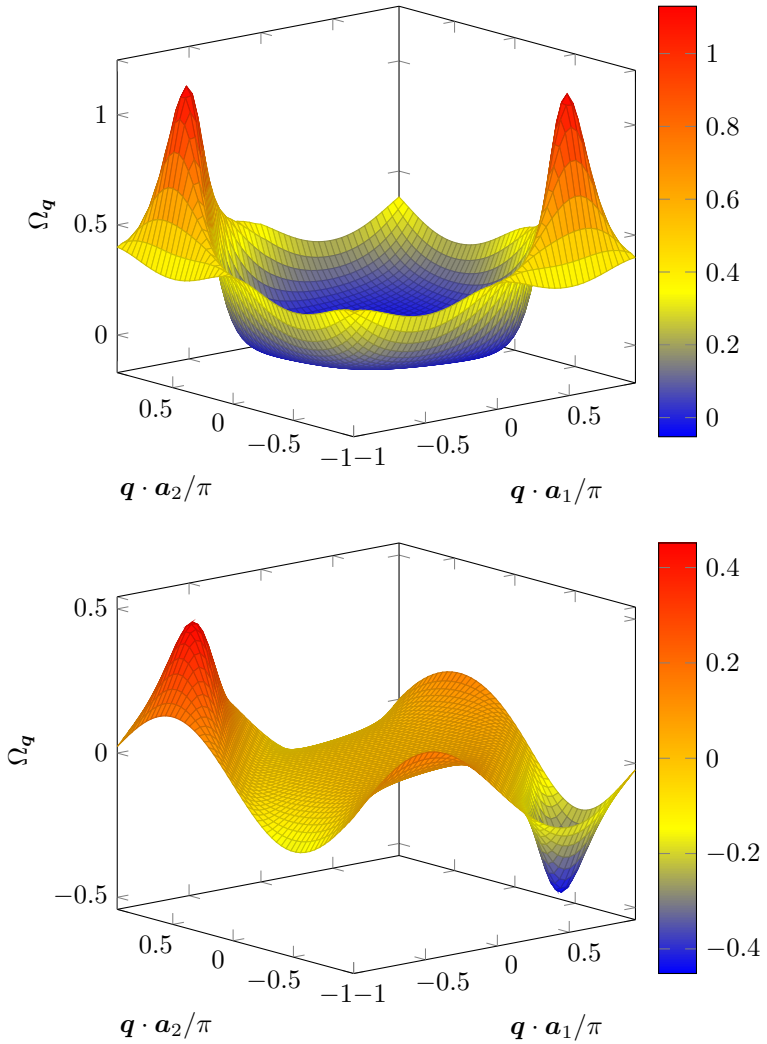

Figure 8. *Berry curvature $\Omega_{\boldsymbol{q}}$ for the lower band of the brick wall lattice, with Bloch states (32) "without encoding the position". Top: topological band, with a coupling to second neighbors $J' = 0.2\,J$, $\phi_0 = \pi/2$ and $\Delta = 0$. The corresponding Chern number (integral of $\Omega_{\boldsymbol{q}}$ divided by 2π) is equal to 1. Bottom: non topological band, with $J' = 0$, $\Delta = J$. In this time-reversal invariant case, we have $\Omega_{-\boldsymbol{q}} = -\Omega_{-\boldsymbol{q}}$ and the integral over the Brillouin zone is zero, thus $\mathcal{C} = 0$.*

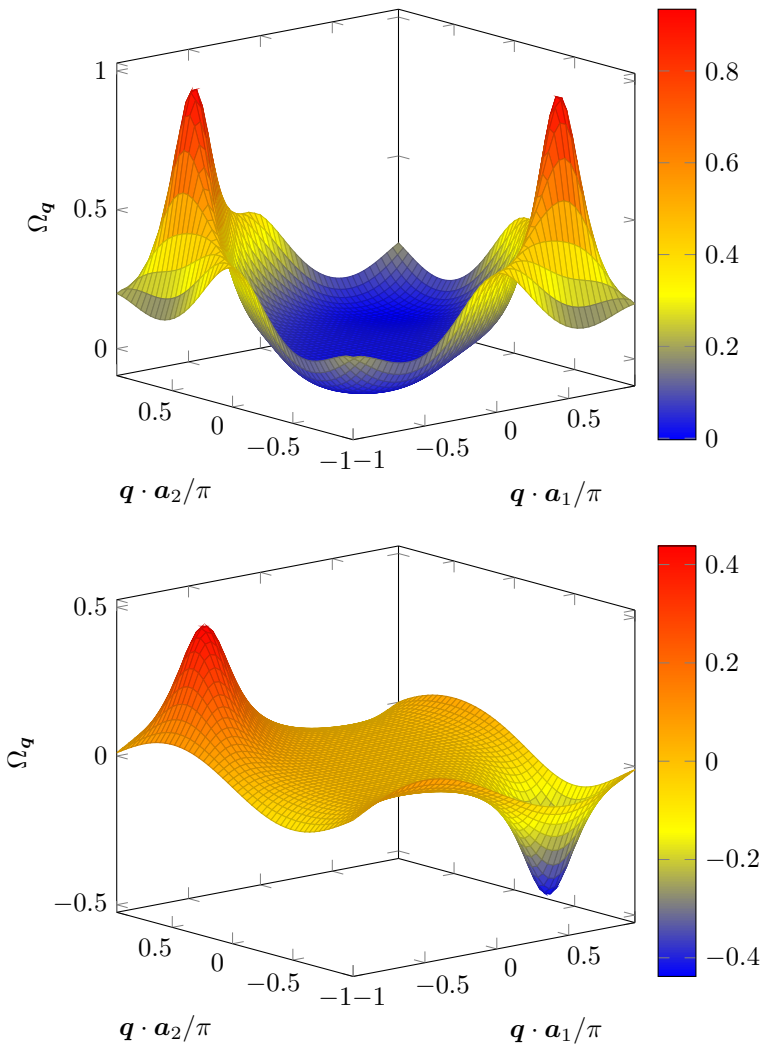

Figure 9. *Berry curvature $\Omega_{\boldsymbol{q}}$ for the lower band of the brick wall lattice, with Bloch states (33) "with the encoding of the position". Top: topological band, with a coupling to second neighbors $J' = 0.2\,J$, $\phi_0 = \pi/2$ and $\Delta = 0$. The corresponding Chern number (integral of $\Omega_{\boldsymbol{q}}$ divided by 2π) is equal to 1. Bottom: non topological band, with $J' = 0$, $\Delta = J$. In this time-reversal invariant case, we have $\Omega_{-\boldsymbol{q}} = -\Omega_{-\boldsymbol{q}}$ and the integral over the Brillouin zone is zero, thus $\mathcal{C} = 0$.*

parameters located at the center of the topological region: $J' = 0.2\,J$, $\phi_0 = \pi/2$ and $\Delta = 0$. This calculation has been done with the version (32) of the Bloch states, i.e. without encoding the position for figure 8 (resp. with the encoding of the position for figure 9). We can see in both cases that this curvature takes values significantly different from 0 around the position of the (former) Dirac points. We verify in both cases that the integral of $\Omega_{\boldsymbol{q}}$ on the Brillouin zone is equal to 2π, corresponding to a Chern number $\mathcal{C} = 1$. The figures 8 and 9 (on the bottom) are obtained for parameters located in the non-topological region $J' = 0$, $\Delta = J$; the Berry curvature then has a zero integral over the Brillouin zone, i.e. $C = 0$.

2 Time modulation and topology

We now turn to the description of the experimental realization of the Haldane model with cold atoms, performed by Jotzu, Messer, et al. (2014). Its principle is to start from a brick wall lattice with its two Dirac points, and to lift the degeneracy at these points to obtain two disjoint and topological bands.

As we have seen, the simplest method to lift the degeneracy in this type of lattice is to give different energies $\pm\Delta$ to the two sites A and B, but it does not lead to topological bands, since it does not break the time reversal invariance. The Berry curvature at the two Dirac points takes opposite values, and its integral over the Brillouin zone remains zero [figures 8 or 9 (bottom)].

In order to obtain two topological bands, one must "rectify" the Berry curvature, i.e. open the gap at the Dirac points while making sure that the resulting Berry curvature has the same sign at these two points [figures 8 or 9 (top)]. This can be achieved by modulating in time the parameters of the lattice: this is the principle of "shaken lattices", which allows to break the time reversal invariance and which we will now describe. Note that this approach was first proposed in condensed matter physics by Oka & Aoki (2009), who suggested to illuminate a graphene sheet with circularly polarized light to open a topologically non-trivial gap at the Dirac points (see also Gu, Fertig, et al. (2011)).

2-1 The shaken lattices

A convenient method to obtain complex tunnel coefficients in an optical lattice is to modulate in time some parameters of the lattice, and then to look for the resulting effective time-independent Hamiltonian. For a lattice in the tight-binding limit, a relatively simple modulation to implement is a global displacement $\boldsymbol{\rho}_t$ of all sites. For a 2D system, this displacement can be done in a chiral way by taking for example a uniform circular motion for $\boldsymbol{\rho}_t$, which allows to obtain non-trivial phases for the tunnel coefficients.

Let us start with an optical lattice described in the tight-binding approximation, with sites located at the points $\boldsymbol{r}_\alpha$. When the lattice is stationary in a Galilean reference frame ($\boldsymbol{\rho} = 0$), the Hamiltonian describing the motion of a particle in this lattice is written

$$\hat{H}_{\rm rest} = \sum_\alpha E_\alpha \hat{P}_\alpha - \sum_{\alpha,\beta} J^{(0)}_{\alpha,\beta}\, |\boldsymbol{r}_\alpha\rangle\langle\boldsymbol{r}_\beta| \tag{38}$$

with $\hat{P}_\alpha = |\boldsymbol{r}_\alpha\rangle\langle\boldsymbol{r}_\alpha|$. The coefficients $J^{(0)}_{\alpha,\beta}$ are real and positive. When the whole lattice moves, the simplest way to describe the dynamics of the system is to switch to the accelerated reference frame linked to the lattice. In this frame, the motion of the lattice is described as an inertial force

$$\boldsymbol{F}_t = -m\ddot{\boldsymbol{\rho}}_t, \tag{39}$$

and the Hamiltonian describing the motion of the particle is then

$$\hat{H}_t = \hat{H}_{\rm rest} - \boldsymbol{F}_t \cdot \hat{\boldsymbol{r}}, \tag{40}$$

where $\hat{\boldsymbol{r}}$ is the position operator in this tight-binding model:

$$\hat{\boldsymbol{r}} = \sum_\alpha \boldsymbol{r}_\alpha\, \hat{P}_\alpha. \tag{41}$$

The additional term in (40) coming from the motion of the lattice is proportional to the acceleration of the lattice, i.e. $\sim \omega^2\rho_0$ for a sinusoidal motion of amplitude ρ_0 and of frequency ω. Here, we are going to study the limit of large ω (compared to the Bohr frequencies of the problem) and we will treat this additional term as a perturbation. The form (40) is therefore not very suitable for this perturbative development and we will start by "lowering the degree" in ω of the perturbation by using an exact unitary transformation.

This unitary transformation has in fact already been encountered in the previous chapter. We introduce

$$\hat{U}_t = \exp[-\mathrm{i}\,\hat{\boldsymbol{r}}\cdot\boldsymbol{A}_t] \qquad \text{with} \quad \boldsymbol{A}_t = \frac{1}{\hbar}\int^t \boldsymbol{F}_{t'}\,\mathrm{d}t' = -\frac{m}{\hbar}\dot{\boldsymbol{\rho}}_t, \tag{42}$$

and we obtain the new Hamiltonian after transformation:

$$\hat{H}_t = \hat{U}_t\hat{H}_t\hat{U}_t^\dagger + \mathrm{i}\hbar\frac{\mathrm{d}\hat{U}_t}{\mathrm{d}t}\hat{U}_t^\dagger. \tag{43}$$

In the present case, the part $E_\alpha\hat{P}_\alpha$ corresponding to the on-site energy in (38) commutes with the unit operator $\hat{U}_t$ and is therefore unchanged. For the terms describing the jump from a β site to an α site, we find

$$\hat{U}_t\, |\boldsymbol{r}_\alpha\rangle\langle\boldsymbol{r}_\beta|\, \hat{U}_t^\dagger = \mathrm{e}^{\mathrm{i}m(\boldsymbol{r}_\alpha-\boldsymbol{r}_\beta)\cdot\dot{\boldsymbol{\rho}}/\hbar}\, |\boldsymbol{r}_\alpha\rangle\langle\boldsymbol{r}_\beta| \tag{44}$$

so that the Hamiltonian of the particle in the reference frame of the lattice after the unitary transformation is written

$$\hat{\tilde{H}}_t = \sum_\alpha E_\alpha\hat{P}_\alpha - \sum_{\alpha,\beta} J_{\alpha,\beta}(t)|\boldsymbol{r}_\alpha\rangle\langle\boldsymbol{r}_\beta|. \tag{45}$$

The global motion of the lattice is then taken into account by a time modulation of the tunnel coefficients:

$$J_{\alpha,\beta}(t) = J^{(0)}_{\alpha,\beta}\, \mathrm{e}^{\mathrm{i}m(\boldsymbol{r}_\alpha-\boldsymbol{r}_\beta)\cdot\dot{\boldsymbol{\rho}}/\hbar}. \tag{46}$$

We note that the time dependence intervenes here via the velocity of the lattice, and not the acceleration as in (40). This corresponds to the lowering of degree in ω mentioned above. More precisely, for a coupling between sites typically $\lambda/2$ apart, where λ is the wavelength of the light used to create the lattice, the argument of the exponential is on the order of

$$K_0 = \frac{m\lambda\omega\rho_0}{2\hbar} = \pi^2\frac{\rho_0}{\lambda}\frac{\hbar\omega}{E_{\rm r}}, \tag{47}$$

a quantity that is chosen ~ 0.8 in the experiments of Jotzu, Messer, et al. (2014).

2-2 Effective Hamiltonian

The treatment of a time-periodic Hamiltonian is in general complicated and one must resort to a numerical approach using the Floquet method to accurately describe the underlying dynamics. However, when the modulation frequency ω of the Hamiltonian is large compared to the Bohr frequencies of the system (here the width and energy band gap of $\hat{H}_{\rm rest}$), one can use an expansion in powers of $1/\omega$ to obtain the most important components of the dynamics.

We will not detail here the whole formalism leading to this effective Hamiltonian and we refer the reader for example to[3] the article by Goldman & Dalibard (2014), which details its derivation as well as the additional terms describing the micro-motion associated with the fast oscillations of the Hamiltonian. The main result is as follows: starting from a time-periodic Hamiltonian represented by its Fourier components $\hat{H}^{(n)}$:

$$\hat{H}_t = \hat{H}^{(0)} + \sum_{n>0} \left(\hat{H}^{(n)} \mathrm{e}^{-\mathrm{i}n\omega t} + \hat{H}^{(-n)} \mathrm{e}^{-\mathrm{i}n\omega t} \right), \tag{48}$$

the effective *time-independent* Hamiltonian is written:

$$\hat{H}_{\rm eff} = \hat{H}^{(0)} + \frac{1}{\hbar\omega} \sum_{n>0} \frac{1}{n} \left[\hat{H}^{(n)}, \hat{H}^{(-n)} \right] + \mathcal{O}(1/\omega^2). \tag{49}$$

The procedure to follow to obtain $\hat{H}_{\rm eff}$ is thus well defined. Starting from the expression of $\hat{H}_t$ in which the time dependence comes from the modulation of the tunnel coefficients, we decompose these tunnel coefficients into Fourier series using

$$\mathrm{e}^{\mathrm{i}z\sin(\omega t)} = \sum_n \mathcal{J}_n(z)\, \mathrm{e}^{\mathrm{i}n\omega t} \tag{50}$$

where $\mathcal{J}_n(z)$ is the Bessel function of order n, which leads to the $\hat{H}^{(n)}$ components of the Hamiltonian. We will now implement this procedure for the brick wall lattice.

[3] We can also refer to the precursor articles of Avan, Cohen-Tannoudji, et al. (1976) and Rahav, Gilary, et al. (2003), as well as Bukov, D'Alessio, et al. (2015) and Eckardt (2017).

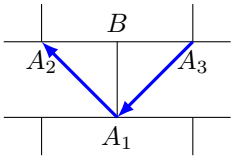

Figure 10. *Site B and its three neighbors A_α, $\alpha = 1, 2, 3$, with couplings induced by lattice vibration.*

2-3 Tunnel coefficients between second neighbors

We wish to apply the general result (49), valid at order 1 in $1/\omega$, to the brick wall lattice. To simplify the algebra, we will focus on a given cell, more precisely on the B site of this cell which we will take localized at $\boldsymbol{r} = 0$. This site is coupled by tunneling to the three sites A which surround it: site A_1 belonging to the same cell and located at $\boldsymbol{r}_1 = -a\,\boldsymbol{u}_x$, and sites A_2 and A_3 located at $\boldsymbol{r}_{2,3} = \pm a\,\boldsymbol{u}_y$ (figure 10).

In the absence of lattice modulation, the part of the Hamiltonian that involves the B site under consideration is

$$-J \left(\sum_{\alpha=1,2,3} |A_\alpha\rangle\langle B| \right) + \text{H.c.} \tag{51}$$

Let us assume that the lattice is shaken according to the elliptical motion

$$\dot{\boldsymbol{\rho}}_t = v_{0,x} \sin(\omega t + \varphi_x)\, \boldsymbol{u}_x + v_{0,y} \sin(\omega t + \varphi_y)\, \boldsymbol{u}_y, \tag{52}$$

so that the Hamiltonian corresponding to the tunneling is written, after the change to the reference frame of the lattice and the unitary transformation:

$$\begin{aligned} \hat{\tilde{H}}_t \;=\; & -J \Big\{ \mathrm{e}^{-\mathrm{i}\kappa_y \sin(\omega t+\varphi_y)} |A_1\rangle\langle B| + \mathrm{e}^{-\mathrm{i}\kappa_x \sin(\omega t+\varphi_x)} |A_2\rangle\langle B| \\ & + \mathrm{e}^{+\mathrm{i}\kappa_x \sin(\omega t+\varphi_x)} |A_3\rangle\langle B| \Big\} + \text{H.c.} \end{aligned} \tag{53}$$

where we have defined $\kappa_{x/y} = mav_{0,x/y}/\hbar$. The Fourier series decomposition of these coefficients then gives [4]

$$\begin{aligned} \hat{H}^{(n)} \;=\; & -J\mathcal{J}_n(\kappa_y)\, \mathrm{e}^{\mathrm{i}n\varphi_y} \left[|B\rangle\langle A_1| + (-1)^n |A_1\rangle\langle B| \right] \\ & - J\mathcal{J}_n(\kappa_x)\, \mathrm{e}^{\mathrm{i}n\varphi_x} \left[|B\rangle\langle A_2| + (-1)^n |A_2\rangle\langle B| + |A_3\rangle\langle B| + (-1)^n |B\rangle\langle A_3| \right] \end{aligned} \tag{54}$$

[4] Note that $\hat{H}^{(n)}$ is not Hermitian, but verifies $(\hat{H}^{(n)})^\dagger = \hat{H}^{(-n)}$.

As we have written above, the parameter $\kappa_{x/y}$ in the Zurich experiment is on the order of 1, so that only the first two Bessel functions $\mathcal{J}_0$ and $\mathcal{J}_1$ take significant values. Let us take from now on

$$\kappa_x = \kappa_y \equiv \kappa \tag{55}$$

to simplify the notations. The term $n = 0$ associated to $\mathcal{J}_0(\kappa)$ corresponds to a renormalization of the tunnel coefficient between nearest neighbors:

$$J \longrightarrow \bar{J} = J\ \mathcal{J}_0(\kappa). \tag{56}$$

The term corresponding to $n = 1$ has the contribution

$$\frac{1}{\hbar\omega}\left[\hat{H}^{(1)}, \hat{H}^{(-1)}\right] \tag{57}$$

which is explicitly calculated by writing $\hat{H}^{(\pm 1)}$ in the form

$$\begin{aligned} \hat{H}^{(+1)} &= +J\ \mathcal{J}_1(\kappa)\left(\mathrm{e}^{+\mathrm{i}\varphi_y}\ \hat{O}_1 + \mathrm{e}^{+\mathrm{i}\varphi_x}\ \hat{O}_{23}\right) \\ \hat{H}^{(-1)} &= -J\ \mathcal{J}_1(\kappa)\left(\mathrm{e}^{-\mathrm{i}\varphi_y}\ \hat{O}_1 + \mathrm{e}^{-\mathrm{i}\varphi_x}\ \hat{O}_{23}\right) \end{aligned} \tag{58}$$

where we have introduced the operators

$$\begin{aligned} \hat{O}_1 &= |A_1\rangle\langle B| - |B\rangle\langle A_1| \\ \hat{O}_{23} &= |A_2\rangle\langle B| - |B\rangle\langle A_2| - |A_3\rangle\langle B| + |B\rangle\langle A_3| \end{aligned} \tag{59}$$

The commutator is then:

$$\left[\hat{H}^{(1)}, \hat{H}^{(-1)}\right] = -\mathrm{i}\ 2J^2\ \mathcal{J}_1^2(\kappa)\sin(\varphi_y - \varphi_x)\ [\hat{O}_1, \hat{O}_{23}] \tag{60}$$

which makes the desired coupling between second neighbors appear in the effective Hamiltonian

$$-\ \bar{J}'\left(\mathrm{e}^{+\mathrm{i}\pi/2}|A_2\rangle\langle A_1| + \mathrm{e}^{+\mathrm{i}\pi/2}|A_1\rangle\langle A_3|\right)\ +\ \mathrm{H.c.} \tag{61}$$

with

$$\bar{J}' = 2\frac{J^2}{\hbar\omega}\ \mathcal{J}_1^2(\kappa)\ \sin(\varphi_y - \varphi_x) \tag{62}$$

This coupling is maximal for a circular motion of the lattice ($\varphi_y - \varphi_x = \pm\pi/2$) and cancels for a linear motion. Whatever the value of $\varphi_y - \varphi_x$,

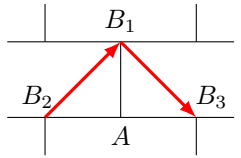

Figure 11. *Site A and its three neighbors B_α, $\alpha = 1, 2, 3$, as well as the couplings induced by the lattice vibration.*

it corresponds to a phase factor $\mathrm{e}^{\pm\pi/2}$ for the links between second neighbors $A-A$, as represented on figure 10. The amplitude J' is by construction small compared to the initial tunnel amplitude J between nearest neighbors, since we have assumed $J \ll \hbar\omega$ for our development.

One can of course do an identical treatment to find the coupling between second neighbors $B-B$. By isolating by thought a site A surrounded by its three immediate neighbors B, we arrive at the couplings shown in figure 11:

$$-\bar{J}'\left(\mathrm{e}^{+\mathrm{i}\pi/2}|B_1\rangle\langle B_2| + \mathrm{e}^{+\mathrm{i}\pi/2}|B_3\rangle\langle B_1|\right)\ +\ \mathrm{H.c.}, \tag{63}$$

which corresponds to the choice made in the first part of this chapter. One can check that at this order of the calculation in $1/\omega$, there is no coupling at longer distance which appears between the different sites of the brick wall lattice.

2-4 The experimental results from Zurich

The experiment by Jotzu, Messer, et al. (2014) was conducted with spin-polarized ^{40}K fermionic atoms. These atoms evolve in a 2D lattice corresponding to a slightly distorted "brick wall", obtained by superposing two standing waves along the x axis and one standing wave along y (figure 12). The energy gap $\pm\Delta$ is controlled by adjusting the relative position of the two standing waves along the x axis. The confinement along the z axis is a weak harmonic trap, so that the experiment is effectively conducted with atomic tubes parallel to the z axis.

The atoms are first prepared in the lowest band of the static lattice,

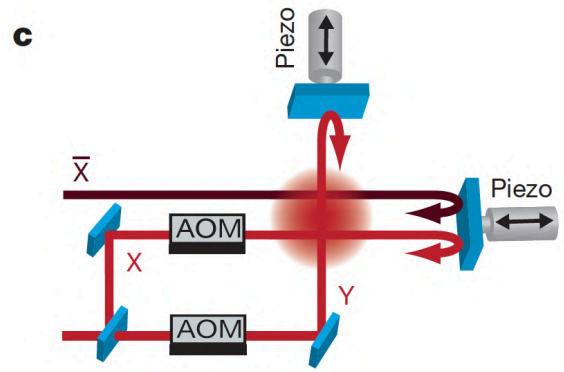

Figure 12. *Experimental diagram used by Jotzu, Messer, et al. (2014) to make an oscillating brick wall lattice, so as to obtain two topologically non-trivial bands.*

then the modulation is switched on within 20 ms. This modulation is obtained by vibrating the retroreflecting mirrors with piezoelectric actuators, in combination with acousto-optic modulators located upstream. This allows to achieve the desired global displacement of the lattice.

Once the degeneracy was lifted at the Dirac points, Jotzu, Messer, et al. (2014) measured the sign of the Berry curvature at these points. To do this, they prepared a wave packet at the center of the Brillouin zone, and then used the Bloch oscillation technique. More precisely, they applied a force $\boldsymbol{F}$ which made this wave packet evolve towards one of the two Dirac points. We have established in the previous chapter the corresponding equations of motion:

$$\hbar \frac{\mathrm{d}\boldsymbol{q}}{\mathrm{d}t} = \boldsymbol{F} \tag{64}$$

$$\hbar \boldsymbol{v}_{\boldsymbol{q}} = \boldsymbol{\nabla} E_{\boldsymbol{q}} + \boldsymbol{\Omega}_{\boldsymbol{q}} \times \boldsymbol{F} \tag{65}$$

The first equation indicates that the quasi-momentum $\boldsymbol{q}$ evolves in the direction of the $\boldsymbol{F}$ force. In the second equation, the term in $\nabla E_{\boldsymbol{q}}$ plays no role after integration over a Bloch period; the term $\boldsymbol{\Omega}_{\boldsymbol{q}} \times \boldsymbol{F}$ is on the contrary essential: it will cause a deflection of the velocity of the wave packet in a direction perpendicular to $\boldsymbol{F}$ and the sign of this deflection informs us directly about the sign of the Berry curvature $\Omega_{\boldsymbol{q}}$.

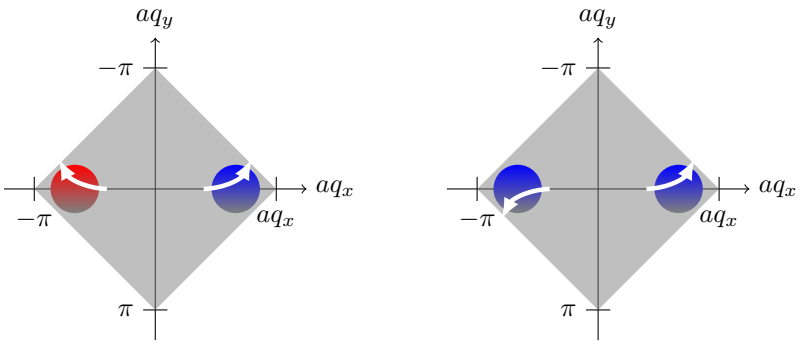

Figure 13. *Principle of the measurement of Berry curvature around Dirac points. If the gap is open without breaking the time reversal invariance (on the left), the Berry curvatures at the two Dirac points are opposite and the deflection of a wave packet at these points will be with opposite chiralities. On the contrary, for topological bands, we expect equal chiralities at these two points (on the right).*

Let us limit ourselves to the two limiting cases (*cf.* figures 4 and 13):

- $\Delta \neq 0$, $J' = 0$, which must correspond to non-topological bands, since we break the invariance by reflection, but not the invariance by time reversal. We must therefore have $\Omega_{\boldsymbol{Q}_-} = -\Omega_{\boldsymbol{Q}_+}$, which means that the wave packets rotate in opposite directions at the two Dirac points, one in the direct direction and the other in the retrograde direction.
- $\Delta = 0$, $J' \neq 0$, which should instead lead to topological bands. The Berry curvature must then take the same value at both Dirac points, and the two wave packets must rotate in the same direction.

The results of Jotzu, Messer, et al. (2014) confirmed these predictions (figure 14). The force $\boldsymbol{F}$, created by a magnetic field gradient, can be applied in either direction (blue and red dots in this figure) to probe the two Dirac points. The authors observed a deflection which reflects a curvature of the trajectories identical to the two Dirac points in the topological case: the Berry curvature has indeed been "rectified".

Jotzu, Messer, et al. (2014) then systematically explored the Δ, J' parameter space and reconstructed a phase diagram that mimics what is ex-

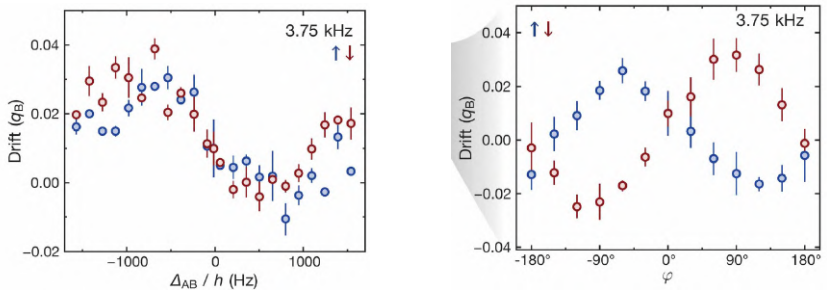

Figure 14. *Displacement of the center of mass of the cloud after passing over one of the two Dirac points. An identical displacement for the two Dirac points means a Berry curvature of opposite sign* (cf. *figure 13). The left figure corresponds to the non topological case : $\phi_0 = 0$ and Δ is varied. The figure on the right corresponds to the topological case: $\Delta = 0$ and $\varphi_x - \varphi_y$ (hence J') is varied. Figures extracted from Jotzu, Messer, et al. (2014).*

pected for the Haldane model, with two "topological lobes" surrounded by a normal region (figure 15).

3 The edge states

We now turn to an essential aspect of the topology of energy bands: the edge states that appear at the junction between two phases of different topology. We have already encountered these states in 1D problems and we will justify in a qualitative way their existence in two dimensions. A more rigorous discussion can be found for example in the article of Hatsugai (1993). We will then give concrete examples[5] using the lattice brick wall and we will end with the description of recent experiments conducted in photonics highlighting these edge states very clearly.

[5]The arguments that we develop here are well adapted to the case of lattices described in a tight-binding model, with a finite number n of bands with $\sum_{j=1}^{n} \mathcal{C}^{(j)} = 0$. The case of Landau levels with an infinite number of bands with each a Chern number $\mathcal{C} = 1$ must be treated differently (see for example the 2013-14 lecture series and references therein).

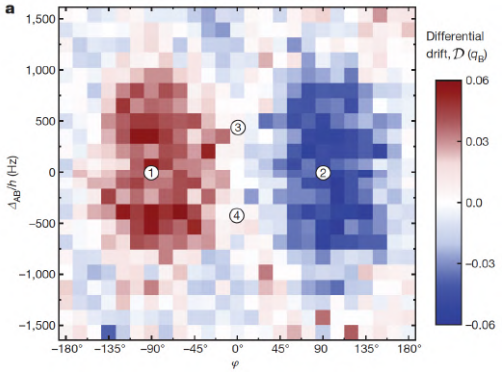

Figure 15. *Phase diagram reconstructed from the Dirac point deflection experiments, to be compared with the theoretical prediction in Figure 4. Figure taken from Jotzu, Messer, et al. (2014).*

3-1 The bulk-edge correspondence

We have already encountered edge states in Chapter 2 in the context of our study of one-dimensional periodic chains. Let us briefly recall the result: when we connect two topologically different versions of a lattice, for example the SSH lattice, a discrete state appears inside the energy gap that exists for an infinite chain. This state is spatially localized around the point where the two half-chains touch (figure 16). A particle prepared in this state remains there indefinitely.

In two dimensions, the junction between two lattices of different topology is done along one or more lines, and the simplest geometric case corresponds to two half-planes of different nature, separated by the axis $y = 0$. We can have for example the vacuum (topologically trivial) in the part $y > 0$ and a topologically non-trivial material in the part $y < 0$.

We will see that in this case edge states also appear, or more precisely an edge channel. This channel includes an infinite number of states, localized near the $y = 0$ axis and propagating along the x axis. Each state is characterized by its momentum q_x and its energy $E(q_x)$.

To be more precise, let us consider a topological material with two

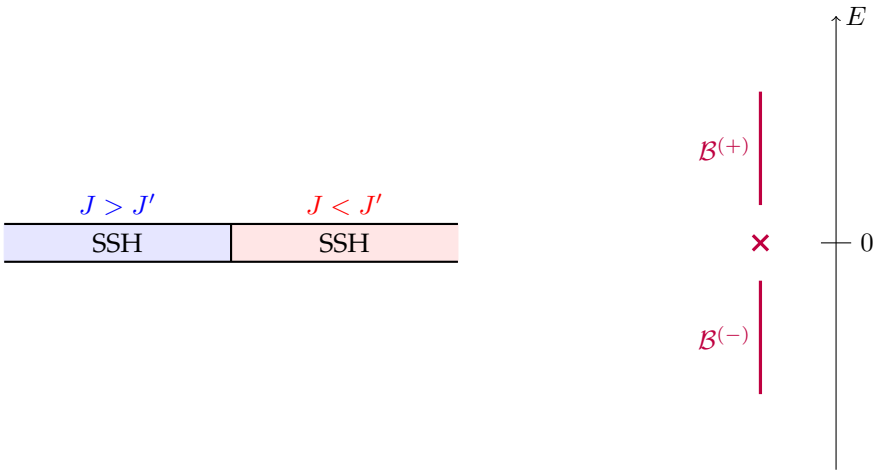

Figure 16. *Appearance of an edge state in a one-dimensional geometry, at the contact point between two SSH chains of different topologies. The energy $E = 0$ of this state is located in the gap between the two bulk energy bands $\mathcal{B}^{(\pm)}$.*

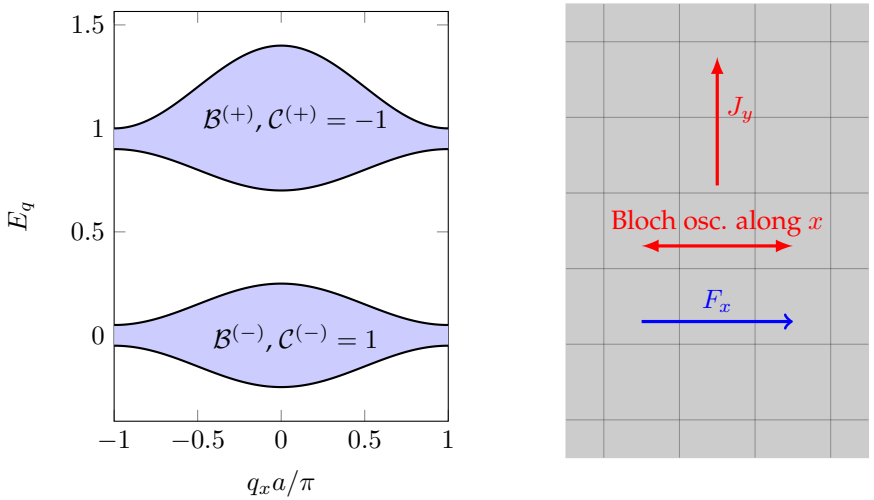

Figure 17. *Topological 2D material with two bands $\mathcal{B}^{(\pm)}$. This material is assumed to be edgeless (it covers the whole plane or occupies a region $L_x \times L_y$ with periodic boundary conditions). The $\mathcal{B}^{(-)}$ band is assumed to be filled and the other empty. A force applied along the x axis induces a Bloch oscillation along the x axis as well as a quantized current density J_y along the y axis.*

bands, whose lowest band $E_{\boldsymbol{q}}^{(-)}$ is characterized by a non-zero Chern number $\mathcal{C}^{(-)}$ (and thus $\mathcal{C}^{(+)} = -\mathcal{C}^{(-)}$). These bands are represented on figure 17 when the index q_x varies in the Brillouin zone. We will assume that the lowest band is filled and the excited band is empty, i.e. there is one particle per lattice cell. If this material fills the whole space, we know that a force applied along the x axis will induce a Bloch oscillation along the x axis, and a quantized current along the y axis. More precisely, during one Bloch period, the index q_x will describe the whole Brillouin zone and a current of $\mathcal{C}^{(-)}$ particles/unit cell will flow along the y axis, for example towards the positive y if the direction of the F_x force is chosen appropriately.

Let us now assume that this same material only fills the half-space $y < 0$ (figure 18). We thus lose the periodicity in y, but we keep the periodicity in x. The q_x component of the Bloch vector remains a "good quantum number", and we can continue to plot the energies of the states as a function of q_x. For the core of the material located far from the interface in the $y < 0$ region, we expect to find the same energy diagram as for the initial case, so at least part of figure 17 remains valid. However, let us examine what happens when we apply the force F_x. It is expected that in the core of the material, the Bloch oscillations will continue to occur along the x direction and a current will be generated in the positive y direction. But there is a problem when the particles arrive at $y = 0$: they cannot pass to the $y > 0$ side (the vacuum) and they cannot accumulate on this line either[6]. How to solve this paradox?

The edge channels will come to our rescue. If there are in the energy diagram $\mathcal{C}^{(-)}$ lines that connect the considered band and the upper band, we will be able to send by this "detour" $\mathcal{C}^{(-)}$ particles to the upper band during each Bloch oscillation, for each unit cell. This compensates exactly the arrival of the quantized current at the $y = 0$ boundary. Once in the

[6] If we are dealing with fermions, we can invoke Pauli's principle directly, but the result is the same for bosons: two initially orthogonal states (located at (x, y_1) and (x, y_2)) must remain orthogonal in the course of a unitary evolution.

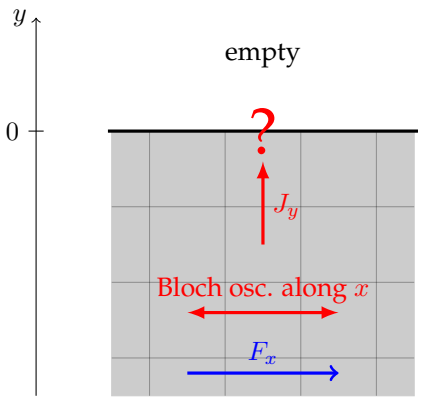

Figure 18. *Material with a topological lowest band as in figure 17, but occupying only half a space. What happens to the current J_y at the interface?*

upper band, the action of the F_x force is reversed and the particles leave towards $y = -\infty$.

We have here a simple illustration of the *bulk-edge* correspondence. Figure 19 illustrates this principle for the case $\mathcal{C}^{(-)} = 1$, with thus a single edge channel, characterized by the energy $E_{q_x}^{(\mathrm{edge})}$ and the group velocity $v_x = \frac{1}{\hbar}\frac{\mathrm{d}}{\mathrm{d}q_x}E_{q_x}^{(\mathrm{edge})}$. The robustness of this edge state is almost obvious on this drawing: it is a link that must necessarily connect two distinct energy bands. If we deform the lattice parameters moderately, this link cannot disappear; the only way to get rid of it is to make the bands touch and then separate again. If the lowest band becomes topologically trivial in this operation, the edge channel disappears.

A pictorial representation of these edge states is often proposed in the framework of the quantum Hall effect. One considers a 2D gas of electrons in a magnetic field perpendicular to the plane. In this case, the energy bands are the Landau levels and they all have a Chern number of 1, so that one effectively expects the presence of edge states. In the core of the material, a classical representation of the motion of an electron corresponds to a circular cyclotron trajectory. There is therefore no transport. On the other hand, these trajectories are interrupted when the electron touches the

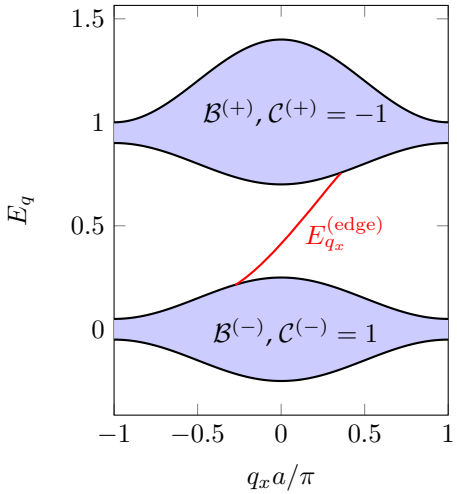

Figure 19. *A typical energy diagram for a material filling only half a space and topologically non-trivial (here $\mathcal{C}^{(-)} = 1$). The quasi-momentum q_x remains a "good quantum number" and we find the same bands as for the whole space (figure 17). We find in addition an edge state, indicated in red, of energy $E_{q_x}^{(\mathrm{edge})}$. This channel allows to "evacuate" towards the upper band the particles which arrive in the vicinity of the $y = 0$ axis, as a consequence of the transport which occurs within the core of the material when a force is applied parallel to its border.*

edge of the sample and one obtains a "skipping orbit" which corresponds to a displacement along the boundary. However, this simple picture does not generalize easily to the general case of a topological band, contrary to the reasoning above based on Bloch oscillations.

3-2 The example of the brick wall lattice: half plane

To make this discussion more quantitative, we have plotted in figures 22 and 23 the eigenenergies E_{q_x} for a half-plane covered by a brick wall lattice, as represented on figure 22. Figure 22 is obtained in the topological case, for $\Delta = 0$, $\phi_0 = \pi/2$. The figure 23 corresponds on the contrary to the normal case $\Delta = J$, $\phi_0 = 0$. In both cases, we have also indicated in the

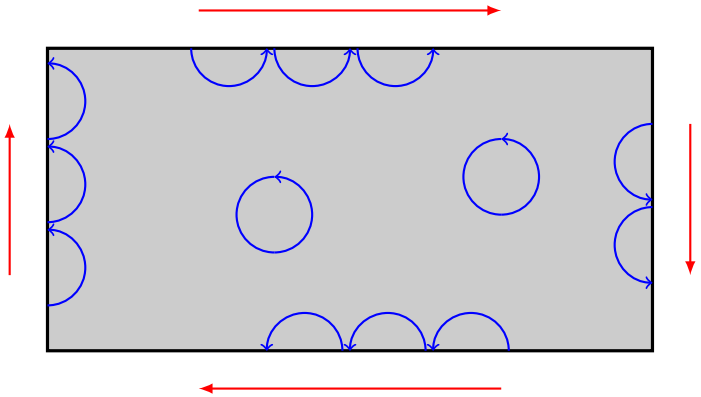

Figure 20. *Interpretation of edge states in the case of charged particles placed in a uniform magnetic field, perpendicular to the plane (the situation of the integer quantum Hall effect).*

upper part of the figure the energy diagram obtained for a whole plane, thus without edge state.

These two diagrams confirm the intuition we have developed above. First, we see that the bulk energy diagram (the bands) are unchanged when we go from the full plane to the half plane. In the topological case, an edge channel appears, corresponding to the $E_{q_x}^{(\text{edge})}$ branch that joins the two $\mathcal{B}^{(\pm)}$ energy bands. In the non-topological case, there are also visible edge state branches, but they do not connect the two bands $\mathcal{B}^{(+)}$ and $\mathcal{B}^{(-)}$. Therefore, these branches have no topological robustness and they can disappear when we deform the lattice. They also strongly depend on the way we cut the material-vacuum interface. This point has been studied in detail for graphene, see for example the book by Bernevig & Hughes (2013) and the references given.

3-3 Example: ribbon in a brick wall lattice

The example of the half-plane that we have developed above has the advantage of being very close to the infinite system from which we started, but it does not allow us to follow the variation of the energies of the different states individually. To remedy this, it is useful to also look at the ribbon geometry, where the system is infinite in one direction, x for example, and has only a finite number n_y of lines in the other direction (figure 24).

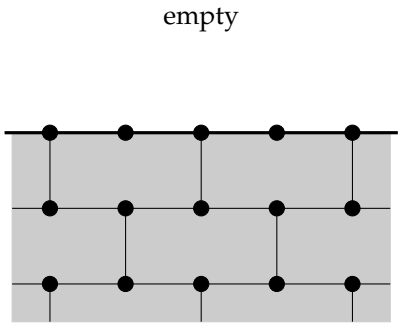

Figure 21. *Brick wall lattice covering the $y < 0$ half-plane. We have not represented the couplings to second neighbors responsible for the appearance of topological properties.*

To search for the eigenstates of this system, one can always use Bloch's theorem in the x direction. For each value of q_x, we have an eigenvalue problem for a Hamiltonian of size $(2n_y) \times (2n_y)$ which we diagonalize numerically. Using the same parameters as in the previous paragraph, we find edge channels connecting the two energy bands in the topological case (figure 25, bottom). Note that we now have two edge channels instead of one, since there is a channel propagating on the top of the ribbon, and a channel propagating on the bottom. For a given value of q_x, the group velocities of these two channels $v_x = \frac{1}{\hbar} \frac{\mathrm{d}}{\mathrm{d}q_x} E_{q_x}^{(\text{edge})}$ are equal in absolute value, and of opposite sign.

In the non-topological case (figure 26, bottom), this study with the ribbon also confirms the results obtained with the half-plane: no edge states connecting the two energy bands, but new states in the vicinity of each band. Note that these edge channels, topological or not, disappear when we take periodic boundary conditions between the two edges of the rib-

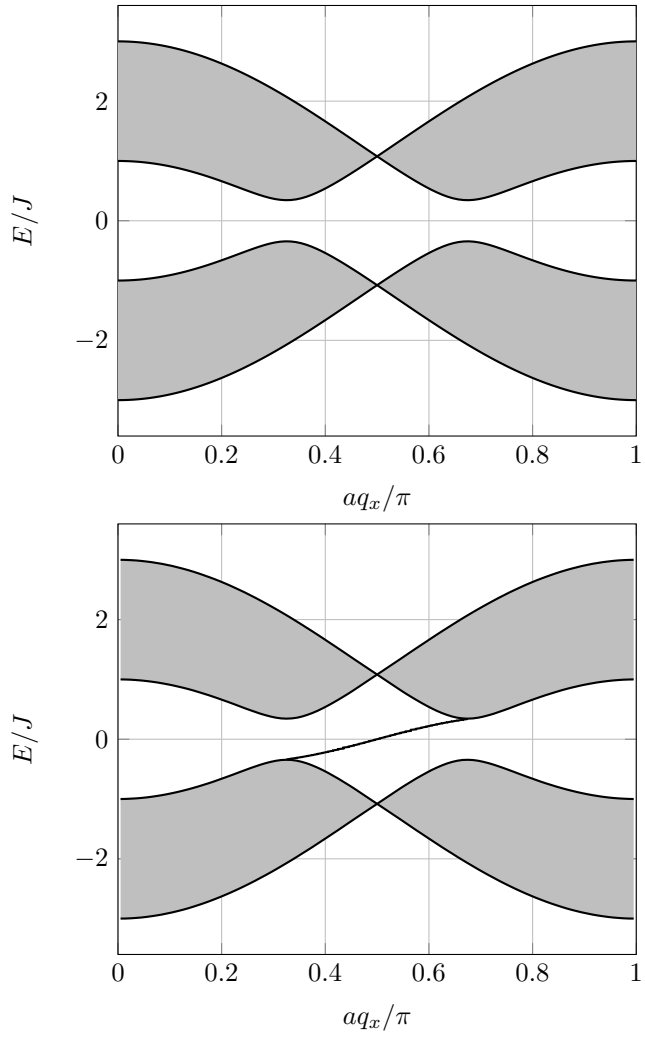

Figure 22. *Energies E_{q_x} for a brick wall lattice in the topological case $J' = J/10$, $\Delta = 0$, $\phi_0 = \pi/2$. Top: whole plane. Bottom: half plane with the presence of an edge state.*

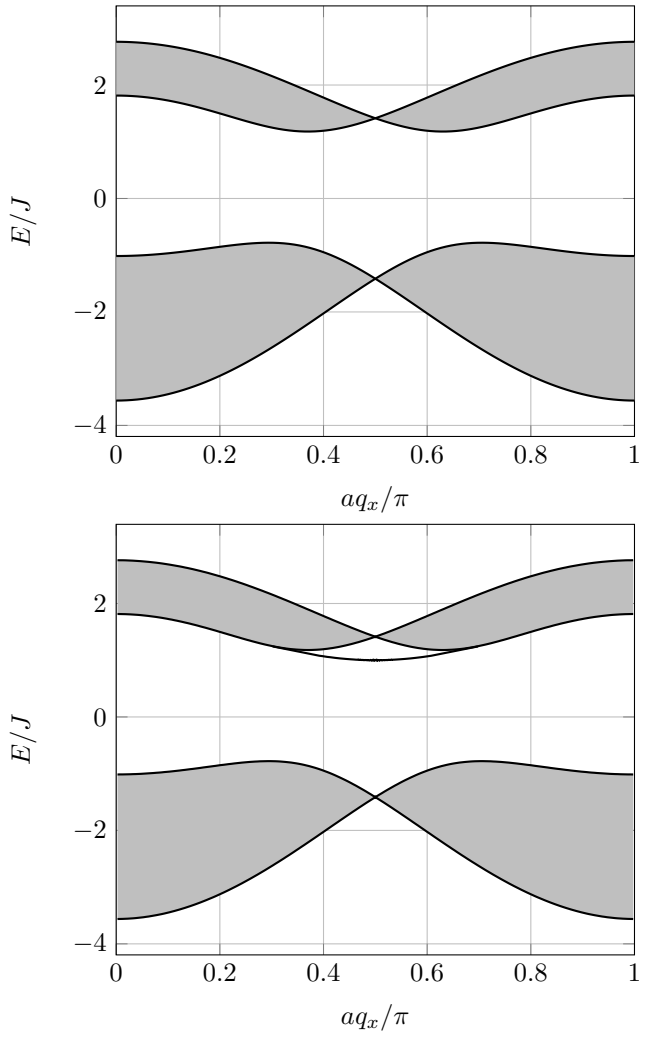

Figure 23. *Energies E_{q_x} for a brick wall lattice in the non-topological case $J' = J/10$, $\Delta = J$, $\phi_0 = 0$. Top: whole plane. Bottom: half plane.*

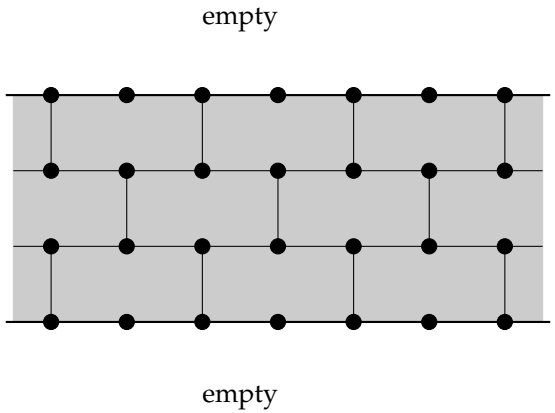

Figure 24. *A ribbon formed with the brick wall lattice, infinite in the x direction and having n_y lines in the y direction (here $n_y = 4$). One can take open boundary conditions along y or periodic boundary conditions by identifying line 1 with line $n_y + 1$.*

bon, as expected (*cf.* top of figures 25 and 26).

To complete our description of these edge channels, we have plotted the energies of a ribbon of only $n_y = 6$ lines in figure 27, which makes it easy to follow each energy level. We have chosen an extended Brillouin zone representation, which allows to visualize what happens in a Bloch oscillation. Let us consider for example a particle prepared at $t = 0$ in the state highlighted in red with the quasi-momentum $q_x = 0$. This is a bulk state since its population is rather concentrated on the central lines of the ribbon. In the presence of a force F_x, the momentum q_x will increase according to the law $q_x = F_x t/\hbar$ and the particle will follow the highlighted state if the force F is not too large. When $q_x a \sim \pi/2$, this state has become an edge state, localized essentially on the top of the ribbon. For $q_x a \sim \pi$, the particle is again localized towards the center of the ribbon, but it has passed into the higher energy band. It then goes back down to the lower band,

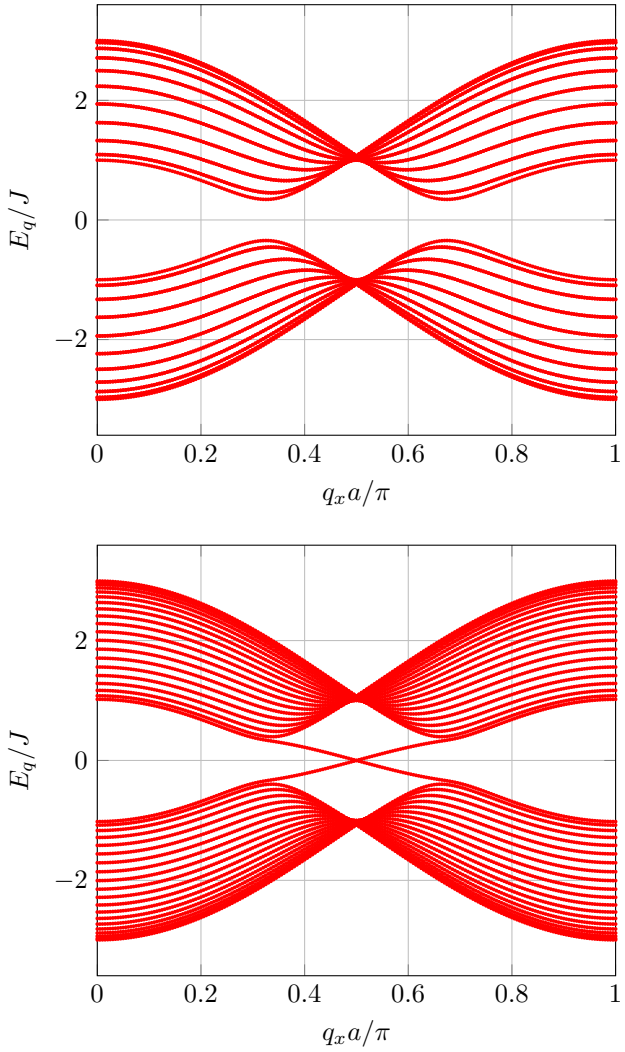

Figure 25. *Brick wall lattice with a ribbon of $n_y = 20$ lines, topological case: $J' = J/10$, $\Delta = 0$, $\phi_0 = \pi/2$. Top: periodic boundary conditions according to y. Bottom: open boundary conditions.*

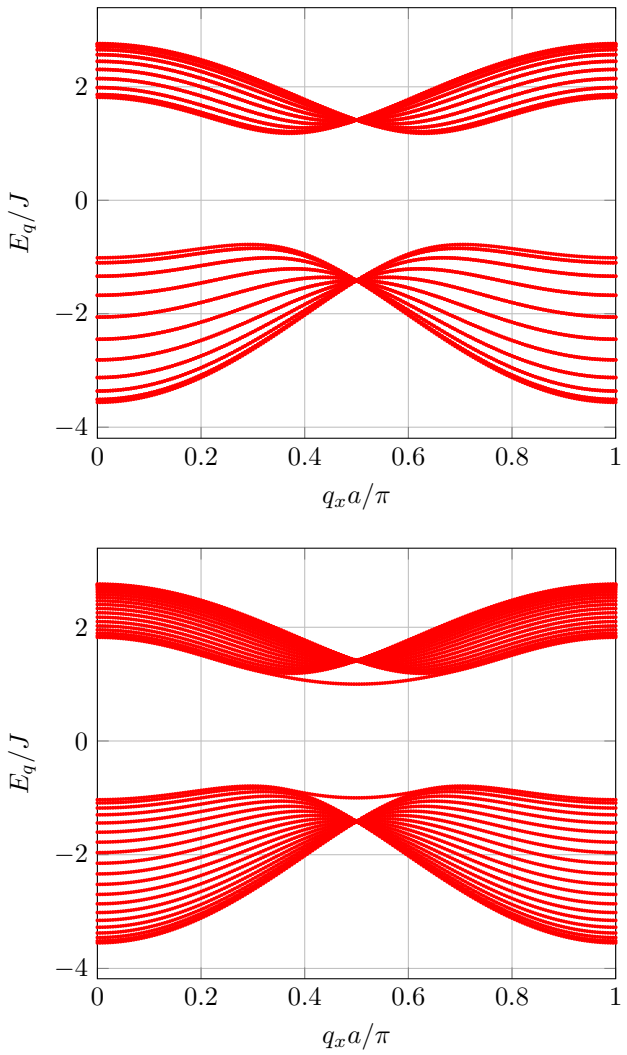

Figure 26. *Brick wall lattice with a ribbon of $n_y = 20$ lines, non-topological case: $J' = J/10$, $\Delta = J$, $\phi_0 = 0$. Top: periodic boundary conditions according to y. Bottom: open boundary conditions.*

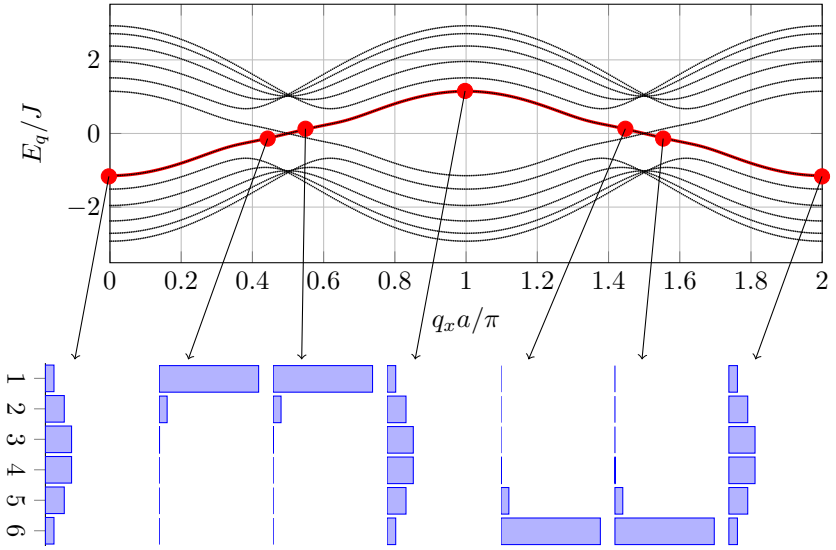

Figure 27. *Top: representation with an extended Brillouin zone of the eigenstates of a ribbon of the brick wall lattice. We chose $n_y = 6$ lines with the same topological situation as in figure 25, $J' = J/10$, $\Delta = 0$, $\phi_0 = \pi/2$. Bottom: the population of the edge channel on the $n_y = 6$ lines is shown for some values of the index q_x.*

this time being localized on the bottom of the ribbon for $q_x a \sim 3\pi/2$. It finally returns to its initial state (at one phase) for $q_x a = 2\pi$. This behavior confirms the argument we have developed earlier for a half-plane.

3-4 Reservoir and quantified transport

The arguments developed above allow to explain the quantization of the transport on a concrete case, when the band is coupled to a reservoir imposing its chemical potential μ. More precisely, let us suppose that μ is located in the gap that separates the lowest band from the excited band. Let us consider a band of finite size L_x along x, having $n_x = L_x/a$ sites with periodic boundary conditions along this axis. The quasi-momentum

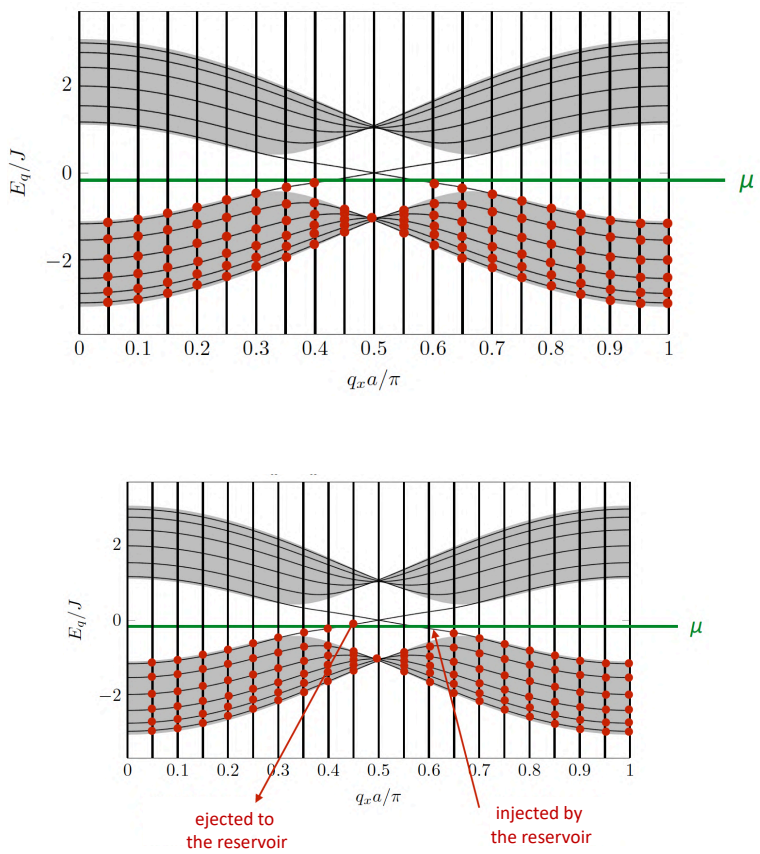

Figure 28. *Quantization of the current when a reservoir imposes its chemical potential μ. Top: we consider a ribbon of finite size $L_x = n_x a$ along x with periodic boundary conditions along this axis, so that the quasi-momenta q_x are quantized. Bottom: we apply a force F_x along the x axis creating a Bloch oscillation of period t_B. In a time $\delta t = t_B/n_x$, each quasi-momentum has increased by one quantum, so the reservoir must move a particle from the top of the ribbon to the bottom of the ribbon to maintain equilibrium.*

q_x is thus quantized and can take one of n_x values

$$q_x = \frac{\pi}{a}\left(-1 + \frac{2j_x}{n_x}\right) \qquad \text{with} \quad j_x = 1, \ldots, n_x. \tag{66}$$

Assume that the lowest band is filled up to the value μ (figure 28, top) and apply a force F_x along the x axis. The equation of motion $\hbar \dot{q}_x = F_x$ tells us that the period of the Bloch oscillation, i.e. the time needed to travel through the Brillouin zone of width $2\pi/a$, is $t_B = 2\pi\hbar/(Fa)$. During the time

$$\delta t = \frac{t_B}{n_x} = \frac{2\pi\hbar}{F_x L_x}, \tag{67}$$

all the quasi-momenta have shifted by a quantum $2\pi/L_x$ to the right. A particle on the rising edge channel has therefore shifted above μ and a particle on a state below μ is missing on the falling edge channel. The role of the reservoir is to restore the equilibrium, which amounts to transferring a particle located at the top of the ribbon to the bottom of the ribbon, the rest of the particles readjusting inside the lowest band. This creates a current along the y direction, and the corresponding current density is

$$J_y = \frac{1/\delta t}{L_x} = \frac{F_x}{2\pi\hbar}, \tag{68}$$

or a conductivity

$$\sigma_{yx} = \frac{J_y}{F_x} = \frac{1}{h}. \tag{69}$$

This conductivity is indeed quantized in units of $1/h$ with a quantum number $\mathcal{C} = 1$, which corresponds to the fact that there is only one rising edge channel.

3-5 Waveguides and passive systems

A nice illustration of the existence of edge states in a Haldane-like model has been provided by Rechtsman, Zeuner, et al. (2013a). These are experiments carried out with a series of parallel waveguides as shown in figure 29. These waveguides are laser etched in silica (refractive index $n_0 = 1.45$) and they correspond to a slight increase of the local index $\Delta n(\boldsymbol{r}) \sim 10^{-3}$.

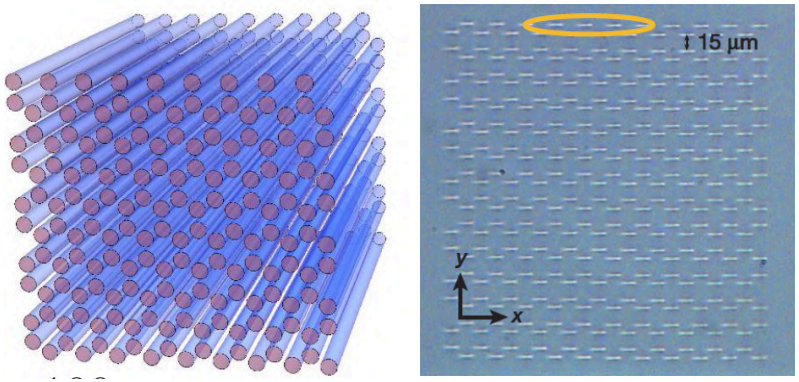

Figure 29. *Series of parallel waveguides forming a hexagonal lattice of side $a = 15\,\mu m$. The propagation length is 10 cm. Each guide is elliptical with major and minor axes 11 and 4 µm. Left: figure extracted from Rechtsman, Zeuner, et al. (2013b). Right: figure extracted from Rechtsman, Zeuner, et al. (2013a).*

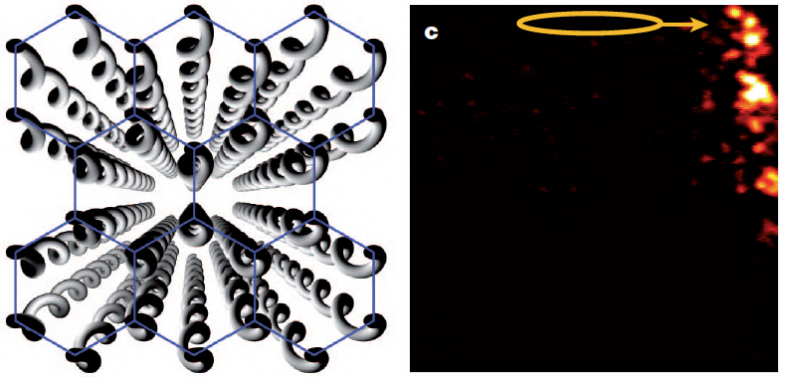

Figure 30. *Left: twisted waveguides, enabling the implementation of the time modulation studied in this chapter and leading to topological bands. Right: edge states observed for a helix radius equal to 8 µm. Figures extracted from Rechtsman, Zeuner, et al. (2013a).*

In the transverse plane, these waveguides are arranged to form a hexagonal lattice. The propagation of the light along the axis of the waveguides is done with a wave number k_0 and it plays the role of time as it was appearing in the 2D problems we have treated so far. We can thus write an equation for the electric field $\mathcal{E}(\boldsymbol{r})$ which is formally identical to that of a massive particle evolving in two dimensions:

$$\mathrm{i}\frac{\partial \mathcal{E}}{\partial z} = -\frac{1}{2k_0}\left(\frac{\partial^2 \mathcal{E}}{\partial x^2} + \frac{\partial^2 \mathcal{E}}{\partial y^2}\right) - \frac{k_0\,\Delta n(\boldsymbol{r})}{n_0}\mathcal{E}. \tag{70}$$

More precisely, each waveguide contains only one transverse mode and the light can pass from one guide to the neighbouring one, thanks to evanescent wave coupling. We thus realize a situation very close to the tight-binding model to describe the motion of a particle on a lattice. In particular, for an infinite lattice, the dynamics of the electric field $\mathcal{E}(r)$ in the xy plane as it progresses along the z axis is well described by energy bands $E(q_x, q_y)$.

To go from the simple hexagonal lattice to the Haldane model, the time modulation studied above is implemented here by giving a helical shape to the waveguides, with about 20 helix turns over the total propagation distance of 10 cm (figure 30a). As explained above, this gives the energy bands $E(q_x, q_y)$ a topological character and results in edge states for a finite sample size. Rechtsman, Zeuner, et al. (2013a) have worked with samples of square section, comprising between one hundred to a few hundred waveguides. To probe these edge states, they injected light on one side of the square and measured the distribution of the light at the output, after propagation over 10 cm.

A typical example is shown in Figure 30b, with two important features:

- The light hardly scattered towards the core of the sample.
- The light progressed along the edge in a chiral fashion, running clockwise along the boundary of the sample.
- This chiral edge condition is robust: even when passing over the upper right corner of the sample, there was virtually no retroreflection; the light then traveled down the right edge of the sample.

In their paper, Rechtsman, Zeuner, et al. (2013a) performed additional tests to verify the relevance of the model, such as the influence of the radius

of curvature of the helix, and the role of defects deliberately added on the edge of the sample.

3-6 Spin Hall effect

We focused in this chapter on the simplest method to create energy bands of non-trivial topology: we considered a spinless particle and placed ourselves in a situation where the time reversal invariance is broken. This allowed us to obtain a Berry curvature such that $\Omega_{-\boldsymbol{q}} \neq -\Omega_{\boldsymbol{q}}$ and thus a non-zero integral for this Berry curvature (i.e. a Chern number $\mathcal{C} \neq 0$).

Starting in 2005, the idea started to arise that it was also possible to obtain a non-trivial topology for time-reversal invariant problems, by taking advantage of a spin (or pseudo-spin) degree of freedom (Kane & Mele 2005a; Kane & Mele 2005b; Bernevig, Hughes, et al. 2006). The basic idea is to realize a situation where the Chern numbers $\mathcal{C}_\uparrow$ and $\mathcal{C}_\downarrow$ are equal in absolute value, but of opposite sign. There are always $|\mathcal{C}|$ edge channels per spin; these channels propagate in opposite directions, which is indeed compatible with time reversal invariance. The first experimental demonstration of the spin Hall effect was described by König, Wiedmann, et al. (2007).

We will not demonstrate here the algebra corresponding to the description of this spin Hall effect, which is close to what we have encountered so far – with the complication due to the existence of two internal states for the particles instead of one. Let us simply point out that the robustness of the edge states is ensured if there can be no scattering from the $\uparrow$ channel to the $\downarrow$ channel, and vice versa. For fermions, the time-reversal invariance[7] guarantees a topological protection by preventing hybridization between these two channels and thus backscattering on possible defects. For bosons, in particular for photons, this protection does not exist in such a strong way, even if weaker versions have been analyzed (Wu & Hu 2015).

A recent experiment conducted at the JQI (University of Maryland) has demonstrated these edge channels for single photons (Barik, Karasahin, et al. 2018). One starts again with a material formed by hexagonal cells, in this case a photonic crystal (GaAs membrane of $0.16\,\mu$m thickness) in

[7] valid in the absence of magnetic impurities

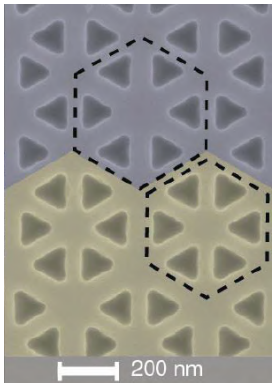

Figure 31. *Figure taken from Barik, Karasahin, et al. (2018).*

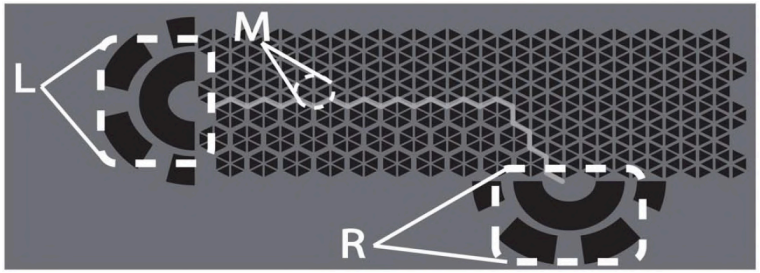

Figure 32. *Figure taken from Barik, Karasahin, et al. (2018)*

which one cuts sets of 6 equilateral triangles as in figure 31. One realizes two topologically distinct phases in

- pushing the triangular holes to the outside of each hexagon, as on the upper part of figure 31;
- pushing the triangular holes toward the inside of each hexagon, as in the lower part of figure 31;

At the boundary between two zones corresponding to these phases (figure 32), we expect to see edge currents appear. More precisely, we are interested in the propagation of an electromagnetic field, with the magnetic

field perpendicular to the plane of the hexagons and the electric field in the plane. The pseudo-spin corresponds to the polarization of this electric field: the two edge channels propagating in opposite directions correspond to the two circular polarizations σ^- or σ^+.

Light is injected into this material thanks to quantum boxes placed inside the GaAs membrane. A precise area of the sample is illuminated in order to excite only the boxes in this area (50 boxes/μm^2). A strong magnetic field (9 Tesla) lifts the degeneracy between the $\sigma_\pm$ polarizations, which allows to determine the polarization of a detected photon by measuring its wavelength. In figure 32, one illuminates zone M and detect the photons in zones L (left) and R (right). One can check that there is a one-to-one relation between the polarization of the photon and the direction of the edge channel (figure 33). One also checks the (relative) robustness of these edge channels. The photons have successfully "taken the bend" of the boundary between the two regions. An analysis of the temporal distribution of the photons (the intensity correlation function $g^2(\tau)$) shows the "particle" character of this propagation by edge channels. The antibunching of the photons emitted by a quantum box can be checked at the level of the detectors.

This type of topologically protected device allows to consider new applications in terms of quantum entanglement between transmitters, as well as the construction of integrated quantum logic gates [see for example Lodahl, Mahmoodian, et al. (2017) and Amo (2018)].

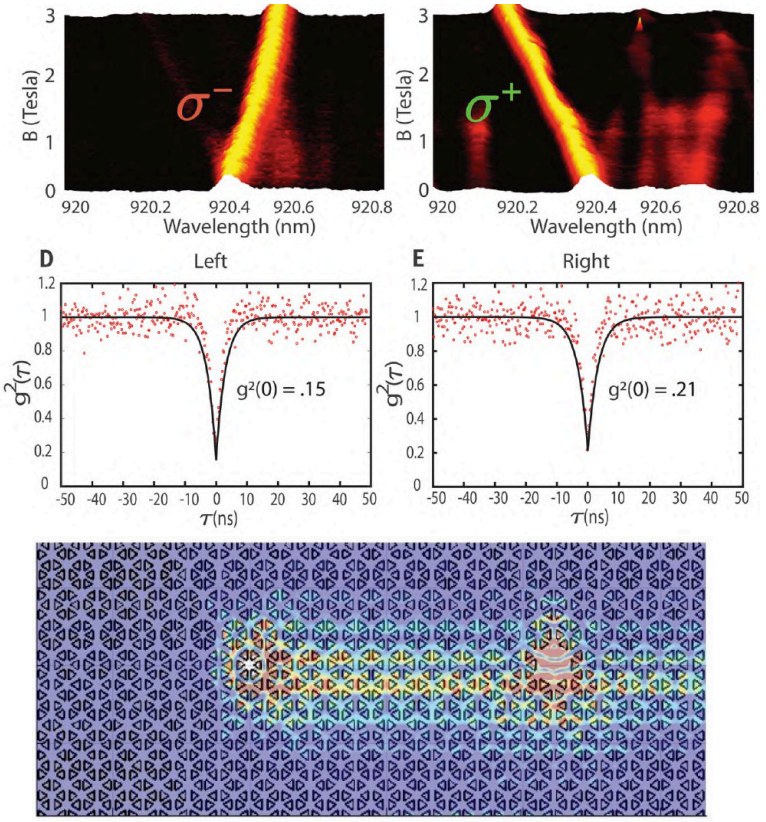

Figure 33. *Figure taken from Barik, Karasahin, et al. (2018)*

Appendix: second neighbor couplings

Haldane model

With the convention of figure 2, the couplings of the A site of the cell $\boldsymbol{r_j}$ to its six second neighbors are written for the Haldane model:

$$-J' \sum_{\alpha=1}^{3} \left(\mathrm{e}^{+\mathrm{i}\phi_0} |A, \boldsymbol{r}_j\rangle\langle A, \boldsymbol{r}_j - \boldsymbol{\rho}_\alpha| \; + \; \mathrm{e}^{-\mathrm{i}\phi_0} |A, \boldsymbol{r}_j\rangle\langle A, \boldsymbol{r}_j + \boldsymbol{\rho}_\alpha| \right) + \text{H.c.} \quad (71)$$

and for the B site of this same cell:

$$-J' \sum_{\alpha=1}^{3} \left(\mathrm{e}^{-\mathrm{i}\phi_0} |B, \boldsymbol{r}_j\rangle\langle B, \boldsymbol{r}_j - \boldsymbol{\rho}_\alpha| \; + \; \mathrm{e}^{+\mathrm{i}\phi_0} |B, \boldsymbol{r}_j\rangle\langle B, \boldsymbol{r}_j + \boldsymbol{\rho}_\alpha| \right) + \text{H.c.} \quad (72)$$

Starting from the Bloch function

$$|\psi_{\boldsymbol{q}}\rangle = \sum_{\boldsymbol{j}} \mathrm{e}^{\mathrm{i}\boldsymbol{q}\cdot\boldsymbol{r}_j} \left(\alpha_{\boldsymbol{q}} |A, \boldsymbol{r}_j\rangle + \beta_{\boldsymbol{q}} |B, \boldsymbol{r}_j\rangle \right), \quad (73)$$

we write the eigenvalue equation for the Hamiltonian

$$\hat{H}|\psi_{\boldsymbol{q}}\rangle = E_{\boldsymbol{q}} \, |\psi_{\boldsymbol{q}}\rangle \quad \Rightarrow \quad \langle A, \boldsymbol{r}_j|\hat{H}|\psi_{\boldsymbol{q}}\rangle = E_{\boldsymbol{q}} \, \langle A, \boldsymbol{r}_j|\psi_{\boldsymbol{q}}\rangle \quad (74)$$

which gives for the coupling to second neighbors

$$-J'\alpha_{\boldsymbol{q}} \sum_{\alpha=1}^{3} \left(\mathrm{e}^{+\mathrm{i}\phi_0} \mathrm{e}^{\mathrm{i}\boldsymbol{q}\cdot(\boldsymbol{r}_j - \boldsymbol{\rho}_\alpha)} \; + \; \mathrm{e}^{-\mathrm{i}\phi_0} \mathrm{e}^{\mathrm{i}\boldsymbol{q}\cdot(\boldsymbol{r}_j + \boldsymbol{\rho}_\alpha)} \right) = E_{\boldsymbol{q}} \, \alpha_{\boldsymbol{q}} \, \mathrm{e}^{\mathrm{i}\boldsymbol{q}\cdot\boldsymbol{r}_j} \quad (75)$$

or

$$\begin{aligned} \hat{H}_{\boldsymbol{q},AA} &= -J' \sum_{\alpha=1}^{3} \left(\mathrm{e}^{+\mathrm{i}(\phi_0 - \boldsymbol{q}\cdot\boldsymbol{\rho}_\alpha)} + \mathrm{e}^{\mathrm{i}(-\phi_0 + \boldsymbol{q}\cdot\boldsymbol{\rho}_\alpha)} \right) \\ &= -2J' \sum_{\alpha=1}^{3} \cos\left(\boldsymbol{q}\cdot\boldsymbol{\rho}_\alpha - \phi_0\right). \end{aligned} \quad (76)$$

The passage from $\hat{H}_{\boldsymbol{q},AA}$ to $\hat{H}_{\boldsymbol{q},BB}$ is done by changing ϕ_0 to $-\phi_0$ [*cf.* (71-72)].

The brick wall

In parallel with what we did for the hexagonal lattice, let us introduce the two vectors ρ_α with $\alpha = 1, 2$:

$$\boldsymbol{\rho}_1 = -\boldsymbol{a}_1 = \begin{pmatrix} -1 \\ -1 \end{pmatrix}, \qquad \boldsymbol{\rho}_2 = \boldsymbol{a}_2 = \begin{pmatrix} -1 \\ 1 \end{pmatrix}. \quad (77)$$

The convention of figure 2 that we have adopted to determine the phase associated with a tunnel link thus gives for the choice represented in figure 7:

$$-J' \sum_{\alpha=1}^{2} \left(\mathrm{e}^{+\mathrm{i}\phi_0} |A, \boldsymbol{r}_j\rangle\langle A, \boldsymbol{r}_j - \boldsymbol{\rho}_\alpha| \; + \; \mathrm{e}^{-\mathrm{i}\phi_0} |A, \boldsymbol{r}_j\rangle\langle A, \boldsymbol{r}_j + \boldsymbol{\rho}_\alpha| \right) + \text{H.c.} \quad (78)$$

The algebra is then identical to the one above for the Haldane model [*cf.* eq. (76)], the only difference being that the sum on α goes from 1 to 2 (instead of 1 to 3).

Chapter VI

Harper-Hofstadter model and integer quantum Hall effect

In this last chapter, we address the problem at the origin of the notion of topological bands: the quantum Hall effect. It is indeed the analysis of the two-dimensional quantum motion of an ensemble of charges placed in a magnetic field that has shown the quantization of quantities related to transport, such as the Hall conductivity, and that has highlighted the importance of edge states. It is also this analysis that has led to the notion of topological robustness in condensed matter physics.

A priori the study of the quantum Hall effect does not require an underlying lattice. This effect occurs when the particles move freely in the xy plane, under the sole effect of the magnetic field $B = B\,\boldsymbol{u}_z$; the energy spectrum then corresponds to the Landau levels. However, in order to make the link with the previous lectures and to describe recent experiments in photonics and cold atom physics, we will mainly concentrate on the case where a periodic potential $V(\boldsymbol{r})$ is also present in the xy plane. The possibility to treat this potential in the tight-binding limit allows one to simplify the analysis considerably: this is the Harper–Hofstadter model.

Once this model is established, we will study its recent implementations in atomic physics and photonics. We will see how they have allowed the explicit measurement of the Chern number of energy bands. We will also show how the edge states associated with this non-trivial topology allow the realization of new devices, topological *lasers*, which exploit the robustness of the bands thus formed.

We will end this chapter with a brief overview of the new possibilities opened by the exploitation of the internal atomic degrees of freedom. These degrees of freedom can form a spatial dimension on their own, a so-called *synthetic dimension*. They can also be used to enrich the energy landscape in which the particles evolve: the energy bands that appear for these "dressed states" can also have a non-trivial topology, very similar to the one of a Landau level. Finally, we will show how this dressing of atoms by light can give rise to non-local interactions between particles.

1 The Harper–Hofstadter Model

The quantum Hall effect concerns the motion of charged particles in the xy plane, in the presence of a magnetic field $\boldsymbol{B} = B\,\boldsymbol{u}_z$ perpendicular to this plane. The Harper–Hofstadter model[1] is a discretized version of this problem: the particles are placed on a regular lattice, square or triangular, described in the tight-binding limit with only couplings between nearest neighbors. The presence of the magnetic field is taken into account by non-real hopping amplitudes between adjacent sites.

In this section, we will first recall some results of the continuous problem, in particular the spectrum consisting in equidistant Landau levels,

[1] More precisely, Harper (1955) showed that the study of this motion can be reduced to a one-dimensional problem, the weak field limit of which he studied, thus recovering the Landau levels. Hofstadter (1976) deepened this study by showing the fractal nature of the spectrum, which becomes significant for large magnetic fields.

before moving on to the discretized problem.

1-1 Landau levels

We begin our discussion with a brief reminder about the quantum treatment of the motion of a charged particle in a uniform magnetic field $\boldsymbol{B} = B\,\boldsymbol{u}_z$. This problem is discussed in most quantum mechanics textbooks and we studied it in detail in the lecture of years 2013-14. We will therefore limit ourselves to giving the few relevant elements in relation to our main topic, topological energy bands.

The Hamiltonian describing the motion of the particle of mass m and charge e is written

$$\hat{H} = \left(\hat{\boldsymbol{p}} - e\boldsymbol{A}(\hat{\boldsymbol{r}})\right)^2 / 2m \tag{1}$$

where $\hat{\boldsymbol{r}}$ and $\hat{\boldsymbol{p}} = -\mathrm{i}\hbar\boldsymbol{\nabla}_{\boldsymbol{r}}$ denote the position and momentum operators of the particle. The vector potential is defined up to a gauge transform and satisfies the equation

$$\boldsymbol{\nabla} \times \boldsymbol{A} = \boldsymbol{B}. \tag{2}$$

We will limit ourselves here to the motion of the particle in the xy plane perpendicular to the magnetic field. The energy spectrum is simply obtained by noting that the Hamiltonian can be written

$$\hat{H} = \frac{1}{2m}\left(\hat{\Pi}_x^2 + \hat{\Pi}_y^2\right), \tag{3}$$

where we introduced the *kinetic momentum* operator

$$\hat{\boldsymbol{\Pi}} = \hat{\boldsymbol{p}} - e\boldsymbol{A}(\hat{\boldsymbol{r}}). \tag{4}$$

The two components of this operator verify the commutation relation

$$[\hat{\Pi}_x, \hat{\Pi}_y] = \mathrm{i}\,\hbar e B \tag{5}$$

so that the algebra of these components is formally identical to that of a harmonic oscillator

$$\hat{H} = \frac{\hbar\omega}{2}\left(\hat{X}^2 + \hat{P}^2\right) \qquad \text{with} \quad [\hat{X}, \hat{P}] = \mathrm{i}. \tag{6}$$

We deduce from this equivalence that the spectrum is composed of equidistant levels called *Landau levels*:

$$E_n = \hbar\omega_c\,(n + 1/2) \qquad \text{with} \quad \omega_c = eB/m, \tag{7}$$

ω_c representing the cyclotron frequency of the particle in the B field.

A detailed study of the eigenstates associated with this energy spectrum shows that each Landau level has a macroscopic degeneracy

$$\text{degeneracy} = \frac{\mathcal{S}}{2\pi\ell^2} \tag{8}$$

where $\mathcal{S}$ is the surface area of the sample and

$$\ell = (\hbar/eB)^{1/2} \tag{9}$$

is the *magnetic length*.

We thus obtain a band spectrum similar to that of a particle in a periodic potential, except that each band is infinitely narrow. A detailed calculation shows that the Chern number $\mathcal{C}$ of each Landau level is 1. This leads to a non-zero Hall conductivity σ_{xy}, which in fact generalizes a well-known result of classical mechanics: when a force $\boldsymbol{F} = F\boldsymbol{u}_x$ is applied (for example by an electric field) on a charged particle placed in a magnetic field oriented along z, the particle moves on average along the y axis. This displacement can be seen as a particular case of the *anomalous velocity* that we have met in chapter 4.

1-2 Square lattice and magnetic field

We now turn to the Harper–Hofstadter problem, which consists in transposing the previous question to a discretized space. More precisely, we wish to model the motion of a particle on a square lattice of period a, in the case where the particle has a charge and is placed in a uniform magnetic field perpendicular to the plane of the lattice (figure 1). We will assume that we can consider only the couplings between nearest neighbors and we will restrict ourselves to the single-band approximation: a basis of the Hilbert space is given by $\{|A_{\boldsymbol{j}}\rangle\}$, where the pair of integers $\boldsymbol{j} = (j_x, j_y)$ indicates the position of each site:

$$A_{\boldsymbol{j}}: \quad \boldsymbol{r}_j = a\,(j_x\boldsymbol{u}_x + j_y\boldsymbol{u}_y)\,. \tag{10}$$

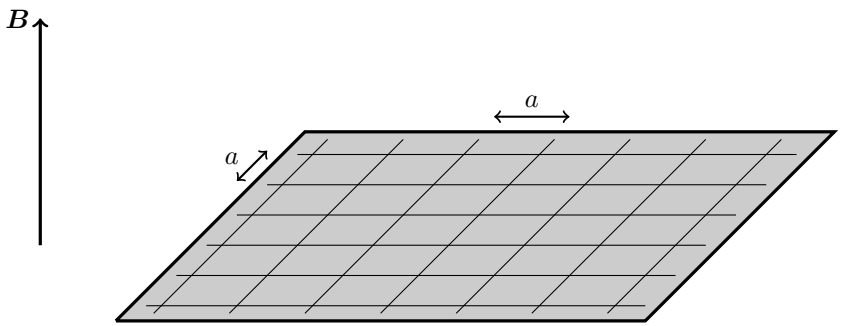

Figure 1. *Two-dimensional square lattice of period a in the presence of a magnetic field B orthogonal to the plane.*

With a zero magnetic field, the Hamiltonian is written

$$\hat{H}_0 = -J \sum_{\langle \boldsymbol{j},\boldsymbol{j}'\rangle} |A_{\boldsymbol{j}}\rangle\langle A_{\boldsymbol{j}'}|, \tag{11}$$

where the notation $\langle \boldsymbol{j},\boldsymbol{j}'\rangle$ restricts the sum over pairs of nearest neighbors. As we have seen in the previous chapters, the eigenstates of this periodic Hamiltonian for a unit cell with one site are the Bloch functions

$$|\psi_{\boldsymbol{q}}\rangle = \sum_{\boldsymbol{j}} \mathrm{e}^{\mathrm{i}\boldsymbol{q}\cdot\boldsymbol{r}_{\boldsymbol{j}}} |A_{\boldsymbol{j}}\rangle \tag{12}$$

and their energy is

$$E_{\boldsymbol{q}} = -2J\left[\cos(q_x a) + \cos(q_y a)\right], \tag{13}$$

which corresponds to an energy band of width $8J$.

The presence of the magnetic field is taken into account in this one-band model by assigning a complex value to the tunnel matrix elements between adjacent sites (Peierls phase):

$$J \qquad \text{replaced by} \qquad J\ \exp[\,\mathrm{i}\,\gamma(\boldsymbol{j}\to\boldsymbol{j}')]. \tag{14}$$

The Hermitian character of the Hamiltonian is preserved if

$$J\mathrm{e}^{\mathrm{i}\gamma(\boldsymbol{j}'\to\boldsymbol{j})} = \left(J\mathrm{e}^{\mathrm{i}\gamma(\boldsymbol{j}\to\boldsymbol{j}')}\right)^* \quad \Rightarrow \quad \gamma(\boldsymbol{j}'\to\boldsymbol{j}) = -\gamma(\boldsymbol{j}\to\boldsymbol{j}'). \tag{15}$$

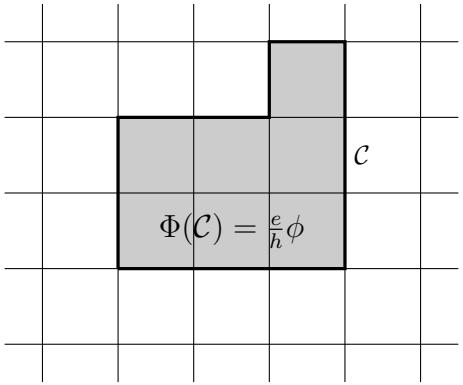

Figure 2. *For any contour $\mathcal{C}$ on the square lattice, the choice of phases $\gamma(\boldsymbol{j}\to\boldsymbol{j}')$ must lead to the correct value of the Aharonov–Bohm phase $\Phi(\mathcal{C}) = (e/h)\phi$, where ϕ is the flux of the magnetic field through the contour.*

The individual phases $\gamma(\boldsymbol{j}\to\boldsymbol{j}')$ are chosen so that the Aharonov–Bohm phase $\Phi(\mathcal{C})$ accumulated along a closed contour :

$$\Phi(\mathcal{C}) \equiv \sum_{\text{contour}} \gamma(\boldsymbol{j}\to\boldsymbol{j}') \tag{16}$$

is such that

$$\Phi(\mathcal{C}) = \frac{e}{\hbar}\phi \qquad \mod(2\pi), \tag{17}$$

where ϕ is the flux of $\boldsymbol{B}$ through the considered contour (figure 2). Due to gauge invariance, there are an infinite number of possible choices for the $\gamma(\boldsymbol{j}\to\boldsymbol{j}')$.

Using the additivity deduced from (15), one can easily check that a necessary and sufficient condition for the relation (17) to be verified for any contour $\mathcal{C}$ is to satisfy it for each elementary square cell. Following the edges of a square unit cell of area a^2 counterclockwise (figure 3), we must therefore have:

$$\begin{aligned}\Phi_{\text{cell}} &= \gamma(\boldsymbol{j}\to\boldsymbol{j}+\boldsymbol{u}_x) + \gamma(\boldsymbol{j}+\boldsymbol{u}_x\to\boldsymbol{j}+\boldsymbol{u}_x+\boldsymbol{u}_y) \\ &- \gamma(\boldsymbol{j}+\boldsymbol{u}_y\to\boldsymbol{j}+\boldsymbol{u}_x+\boldsymbol{u}_y) - \gamma(\boldsymbol{j}\to\boldsymbol{j}+\boldsymbol{u}_y) = \frac{qa^2B}{\hbar} \qquad \mod(2\pi)\end{aligned} \tag{18}$$

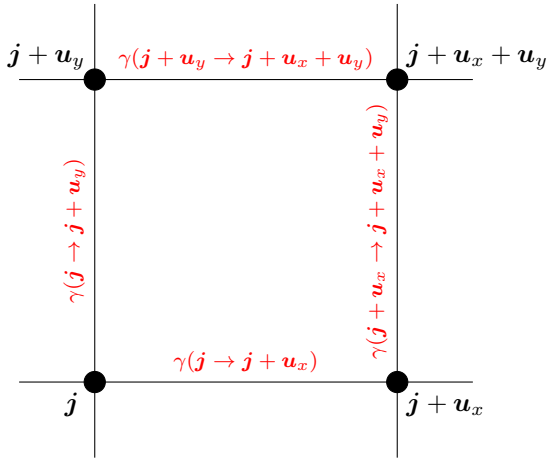

Figure 3. *Phase factors on the edges of a given unit cell. The algebraic sum of the coefficients γ must satisfy the constraint (18).*

Peierls substitution. A simple way to find a set of coefficients $\gamma(\boldsymbol{j} \to \boldsymbol{j}')$ satisfying (18) is to start with a vector potential $\boldsymbol{A}(\boldsymbol{r})$ for the continuous problem (i.e., to make a gauge choice) and to pose that

$$\gamma(\boldsymbol{j} \to \boldsymbol{j}') = \frac{e}{\hbar} \int_{a\boldsymbol{j}}^{a\boldsymbol{j}'} \boldsymbol{A}(\boldsymbol{r}) \cdot \mathrm{d}\boldsymbol{r}. \tag{19}$$

This prescription provides a suitable set for the γ coefficients since the contour integral $\oint_{\mathcal{C}} \boldsymbol{A} \cdot \mathrm{d}\boldsymbol{r}$ is by definition equal to the magnetic field flux through this contour $\mathcal{C}$.

Values of the magnetic field. In this discretized model, the magnetic field is entirely characterized by the phase Φ_{cell} that it creates through a unit cell, i.e. by the number α defined by

$$\alpha = \frac{\Phi_{\text{cell}}}{2\pi}. \tag{20}$$

This imposes a maximum relevant value: if the field is such that $\Phi_{\text{cell}} = 2\pi$, it will have no effect since it can be described by real and positive tunnel coefficients, as for the field $\boldsymbol{B} = 0$.

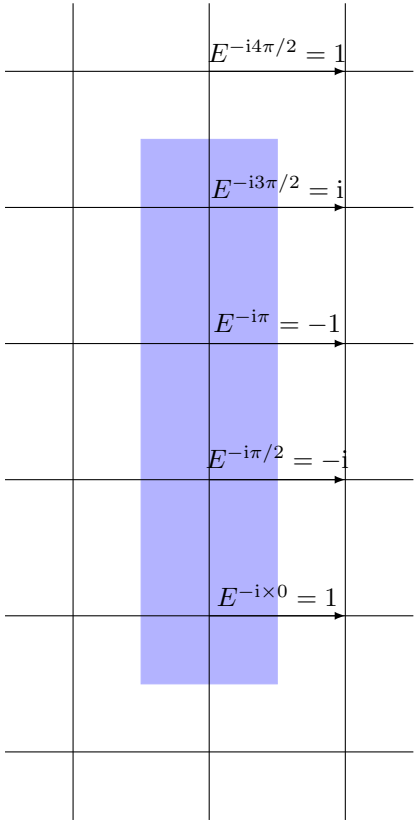

Figure 4. *Landau gauge for the Harper–Hofstadter problem with a flux $1/4$, i.e. an Aharonov–Bohm phase $\Phi_{\text{cell}} = \pi/2$ per cell of the initial square lattice (phase measured in the trigonometric direction). The shaded area $4a^2$ represents a possible unit magnetic cell for this choice of gauge.*

1-3 New periodicity in the rational case

When a non-zero phase $\gamma(\boldsymbol{j} \to \boldsymbol{j}')$ is assigned to the tunneling coefficients, the initial periodicity of the problem is lost and the search for the spectrum of the Hamiltonian is much more complicated. However, we can recover a periodic problem – but with a larger spatial period – when α is a rational number:

$$\alpha = \frac{p'}{p}. \tag{21}$$

Let us indeed consider the following choice, deduced from the Landau gauge $\boldsymbol{A}(\boldsymbol{r}) = -By\,\boldsymbol{u}_x$:

- The tunnel coefficients along the y direction all remain real and equal to J, i.e.:
$$\gamma(\boldsymbol{j} \to \boldsymbol{j} \pm \boldsymbol{u}_y) = 1. \tag{22}$$
- The tunnel coefficients along the x direction have the value $J\ \exp[\mathrm{i}\,\gamma(\boldsymbol{j} \to \boldsymbol{j}')]$ with
$$\gamma(\boldsymbol{j} \to \boldsymbol{j} + \boldsymbol{u}_x) = -2\pi\,\frac{p' j_y}{p}. \tag{23}$$

With this choice, we see that the Hamiltonian is periodic with period a along x and period pa along y. These tunnel coefficients are shown in figure 4 for the particular case $\alpha = 1/4$, i.e. $p' = 1$, $p = 4$, corresponding to an Aharonov–Bohm phase of $\pi/2$ per plaquette.

Finding a periodic problem will allow us to use Bloch's theorem again to search for the eigenstates and associated energies. However, we note that the new unit cell, called *unit magnetic cell*, has now a size $a \times pa$. There are thus p sites per unit magnetic cell, which will give rise to p energy bands from the initial band of width $8J$ found in the absence of magnetic field. This point is to be contrasted with the Haldane model, for which the introduction of non-zero phases on the tunnel coefficients did not change the size of the initial unit cell.

This choice for the unit magnetic cell is of course not the only one possible. In the case of $\Phi_{\text{cell}} = \pi/2$, another possibility is indicated in figure 5. It leads to a square magnetic unit cell $2a \times 2a$ (its total area $4a^2$ is not

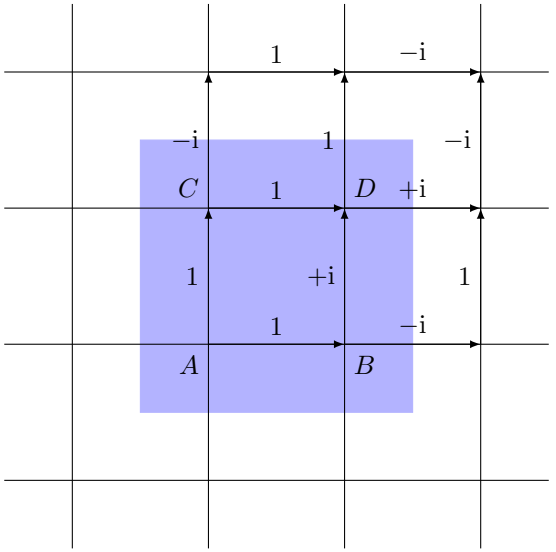

Figure 5. *Another possible gauge choice for the Harper–Hofstadter problem with a flux $1/4$, i.e. an Aharonov–Bohm phase $\Phi_{\text{cell}} = \pi/2$ per cell of the initial square lattice (phase measured in the trigonometric direction). The shaded area of $4a^2$ represents a possible unit magnetic cell for this choice of gauge.*

modified compared to figure 4); this second possibility is in fact more relevant for the experiment by Aidelsburger, Lohse, et al. (2015) that we will describe later, because the complex coefficients chosen here connect more naturally to those obtained when the light beams forming the optical lattice are switched on or off.

1-4 Spectrum of the Hamiltonian

We assume in what follows that the parameter α is a rational number which is written $\alpha = p'/p$. Of course, the spectrum of the Hamiltonian does not depend on the choice of gauge. Let us use the Landau gauge, with the position of a unit cell indexed by:

$$\boldsymbol{r}_{\boldsymbol{j}} = a(j_x\,\boldsymbol{u}_x\ + pj_y\,\boldsymbol{u}_y). \tag{24}$$

For a given quasi-momentum $\boldsymbol{q}$, a periodic function on the lattice is characterized by its p amplitudes $\alpha_{\boldsymbol{q},\nu}$, $\nu = 1, \ldots, p$ on the p sites $A_{\boldsymbol{j},\nu}$ composing the magnetic cell $\boldsymbol{j}$:

$$|u_{\boldsymbol{q}}\rangle = \sum_{\nu=1}^{p} \alpha_{\boldsymbol{q},\nu} \left(\sum_{\boldsymbol{j}} |A_{\boldsymbol{j},\nu}\rangle \right). \tag{25}$$

The Bloch states are written as follows

$$|\psi_{\boldsymbol{q}}\rangle = \sum_{\boldsymbol{j}} \mathrm{e}^{\mathrm{i}\boldsymbol{q}\cdot\boldsymbol{r}_j} \left(\sum_{\nu=1}^{p} \alpha_{\boldsymbol{q},\nu} |A_{\boldsymbol{r}_j,\nu}\rangle \right). \tag{26}$$

Transferring this expression into the eigenvalue equation for the Hamiltonian for the energy $E_{\boldsymbol{q}}$, we obtain a matrix equation for the p-component column vector

$$V_{\boldsymbol{q}} = \begin{pmatrix} \alpha_{\boldsymbol{q},1} \\ \alpha_{\boldsymbol{q},2} \\ \vdots \\ \alpha_{\boldsymbol{q},p} \end{pmatrix} \tag{27}$$

which is written in the form

$$\hat{H}_{\boldsymbol{q}} V_{\boldsymbol{q}} = E_{\boldsymbol{q}} V_{\boldsymbol{q}}. \tag{28}$$

The square matrix $\hat{H}_{\boldsymbol{q}}$ has size $p \times p$ and it is written for example for $\alpha = 1/4$:

$$\hat{H}_{\boldsymbol{q}} = -J \begin{pmatrix} 2\cos(aq_x) & 1 & 0 & \mathrm{e}^{4\mathrm{i}aq_y} \\ 1 & 2\cos(aq_x + \pi/2) & 1 & 0 \\ 0 & 1 & 2\cos(aq_x + \pi) & 1 \\ \mathrm{e}^{-4\mathrm{i}aq_y} & 0 & 1 & 2\cos(aq_x + 3\pi/2) \end{pmatrix}. \tag{29}$$

The four corresponding energy bands,

$$E_{\boldsymbol{q}} = \pm J \left\{ 4 \pm 2 \left[2 + \cos^2(2aq_x) + \cos^2(2aq_y) \right]^{1/2} \right\}, \tag{30}$$

plotted in figure 6, are form a symmetric ensemble with respect to $E = 0$. The two extreme bands are separated from the others by a gap while

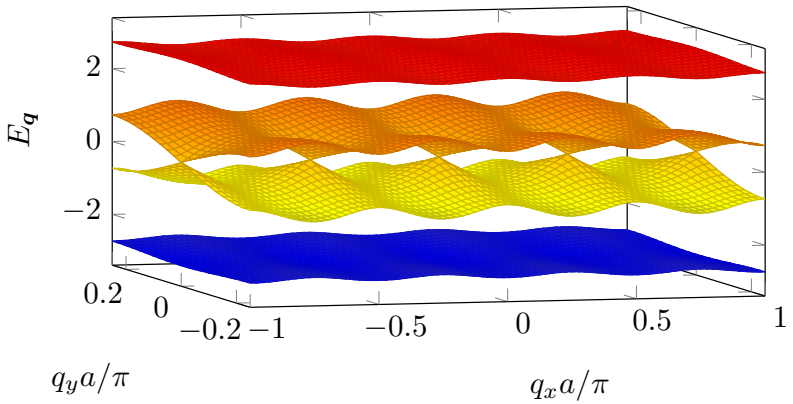

Figure 6. *Energy bands for the Harper–Hofstadter model for a flux $\alpha = 1/4$, with the unit magnetic cell in figure 4, corresponding to the Landau gauge.*

the two intermediate bands touch each other at 4 Dirac points inside the Brillouin zone $]-\pi/a, +\pi/a] \times]-\pi/(4a), +\pi/(4a)]$.

One can also carry out this research of energies with the choice of a square magnetic unit cell. By locating the four sites which compose it by the letters A, B, C, D as indicated in figure 5, we can write a Bloch function in the form

$$|\psi_{\boldsymbol{q}}\rangle = \sum_{\boldsymbol{j}} \mathrm{e}^{\mathrm{i}\boldsymbol{q}\cdot\boldsymbol{r}_j} \left(a_{\boldsymbol{q}} |A_{\boldsymbol{j}}\rangle + b_{\boldsymbol{q}} |B_{\boldsymbol{j}}\rangle + c_{\boldsymbol{q}} |C_{\boldsymbol{j}}\rangle + d_{\boldsymbol{q}} |D_{\boldsymbol{j}}\rangle \right) \tag{31}$$

where $\boldsymbol{j}$ now denotes the position of the magnetic cell unit of size $2a \times 2a$

$$\boldsymbol{r}_{\boldsymbol{j}} = 2a \left(j_x \boldsymbol{u}_x + j_y \boldsymbol{u}_y \right). \tag{32}$$

The eigenvalue equation for the Hamiltonian is written

$$\hat{H}_{\boldsymbol{q}} V_{\boldsymbol{q}} = E_{\boldsymbol{q}} V_{\boldsymbol{q}} \tag{33}$$

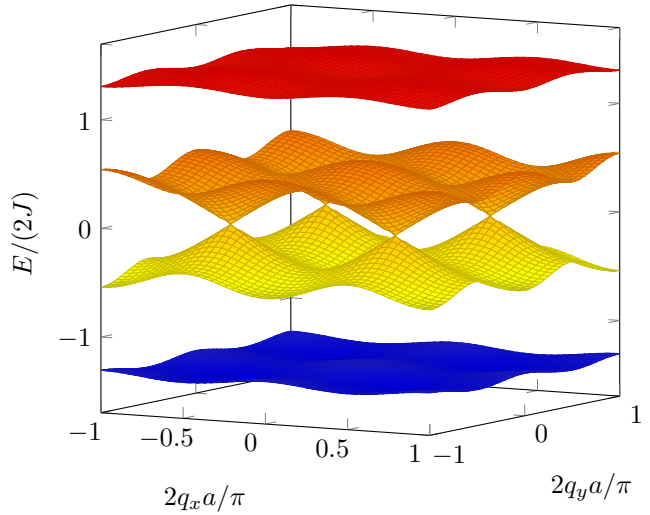

Figure 7. *Energy bands for the Harper–Hofstadter model for the flux $\alpha = 1/4$, with the square unit magnetic cell of figure 5.*

with

$$\hat{H}_{\boldsymbol{q}} = -J \begin{pmatrix} 0 & 1-\mathrm{i}\mathrm{e}^{-\mathrm{i}Q_x} & 1-\mathrm{i}\mathrm{e}^{-\mathrm{i}Q_y} & 0 \\ 1+\mathrm{i}\mathrm{e}^{\mathrm{i}Q_x} & 0 & 0 & -\mathrm{i}+\mathrm{e}^{-\mathrm{i}Q_y} \\ 1+\mathrm{i}\mathrm{e}^{\mathrm{i}Q_y} & 0 & 0 & 1+\mathrm{i}\mathrm{e}^{-\mathrm{i}Q_x} \\ 0 & \mathrm{i}+\mathrm{e}^{\mathrm{i}Q_y} & 1-\mathrm{i}\mathrm{e}^{\mathrm{i}Q_x} & 0 \end{pmatrix}, \quad V_{\boldsymbol{q}} = \begin{pmatrix} a_{\boldsymbol{q}} \\ b_{\boldsymbol{q}} \\ c_{\boldsymbol{q}} \\ d_{\boldsymbol{q}} \end{pmatrix} \tag{34}$$

where $Q_x = 2aq_x$ and $Q_y = 2aq_y$. The four eigenvalues of $\hat{H}_{\boldsymbol{q}}$ for this choice of unit magnetic cell are written

$$E_{\boldsymbol{q}} = \pm J \left\{ 4 \pm 2 \left[4 - \cos^2(2q_x a) - \cos^2(2q_y a) \right]^{1/2} \right\}^{1/2}, \tag{35}$$

and are plotted in figure 7 when $\boldsymbol{q}$ varies in the square Brillouin zone $-\frac{\pi}{2a} < q_x, q_y \leq \frac{\pi}{2a}$. Of course, we recover globally the same values as in figure 6, but with a different arrangement.

Let us finally recall the shape of the spectrum of the Hamiltonian obtained when we vary the parameter α between 0 and 1, but restricting ourselves to rational values in order to keep the problem periodic. This

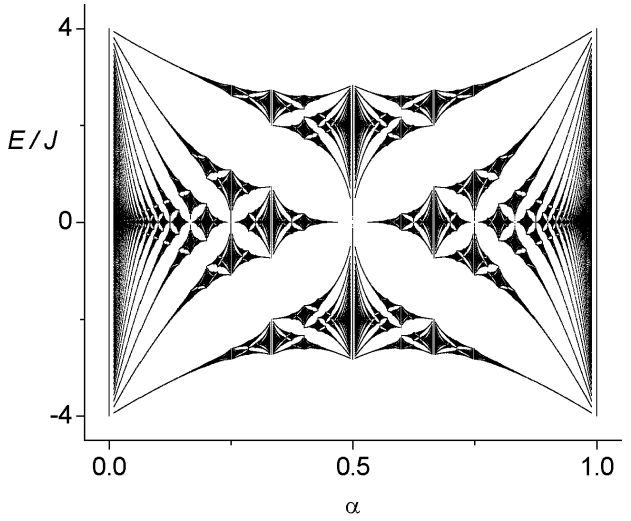

Figure 8. *The Hofstadter "butterfly" : spectrum of the Harper-Hofstadter Hamiltonian computed for a flux per initial unit cell $\Phi_{\mathrm{cell}} = 2\pi\alpha$ with $\alpha = p'/p$ rational between 0 and 1, and p, p' integers less than 100.*

spectrum, of fractal nature and called Hofstadter's butterfly, is represented in figure 8. The numerical calculation has been done for all rationals p'/p with the integers p, p' ranging from 1 to 100. A detailed discussion of this spectrum was done in the lecture of years 2013-14.

1-5 Topology of energy bands

Once the energies and eigenstates of the periodic Hamiltonian $\hat{H}_{\boldsymbol{q}}$ are determined, one can calculate the Berry curvature $\Omega_{\boldsymbol{q}}^{(j)}$ and the Chern number $\mathcal{C}^{(j)}$ for each energy band. The calculation of $\mathcal{C}^{(j)}$ has been done by Thouless, Kohmoto, et al. (1982); it involves the solution of a diophantine equation, i.e. an algebraic equation with integer coefficients. We will not discuss the general case, which is rather technical, and we will concentrate

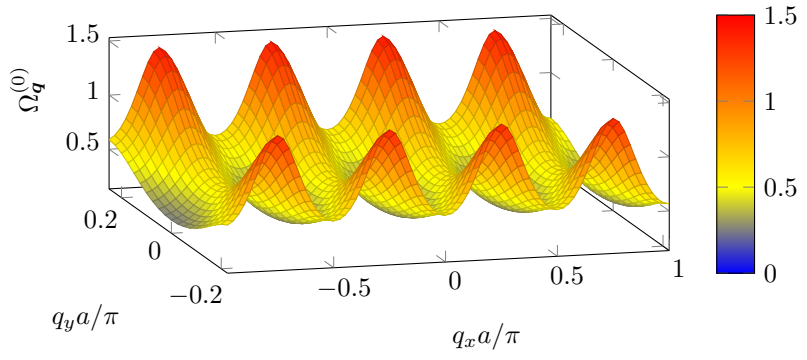

Figure 9. *Berry curvature for the lowest band of the Harper–Hofstadter model for the $1/4$ flux. This result was obtained with an encoding of the position of each site within the magnetic unit cell [see (36)].*

on the case $\alpha = 1/p$. We then find the following simple result:

- If p is odd, all the bands have Chern number $\mathcal{C} = 1$, except the central band for which we find $\mathcal{C} = -p + 1$. The sum of all Chern numbers is zero as expected (see chapter 5).
- If p is even, the two central bands touch each other at Dirac points, as we have seen in the case $\alpha = 1/4$. The Chern number for this pair of bands is $\mathcal{C} = -p + 2$ and all other bands have Chern number $\mathcal{C} = 1$. Again, the sum of all Chern numbers is zero.

We have already indicated in chapter 5 that the Berry curvature $\Omega_{\boldsymbol{q}}$ depends on how one encodes the position of each site inside a unit cell. For experiments in which atoms are driven by an external force, it makes sense to explicitly encode this position $\boldsymbol{R}_\nu$, $\nu = 1, \ldots, p$ in the definition of $|u_{\boldsymbol{q}}\rangle$ and $|\psi_{\boldsymbol{q}}\rangle$. This amounts to writing the periodic function (25) rather in the form:

$$|u_{\boldsymbol{q}}\rangle = \sum_{\nu=1}^{p} \tilde{\alpha}_{\boldsymbol{q},\nu}\, \mathrm{e}^{\mathrm{i}\boldsymbol{q}\cdot\boldsymbol{R}_\nu} \left(\sum_{\boldsymbol{j}} |A_{\boldsymbol{j},\nu}\rangle \right). \tag{36}$$

and use the periodic Hamiltonian $\hat{\tilde{H}}_{\boldsymbol{q}}$ defined from the coefficients $\tilde{\alpha}_{\boldsymbol{q},\nu}$.

The Berry curvature for the lowest band and for this position encoding is plotted in figure 9 for $\alpha = 1/4$ (calculation made in the Landau gauge). One can check numerically that its integral over the Brillouin zone is equal to 2π, which corresponds to $\mathcal{C} = 1$. A similar plot would be obtained from the square magnetic unit zone of figure 5.

When we decrease the value of $\alpha = 1/p$, we notice that the Berry curvature of the lowest band becomes more and more homogeneous on the whole Brillouin zone. For example for $\alpha = 1/8$, the relative variation of $\Omega_{\boldsymbol{q}}$ is less than 5 %. Note that this result is only valid if we have encoded the position as in (36). For the choice (25), the Berry curvature remains strongly modulated even for very small values of α.

2 The HH model with atoms

2-1 First proposals, first experiments

A simple way to print the phase $\gamma(\boldsymbol{j} \to \boldsymbol{j}')$ when an atom jumps from the site $\boldsymbol{j}$ to the site $\boldsymbol{j}'$ is to induce this jump with light: the hopping occurs if and only if the atom performs a stimulated Raman process between two states corresponding to neighboring sites. In such a process, called laser-assisted tunneling, the atom absorbs a photon of wave vector $\boldsymbol{k}_1$ and performs a stimulated emission of a photon of wave vector $\boldsymbol{k}_2$. The relative phase of the two light beams is then printed on the atomic wave function via the tunnel coefficient J which becomes non real.

This proposal was originally made by Jaksch & Zoller (2003). We start with a standard square lattice in which ordinary tunneling along one direction, y for example, is inhibited by applying a magnetic field gradient b' so that two adjacent sites $\boldsymbol{j}$ and $\boldsymbol{j} + \boldsymbol{u}_y$ have an energy difference $\Delta = \mu b' a$ much larger than the tunneling J (it is assumed here that the atoms are prepared in a Zeeman sublevel of non-zero magnetic moment μ). We then send a pair of laser beams with wave vectors $\boldsymbol{k}_i$ and frequency ω_i, $i = 1, 2$, with the choice of frequency $\omega_1 - \omega_2 = \Delta$ which allows to induce a resonant transition between adjacent sites (figure 10). The phase of the tunnel coefficient associated with this transition is directly linked to the relative phase of the laser beams at this point, i.e. $\mathrm{e}^{\mathrm{i}(\boldsymbol{k}_1 - \boldsymbol{k}_2)\cdot\boldsymbol{r}_{\boldsymbol{j}}}$.

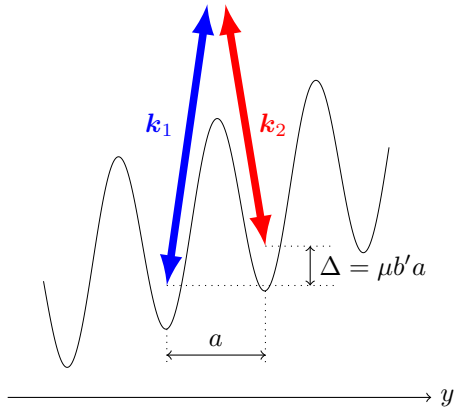

Figure 10. *Principle of laser-assisted tunneling for atoms of magnetic moment μ. A magnetic field gradient b' lifts the degeneracy between adjacent sites and blocks the direct tunneling. A pair of light beams with frequency difference $\omega_1 - \omega_2 = \mu b' a/\hbar$ restores resonant coupling between sites, with the phase $\mathrm{e}^{\mathrm{i}(\boldsymbol{k}_1 - \boldsymbol{k}_2)\cdot \boldsymbol{r}_j}$ "printed" on the tunneling coefficient.*

This method has been implemented by Aidelsburger, Atala, et al. (2013) in Munich and Miyake, Siviloglou, et al. (2013) at MIT for $\alpha = 1/4$ and $\alpha = 1/2$, respectively. These early experiments essentially consisted in measuring the band structure and observing the cyclotron motion; they have been described in the lecture of years 2013-14, therefore we will not detail them here again. Since a periodically time-dependent potential is applied to the atoms, its quantitative theoretical treatment uses the Floquet formalism. It is close to what we did in the previous chapter for the Haldane model, except that we are interested here in a resonant perturbation whereas we used previously a high frequency perturbation.

The result is simply stated in the framework of a model with two sites $|a\rangle$ and $|b\rangle$, by taking a periodic perturbation consisting in modulating the energy of one of the two sites. Starting from the Hamiltonian

$$\hat{H}(t) = -J\left(|a\rangle\langle b| + |b\rangle\langle a|\right) + \Delta\,\hat{P}_b + \kappa\cos(\omega t + \phi)\hat{P}_a, \tag{37}$$

where $\hat{P}_a$ and $\hat{P}_b$ are the projectors onto the a and b states, it can be shown that in the resonant case $\Delta = \hbar\omega \gg J$, the long-term dynamics is governed by the effective Hamiltonian (Eckardt & Holthaus 2007)

$$\hat{H}_{\text{eff}} = -J\mathcal{J}_1(\kappa/\hbar\omega)\,\left(\mathrm{e}^{\mathrm{i}\phi}\,|a\rangle\langle b| + \mathrm{e}^{-\mathrm{i}\phi}\,|b\rangle\langle a|\right) \tag{38}$$

where $\mathcal{J}_1$ is the Bessel function of the first kind. The tunneling effect between the two sites a and b is thus restored, with a Peierls phase factor that depends on the phase of the modulation. Note that in this two-site model, the phase ϕ can be eliminated[2] by a gauge change which consists in redefining the state a: $|\tilde{a}\rangle = \mathrm{e}^{\mathrm{i}\phi}|a\rangle$. This is fortunately not the case for a two-dimensional lattice, where the phase ϕ depends on space; this case is analyzed in detail in Goldman, Dalibard, et al. (2015).

2-2 Super lattice and band projection

The use of a magnetic field gradient to lift the degeneracy between neighboring sites poses practical problems due to fluctuations of the ambient magnetic field. These fluctuations interfere with the Peierls phase that we try to impose with the laser-assisted tunneling, and have prevented the Munich and MIT groups from demonstrating the topological properties of their lattice.

To circumvent this difficulty, the Munich group adopted a slightly different strategy that does not use any the magnetic field (Aidelsburger, Lohse, et al. 2015). The degeneracy lifting between adjacent sites is now done by a superlattice, a method we have already encountered in 1D problems and which had been proposed in this context by Gerbier & Dalibard (2010). More precisely, we have the following ingredients (figure 11):

- A square lattice in which all sites are equivalent with a tunnel coefficient J between nearest neighbors.
- A superlattice along the x axis so that sites B, D shown in Fig. 5 have a increase of energy Δ compared to sites A, C:

$$E_A = E_C = 0, \quad E_B = E_D = \Delta. \tag{39}$$

[2] In other words, the physics cannot depend on the choice of the origin of time in (37).

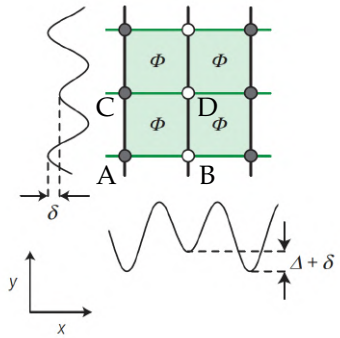

Figure 11. *A two-dimensional superlattice potential allows to lift the degeneracy between 4 sites of a square lattice, with energies $E_A = 0$, $E_B = \Delta + \delta$, $E_C = \delta$, $E_D = \Delta + 2\delta$, where the labeling of the states A, B, C, D is the same as in figure 5. A time modulation with frequency $\delta/\hbar$ then allows (in the rotating-wave approximation) to arrive at the energies (40).*

To first approximation, the "bare" tunneling effect is unchanged along y but is blocked along x due to the energy difference Δ between neighboring sites. The modulation will therefore be performed with frequency $\Delta/\hbar$ to restore the tunneling along x while inducing a different Peierls phase on the links $A - B$ and $C - D$.

- A second superlattice along the two axes x and y increases the energy of sites B and C by δ, and the energy of site D by 2δ.

Once we take into account the additional potential modulated in time at frequency $\Delta/\hbar$, we obtain an effective Hamiltonian with the on-site energies :

$$E_A = -\delta, \quad E_B = E_C = 0, \quad E_D = +\delta \tag{40}$$

which are added to the Harper Hamiltonian studied in the first part.

The interest of the superlattice providing the energy shift δ is to produce a four-site unit cell like the Harper Hamiltonian, but with an additional control parameter. For large δ, the lowest band simply corresponds to placing the atoms on the A sites. Further study shows that the corresponding periodic Hamiltonian

$$\hat{H}_{\boldsymbol{q}}(\delta) = -J \begin{pmatrix} \delta/J & 1 - \mathrm{i}\mathrm{e}^{-\mathrm{i}Q_x} & 1 - \mathrm{i}\mathrm{e}^{-\mathrm{i}Q_y} & 0 \\ 1 + \mathrm{i}\mathrm{e}^{\mathrm{i}Q_x} & 0 & 0 & -\mathrm{i} + \mathrm{e}^{-\mathrm{i}Q_y} \\ 1 + \mathrm{i}\mathrm{e}^{\mathrm{i}Q_y} & 0 & 0 & 1 + \mathrm{i}\mathrm{e}^{-\mathrm{i}Q_x} \\ 0 & \mathrm{i} + \mathrm{e}^{\mathrm{i}Q_y} & 1 - \mathrm{i}\mathrm{e}^{\mathrm{i}Q_x} & -\delta/J \end{pmatrix} \tag{41}$$

leads to topologically non-trivial bands if and only if

$$|\delta| < 2J. \tag{42}$$

One can then adopt the following experimental procedure:

1. One switches on the lattices and superlattices at δ and Δ, so that all atoms are placed in the low energy sites (A).
2. One slowly (30 ms) switches on the modulation at frequency $\omega = \Delta/\hbar$, while keeping δ large ; at this stage, the dynamics of the atoms is still frozen.
3. One adiabatically decreases δ to the value 0 to reach the Harper Hamiltonian for a flux $\alpha = 1/4$. This decrease implies a passage through the singular point $\delta = 2J$ where the topology of the lowest band becomes non-trivial. However, the populations of the four bands remain approximately constant in this operation which also lasts 30 ms.
4. The desired experiment is carried out.
5. To analyze the result, one follows the reverse path. One analyzes the final populations of the different bands by the usual method of *band projection*, i.e. an adiabatic extinction of the optical lattice followed by a time of flight. Each band is then associated to a site A, B, C, D and to a well-defined momentum zone, which allows to determine the population of each of these bands.

2-3 Measurement of the Chern number

The central point of the experiment by Aidelsburger, Lohse, et al. (2015) was the measurement of the Chern number associated with the lowest

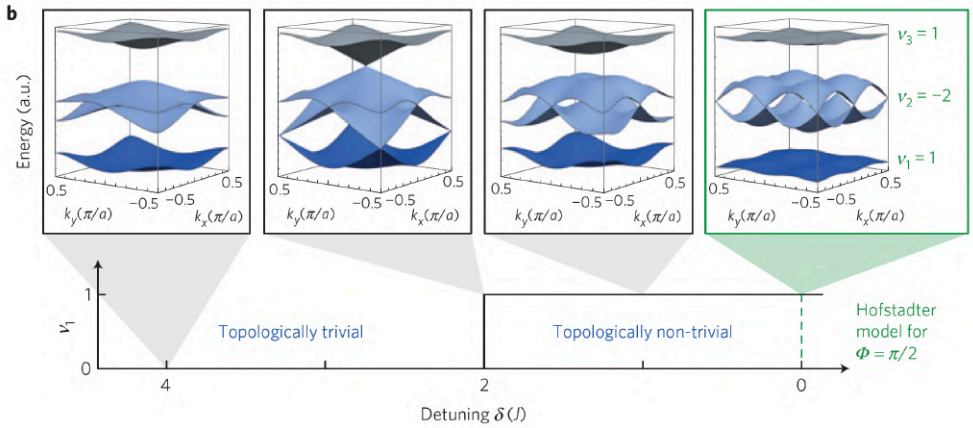

Figure 12. *Loading procedure of the lowest band of the Harper–Hofstadter lattice used by Aidelsburger, Lohse, et al. (2015) for the flux $\alpha = 1/4$. One starts from the situation where the energy difference δ is large compared to the tunnel coupling, which allows to position the atoms on the lowest band where essentially only the A sites contribute, this band being non-topological. One then slowly decreases the value of δ to enter a topological band regime for $\delta = 2J$, then arrive at the case of the Harper–Hoftsadter Hamiltonian with $\delta = 0$ and a flux $\Phi_{\text{cell}} = \pi/2$ (i.e. $\alpha = 1/4$).*

band. Although this experiment was conducted with bosons, the principle of the measurement is directly inspired by the result we encountered in the previous chapter for non-interacting fermions. In this case, if the band is uniformly filled, we know that we have a quantized current I_y along y when a uniform force F_x is applied along x:

$$I_y \equiv \left.\frac{\mathrm{d}N}{\mathrm{d}t}\right|_{\text{along } y} = \frac{\mathcal{C}}{2\pi}\,\frac{L_x F_x}{\hbar}. \tag{43}$$

We know that there is in this case a surface density $\rho^{(2D)} = 1/\ell^2$ where ℓ is the size of the unit cell ($\ell = 2a$ for the HH lattice for a $\alpha = 1/4$ flux). This means that the average particle velocity v_y along the y axis defined by

$$\rho^{(2D)} v_y = \frac{1}{L_x}\left.\frac{\mathrm{d}N}{\mathrm{d}t}\right|_{\text{along } y} \tag{44}$$

is equal to

$$v_y = \mathcal{C}\,\frac{F_x \ell^2}{2\pi\hbar}. \tag{45}$$

This last result for the velocity of the particles in fact does not depend on the assumption of a completely filled band. If we examine the demonstration of the quantization of conductance (43), we see that the important point is the uniform filling of the Brillouin zone, i.e. an identical population for all Bloch states. It is on this condition that the integral of the Berry curvature over the quasi-momentum reveals the Chern number. On the other hand, the exact value of this population is not important to establish (45).

The result (45) can therefore be transposed to bosons, provided that the band considered, in this case the lowest band, is uniformly filled and that the other bands are empty. Such a situation can be obtained if the width of the lowest band ΔE_0 is small compared to the gap between the lowest band and the first excited band $\bar{E}_1 - \bar{E}_0$. It is then sufficient to choose the temperature T such that

$$\Delta E_0 \ll k_{\text{B}} T \ll \bar{E}_1 - \bar{E}_0 \tag{46}$$

for this hypothesis to be verified. In practice, for the HH lattice with $\alpha = 1/4$, we find $(\bar{E}_1 - \bar{E}_0)/\Delta E_0 \sim 7$, which allows to validate in first approximation the condition (46).

In the experiment of Aidelsburger, Lohse, et al. (2015) the force F_x is a dipolar force, created by the gradient of intensity of an auxiliary beam. This force is applied for a variable time t and one measures the displacement of the center of mass of the atomic cloud as a function of time. At short times, typically less than 50 ms, the displacement along y, similar to a Hall current, is proportional to t (figure 13). The value found for the velocity v_y is in agreement with the value expected from (45) for the Chern number $\mathcal{C} = 1$ of the lowest band. More precisely, taking into account the measured populations of the four bands, Aidelsburger, Lohse, et al. (2015) find $\mathcal{C} = 0.9\,(2)$. At longer times, the heating from the resonant modulation induces transitions between the different bands, which end up being equally populated. The drift along the y axis then stops, since the sum of the four Chern numbers is zero. A precise analysis of this dynamics at long times, coupled with an independent measurement of the populations of each band, leads to $\mathcal{C}_{\text{exp}} = 0.99\,(5)$.

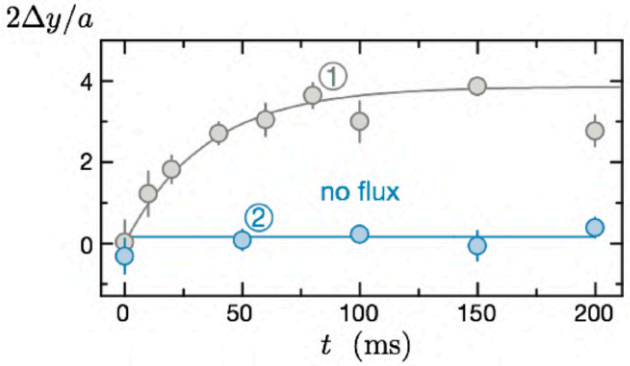

Figure 13. *Transport in a square lattice with a flux $\Phi_{\text{cell}} = \pi/2$ (data 1) measured by Aidelsburger, Lohse, et al. (2015). A Hall current is observed via the displacement of the center of mass of the cloud along the y direction when a uniform force inducing Bloch oscillations is applied along the x axis for an adjustable time. At short times, only the lowest band is appreciably populated, which leads to a displacement y linear in time. The corresponding slope is in good agreement with the expected Chern number $\mathcal{C} = 1$ for this band. At longer times, heating processes equalize the populations of the different bands and the current stops. Data 2 have been obtained for a zero flux. This figure was prepared with the help of Monika Aidelsburger.*

2-4 The heating problem

The fact that the Hamiltonian has an explicit time dependence introduces an additional difficulty as soon as we are interested in an assembly of interacting particles. Indeed, there is no conservation of energy associated to the effective Hamiltonian; the energy of the micro-motion can be converted into heating during inelastic processes occurring during the collision between two particles. For a Hamiltonian containing terms oscillating at frequency ω, these inelastic processes correspond to the absorption or emission of phonons of energy $\hbar\omega$. In the long run (except if the phenomenon of many-body localization can occur), we expect an interacting system with a Hamiltonian modulated in this way to reach an infinite temperature, i.e. an equal population for all energy levels (Lazarides, Das, et al. 2014).

A description of these inelastic two-body processes in the framework of the Bloch wave formalism has been proposed by Bilitewski & Cooper (2015b) and Bilitewski & Cooper (2015a). This analysis, based on the Fermi golden rule written in the Floquet formalism, is in very good agreement with the heating measured experimentally by Aidelsburger, Lohse, et al. (2015). It shows in particular the important role of the degree of freedom along the z direction perpendicular to the lattice plane. The experiment by Aidelsburger, Lohse, et al. (2015) was performed in tubes parallel to the z axis, and this direction was therefore only weakly confined. Significant heating could then occur during collisions by transferring energy from the micromotion to the motion along the z direction. Bilitewski & Cooper (2015a) have shown that a much stronger confinement along the z axis could strongly reduce this source of heating: if the energy needed to excite a quantum of this motion is much larger than the energy related to the modulation at $\hbar\omega$, the density of states involved in Fermi's golden rule is strongly reduced from its 3D value (large) to its 2D value for the xy plane only (much smaller). This type of analysis has been generalized to the case of a superfluid described by the Gross–Pitaevskii equation by Choudhury & Mueller (2015) and Lellouch, Bukov, et al. (2017).

3 The Hall effect in photonics

The first way to simulate the quantum Hall effect in photonics has been to use opto-magnetic effects induced by a large magnetic field (0.2 T) on a photonic crystal operating in the microwave range and composed of ferrite rods (Wang, Chong, et al. 2009). We will present here more recent experiments, carried out without magnetic field and in the visible (or near infrared) domain. Note that in the range of visible wavelengths, the magneto-optical response of the materials is generally very weak and it was therefore necessary to use other methods to induce a "Hall effect" type behavior in these systems.

We will successively focus on "passive" experiments, in which one probes the linear optical response of the system, and then "active" experiments, in which topology is used to fabricate new robust laser sources. Several of these experiments use an array of ring micro-resonators, and we will start by describing this system, that was initially proposed by Hafezi,

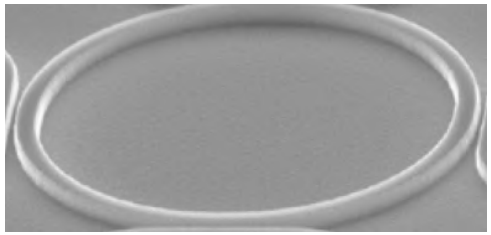

Figure 14. *A ring micro-resonator, used as a "site" of a lattice for light, formed by a circular waveguide. This figure is taken from Bandres, Wittek, et al. (2018). The radius of the ring is* $5\,\mu m$*, the width and height of the guide are respectively* $0.5\,\mu m$ *and* $0.2\,\mu m$ *.*

Demler, et al. (2011), before presenting some representative results.

In the photonic implementations we will consider here, the elementary site of the lattice is a ring-shaped micro-resonator like the one shown in figure 14. These are single mode silica waveguides, in which the light can propagate clockwise or counterclockwise. The light is chosen to be resonant with these rings, with a quality factor higher than 10^4. It is injected into one of the rings composing the lattice thanks to a tangential waveguide, which imposes the direction of circulation in this ring, and consequently – as we will see – in all the rings of the lattice. In what follows, we will first consider the case where the light rotates exclusively counterclockwise in these rings, and we will come back on this hypothesis at the end of the paragraph.

3-1 Ring micro-resonators

The equivalent of the tunnel coupling between sites in the tight-binding model is obtained by inserting between two rings a rectangle-shaped link with rounded edges (figure 15). This link is designed to be non-resonant with light (Hafezi, Demler, et al. 2011). From a dynamical point of view, we can consider that a photon resides for a rather long time on the ring A_1 by rotating counterclockwise, then jumps to the ring A_2 by passing through the link L located between A_1 and A_2 (figure 16). It will then stay for a long time on A_2, always rotating counterclockwise. The non-resonant character

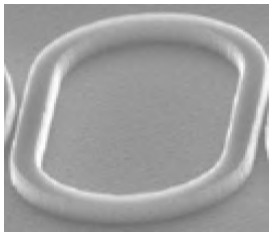

Figure 15. *Link connecting two rings in the experiment of Bandres, Wittek, et al. (2018). This link is assumed to be non-resonant.*

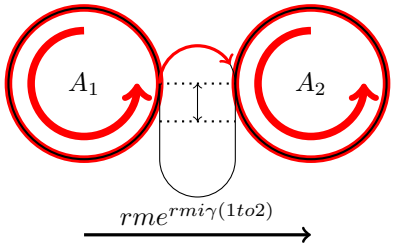

Figure 16. *Passage from ring* A_1 *to ring* A_2 *via the link inserted between the two. For the light rotating counterclockwise in the rings, this passage* $A_1 \to A_2$ *is done on the upper edge of the link.*

of the L link means that the passage on L is very short. For the geometry shown in figure 16, this passage from A_1 to A_2 is done via the upper part of the link L. The accumulated phase $\gamma(1 \to 2)$ thus depends on the optical length of this upper part.

Let us now consider the passage from the ring A_2 to the ring A_1, still for light rotating counterclockwise in the rings (figure 17). We see that a photon must in this case take the path on the bottom of the rectangular link. The optical length of this path is different from the previous one if the rectangular link is not perfectly centered on the segment A_1A_2. We thus have a way to induce a coupling $1 \to 2$ which does not have the same phase as the coupling $2 \to 1$. If we choose the phase reference to be zero for a centered rectangle, we obtain $\gamma(2 \to 1) = -\gamma(1 \to 2)$: this is the necessary ingredient to build the Harper Hamiltonian.

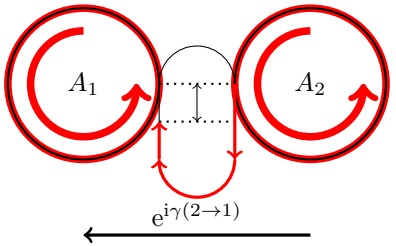

Figure 17. *Passage from ring A_2 to ring A_1 via the link inserted between the two. For the light rotating counterclockwise in the rings, this passage $A_2 \to A_1$ is done on the lower edge of the link. The optical path is therefore different from that of figure 16, for the passage $A_1 \to A_2$.*

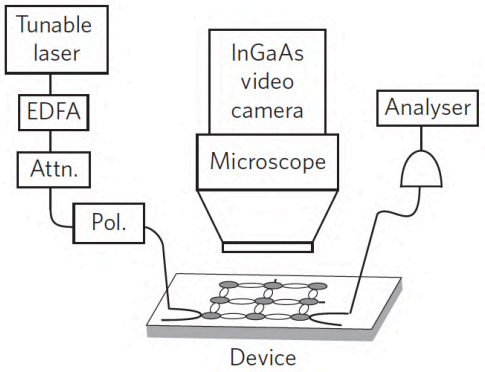

Figure 18. *Schematic of the experiment of Hafezi, Mittal, et al. (2013).*

3-2 Passive photonic implementation

The idea proposed by Hafezi, Demler, et al. (2011) was put into practice by Hafezi, Mittal, et al. (2013). The experiment was done with a square array of 8 rings connected by links (figure 18). The light is injected in one of the rings located at the periphery. One measures the light scattered by each of the 64 rings with a microscope.

A unit cell of this lattice is shown in figure 19. It represents a direct implementation of the Harper–Hofstadter Hamiltonian in the Landau gauge. The links along the y direction are centered on the rings, so that the associated phase is zero. On the other hand, the links along the x direction are shifted by an adjustable distance, so that the accumulated phase when the light travels around the cell in the $1 \to 2 \to 4 \to 3 \to 1$ direction is non-zero and constant over the whole lattice. It takes the opposite value for light traveling in the $1 \to 3 \to 4 \to 2 \to 1$ direction. The experiment of Hafezi, Mittal, et al. (2013) was performed for a flux per unit cell of $2\pi\alpha$ with $\alpha = 0.15$.

The experiment confirmed the existence of edge channels that propagate without interruption even in the presence of defects. By changing the wavelength of the light, one can excite a channel of positive or negative group velocity, i.e. propagating clockwise or counterclockwise, in good agreement with predictions (figure 20).

Time reversal invariance and spin Hall effect. In the experiment we have just described, there is no physical element that breaks the time reversal invariance. How is it possible to obtain a Hall effect type behavior with chiral edge states under these conditions?

The crucial point is that we have restricted ourselves in the above to a specific direction of propagation of light in a given ring, assuming that this motion was counterclockwise. We can take the same problem by considering the case where the light rotates clockwise, and we then find that each phase is changed into its opposite. Thus the figure 16 giving the passage $A_1 \to A_2$ is modified to give figure 21.

We find here a situation characteristic of the spin Hall effect, for which we can obtain a non-trivial topology for time-reversal invariant problems, provided that we take advantage of a spin $\uparrow$ and $\downarrow$ (or pseudo-spin) degree of freedom (Kane & Mele 2005a; Kane & Mele 2005b; Bernevig, Hughes, et al. 2006). This situation has already been briefly presented in the previous chapter. In the present case, the pseudo-spin is associated to the direction of rotation of the light in a ring; the robustness of the edge states is ensured by the fact that backscattering of light, which would reverse its direction of rotation in ring resonators, plays a negligible role.

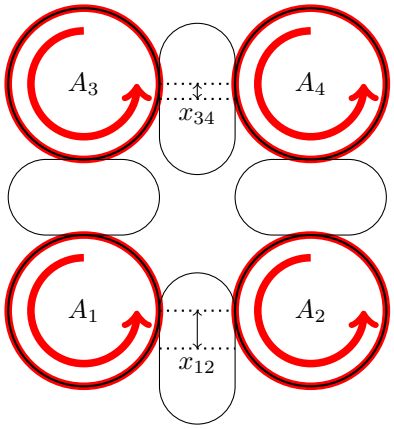

Figure 19. *Unit cell in the experiment of Hafezi, Mittal, et al. (2013). The light is resonant with the rings located at sites A_j, which form the nodes of a square lattice. The light is injected into the lattice in such a way that it rotates counterclockwise in each ring. It passes from one site to the other through the links, whose position determined by the distances x_{12} and x_{34} allows to adjust the phase $2\pi\alpha$ acquired by the electromagnetic field on a cell ($\alpha = 0.15$ in the experiment). One thus generates a Harper–Hofstadter lattice.*

3-3 Active photonic implementation

A similar scheme based on a square array of resonators has recently been used to create[3] a two-dimensional "topological laser" by Bandres, Wittek, et al. (2018) and Harari, Bandres, et al. (2018). Figure 22 shows a square array of 10 site resonators, arranged on a platform featuring InGaAsP quantum wells that can amplify the electromagnetic field in the presence of a proper pumping. The experiment is performed for the case $\alpha = 1/4$ that we have studied above. The resonators and links are shown in figures 14 and 15. For comparison, the same experiments are carried out with a lattice of the same nature but without the shift of the links, which leads to $\alpha = 0$ (trivial topology).

The lasing effect on the edge channels is achieved by directing the pumping light onto the edge of the sample (figure 23). One measures the light emitted by the sample, both from each of the resonators and also on output couplers placed at a corner of the sample. Figure 24 shows some important characteristics of this laser:

- The output power plotted against the pump power shows that the topological laser operates with a better efficiency than its non-topological equivalent. This is because in the non-topological lattice, the modes involved in lasing extend into the core of the material, resulting in significant losses. These modes also tend to minimize the amplitude at the output coupler. On the contrary, the topological edge mode is by definition localized on the sample boundary, it occupies

[3] Bahari, Ndao, et al. (2017) discuss the realization of a topological laser using a magnetic medium (yttrium iron garnet, YIG) to explicitly break the time-reversal invariance.

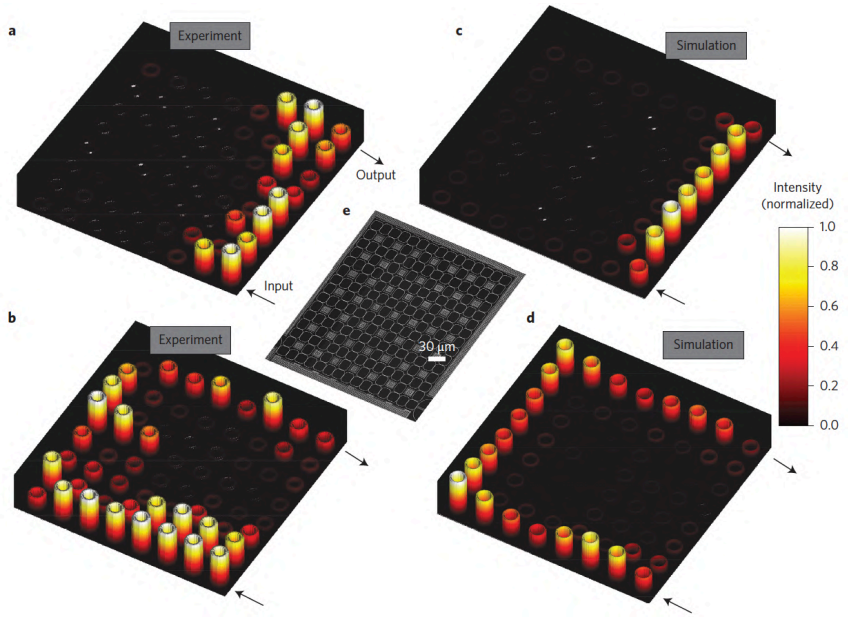

Figure 20. *Evidence of edge channels in the experiment by Hafezi, Mittal, et al. (2013). Depending on the wavelength of the light, an edge channel is excited with positive or negative chirality. The images on the left correspond to experimental results and the images on the right to numerical simulations.*

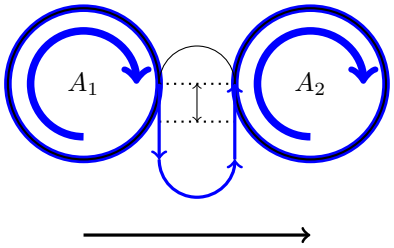

Figure 21. *Passage from ring A_1 to ring A_2 via the link inserted between the two. For light rotating clockwise in the rings, this passage $A_1 \to A_2$ is done on the lower edge of the link. The accumulated phase is thus opposite to the one found for light turning counterclockwise in the rings (figure 16). This result is consistent with the time reversal invariance of the system.*

this boundary in a uniform way and thus has a significant amplitude at the output coupler.

- The spectrum of the emitted light is narrower for the topological laser, indicating that it operates in a single mode regime, whereas the non-topological laser is multi-mode: the power emitted in the dominant longitudinal mode is higher by one order of magnitude in the topological case. This is due to the fact that in the non-topological case, different regions of the sample tend to lase at different frequencies, due to the unavoidable disorder that occurs during sample fabrication. This favors a longitudinal multimode operation, which is not the case for the topological laser.

These different characteristics show the interest of topology in photonics. The robustness it brings allows to consider devices whose operation will be less sensitive to random defects that may occur during manufacturing. We have given here the example of the laser effect where the gain brought by topology is clear, but we can also mention the fabrication of controlled delay lines, which are an essential component of optical information processing and for which disorder is also a limiting factor.

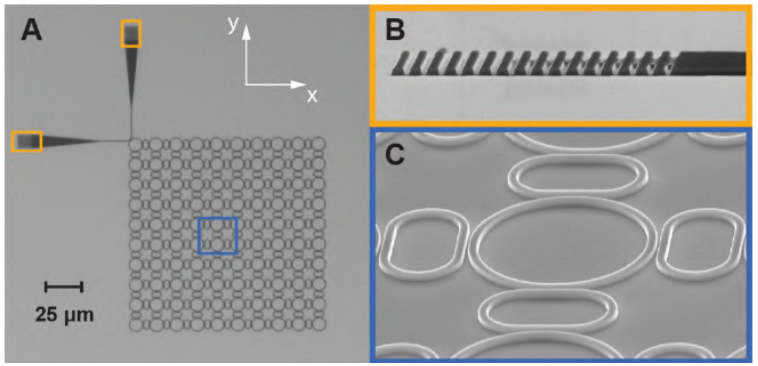

Figure 22. *Lattice of 10×10 resonators used by Bandres, Wittek, et al. (2018) to fabricate a laser in a topology described by the Harper–Hofstadter Hamiltonian. Structures for efficiently extracting light from the resonator array have been arranged in the upper left corner.*

4 Use of the internal atomic structure

In this lecture, we have mainly focused on the motion of particles in periodic potentials neglecting any internal structure of these particles. Topological effects have appeared by taking advantage of the spatial variation of the tunnel coefficients, as for the SSH model, or the complex phase of these tunnel coefficients, as for the Haldane model. The possibility to use the internal structure of the atoms opens new possibilities. The sites of the topological lattices can then correspond to different internal states; the transition from one site to another is no longer done by a standard tunneling effect, but by the change of the internal state resulting from the absorption or emission of photons.

In the lecture of years 2013-14, we discussed the description of some of the mechanisms that allow to create an artificial magnetic field on a gas of atoms. Once this field is created, topological bands can appear naturally, as in the case of the quantum Hall effect. We will start this part with a brief reminder of two mechanisms already studied in the 2013-14 lecture: the tunneling effect assisted by Raman transitions and the notion of synthetic dimension, before focusing on another type of systems, called *flux lattices*.

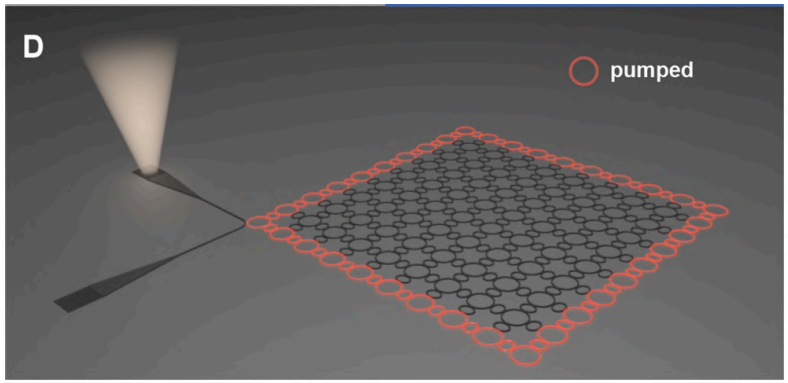

Figure 23. *Schematic diagram of a topological laser: the pump light is sent on the sample boundary in order to create a population inversion for an edge channel. This channel propagates chirally along the sample, and one detects the laser light in one of the two output channels. Image taken from Bandres, Wittek, et al. (2018).*

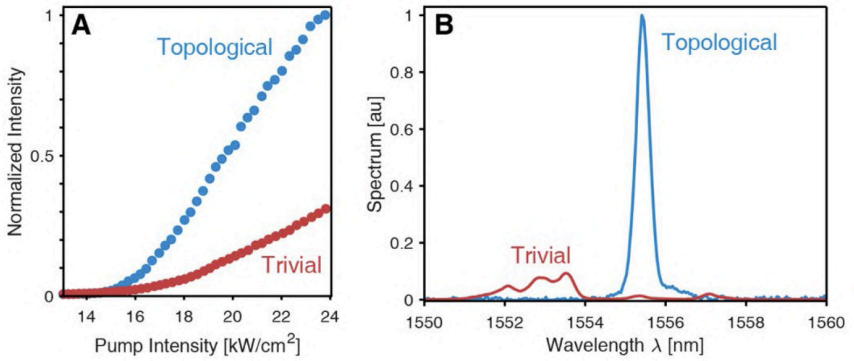

Figure 24. *Left: laser output power versus pump power. Right: spectrum measured for a pump power of 23.5 kW/cm^2. Image extracted from Bandres, Wittek, et al. (2018).*

4-1 Raman transitions and synthetic dimensions

In § 2-1, we described *laser-assisted tunneling* as a process capable of imprinting a complex phase factor on the tunnel coefficient between two sites. In the discussion of § 2-1 we limited ourselves to the case where only the external state of the atom was modified. However, we can generalize this principle to the case where the transition represented in figure 25 also affects the internal state of the atom.

More precisely, let us consider a system with two spatially separated sites A and B trapping respectively atoms in the internal states $|a\rangle$ and $|b\rangle$ (figure 25). We can induce the jump of a particle from site A to site B by illuminating this particle with a running electromagnetic wave $E_0\ \mathrm{e}^{\mathrm{i}(ky-\phi)}$ which induces (for example) the transition

$$|a\rangle\ +\ \text{photon}\ \longrightarrow\ |b\rangle. \tag{47}$$

During this transition, the phase ϕ of the electromagnetic wave on the segment AB is printed on the matrix element V_{AB}. By generalizing this idea to the scale of an entire lattice, one can reproduce the essential elements of the Harper–Hofstadter model (Jaksch & Zoller 2003; Gerbier & Dalibard 2010). One possible scheme is to alternate columns of sites that trap $|a\rangle$ states and $|b\rangle$ states, and then engineer laser-assisted tunneling to reproduce (for example) the matrix elements of the Harper–Hofstadter model in figure 4.

If one simply wishes to realize a ribbon whose width does not exceed a few sites, one can use the concept of *synthetic dimension*, represented in figure 26. We use an atom whose ground state has an angular momentum J ($J = 1$ for this figure), thus $2J+1$ Zeeman states $|J,m\rangle$ with $m = -J, -J+1, \ldots, J$; each Zeeman state plays the role of a line of the ribbon. The orthogonal axis (x on the figure 26) is a dimension of the usual space along which a 1D lattice has been set-up. The motion along this axis corresponds to the usual tunneling effect while the motion along the synthetic direction is initiated by stimulated Raman transitions

$$|J,m\rangle \rightarrow |J,m\pm 1\rangle. \tag{48}$$

These transitions are induced by a pair of auxiliary light beams, one with polarization σ_+ and the other with polarization π, which impart the desired phase during the transition. The principle of this synthetic dimension was proposed by Celi, Massignan, et al. (2014) and has been implemented in several groups in recent years, first with Raman transitions between

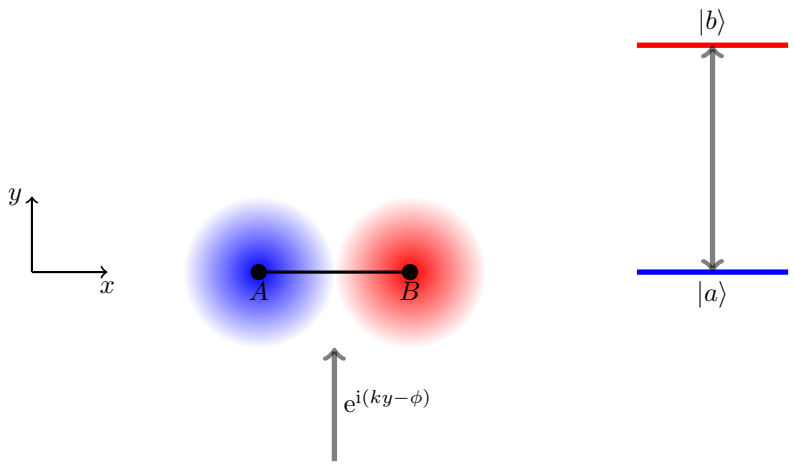

Figure 25. *Laser-assisted tunneling accompanied by an internal state change.*

ground sublevels (Stuhl, Lu, et al. 2015; Mancini, Pagano, et al. 2015), and then on the narrow line (clock transition) of atoms with two outer electrons (Kolkowitz, Bromley, et al. 2017; Livi, Cappellini, et al. 2016).

4-2 Adiabatic following of a dressed state

In the situations we have just considered, we started from a periodic lattice (1D or 2D), to which we superimposed an auxiliary light beam that induces a complex tunnel coupling between sites. The optical lattice was therefore not topological, but simply a basis to "discretize" the space. We will now investigate whether a periodic optical lattice can possess all the necessary characteristics to create topological bands, without having to resort to temporal modulations of the coefficients or to auxiliary light beams. We will see that the answer is positive, and corresponds to the notion of *flux lattice*.

We will limit ourselves here to a lattice created by light beams that are far-detuned from the atomic resonance lines, in order to avoid any spontaneous emission process. In these conditions, the only significant effect of the interaction between the atom and the light is an energy shift of the groundstate, induced by two-photon processes of absorption and stimulated emission.

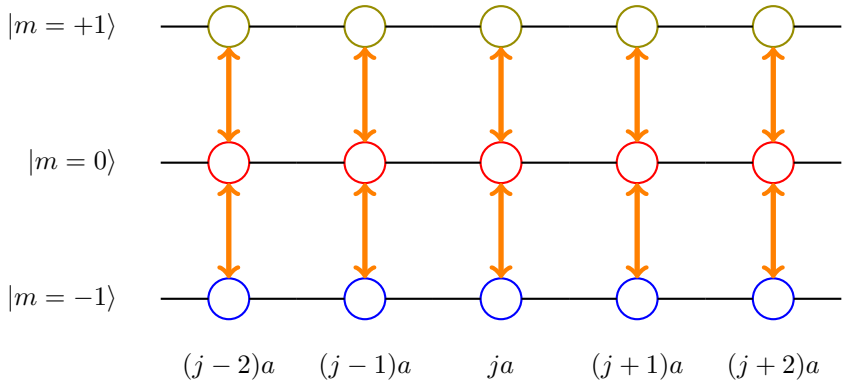

Figure 26. *Use of a synthetic dimension for an atom of spin $J=1$, with three internal states $|J,m\rangle$ and $m=0,\pm1$. The confinement along the x axis is that of a usual 1D lattice. The y axis corresponds to the 3 possible values of m. The "motion" along this direction is obtained by stimulated Raman processes which induce $\Delta m=\pm1$ transitions between internal states (orange arrows).*

Let us consider alkaline atoms, with a single external electron, which are the mostly used atoms in quantum gas experiments; the light shift is then described at any $\boldsymbol{r}$ point of space by an operator that includes[4]:

- a scalar part $U(\boldsymbol{r})$, which shifts all Zeeman sublevels by the same amount. For an alkaline atom, this scalar part cancels if we choose the wavelength of the light at the barycenter of the two resonance lines D_1 and D_2 with weights 2/3–1/3. We will assume that this condition is fulfilled in the following.
- a vector part:
$$\hat{V}(\boldsymbol{r}) = \boldsymbol{\kappa}(\boldsymbol{r}) \cdot \hat{\boldsymbol{J}}, \tag{49}$$
where $\kappa(\boldsymbol{r})$ depends on the amplitude and the polarization of the electric field of the light at the point $\boldsymbol{r}$. To simplify our analysis, we will neglect the hyperfine structure of the ground level of the atom and

[4]The lecture of years 2012-13, chapter 1, includes a detailed discussion of the light-shift operator.

limit ourselves to the spin degree of freedom of the outer electron. The angular momentum operator $\hat{\boldsymbol{J}}$ will therefore be in the following the spin $1/2$ operator, characterized by the Pauli matrices $\hat{\sigma}_x, \hat{\sigma}_y, \hat{\sigma}_z$.

Before treating the motion of the atom in this potential with the quantum formalism, let us start with a classical reasoning and consider the case of an atom at rest at point $\boldsymbol{r}$. The Hamiltonian can be reduced to the single potential $V(\boldsymbol{r})$; for a spin $1/2$ atom, it is a 2×2 matrix that we can diagonalize at any point $\boldsymbol{r}$ to obtain the two dressed states $|\chi_{\boldsymbol{r}}^{(\pm)}\rangle$, linear combinations of $|\pm\rangle_z$ with energies $\pm|\boldsymbol{\kappa}(\boldsymbol{r})|$:

$$\hat{V}(\boldsymbol{r})\ |\chi_{\boldsymbol{r}}^{(\pm)}\rangle = \pm|\boldsymbol{\kappa}(\boldsymbol{r})|\ |\chi_{\boldsymbol{r}}^{(\pm)}\rangle. \tag{50}$$

Let us now consider the motion of the atom, described in a quantum manner. The most general state (space+spin) can be written as

$$\psi_+(\boldsymbol{r},t)|\chi_{\boldsymbol{r}}^{(+)}\rangle + \psi_-(\boldsymbol{r},t)|\chi_{\boldsymbol{r}}^{(-)}\rangle. \tag{51}$$

The evolution of the two probability amplitudes $\psi_\pm(\boldsymbol{r},t)$ is obtained by injecting this form into the Schrödinger equation governed by the Hamiltonian

$$\hat{H} = \frac{\hat{p}^2}{2m} + \hat{V}(\hat{\boldsymbol{r}}), \tag{52}$$

and it generally reduces to two coupled partial differential equations for the amplitudes $\psi_\pm(\boldsymbol{r},t)$.

We will place ourselves here in the situation where the atom moves slowly enough to follow adiabatically one of the dressed states, for example the lowest dressed state $|\chi^{(-)}\rangle$, without significantly populating the other level. We therefore take $\psi_+(\boldsymbol{r},t) \approx 0$ for any point $\boldsymbol{r}$ and any time t.

The evolution then reduces to a single differential equation for the amplitude $\psi_-(\boldsymbol{r},t)$, in which the dominant terms are:

$$\mathrm{i}\hbar\frac{\partial\psi_-}{\partial t} = -\frac{\hbar^2}{2m}\boldsymbol{\nabla}^2\psi_- \ - \ |\boldsymbol{\kappa}(\boldsymbol{r})|\ \psi_- + \dots \tag{53}$$

However, we know that the adiabatic approximation brings with it additional terms, such as the geometric phase described by a Berry connection. It is precisely these additional terms that can give rise to topological properties for a flux lattice.

For this problem where the adiabatic approximation is used to describe a motion in real space, the Berry connection is defined for the dressed state $|\chi^{(-)}\rangle$ by

$$\boldsymbol{\mathcal{A}}(\boldsymbol{r}) = \mathrm{i}\,\langle\chi_{\boldsymbol{r}}^{(-)}\ |\ \boldsymbol{\nabla}_{\boldsymbol{r}}\chi_{\boldsymbol{r}}^{(-)}\rangle \tag{54}$$

and it contributes to the equation (53) in the form (*cf.* lecture of years 2013-14)

$$\mathrm{i}\hbar\frac{\partial\psi_-}{\partial t} = \frac{\hbar^2}{2m}\left[-\mathrm{i}\boldsymbol{\nabla} - \mathcal{A}(\boldsymbol{r})\right]^2\psi_- \ - \ |\kappa(\boldsymbol{r})|\ \psi_- + \dots \tag{55}$$

The Berry connection thus plays the role of a vector potential for a particle of fictitious charge $e = 1$. The adiabatic approximation is also at the origin of a scalar gauge potential $W(\boldsymbol{r})$ in (55), but we will not write it explicitly because it plays only a minor role in the following.

With (55), we find a quantum Hall situation since we are dealing with the 2D motion of a particle in a (fictitious) magnetic field. This magnetic field is equal to the curl of the vector potential (Berry connection) $\boldsymbol{\mathcal{A}}$ and is thus a Berry curvature in position space. We will note it $\boldsymbol{\mathcal{B}}$:

$$\boldsymbol{\mathcal{B}}(\boldsymbol{r}) = \boldsymbol{\nabla} \times \boldsymbol{\mathcal{A}}(\boldsymbol{r}) \tag{56}$$

to avoid any confusion with the Berry curvature $\boldsymbol{\Omega}(\boldsymbol{q})$ that we have introduced above in momentum space. The question is now whether this effective magnetic field in real space can lead to a topological band for the Hamiltonian (55).

4-3 Flux lattices

A flux lattice is defined as a configuration of light beams for which the flux of the effective magnetic field $\boldsymbol{\mathcal{B}}(\boldsymbol{r})$ through the unit cell of the lattice is non-zero (Cooper 2011). It is thus a configuration for which it is natural to investigate whether it can give rise to topological bands. To discuss this notion in a concrete way, let us consider the following example. Suppose that the laser configuration results in the light-shift operator

$$\hat{V}(\boldsymbol{r}) = \boldsymbol{\kappa}(\boldsymbol{r})\cdot\hat{\boldsymbol{\sigma}} \qquad \text{with} \quad \boldsymbol{\kappa}(\boldsymbol{r}) = \kappa_0\begin{pmatrix}\cos(kx)\\ \cos(ky)\\ \sin(kx)\sin(ky)\end{pmatrix}. \tag{57}$$

It reads in the $|\pm\rangle_z$ basis of the atomic spin states:

$$\hat{V}(\boldsymbol{r}) = \kappa_0 \begin{pmatrix} \sin(kx)\sin(ky) & \cos(kx) - \mathrm{i}\cos(ky) \\ \cos(kx) + \mathrm{i}\cos(ky) & -\sin(kx)\sin(ky) \end{pmatrix}. \tag{58}$$

A unit cell corresponding to the periodicity of $\hat{V}$ is a square of side $2\pi/k$. This configuration can be obtained by superimposing standing waves along the x and y axes with suitable polarizations (Cooper, Dalibard, et al. 2018).

The energies of the dressed states are written

$$\pm|\boldsymbol{\kappa}(\boldsymbol{r})| = \pm\kappa_0 \left[1 + \cos^2(kx)\cos^2(ky)\right]^{1/2}. \tag{59}$$

For the dressed state of lowest energy , $-|\boldsymbol{\kappa}(\boldsymbol{r})|$, the minima of potential are located on the square lattice $kx = n_x\pi$, $ky = n_y\pi$ (figure 27, top). There are four minima of $-|\boldsymbol{\kappa}|$ per unit cell.

The calculation of the effective magnetic field $\mathcal{B}$ is performed using the formula derived in chapter 4

$$\mathcal{B} = -\frac{1}{2|\boldsymbol{\kappa}|^3}\boldsymbol{\kappa}\cdot\left[(\partial_x\boldsymbol{\kappa})\times(\partial_y\boldsymbol{\kappa})\right] \tag{60}$$

which leads to

$$\mathcal{B}_z = -k^2\,\frac{1-\cos^2(kx)\cos^2(ky)}{2\left[1+\cos^2(kx)\cos^2(ky)\right]^{3/2}}. \tag{61}$$

This field is plotted in figure 27, on the bottom. The calculation shows that the flux of this field through the square unit cell of side $2\pi/k$ is equal to 4π.

The fact that the flux is a multiple of 2π is not surprising: we calculate here the integral of a Berry curvature on a zone (x, y) with periodic boundary conditions. A reasoning identical to the one we did in momentum space for the integral of $\Omega(\boldsymbol{q})$ on a Brillouin zone leads to the conclusion that this flux can be seen as 2π times the associated Chern number, which must be an integer.

In the limit of large potential wells where κ_0 becomes large compared to the recoil energy $E_\mathrm{r} = \hbar^2k^2/2m$, we recover the tight-binding limit, in which we can consider only jumps between nearest neighbors on the

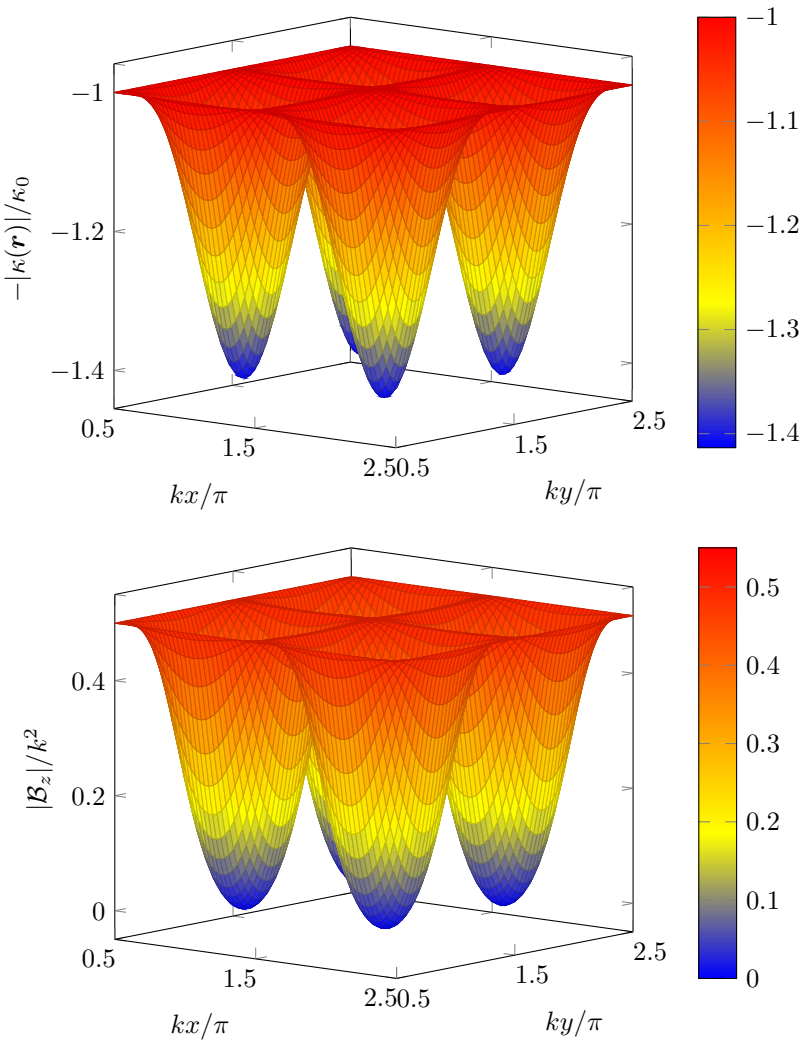

Figure 27. *Top: Variation of the energy of the dressed state $|\chi^{(-)}\rangle$ on a square unit cell of size $2\pi/k$. Bottom: variation of the effective magnetic field $|\mathcal{B}_z|$ for this dressed state.*

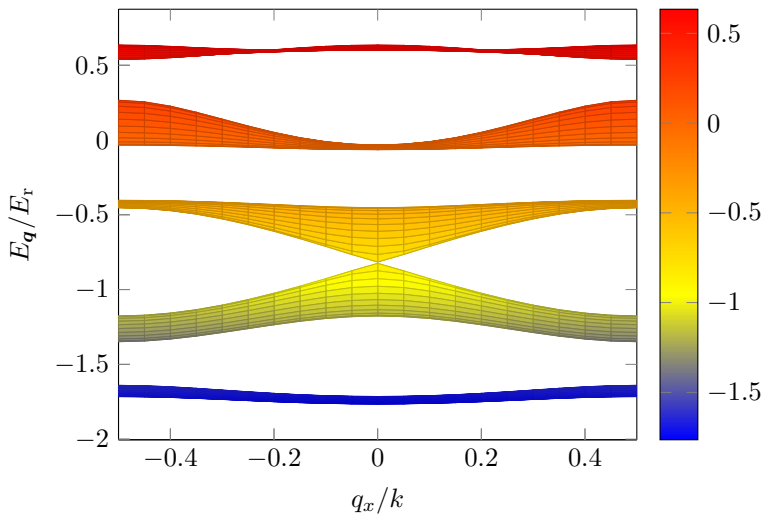

Figure 28. *Lowest energy bands obtained for the Hamiltonian $\hat{H} = \frac{\hat{\boldsymbol{p}}^2}{2m} + \hat{V}(\hat{\boldsymbol{r}})$ where the operator $\hat{V}(\hat{\boldsymbol{r}})$ given in (58) acts in both the space of external and internal variables. The calculation is done for $\kappa_0 = 2E_{\mathrm{r}}$. The lowest band, relatively flat in comparison to the gap that separates it from the first excited band, has Chern number $\mathcal{C} = 1$.*

square lattice composed by the minima of the energy $-|\boldsymbol{\kappa}|$. We have seen (i) that there are four minima per unit cell and (ii) that the flux of $\boldsymbol{B}$ through the unit cell is equal to 4π. This leads to the fact that the flux of $\boldsymbol{B}$ through a single mesh of the lattice of minima is equal to π, and it corresponds to two bands touching at Dirac points.

This regime with bands featuring Dirac points is not favourable to obtaining topological bands. It is better to operate the flux lattice in an intermediate intensity regime, where the coupling κ_0 is of the order of the recoil energy. We then obtain a lowest band separated from the upper bands by a gap, with a Chern number equal to 1. Note that the adiabatic approximation then becomes questionable since the kinetic energy of the particles is comparable to the gap $\pm|\boldsymbol{\kappa}|$ between the dressed potentials. It is therefore more cautious to determine the energy bands from the initial two-component problem, rather than using the approximate expression (55). This is the procedure that has been followed to obtain the energy bands shown in figure 28, for the choice $\kappa_0 = 2\,E_{\mathrm{r}}$.

One of the important points in the physics of flux lattices is the search for quasi-flat energy bands, i.e. with a gap/width ratio as large as possible. The fact that the band is flat makes it easy to obtain a dominant effect of the interactions and thus to approach conditions that are favourable for the observation of effects similar to the fractional quantum Hall effect (Cooper & Dalibard 2013). In practice, for an atom whose ground state has an angular momentum $J = 1$, the gap/width ratio can reach values on the order of 50 (Cooper & Dalibard 2011b).

To our knowledge, the concept of flux lattice has not yet been implemented as such in a laboratory. Let us however point out the recent experiment of Wu, Zhang, et al. (2016) (and its improved version in Sun, Wang, et al. (2017)) which showed the existence of a topological band in a 2D lattice. In both experiments, the scalar part of the light shift played a prominent role; it created a square lattice in which both $|\pm\rangle_z$ spin states were simultaneously trapped, with the experiment taking place in the tight binding regime. The role of the vector part of the light displacement operator was to induce *spin dependent* couplings between nearest neighbors. One then realizes a situation formally similar to the Haldane model, in which there is no flux of the artificial magnetic field $\boldsymbol{B}$, but nevertheless giving rise to a topological band. Wu, Zhang, et al. (2016) have verified the topological nature of this band by measuring the average spin polarization of atoms at different points of the Brillouin zone, following a proposal by Liu, Law, et al. (2013).

4-4 Interactions between dressed states

The whole lecture was almost exclusively dedicated to ensembles of non-interacting particles. The only exception was our discussion of Majorana modes in chapter 2, for which interactions were an indispensable ingredient to make a superconducting gap appear. The combination of topological considerations and interactions in a system with a large number of particles is of course an essential problem, which is still very much open. One can read the article of Repellin & Regnault (2018) as well as part V of the

review of Cooper, Dalibard, et al. (2018) to find a list of recent references on this problem in the context of cold atomic gases.

To conclude this section, we will focus on a binary collision and indicate how the dressing of the levels of an atom allows to modify the interaction in this case. Let us first recall that for atoms in free space and at low temperature, the two-body interaction is dominated by s-wave collisions, which can be described by a contact, and thus local, interaction $g\,\delta(\boldsymbol{r}_1-\boldsymbol{r}_2)$, where the Dirac $\delta(\boldsymbol{r})$ distribution is assumed to be regularized (Huang 1987). We will show that in a flux lattice, the interactions acquire a non-local character due to the momentum dependence of the dressed states.

A dressed state of the lowest band of a flux lattice is written in a general way

$$|\Psi_q\rangle = |\psi_{\boldsymbol{q}}\rangle \otimes |\Sigma_{\boldsymbol{q}}\rangle, \tag{62}$$

i.e. as the product of a Bloch state $|\psi_{\boldsymbol{q}}\rangle$ describing the motion of the center of mass of the atom, and a spin state $|\Sigma_{\boldsymbol{q}}\rangle$. It is the $\boldsymbol{q}$ dependence of this spin state that is at the origin of the non-local interaction that we will find.

Let us start with the simple case of spinless or fully polarized particles. For the contact interaction $\hat{V} = g\,\delta(\hat{\boldsymbol{r}})$, the matrix element of $\hat{V}$ describing the transition of a pair of particles from the initial state $(\boldsymbol{q}_1, \boldsymbol{q}_2)$ to the state $(\boldsymbol{q}_1 + \boldsymbol{q}_t, \boldsymbol{q}_2 - \boldsymbol{q}_t)$ is equal to g (within a normalization factor) and is independent of the transferred momentum $\boldsymbol{q}_t$.

For *indistinguishable* particles, the physical observables involve the sum over the two permutations

$$(\boldsymbol{q}_1, \boldsymbol{q}_2) \quad \rightarrow \quad (\boldsymbol{q}_1 + \boldsymbol{q}_t, \boldsymbol{q}_2 - \boldsymbol{q}_t) \quad \text{and} \quad (\boldsymbol{q}_2 - \boldsymbol{q}_t, \boldsymbol{q}_1 + \boldsymbol{q}_t), \tag{63}$$

with a relative sign $\varepsilon = \pm 1$ depending on whether we are dealing with bosons or fermions. The matrix element of $\hat{V}$ is doubled for polarized bosons and it cancels for polarized fermions: this last result simply reflects the fact that a gas of polarized fermions is insensitive to a contact interaction, since the Pauli principle forbids two fermions to be at the same position.

Now consider the collision between two atoms prepared in the lowest band of a flux lattice (62) and assume for simplicity that the contact interaction is independent of the spin state $|\pm\rangle$. For indistinguishable particles (bosons or fermions), the matrix element of $\hat{V}$ for the two-channel process (63) is

$$\begin{aligned} &\langle \psi_{\boldsymbol{q}_1+\boldsymbol{q}_t}, \psi_{\boldsymbol{q}_2-\boldsymbol{q}_t} | \hat{V} | \psi_{\boldsymbol{q}_1}, \psi_{\boldsymbol{q}_2} \rangle \, \langle \Sigma_{\boldsymbol{q}_1+\boldsymbol{q}_t} | \Sigma_{\boldsymbol{q}_1} \rangle \, \langle \Sigma_{\boldsymbol{q}_2-\boldsymbol{q}_t} | \Sigma_{\boldsymbol{q}_2} \rangle \\ + \varepsilon \quad &\langle \psi_{\boldsymbol{q}_2-\boldsymbol{q}_t}, \psi_{\boldsymbol{q}_1+\boldsymbol{q}_t} | \hat{V} | \psi_{\boldsymbol{q}_1}, \psi_{\boldsymbol{q}_2} \rangle \, \langle \Sigma_{\boldsymbol{q}_2-\boldsymbol{q}_t} | \Sigma_{\boldsymbol{q}_1} \rangle \, \langle \Sigma_{\boldsymbol{q}_1+\boldsymbol{q}_t} | \Sigma_{\boldsymbol{q}_2} \rangle \end{aligned}$$

For fermions, this matrix element is in general no longer zero. In the particular case $\boldsymbol{q}_t = 0$, it is proportional to $\left(1 - |\langle \Sigma_{q_2} | \Sigma_{q_1} \rangle|^2\right)$.

This result indicates that starting from contact-interacting fermions occupying a single energy band, laser dressing leads to an *interacting* gas. More precisely, it can be shown that these interactions in a one-component fermionic gas are essentially in the p wave (Zhang, Tewari, et al. 2008b). This emergence of an interaction between two identical fermions can be seen as a non-adiabatic correction to the laser dressing, which allows two fermions to be at the same point in space, their internal states being slightly different due to their relative velocity (Cooper & Dalibard 2011a).

This conversion from a contact interaction to a momentum-dependent interaction via laser dressing of atomic states also occurs for bosons. For example, Williams, LeBlanc, et al. (2012) have shown that a d-wave collision component appears between ultracold bosons due to this dressing.

References

Adams, EN & EI Blount (1959), "Energy bands in the presence of an external force field—II: Anomalous velocities", in *Journal of Physics and Chemistry of Solids* **10**, pp. 286–303.

Aharonov, Y. & D. Bohm (1959), "Significance of electromagnetic potentials in quantum theory", in *Phys. Rev.* **115**, p. 485.

Aidelsburger, M., M. Atala, M. Lohse, J. T. Barreiro, B. Paredes & I. Bloch (2013), "Realization of the Hofstadter Hamiltonian with Ultracold Atoms in Optical Lattices", in *Phys. Rev. Lett.* **111** (18), p. 185301.

Aidelsburger, M., M. Lohse, C. Schweizer, M. Atala, J. T. Barreiro, S. Nascimbène, N. R. Cooper, I. Bloch & N. Goldman (2015), "Measuring the Chern number of Hofstadter bands with ultracold bosonic atoms", in *Nature Physics* **11**, p. 162.

Alba, E., X. Fernandez-Gonzalvo, J. Mur-Petit, J. K. Pachos & J. J. Garcia-Ripoll (2011), "Seeing Topological Order in Time-of-Flight Measurements", in *Phys. Rev. Lett.* **107**, p. 235301.

Alicea, Jason (2012), "New directions in the pursuit of Majorana fermions in solid state systems", in *Reports on progress in physics* **75**, p. 076501.

Alicea, Jason, Yuval Oreg, Gil Refael, Felix Von Oppen & Matthew PA Fisher (2011), "Non-Abelian statistics and topological quantum information processing in 1D wire networks", in *Nature Physics* **7**, p. 412.

Amo, Alberto (2018), "When quantum optics meets topology", in *Science* **359**, pp. 638–639.

Ashcroft, N. W. & N. D. Mermin (1976), *Solid State Physics*, New York: Holt, Rinehardt and Winston.

Asorey, Manuel (June 2016), "Space, matter and topology", in *Nature Physics* **12**, p. 616.

Atala, Marcos, Monika Aidelsburger, Julio T. Barreiro, Dmitry Abanin, Takuya Kitagawa, Eugene Demler & Immanuel Bloch (2013), "Direct measurement of the Zak phase in topological Bloch bands", in *Nat Phys* **9**, pp. 795–800.

Avan, P, C Cohen-Tannoudji, J Dupont-Roc & C Fabre (1976), "Effect of high-frequency irradiation on dynamical properties of weakly bound electrons", in *Journal de Physique* **37**, 993–1009.

Bahari, Babak, Abdoulaye Ndao, Felipe Vallini, Abdelkrim El Amili, Yeshaiahu Fainman & Boubacar Kanté (2017), "Nonreciprocal lasing in topological cavities of arbitrary geometries", in *Science* **358**, pp. 636–640.

Bandres, Miguel A., Steffen Wittek, Gal Harari, Midya Parto, Jinhan Ren, Mordechai Segev, Demetrios N. Christodoulides & Mercedeh Khajavikhan (2018), "Topological insulator laser: Experiments", in *Science* **359**, p. 4005.

Bardyn, C-E, MA Baranov, E Rico, A İmamoğlu, P Zoller & S Diehl (2012), "Majorana modes in driven-dissipative atomic superfluids with a zero Chern number", in *Physical review letters* **109**, p. 130402.

Barik, Sabyasachi, Aziz Karasahin, Christopher Flower, Tao Cai, Hirokazu Miyake, Wade DeGottardi, Mohammad Hafezi & Edo Waks (2018), "A topological quantum optics interface", in *Science* **359**, pp. 666–668.

Beenakker, Carlo & Leo Kouwenhoven (2016), "A road to reality with topological superconductors", in *Nature Physics* **12**, p. 618.

Beenakker, CWJ (2015), "Random-matrix theory of Majorana fermions and topological superconductors", in *Reviews of Modern Physics* **87**, p. 1037.

Bellec, Matthieu, Ulrich Kuhl, Gilles Montambaux & Fabrice Mortessagne (2013), "Topological transition of Dirac points in a microwave experiment", in *Physical Review Letters* **110**, p. 033902.

Bernevig, B Andrei & Taylor L Hughes (2013), *Topological insulators and topological superconductors*, Princeton University Press.

Bernevig, B Andrei, Taylor L Hughes & Shou-Cheng Zhang (2006), "Quantum spin Hall effect and topological phase transition in HgTe quantum wells", in *Science* **314**, pp. 1757–1761.

Berry, M. V. (1984), "Quantal phase factors accompanying adiabatic changes", in *Proc. Roy. Soc. London A* **392**, pp. 45–57.

– (1989), "The Quantum Phase, Five Years After", in *Geometric Phases in Physics*, ed. by A. Shapere & F. Wilczek, Singapore: World Scientific, , pp. 7–28.

Bilitewski, Thomas & Nigel R. Cooper (2015a), "Population dynamics in a Floquet realization of the Harper-Hofstadter Hamiltonian", in *Phys. Rev. A* **91** (6), p. 063611.

– (2015b), "Scattering theory for Floquet-Bloch states", in *Phys. Rev. A* **91** (3), p. 033601.

Bukov, Marin, Luca D'Alessio & Anatoli Polkovnikov (2015), "Universal high-frequency behavior of periodically driven systems: from dynamical stabilization to Floquet engineering", in *Advances in Physics* **64**, pp. 139–226.

Castro Neto, A. H., F. Guinea, N. M. R. Peres, K. S. Novoselov & A. K. Geim (2009), "The electronic properties of graphene", in *Rev. Mod. Phys.* **81** (1), pp. 109–162.

Celi, A., P. Massignan, J. Ruseckas, N. Goldman, I. B. Spielman, G. Juzeliunas & M. Lewenstein (2014), "Synthetic Gauge Fields in Synthetic Dimensions", in *Phys. Rev. Lett.* **112** (4), p. 043001.

Chang, Ming-Che & Qian Niu (1995), "Berry phase, hyperorbits, and the Hofstadter spectrum", in *Physical Review Letters* **75**, p. 1348.

Chiu, Ching-Kai, Jeffrey C. Y. Teo, Andreas P. Schnyder & Shinsei Ryu (2016), "Classification of topological quantum matter with symmetries", in *Rev. Mod. Phys.* **88** (3), p. 035005.

Choudhury, Sayan & Erich J. Mueller (2015), "Transverse collisional instabilities of a Bose-Einstein condensate in a driven one-dimensional lattice", in *Phys. Rev. A* **91** (2), p. 023624.

Cooper, N. R. (2011), "Optical Flux Lattices for Ultracold Atomic Gases", in *Phys. Rev. Lett.* **106**, p. 175301.

Cooper, N. R. & J. Dalibard (2011a), "Optical flux lattices for two-photon dressed states", in *Europhysics Letters* **95**, p. 66004.

Cooper, Nigel R. & Jean Dalibard (2011b), "Optical Flux Lattices for Two-Photon Dressed States", in *EPL (Europhysics Letters)* **95**, p. 66004.

– (2013), "Reaching Fractional Quantum Hall States with Optical Flux Lattices", in *Phys. Rev. Lett.* **110** (18), p. 185301.

Cooper, NR, J Dalibard & IB Spielman (2018), "Topological Bands for Ultracold Atoms", in *arXiv:1803.00249*.

Dareau, A., E. Levy, M. Bosch Aguilera, R. Bouganne, E. Akkermans, F. Gerbier & J. Beugnon (2017), "Revealing the Topology of Quasicrystals with a Diffraction Experiment", in *Phys. Rev. Lett.* **119** (21), p. 215304.

Delplace, P., D. Ullmo & G. Montambaux (2011), "Zak phase and the existence of edge states in graphene", in *Phys. Rev. B* **84**, p. 195452.

Duca, L., T. Li, M. Reitter, I. Bloch, M. Schleier-Smith & U. Schneider (2015), "An Aharonov–Bohm interferometer for determining Bloch band topology", in *Science* **347**, p. 288.

Eckardt, André (2017), "Colloquium: Atomic quantum gases in periodically driven optical lattices", in *Rev. Mod. Phys.* **89** (1), p. 011004.

Eckardt, Andre & Martin Holthaus (2007), "AC-induced superfluidity", in *EPL (Europhysics Letters)* **80**, p. 50004.

Ehrenberg, W. & R. E. Siday (1949), "The Refractive Index in Electron Optics and the Principles of Dynamics", in *Proceedings of the Physical Society, Series B* **62**, pp. 8–21.

Fläschner, N, BS Rem, M Tarnowski, D Vogel, D-S Lühmann, K Sengstock & C Weitenberg (2016), "Experimental reconstruction of the Berry curvature in a Floquet Bloch band", in *Science* **352**, pp. 1091–1094.

Gerbier, Fabrice & Jean Dalibard (2010), "Gauge fields for ultracold atoms in optical superlattices", in *New Journal of Physics* **12**, p. 033007.

Goldman, N, JC Budich & P Zoller (2016), "Topological quantum matter with ultracold gases in optical lattices", in *Nature Physics* **12**, pp. 639–645.

Goldman, N. & J. Dalibard (2014), "Periodically Driven Quantum Systems: Effective Hamiltonians and Engineered Gauge Fields", in *Phys. Rev. X* **4** (3), p. 031027.

Goldman, N., J. Dalibard, M. Aidelsburger & N.R. Cooper (2015), "Periodically driven quantum matter: The case of resonant modulations", in *Phys. Rev. A* **91**, p. 033632.

Goldman, Nathan, Egidijus Anisimovas, Fabrice Gerbier, P Öhberg, IB Spielman & G Juzeliūnas (2013), "Measuring topology in a laser-coupled honeycomb lattice: from Chern insulators to topological semi-metals", in *New journal of physics* **15**, p. 013025.

Gu, Zhenghao, H. A. Fertig, Daniel P. Arovas & Assa Auerbach (2011), "Floquet Spectrum and Transport through an Irradiated Graphene Ribbon", in *Phys. Rev. Lett.* **107** (21), p. 216601.

Hafezi, Mohammad, Eugene A Demler, Mikhail D Lukin & Jacob M Taylor (2011), "Robust optical delay lines with topological protection", in *Nature Physics* **7**, p. 907.

Hafezi, Mohammad, S Mittal, J Fan, A Migdall & JM Taylor (2013), "Imaging topological edge states in silicon photonics", in *Nature Photonics* **7**, p. 1001.

Haldane, F. D. M. (1988), "Model for a Quantum Hall Effect without Landau Levels: Condensed-Matter Realization of the "Parity Anomaly"", in *Phys. Rev. Lett.* **61**, pp. 2015–2018.

Haldane, F Duncan M (1983), "Nonlinear field theory of large-spin Heisenberg antiferromagnets: semiclassically quantized solitons of the one-dimensional easy-axis Néel state", in *Physical Review Letters* **50**, p. 1153.

Haldane, FDM & S Raghu (2008), "Possible realization of directional optical waveguides in photonic crystals with broken time-reversal symmetry", in *Physical Review Letters* **100**, p. 013904.

Harari, Gal, Miguel A. Bandres, Yaakov Lumer, Mikael C. Rechtsman, Y. D. Chong, Mercedeh Khajavikhan, Demetrios N. Christodoulides & Mordechai Segev (2018), "Topological insulator laser: Theory", in *Science* **359**, p. 1230.

Harper, P. G. (1955), "Single Band Motion of Conduction Electrons in a Uniform Magnetic Field", in *Proceedings of the Physical Society. Section A* **68**, pp. 874–878.

Hasan, M. Z. & C. L. Kane (2010), "*Colloquium* : Topological insulators", in *Rev. Mod. Phys.* **82** (4), pp. 3045–3067.

Hatsugai, Y. & T. Fukui (2016), "Bulk-edge correspondence in topological pumping", in *Phys. Rev. B* **94** (4), p. 041102.

Hatsugai, Yasuhiro (1993), "Chern number and edge states in the integer quantum Hall effect", in *Phys. Rev. Lett.* **71**, pp. 3697–3700.

Hauke, Philipp, Maciej Lewenstein & André Eckardt (2014), "Tomography of Band Insulators from Quench Dynamics", in *Phys. Rev. Lett.* **113**, p. 045303.

Hofstadter, D. R. (1976), "Energy levels and wave functions of Bloch electrons in rational and irrational magnetic fields", in *Phys. Rev. B* **14**, pp. 2239–2249.

Huang, K. (1987), *Statistical Mechanics*, New York: Wiley.

Huber, Sebastian D (2016), "Topological mechanics", in *Nature Physics* **12**, p. 621.

Iemini, Fernando, Leonardo Mazza, Davide Rossini, Rosario Fazio & Sebastian Diehl (2015), "Localized Majorana-Like Modes in a Number-Conserving Setting: An Exactly Solvable Model", in *Phys. Rev. Lett.* **115** (15), p. 156402.

Jacqmin, Thibaut, Iacopo Carusotto, Isabelle Sagnes, Marco Abbarchi, DD Solnyshkov, Guillaume Malpuech, Elisabeth Galopin, Aristide Lemaître, Jacqueline Bloch & Alberto Amo (2014), "Direct observation of Dirac cones and a flatband in a honeycomb lattice for polaritons", in *Physical Review Letters* **112**, p. 116402.

Jaksch, D. & P. Zoller (2003), "Creation of effective magnetic fields in optical lattices: the Hofstadter butterfly for cold neutral atoms", in *New Journal of Physics* **5**, p. 56.1.

Jotzu, G., M. Messer, R. Desbuquois, M. Lebrat, T. Uehlinger, D. Greif & T. Esslinger (2014), "Experimental realization of the topological Haldane model with ultracold fermions", in *Nature* **515**, pp. 237–240.

Kane, Charles L & Eugene J Mele (2005a), "Quantum spin Hall effect in graphene", in *Phys. Rev. Lett.* **95**, p. 226801.

– (2005b), "Z 2 topological order and the quantum spin Hall effect", in *Phys. Rev. Lett.* **95**, p. 146802.

Karplus, Robert & J. M. Luttinger (1954), "Hall Effect in Ferromagnetics", in *Phys. Rev.* **95** (5), pp. 1154–1160.

Khanikaev, Alexander B & Gennady Shvets (2017), "Two-dimensional topological photonics", in *Nature Photonics* **11**, p. 763.

Kitaev, A. Y. (2001), "Unpaired Majorana fermions in quantum wires", in *Physics Uspekhi* **44**, p. 131.

Kohmoto, M. (1985), "Topological Invariant and the Quantization of the Hall Conductance", in *Annals of Physics* **160**, pp. 343–354.

Kolkowitz, S, SL Bromley, T Bothwell, ML Wall, GE Marti, AP Koller, X Zhang, AM Rey & J Ye (2017), "Spin–orbit-coupled fermions in an optical lattice clock", in *Nature* **542**, p. 66.

König, Markus, Steffen Wiedmann, Christoph Brüne, Andreas Roth, Hartmut Buhmann, Laurens W Molenkamp, Xiao-Liang Qi & Shou-Cheng Zhang (2007), "Quantum spin Hall insulator state in HgTe quantum wells", in *Science* **318**, pp. 766–770.

Kraus, Yaacov E & Oded Zilberberg (2016), "Quasiperiodicity and topology transcend dimensions", in *Nature Physics* **12**, p. 624.

Lazarides, Achilleas, Arnab Das & Roderich Moessner (2014), "Periodic Thermodynamics of Isolated Quantum Systems", in *Phys. Rev. Lett.* **112** (15), p. 150401.

Lellouch, S., M. Bukov, E. Demler & N. Goldman (2017), "Parametric Instability Rates in Periodically Driven Band Systems", in *Phys. Rev. X* **7** (2), p. 021015.

Liu, Xiong-Jun, Kam-Tuen Law, Tai-Kai Ng & Patrick A Lee (2013), "Detecting topological phases in cold atoms", in *Phys. Rev. Lett* **111**, p. 120402.

Livi, LF, G Cappellini, M Diem, L Franchi, C Clivati, M Frittelli, F Levi, D Calonico, J Catani, M Inguscio, et al. (2016), "Synthetic dimensions and spin-orbit coupling with an optical clock transition", in *Phys. Rev. Lett.* **117**, p. 220401.

Lodahl, Peter, Sahand Mahmoodian, Søren Stobbe, Arno Rauschenbeutel, Philipp Schneeweiss, Jürgen Volz, Hannes Pichler & Peter Zoller (2017), "Chiral quantum optics", in *Nature* **541**, p. 473.

Lohse, M., C. Schweizer, O. Zilberberg, M. Aidelsburger & I. Bloch (Apr. 2016), "A Thouless quantum pump with ultracold bosonic atoms in an optical superlattice", in *Nat Phys* **12**, pp. 350–354.

Lu, H.-I, M. Schemmer, L. M. Aycock, D. Genkina, S. Sugawa & I. B. Spielman (2016), "Geometrical Pumping with a Bose-Einstein Condensate", in *Phys. Rev. Lett.* **116**, p. 200402.

Lu, Ling, John D Joannopoulos & Marin Soljačić (2014), "Topological photonics", in *Nature Photonics* **8**, p. 821.

– (2016), "Topological states in photonic systems", in *Nature Physics* **12**, p. 626.

Majorana, Ettore (1937), "Teoria simmetrica dell'elettrone e del positrone", in *Il Nuovo Cimento (1924-1942)* **14**, p. 171.

Mancini, M, G Pagano, G Cappellini, L Livi, M Rider, J Catani, C Sias, P Zoller, M Inguscio, M Dalmonte, et al. (2015), "Observation of chiral edge states with neutral fermions in synthetic Hall ribbons", in *Science* **349**, pp. 1510–1513.

Mead, C. Alden & Donald G. Truhlar (1979), "On the determination of Born–Oppenheimer nuclear motion wave functions including complications due to conical intersections and identical nuclei", in *J. Chem. Phys.* **70**, pp. 2284–2296.

Messiah, A. (1961), *Quantum Mechanics, Chapter XVII, § 13*, vol. II, Amsterdam: North-Holland Publishing Company.

– (2003), *Mécanique Quantique*, Dunod.

Mikitik, G. P. & Yu. V. Sharlai (1999), "Manifestation of Berry's Phase in Metal Physics", in *Phys. Rev. Lett.* **82**, pp. 2147–2150.

Milićević, Marijana, Tomoki Ozawa, Gilles Montambaux, Iacopo Carusotto, Elisabeth Galopin, Aristide Lemaître, L Le Gratiet, Isabelle Sagnes, Jacqueline Bloch & Alberto Amo (2017), "Orbital edge states in a photonic honeycomb lattice", in *Physical Review Letters* **118**, p. 107403.

Miyake, Hirokazu, Georgios A. Siviloglou, Colin J. Kennedy, William Cody Burton & Wolfgang Ketterle (2013), "Realizing the Harper Hamiltonian with Laser-Assisted Tunneling in Optical Lattices", in *Phys. Rev. Lett.* **111** (18), p. 185302.

Montambaux, G., F. Piéchon, J.-N. Fuchs & M. O. Goerbig (2009), "Merging of Dirac points in a two-dimensional crystal", in *Phys. Rev. B* **80** (15), p. 153412.

Mourik, Vincent, Kun Zuo, Sergey M Frolov, SR Plissard, Erik PAM Bakkers & Leo P Kouwenhoven (2012), "Signatures of Majorana fermions in hybrid superconductor-semiconductor nanowire devices", in *Science* **336**, pp. 1003–1007.

Nadj-Perge, Stevan, Ilya K Drozdov, Jian Li, Hua Chen, Sangjun Jeon, Jungpil Seo, Allan H MacDonald, B Andrei Bernevig & Ali Yazdani (2014), "Observation of Majorana fermions in ferromagnetic atomic chains on a superconductor", in *Science* **346**, pp. 602–607.

Nakajima, Shuta, Takafumi Tomita, Shintaro Taie, Tomohiro Ichinose, Hideki Ozawa, Lei Wang, Matthias Troyer & Yoshiro Takahashi (2016), "Topological Thouless pumping of ultracold fermions", in *Nature Physics* **12**, p. 296.

Nascimbene, Sylvain (2013), "Realizing one-dimensional topological superfluids with ultracold atomic gases", in *J. Phys. B: At. Mol. Opt. Phys.* **46**, p. 134005.

Oka, Takashi & Hideo Aoki (2009), "Photovoltaic Hall effect in graphene", in *Phys. Rev. B* **79** (8), p. 081406.

Ozawa, Tomoki, Hannah M Price, Alberto Amo, Nathan Goldman, Mohammad Hafezi, Ling Lu, Mikael Rechtsman, David Schuster, Jonathan Simon, Oded Zilberberg, et al. (2018), "Topological Photonics", in *arXiv:1802.04173*.

Pancharatnam, S. (1956), "Generalized Theory of Interference, and Its Applications. Part I. Coherent Pencils", in *Proc. Indian Acad. Sci. A* **44**, pp. 247–262.

Poli, Charles, Matthieu Bellec, Ulrich Kuhl, Fabrice Mortessagne & Henning Schomerus (2015), "Selective enhancement of topologically induced interface states in a dielectric resonator chain", in *Nature communications* **6**, p. 6710.

Qi, Xiao-Liang & Shou-Cheng Zhang (2011), "Topological insulators and superconductors", in *Rev. Mod. Phys.* **83** (4), pp. 1057–1110.

Rahav, Saar, Ido Gilary & Shmuel Fishman (2003), "Effective Hamiltonians for periodically driven systems", in *Phys. Rev. A* **68** (1), p. 013820.

Rechtsman, Mikael C, Julia M Zeuner, Yonatan Plotnik, Yaakov Lumer, Daniel Podolsky, Felix Dreisow, Stefan Nolte, Mordechai Segev & Alexander Szameit (2013a), "Photonic Floquet topological insulators", in *Nature* **496**, p. 196.

Rechtsman, Mikael C, Julia M Zeuner, Andreas Tünnermann, Stefan Nolte, Mordechai Segev & Alexander Szameit (2013b), "Strain-induced pseudomagnetic field and photonic Landau levels in dielectric structures", in *Nature Photonics* **7**, p. 153.

Repellin, Cécile & Nicolas Regnault (2018), "Lattices for fractional Chern insulators", in *Science* **360**, pp. 31–32.

Rice, MJ & EJ Mele (1982), "Elementary excitations of a linearly conjugated diatomic polymer", in *Physical Review Letters* **49**, p. 1455.

Ruhman, Jonathan, Erez Berg & Ehud Altman (2015), "Topological States in a One-Dimensional Fermi Gas with Attractive Interaction", in *Phys. Rev. Lett.* **114** (10), p. 100401.

St-Jean, P, V Goblot, E Galopin, A Lemaître, T Ozawa, L Le Gratiet, I Sagnes, J Bloch & A Amo (2017), "Lasing in topological edge states of a one-dimensional lattice", in *Nature Photonics* **11**, p. 651.

Stuhl, BK, H-I Lu, LM Aycock, D Genkina & IB Spielman (2015), "Visualizing edge states with an atomic Bose gas in the quantum Hall regime", in *Science* **349**, pp. 1514–1518.

Su, W. P., J. R. Schrieffer & A. J. Heeger (1979), "Solitons in Polyacetylene", in *Phys. Rev. Lett.* **42**, pp. 1698–1701.

Sun, Wei, Bao-Zong Wang, Xiao-Tian Xu, Chang-Rui Yi, Long Zhang, Zhan Wu, Youjin Deng, Xiong-Jun Liu, Shuai Chen & Jian-Wei Pan (2017), "Long-lived 2D Spin-Orbit coupled Topological Bose Gas", in *ArXiv eprints*, p. 1710.00717.

Tarruell, Leticia, Daniel Greif, Thomas Uehlinger, Gregor Jotzu & Tilman Esslinger (2012), "Creating, moving and merging Dirac points with a Fermi gas in a tunable honeycomb lattice", in *Nature* **483**, p. 302.

Thouless, D. J. (1983), "Quantization of particle transport", in *Phys. Rev. B* **27**, pp. 6083–6087.

Thouless, D. J., M. Kohmoto, M. P. Nightingale & M. den Nijs (1982), "Quantized Hall Conductance in a Two-Dimensional Periodic Potential", in *Phys. Rev. Lett.* **49**, pp. 405–408.

Torrent, Daniel & José Sánchez-Dehesa (2012), "Acoustic analogue of graphene: observation of Dirac cones in acoustic surface waves", in *Physical Review Letters* **108**, p. 174301.

Velasco, Carlos G & Belén Paredes (2017), "Realizing and Detecting a Topological Insulator in the AIII Symmetry Class", in *Physical Review Letters* **119**, p. 115301.

Von Klitzing, Klaus (1986), "The quantized Hall effect", in *Reviews of Modern Physics* **58**, p. 519.

Wang, Zheng, Yidong Chong, John D Joannopoulos & Marin Soljačić (2009), "Observation of unidirectional backscattering-immune topological electromagnetic states", in *Nature* **461**, p. 772.

Weimann, S, M Kremer, Y Plotnik, Y Lumer, S Nolte, KG Makris, M Segev, MC Rechtsman & A Szameit (2017), "Topologically protected bound states in photonic parity–time-symmetric crystals", in *Nature materials* **16**, p. 433.

Williams, R. A., L. J. LeBlanc, K. Jimenez-Garcia, M. C. Beeler, A. R. Perry, W. D. Phillips & I. B. Spielman (2012), "Synthetic Partial Waves in Ultracold Atomic Collisions", in *Science* **335**, pp. 314–317.

Wimmer, Martin, Hannah M Price, Iacopo Carusotto & Ulf Peschel (2017), "Experimental measurement of the Berry curvature from anomalous transport", in *Nature Physics* **13**, p. 545.

Wu, Long-Hua & Xiao Hu (2015), "Scheme for achieving a topological photonic crystal by using dielectric material", in *Physical review letters* **114**, p. 223901.

Wu, Zhan, Long Zhang, Wei Sun, Xiao-Tian Xu, Bao-Zong Wang, Si-Cong Ji, Youjin Deng, Shuai Chen, Xiong-Jun Liu & Jian-Wei Pan (2016), "Realization of two-dimensional spin-orbit coupling for Bose-Einstein condensates", in *Science* **354**, pp. 83–88.

Xiao, Di, Ming-Che Chang & Qian Niu (2010), "Berry phase effects on electronic properties", in *Rev. Mod. Phys.* **82** (3), pp. 1959–2007.

Yan, Zhongbo, Shaolong Wan & Zhong Wang (2015), "Topological Superfluid and Majorana Zero Modes in Synthetic Dimension", in *Scientific Reports* **5**, p. 15927.

Zak, J. (1989), "Berry's phase for energy bands in solids", in *Phys. Rev. Lett.* **62** (23), pp. 2747–2750.

Zhang, Chuanwei, Sumanta Tewari, Roman M. Lutchyn & S. Das Sarma (2008a), "$p_x + ip_y$ Superfluid from s-Wave Interactions of Fermionic Cold Atoms", in *Phys. Rev. Lett.* **101** (16), p. 160401.

– (2008b), "$p_x + ip_y$ Superfluid from s-Wave Interactions of Fermionic Cold Atoms", in *Phys. Rev. Lett.* **101** (16), p. 160401.

Zhang, Peng, Koichiro Yaji, Takahiro Hashimoto, Yuichi Ota, Takeshi Kondo, Kozo Okazaki, Zhijun Wang, Jinsheng Wen, GD Gu, Hong Ding, et al. (2018), "Observation of topological superconductivity on the surface of an iron-based superconductor", in *Science*, p. 4596.

Zhang, Shou-Cheng & Jiangping Hu (2001), "A four-dimensional generalization of the quantum Hall effect", in *Science* **294**, pp. 823–828.